HYDROGEN PRODUCTION BY ETHANOL STEAM REFORMING USING Ni/Al_2O_3 CATALYST

AHMED M. BSHISH

THESIS SUBMITTED IN FULFILMENT FOR THE DEGREE OF DOCTOR OF PHILOSOPHY

FACULTY OF ENGINEERING AND BUILT ENVIRONMENT
UNIVERSITI KEBANGSAAN MALAYSIA
BANGI

2014

PENGELUARAN HIDROGEN MELALUI PEMBENTUKAN SEMULA STIM ETANOL MENGGUNAKAN MANGKIN Ni/Al_2O_3

AHMED M. BSHISH

TESIS YANG DIKEMUKAKAN UNTUK MEMPEROLEH IJAZAH
DOKTOR FALSAFAH

FAKULTI KEJURUTERAAN DAN ALAM BINA
UNIVERSITI KEBANGSAAN MALAYSIA
BANGI

2014

DECLARATION

I hereby declare that the work in this thesis is my own except for quotations and summaries, which have been duly acknowledged.

20 March 2014

AHMED M. BSHISH
P46835

ACKNOWLEDGEMENTS

(All praise be to Allah, the Beneficent, the Merciful)

I am pleased to express my deepest sense of gratitude and sincere devotion to my supervisor Prof. Ir. Dr. Zahira Yaakob, Department of chemical& Process Engineering Faculty of Engineering & Built Environment Universiti Kebangsaan (UKM) for her continuous supervision and helpful suggestions during the entire progress of this research. She gave me a valuable chance to come to Malaysia and made me more independent. Such a flexible supervision helped me achieve a fruitful scientific output during my research.

I dedicate this work to my father Mohammed Bshish who passed away recently and my mother Salha Salem for her encouragement and patience. I believe that she was always around to support me during the hard time doing a PhD in Malaysia. I can imagine how happy she is when I get the PhD. Happens doubled especially when she sees her grandchildren first time.

I would like to thank my wife Sumia. Her support, encouragement, and quiet patience were undeniably the bedrock upon which the past six years of my life have been built.

The author wishes to extend the thanks to all staff members of Department of Chemical& Process Engineering Faculty of Engineering & Built Environment, Faculty of Engineering and Built Environment for their co-operation.

I am very grateful to Prof. Dr. Mohammed Alghoul for his assistance and advices regarding to my work. My great thanks are devoted to my close friend Dr. Aouache Mustapha for his valuable knowledge and advices related to the modelling part.

The author wishes to thank his brothers and sisters for their encouragement throughout the research work.

My journey as a student has come to an end with the completion of this dissertation. Many people have shared my best and worst moment during the past few years at the National University of Malaysia. I would like to thank them all, and special thanks to my uncle Ali on his wisdom especially during the hard time.

ABSTRACT

Hydrogen production by steam reforming of ethanol is an interesting choice since ethanol can be produced from renewable sources. There is no agreement on the most suitable catalytic system for hydrogen production via ethanol steam reforming. Hence, the work to develop an active and selective catalytic system for this application is still in progress. Thus, the aim of this work is firstly to carry out a complete thermodynamic analysis to understand the effect of operating conditions on ethanol conversion and gaseous products. Then, attention was paid to developing a high performance catalyst system for production of hydrogen via ethanol steam reforming, and also on developing an integrated system capable of predicting H_2 yield using artificial neural network (ANN) model. Therefore, a thermodynamic equilibrium analysis was performed over the following variable ranges: pressure 1–50 atm, temperature 300–900 K, and water-to-ethanol feed ratio 3:1-12:1. A catalyst study was performed to investigate the performance of nickel as an active metal, supported on γ-Al_2O_3. Two series of catalysts with various Ni loadings (6, 8, 10, 12, and 20 wt%) were prepared by impregnation and precipitation methods and were tested in ethanol reforming reaction. The catalysts were characterized by BET, XRD, TPR, and SEM–EDAX. The result showed that lower Ni loading catalysts were more efficient in H_2 production, as evidenced by the finding that a 6 wt% Ni catalyst, synthesized via the precipitation method, yielded 3.68 mol H_2 per mol ethanol fed. Moreover, sol gel made alumina supports prepared for nickel catalysts were calcined at different temperatures. A series of sol gel made alumina support catalysts were synthesized by an impregnation procedure. The nickel content in all samples was fixed at 6 wt %. These catalysts were characterized by BET, XRD, TPR, TPD, and CHNS elemental analysis. The influence of varying the calcination temperature of the sol gel made supports on catalyst activity was tested. The result showed that, the structure of the sol gel made alumina supports was transformed in the order of $\gamma \rightarrow (\gamma + \theta) \rightarrow \theta$- alumina as the calcination temperature of the supports increased from 600 °C to 1000 °C. Both hydrogen yield and ethanol conversion presented a volcano-shaped behaviorwith maximum values of 4.3 mol/mol ethanol fed and 99.5%, respectively. The highest performance was exhibited over a catalyst calcined at 800^{o}C which may be attributed to the strong interaction of Ni species and sol gel made alumina that led to high nickel dispersion and small particle size. Statistical approach using response surface methodology (RSM) and central composite design (CCD) was employed to optimize the process variables. The optimal conditions were obtained at a temperature of 500 °C, a water–ethanol molar ratio of 20, and liquid hourly space velocity (LHSV) of 0.72 h^{-1}. These optimal conditions resulted in a hydrogen yield of 4.7 mol/mol of ethanol fed, an ethanol gasification of 85%, and a CO yield of 0.25 mol/mol of ethanol fed. Finally, a multi-layer ANN model was examined and trained to predict H_2 yield, CO yield, and ethanol conversion. The study considered the effect of temperature, water–ethanol molar ratio, and LHSV as ANN inputs on hydrogen yield, ethanol gasification, and CO yield as outputs. The performance of the ANN model has verified and demonstrated effectiveness with a significant efficiency of 0.91, 0.84, and 0.95 for H_2, CO, and ethanol, respectively. In conclusion, this research has achieved its stated goal of developing a catalyst system for ethanol steam reforming reaction capable of maximizing hydrogen yield.

ABSTRAK

Pengeluaran hidrogen melalui pembentukan semula stim etanol adalah satu pilihan menarik memandangkan etanol boleh dihasilkan daripada sumber boleh diperbaharui. Tiada terdapat persetujuan tentang sistem bermangkin paling sesuai untuk pengeluaran hidrogen melalui pembentukan semula stim etanol. Maka, dalam bidang penyelidikan ini kerja membangunkan sistem bermangkin yang aktif dan terpilih untuk aplikasi ini masih dimajukan. Oleh itu, tujuan kajian ini adalah pertamanya, untuk menjalankan analisis termodinamik bagi memahami kesan keadaan pengendalian ke atas penukaran etanol dan produk bergas dan keduanya, membangunkan sistem mangkin berprestasi tinggi bagi menghasilkan hidrogen melalui pembentukan semula stim etanol dan satu sistem bersepadu yang mampu meramalkan hasil H_2 menggunakan model rangkaian neural buatan (ANN). Satu analisis keseimbangan termodinamik telah dilakukan ke atas pembolehubah berikut: tekanan 1-50atm, suhu – 300-900K, dan nisbah air ke atas suapan etanol 3:1-12:1. Satu kajian mangkin untuk menyiasat prestasi nikel sebagai logam aktif, disokong atas γ-Al_2O_3 telah dijalankan. Dua siri mangkin dengan pelbagai bebanan Ni (6, 8, 10, 12, dan 20 % berat) telah disediakan dengan kaedah pengisitepuan dan pemendakan dan diuji dalam tindak balas pembentukan semula etanol. Mangkin telah dicirikan oleh BET, XRD, TPR, dan SEM-EDAX. Hasil kajian menunjukkan mangkin bebanan Ni yang lebih rendah lebih berkesan dalam penghasilan H_2, seperti dibuktikan oleh dapatan di mana mangkin Ni 6 % berat, disintesiskan melalui kaedah PT, menghasilkan 3.68 mol H_2 per etanol disuap. Sokongan sol-gel alumina yang disediakan untuk mangkin nikel telah dikalsin pada suhu berbeza. Beberapa siri mangkin sokongan sol-gel alumina telah disintesiskan oleh satu prosedur pengisitepuan. Kandungan nikel dalam kesemua sampel ditetapkan pada 6 % berat. Mangkin-mangkin ini telah dicirikan oleh analisis unsur BET, XRD, TPR, TPD, dan CHNS. Pengaruh mempelbagaikan suhu pengkalsinan sokongan sol-gel ke atas keaktifan mangkin telah diuji. Hasil menunjukkan struktur sokongan sol-gel alumina telah dijelmakan dalam turutan alumina $\gamma \rightarrow (\gamma + \theta) \rightarrow \theta$ bila suhu kalsinasi sokongan meningkat dari 600 °C to 1000 °C. Kedua-dua hasil hidrogen dan penukaran etanol menunjukkan kelakuan berbentuk gunung berapi dengan nilai maksima masing-masing 4.3 mol/mol etanol disuap dan 99.5%. Prestasi tertinggi dipamerkan oleh mangkin dikalsin pada 800^{o}C yang boleh dikaitkan dengan interaksi kuat spesies Ni dan sol-gel alumina yang membawa kepada serakan nikel yang tinggi dan saiz zarah yang kecil. Pendekatan statistik menggunakan perkaedahan tindak balas permukaan telah digunakan untuk mengoptimumkan pembolehubah proses. Keadaan optima telah diperolehi pada suhu 500 °C, nisbah molar air-etanol 20, dan LHSV 0.72 h^{-1}. Keadaan optima ini menghasilkan pengeluaran hidrogen sebanyak 4.7 mol/mol etanol disuap, pengegasan etanol sebanyak 85%, dan hasil CO sebanyak 0.25 mol/mol etanol disuap. Satu model ANN pelbagai lapisan telah dikaji dan dilatih untuk meramalkan hasil H_2, CO, dan penukaran etanol. Kesan suhu, nisbah molar air-etanol, dan LHSV sebagai input ANN ke atas hasil hidrogen, pengegasan etanol, dan hasil CO sebagai output telah dipertimbangkan. Prestasi model ANN telah disahkan dan ditunjukkan keberkesanannya dengan kecekapan signifikan pada 0.91, 0.84, dan 0.95 masing-masing untuk H_2, CO, dan etanol. Kesimpulannya, kajian ini telah mencapai matlamatnya untuk membangunkan satu sistem mangkin bagi tindak balas pembentukan semula stim etanol yang mampu memaksimakan hasil hidrogen.

CONTENTS

LIST OF FIGURES

LIST OF TABLES

NOMENCLATURE

A_i, B_i, C_i, *and* D_i	Constant for a chemical formula of species *i*
Cp	Heat capacity, kJkg $^{-1}$ K^{-1}
Cp^o	Standard heat capacity
C	Constant
c	Supported metal weight, wt%
D	Particle size of the sample, (nm)
D_m	Metal dispersion
d	Mean particle diameter, (nm)
$F_{ETOH_{in}}$	Molar flow rate of ethanol inlet of the reactor
$F_{ETOH_{out}}$	Molar flow rate of ethanol outlet of the reactor
$F_{i_{,out}}$	Molar flow rate of product gas outlet of the reactor
$\Delta G^O_{298.}$	Standard free Gibbs energy change, Jmol^{-1}
$\Delta G^O_{freact.}$	Standard Gibbs energy of formation of reactants, Jmol^{-1}
$\Delta G^O_{fprod.}$	Standard Gibbs energy of formation of products, Jmol^{-1}
$\Delta H^O_{298.}$	Standard enthalpy change, Jmol^{-1}
$\Delta H^O_{freact.}$	Standard enthalpies of formation of reactants, Jmol^{-1}
$\Delta H^O_{fprod.}$	Standard enthalpies of formation of products, Jmol^{-1}
K_P	Equilibrium constant for ethanol reforming reaction
K	Constant
$max(X_i)$	Maximum data
MW	Supported metal atomic weight

N	Number of values in the dataset
Nor_X	Normalized data of the input and the output
n_T	Total number of moles
$n_i o$	Initial moles of species i
no	Total number of initial moles
P	Operating pressure, atm
P_o	Standard-state pressure, 1 atm
P_r	Reduced pressure, atm
P_c	Critical pressure, atm
R	Ideal gas constant, J mol^{-1} K^{-1}
SD	Standard deviation
$S.A._{.m}$	Metal surface area (per g catalyst)
SF	Stoichiometry factor = 1
T	Reaction temperature, K
T_O	Standard temperature = 298 K
T_r	Reduced temperature, K
T_c	Critical temperature, K
$V_{chem.}$	Chemisorption volume, mol g^{-1}
V	Volume of adsorbed gas at pressure P
V_M	Volume of adsorbed gas in monolayer
V_i	Stoichiometric number of species i
X_i	Actual input /output before scaling (normalization)
x_i and x_j	Input variables

x	Mean of all values in the dataset
$\bar{x}$	Each value in the dataset
y_{Exp}	Vector of n experimental values
y_{ANN}	Vector of predicted values
y_i	Mole fraction of species *i*
Y_i	Response variables ($Y_{H_{2,Y}}$, $Y_{ETOH_{Con.}}$, and $Y_{CO,Y}$)

Greek Letter

ϕ_i	Fugacity coefficient of species *i*
ε	Reaction coordinate
β_{ij}	Formula coefficient matrix
b_j	Element vector
μ_i	Chemical potential of species *i*
λ_j	Lagrangian multiplier
λ	Wavelength usually for Cu Kα radiation
β	Width of diffraction line at (FWHM) in radian
θ	The angle between the incident and diffracted beams
σ_m	Supported metal cross section area = 0.0649 nm atom^{-1}
ρ	Supported metal density
β_0	Constant
β_j, β_{jj}, and β_{ij}	Linear, quadratic, and interaction effect coefficients

Abbreviations

ANN	Artificial neural network
Eff	Efficiency
EXP	Exponential
FWHM	Full width half maximum
MSE	Mean square error
IMP	Impregnation
PT	Precipitation
S.G.	Sol gel
M.R.	Molar ratio
STP	Standard temperature and pressure conditions
GC	Gas-chromatograph
LHSV	Liquid hourly space velocity

CHAPTER I

INTRODUCTION

1.1 BACKGROUND INFORMATION

Hydrogen is considered a promising source of clean energy, specifically as fuel in fuel cell systems. Automakers around the world have spent more than two billion dollars on the research and development of fuel-cell-powered vehicles (buses, cars, and trucks) in the hope of producing environmentally friendly cars by the end of the century (Rifkin 2003). Hydrogen is one of the cleanest and greenest sources of electrical energy, and it can be used in various chemical industries, particularly chemical production. Molecular hydrogen is a clean-burning fuel (the only by-products being heat and water). Unfortunately, hydrogen does not exist in nature in its elemental form and, therefore, has to be produced from hydrocarbons, water, or other hydrogen-containing compounds such as alcohol. The negative environmental and economic impact of fossil fuels and the continuous decline in natural petroleum resources make hydrogen a potential alternative fuel for fuel cells because hydrogen fuel cells are efficient without emitting greenhouse gases (Zinoviev et al. 2010).

1.2 HYDROGEN PRODUCTION

About 38 million tons of hydrogen are produced globally per year. The demand for hydrogen is expected to grow in the near future as hydrogen starts penetrating the transportation sector as a fuel (Levin & Chahine 2010). Considerable work has been conducted to determine hydrogen demand in Malaysia based on its supply of gasoline and diesel from surveys of local stations (Kamarudin et al. 2009).

Several methods are commonly used for hydrogen production, including water electrolysis (Dubey et al. 2010), gasification (Comas et al. 2004), partial oxidation reactions of heavy oil (Wang et al. 2009b) , and steam reforming of hydrocarbons (Chen et al. 2011; Le Valant et al. 2011). The biological production of H_2 (bio-hydrogen) using microorganisms is a possible source of renewable H_2 from biomass. These methods are described in the next chapter.

1.3 ETHANOL REFORMING

Steam reforming is a practicable process of hydrogen production from ethanol, which is easily produced, stored, and safely handled. Ethanol also is more easily transported as it is less toxic than other alcohols (Cavallaro & Freni 1996). Hydrogen production via ethanol is CO_2-neutral because the amount of CO_2 emitted into the atmosphere is absorbed from the air by the agricultural materials used to produce the same amount of ethanol. Thus, the use of ethanol does not contribute to global warming. Furthermore, ethanol only contains carbon, hydrogen, and oxygen atoms, and does not contain any other hetero atoms that may lead to the emission of NO_x and SO_x gases into the atmosphere, therefore making ethanol an important source of energy (Akande et al. 2005). Based on these features, the hydrogen produced from the steam reforming of ethanol is a convenient energy carrier.

In general, the main source of hydrogen varies with the geographical location of hydrogen demand. For instance, in countries with ample electrical resources, water electrolysis is preferred. By contrast, in Malaysia and adjacent countries, bio fuels (e.g., bio ethanol) produced by the fermentation of renewable materials are ideal hydrogen carriers because of the productive agriculture and extensive plantations, such as rice hulls and oil palm plantations, present in these countries.

Steam reforming and partial oxidation are the primary methods of converting ethanol into hydrogen. Ethanol steam-reforming reaction is an endothermic reaction that requires a heat supply (provided by steam) and a reaction temperature of about

300 °C for the reaction to take place. By contrast, partial oxidation is exothermic and the temperature of the reaction may exceed 400 °C.

The ethanol steam-reforming reaction produces 6 moles of H_2 per a mole of reacted ethanol.

$$C_2H_5OH + 3H_2O \rightarrow 6H_2 + 2CO_2, \quad \Delta H^{298} = 174\ KJ\ mol^{-1} \tag{1.1}$$

However, ethanol can undergo other reactions under steam-reforming conditions. Several reaction pathways and the thermodynamics of ethanol steam reforming have been proposed in the literature (Ni et al. 2007; Rabenstein et al. 2008; Rossi et al. 2009; Vaidya & Rodrigues 2006).

1.4 PROBLEM STATEMENT

The production of hydrogen produced by ethanol steam reforming depends on the reaction conditions and the catalyst used. Despite high hydrogen production, a critical issue is the high reaction temperature required, which favors the formation of CO. Therefore, additional purification processes to convert CO are required, resulting in higher production cost and the need for larger ethanol processors.

Different catalyst systems are used for ethanol steam reforming. Noble-metal-based catalysts show high catalyst activity in hydrogen production by means of ethanol steam reforming. However, the high cost of such metals severely limits their use in hydrogen production via ethanol steam reforming. Nickel-based catalysts, particularly Ni/Al_2O_3, are also used in ethanol steam reforming with limitations. Although nickel content plays a significant role in the interaction between the nickel and the support, which affects the dispersion of the nickel species on the support surface, the effect of Ni loading on the characteristics and activities of the Ni/Al_2O_3 catalyst used in ethanol steam reforming do not draw an end conclusion of its effect on catalyst characterization and performance.

The sol-gel technique is significant for catalyst preparation because of its high thermal stability and resistance to catalyst deactivation. Limited studies have used the sol-gel method to prepare catalysts for hydrogen production. A literature survey shows that hydrogen production using nickel supported on sol-gel-made alumina ($Ni/Al_{S.G}$) catalyst via steam reforming of ethanol has yet to be investigated. Therefore, in the present study, we investigate this method at different calcination temperatures to enhance the catalyst properties of Ni/Al_2O_3 and to determine the optimum conditions for a Ni/Al_2O_3 catalyst system that improves H_2 production by means of ethanol steam reforming.

It is important to notice that majority of hydrogen production studies have been determined using the traditional (one-variable-at-a-time) experimental approach that assumes no interaction between the variables (Ghafari et al. 2009), so the correct optimum conditions for hydrogen yield and ethanol conversion are not achieved. Therefore, the application of an experimental design and a mathematical modeling technique as a mathematical tool is essential.

Previous studies indicate that computer-aided analysis and modeling using an artificial neural network (ANN) is feasible and that performing a significant number of experiments can be avoided. Therefore, this study proposes a new method to simulate the relation between reaction parameters and hydrogen production using ANN. In addition, certain catalyst components are costly to purchase in large quantities. The use of advanced modeling techniques such as ANN can prevent the repetition of experiments by developing a modeling strategy that extracts the relation between input/output parameters in the ethanol steam-reforming reaction. Thus, to overcome the above-mentioned problems, a list of objectives is given in the following section.

1.5 RESEARCH OBJECTIVES

The overall objective of this study is to maximize hydrogen yield and ethanol conversion to optimize the performance of Ni/Al_2O_3 catalysts in ethanol steam-

reforming reaction. Therefore, the goal of this study is to find an active and selective Ni/Al_2O_3 catalyst for ethanol steam reforming and to optimize the reaction conditions of this reaction. The specific objectives of this study are divided into the following tasks:

1) To determine the ethanol conversion and H_2, CO, CO_2, and CH_4 yields theoretically using the thermodynamic approaches.
2) To design and fabricate a laboratory scale reactor capable to produce hydrogen via ethanol steam reforming reaction.
3) To synthesize and characterize Ni/Al_2O_3 catalysts prepared by impregnation, precipitation and sol gel methods.
4) To evaluate H_2 production and ethanol conversion over the prepared catalysts.
5) To optimize and predict H_2 yield, CO yield, and ethanol conversion using numerical and ANN models.

1.6 SCOPE OF THE STUDY

The present study was divided into three main sections. First section focused on a thermodynamic analysis of ethanol steam reforming reaction. This section considers the effect of temperature, pressure, and reactants molar ratio on ethanol conversion and product yields. This was performed based on the equilibrium constant and minimization of the Gibbs energy methods. The second section focused on Ni/Al_2O_3 catalyst screening to select the best catalyst conditions for H_2 production. Catalysts were first synthesized by impregnation and precipitation to investigate the effect of Ni loading on catalyst performance. Catalyst characterization was performed by BET surface area, nitrogen adsorption-desorption isotherm, XRD, SEM, and TPR to obtain the relationships between the catalyst characteristics and its performance. Then, sol gel synthesis technique was implemented for further optimization of Ni/Al_2O_3 catalyst. Sol gel supports and catalysts were characterized by BET surface area, pore volume and pore size, nitrogen adsorption-desorption isotherm, XRD, SEM, TPR, TPD, and CHNS elemental analysis. The sol-gel method was not compared with the impregnation and precipitation methods since the alumina support used in sol gel catalysts is not commercial one, and we doubt if we compare with the commercial

alumina will loss the uniformity. Also, the high cost of the precursor used in the synthesis method and that limited our sol gel experiments. The criteria used to evaluate catalyst performance included ethanol conversion and product yield. Modeling section was the last section in this study. First part of this section aimed to optimize reaction variables that control H_2 production. The optimization process was performed using response surface methodology (RSM) with central composite design (CCD) to evaluate maximum hydrogen yield and ethanol conversion, and the minimum CO yield. Second part of the modeling section aimed to predict H_2 yield, ethanol conversion, and CO yield by developing an artificial intelligence model and construct an integrated system for user interface.

1.7 THESIS DESCRIPTION

Chapter 1 provides a background on this research. Chapter 2 presents a literature review of hydrogen production technologies, catalytic systems used for hydrogen production via ethanol steam reforming, and the application of ANNs in catalyst fields.

Chapter 3 is divided into three parts. The first part explains the thermodynamic methods used for thermodynamic analysis, namely, stoichiometric and non-stoichiometric thermodynamic approaches. The second part describes the catalyst preparation and characterization techniques, the analytical method used to evaluate catalyst performance, and the experimental apparatus. The final part of Chapter 3 focuses on the definitions and implementation of the basic elements of the statistical and ANN models.

Chapter 4 reports the results of the thermodynamic analysis of ethanol steam reforming, and discusses the results of catalyst performance in terms of catalyst characterization as well as the evaluation of hydrogen production via ethanol steam reforming. Building statistical and ANN models for the optimization and prediction of hydrogen production are also presented in Chapter 4. Finally, Chapter 5 presents the conclusion of the study and recommendations for future study.

CHAPTER II

LITERATURE REVIEW

2.1 INTRODUCTION

In this chapter, hydrogen production technologies are briefly discussed. Hydrogen production by means of ethanol steam reforming is also reviewed. The thermodynamic aspects of ethanol reforming are discussed. Possible reactions that may occur during ethanol steam reforming are considered with their relative enthalpies. The most active catalytic system in hydrogen production is a subject of debate. Therefore, a review of different catalytic systems (different metals, supports, and preparation methods) available for hydrogen production from ethanol steam reforming is performed as part of the literature review for this study.

The last two sections in this chapter give a brief review of two methods used for modeling: statistical design of experiment and ANN. The review includes a discussion of these two techniques in catalyst fields.

2.2 HYDROGEN PRODUCTION TECHNOLOGIES

Hydrogen may be produced using a number of processes, including water electrolysis, gasification, and catalytic reformation of hydrogen-rich organic compounds.

2.2.1 Hydrogen Production by Water Electrolysis

Production of H_2 by water electrolysis involves passing an electric current through a conductive electrolyte in water to split water molecules into hydrogen and oxygen.

Hydrogen produced by water electrolysis is relatively high quality because no carbon, sulfur, or nitrogenous compounds are generated in the process (Levin & Chahine 2010).

2.2.2 Coal Gasification

Coal gasification is a process that converts coal into gas. Figure 2.1 illustrates the gasification process. The gasification steps are as follows (Song 2003).

a) Gasification

In this step, coal is exposed to hot steam and oxygen under high temperature and pressure. The coal turns into a very hot synthesis gas consisting of carbon dioxide, carbon monoxide, and hydrogen, as well as small quantities of other gases.

b) Cooling and Cleaning

The synthesis gas is cooled and cleaned to remove the other gases and particles, leaving only carbon monoxide, carbon dioxide, and hydrogen. During this step, mercury, sulfur, trace contaminants, and other particles are removed from the synthesis gas.

c) Shifting

After cleaning, the synthesis gas is sent to a shift reactor to convert carbon monoxide into more hydrogen and carbon dioxide.

d) Separation and Purification

Once the synthesis gas shifts, the steam consisting of hydrogen and carbon dioxide is separated. Once separated, the hydrogen is ready for use. The carbon dioxide is captured.

2.2.3 Gasification of Biomass

Hydrogen can also be produced by thermal gasification of biomass, such as straw, solid waste, and forestry by-products. Similar to coal gasification, this process generates a complex mixture of gases, such as CO, CO_2, CH_4, and longer chain hydrocarbons. The most important advantage of this process is that the hydrogen stream contains very low CO concentration, which is ideal for fuel cell applications. However, this technology is very expensive owing to high energy requirements and the energy loss inherent to biomass gasification (Prins et al. 2005). Tanksale et al. (2010) conducted an extensive study of hydrogen production from biomass.

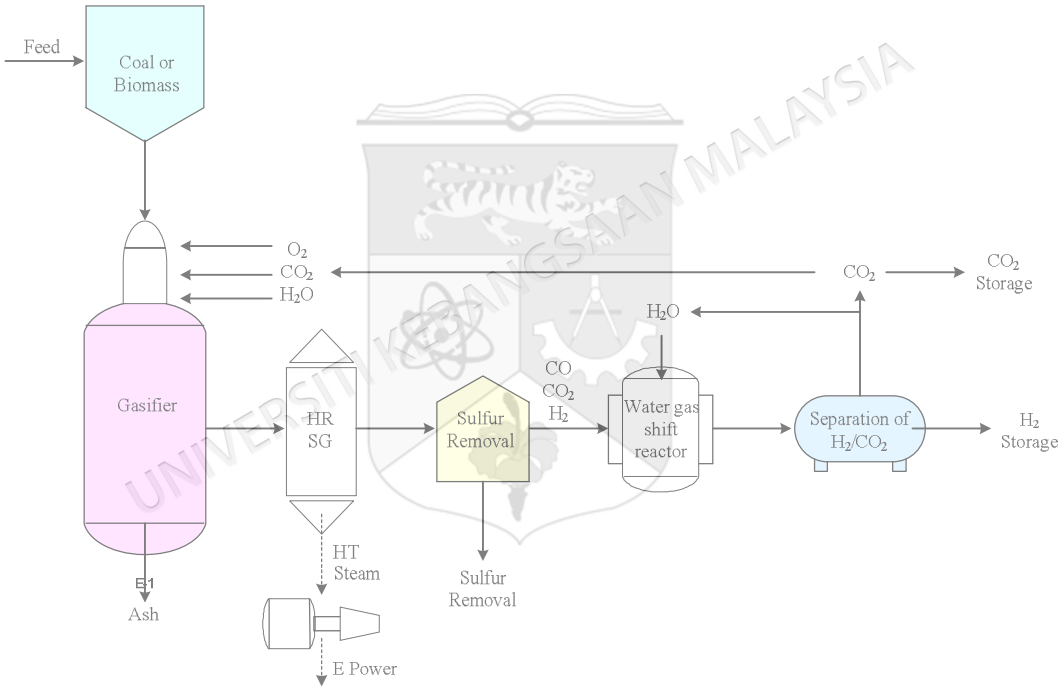

Figure 2.1 Scheme of the gasification process for H_2 production from coal and/or biomass

Source: Song 2003

2.2.4 Hydrogen Production by Steam Reforming of Hydrocarbons

Hydrocarbon steam reforming has been an important process in the production of hydrogen and synthesis gas for decades. Different hydrocarbons, such as ethanol, methanol, and glycerol, are used with a variety of catalyst systems and parameters.

However, in practice, the steam-reforming process faces many challenges. The choice of catalytic system components plays an important role in hydrocarbon steam reforming. The next section in this chapter provides an overview of catalytic steam reforming of ethanol for hydrogen production.

2.3 ETHANOL STEAM REFORMING (ESR)

The variety of possible ethanol steam reforming reactions and the corresponding reactions enthalpies are summarized in Table 2.1. It can be seen that ethanol reforming varies significantly with different reaction pathways as discussed below.

Ethanol steam reforming (ESR) with insufficient steam supply will produce CO and CH_4 as by-products with a decreased amount of H_2 as in Equations (2.2) and (2.3). Dehydrogenation of ethanol leads to the formation of acetaldehyde as a by-product which, upon decomposition, will again lead to the formation of CO and CH_4 (Equations (2.4) and (2.5)). Acetaldehyde steam-reforming will result in the formation of 2 moles of CO per mole of acetaldehyde (Equation (2.6)). The methane produced can also undergo steam reforming which will produce CO in addition to H_2 (Equation (2.7)).

Table 2. 1 Possible reactions of ethanol steam-reforming

Equation	Reaction	ΔH^okJmol^{-1}	Eq. No.
$C_2H_5OH + 3H_2O \rightarrow 2CO_2 + 6H_2$	Ethanol reforming	174	(2.1)
$C_2H_5OH + H_2O \rightarrow 2CO + 4H_2$	Incomplete reforming	256	(2.2)
$C_2H_5OH + 2H_2O \rightarrow 2CH_4 + H_2O$		–157	(2.3)
$C_2H_5OH \rightarrow CH_3CHO + H_2$	Dehydrogenation to acetaldehyde	68	(2.4)
$CH_3CHO \rightarrow CH_4 + CO$	Acetaldehyde decomposition	–18.9	(2.5)
$CH_3CHO + H_2O \rightarrow 3H_2 + 2CO$	Acetaldehyde steam reforming	296.5	(2.6)
$CH_4 + H_2O \rightarrow CO + 3H_2$	Methane steam reforming	205	(2.7)
$C_2H_5OH \rightarrow C_2H_4 + H_2O$	Ethanol dehydration to ethylene	45	(2.8)
$C_2H_5OH \rightarrow 0.5CO_2 + 1.5CH_4$	Ethanol decomposition	–74	(2.9)
$C_2H_5OH \rightarrow CO + CH_4 + H_2$	Ethanol decomposition	49	(2.10)
$2C_2H_5OH \rightarrow CH_3COCH_3 + CO + 3H_2$	Ethanol decomposition	141.5	(2.11)
$2CO \rightarrow CO_2 + C$	Boudouard reaction	–171.5	(2.12)
$C_2H_4 \rightarrow polymers \rightarrow C$	Carbon deposits formation	52.47	(2.13)
$CO + H_2O \rightarrow CO_2 + H_2$	Water gas shift reaction	– 41.2	(2.14)
$CO + 0.5O_2 \rightarrow CO_2$	Oxidation reactions	– 238	(2.15)
$C_2H_5OH + 0.5O_2 \rightarrow CH_3CHO + H_2O$		– 172.9	(2.16)
$CH_4 + 2O_2 \rightarrow CO_2 + 2H_2O$		– 802.5	(2.17)
$C + O_2 \rightarrow CO$		– 110.5	(2.18)

Ethanol dehydration to ethylene is one of the undesirable reactions on the catalysts (Equation (2.8)). The ethylene formed can undergo polymerization leading to coke formation (Equation (2.13)). Decomposition of ethanol results in the production of CO_2, CH_4, as well as acetone. Coke is also formed as a result of the Boudouard reaction from the CO (Equation (2.12)). Water-gas shift reaction converts CO to CO_2

and H_2 is also produced (Equation (2.14)). In the presence of O_2, oxidation reactions can occur, leading to the formation of CO_2, CH_3CHO, CO, and H_2O (Equations (2.15) to (2.18)) (Benito et al. 2005; Frusteri et al. 2004b). The task of developing catalytic systems which can give a high hydrogen yield, low carbon monoxide concentration, and inhibit the reactions responsible for coke formation is regarded as a major challenge in this area of research.

2.3.1 A thermodynamic Approach of Ethanol Steam Reforming

The thermodynamic aspects of the ethanol steam reforming system have received great attention among researchers working in this area. Operating conditions such as temperature, pressure, water-to-ethanol molar ratio, and residence time have been optimized to maximize hydrogen production. The thermodynamic analysis provides an insight into the effects of these variables on the process of ethanol reforming.

The effect of temperature on the catalyst performance has been extensively studied in the temperature range of 100–850◦C. As temperature increases, ethanol conversion and hydrogen yield increase and C_2 species are converted to C_1 species. In an earlier study by García and Laborde (1991), it was found that high temperature, high water-to-ethanol feed ratio, and low pressure led to an increase in hydrogen yield and reduced the concentration of by-products. The optimum conditions to maximise hydrogen production and minimise carbon monoxide and methane formation were temperatures above 700◦C, atmospheric pressure, and 10:1 water-to-ethanol molar ratio. Vasudeva et al. (1996) investigated the thermodynamic parameters of ethanol steam-reforming in a temperature range from 525◦C to 925◦C and 20:1water-to-ethanol molar ratio in the feed. Under these conditions, a complete conversion of ethanol was achieved at all temperatures. They also found that, by increasing the temperature up to 925◦C, the equilibrium amount of methane and carbon dioxide decreased, whereas the amount of carbon monoxide increased. The hydrogen-to-ethanol molar ratio increased when temperature increased from 525◦C to 625◦C. A further increase in temperature up to 925◦C resulted in a decline of the H_2 moles.

Freni et al. (1996) studied the influence of temperature, pressure, and water-to-ethanol molar ratio on the yield of hydrogen. They found that, by increasing the temperature from 600◦C to 700◦C, the amount of hydrogen produced increased from 46.8 % to 58.95 %. Also, low pressure enhanced hydrogen production. Undesirable products such as carbon monoxide, carbon, and methane could be reduced by a high water-to-ethanol molar ratio in the feed. The use of a high water-to-ethanol molar ratio resulted in high selectivity for hydrogen, reducing the amount of CO and CH_4 generated as well as preventing carbon deposition on the catalyst (Yang et al. 2006). However, using a ratio higher than the stoichiometric could lead to an increase in the energy requirement for water evaporation.

Another group of researchers proposed a two-stage process for ethanol steam-reforming (Ioannides 2001). First, steam-reforming of ethanol in which ethanol was converted to gaseous products (H_2, CO, CO_2, and CH_4) at a high temperature was followed by a water-gas shift reaction in which CO_2 was formed by reacting CO with water at low temperature. An additional step to remove the remaining CO was needed because the water gas shift reaction is equilibrium-limited. A water-to ethanol molar ratio of 5:1 and a temperature of 727◦C were observed as the best conditions for providing maximum hydrogen yield. The ethanol steam reforming reaction was found to be predominant at or above 700 K when high water-to-ethanol ratios were used which could also minimise carbon dioxide and methane formation (Fishtik et al. 2000).

The effect of pressure has not been widely investigated since most of the studies on ethanol steam reforming have been carried out at ambient pressure. By increasing the pressure, ethanol conversion and hydrogen yield decrease. Aupretre et al. (2005) noted that the activity of the catalyst increased as the pressure increased (up to 11 bar), whereas there was a reduction in the hydrogen yield. Aupretre et al. (2001) and Aupretre et al. (2004) observed that H_2 and CO yields decreased as the total pressure increased, while the equilibrium content of CH_4 increased. Benito et al. (2005) have achieved a complete ethanol conversion and high hydrogen selectivity (70 %) at 700◦C with CO_2, CO, and CH_4 being the only by-products obtained. The hydrogen yield was 4.25 moles of hydrogen per a mole of ethanol fed. Mas et al.

(2006) found that, even though hydrogen production increased at high temperatures and at high water-to-ethanol ratios, low temperatures and lower water-to-ethanol ratios were preferable to minimise CO formation in the product. At a stoichiometric water-to-ethanol molar ratio, temperatures higher than 500 K are required to avoid coke formation.

Ethanol steam reforming was described by a route leading to reducing the Gibbs free energy (Comas et al. 2004). The optimum operating conditions for ethanol steam-reforming were found to be a water-to-ethanol molar ratio of 4, reactor temperature of approximately 700◦C, and atmospheric pressure. Vaidya and Rodrigues (2006) provided a basic reaction scheme for ethanol steam-reforming. Another review by Ni et al. (2007) focused on the type of metal catalyst used, the type of precursors, preparation methods, the type of catalyst support, presence of additives, and the effect of operating conditions on ethanol conversion and hydrogen selectivity.

Another research was conducted for hydrogen production from ethanol using steam reforming, partial oxidation, and combined auto thermal reforming (Rabenstein et al. 2008). This study presented a change in the equilibrium compositions of ethanol-reforming, with a steam-to-ethanol ratio (0-10), oxygen to- ethanol ratio (0-2.5), and temperature (150- 1000◦C) at atmospheric pressure. In ethanol steam reforming, the optimum conditions obtained were: a temperature range of 550-650◦C and steam-to-ethanol ratios above 4 at atmospheric pressure. The hydrogen yield under this condition was 4 moles per mole of ethanol. In partial oxidation, a high hydrogen yield was observed together with high CO concentration. Due to the higher carbon monoxide content found in the product, partial oxidation itself of ethanol was not preferred in hydrogen production from ethanol. The main advantages of the combined method were reduced coke formation and lower energy demand. They concluded that the best method in terms of energy required to run the operation was steam-reforming followed by auto-thermal-reforming and partial oxidation.

Rossi et al. (2009) was thermodynamically analyzed the steam reforming of ethanol and glycerine for hydrogen production, and compare it with previous

experiments in the literature. They suggested that it was desirable to carry out the thermodynamic analysis before actually undertaking the experiment, since it predicted the best operating conditions that could minimise undesirable reactions.

2.4 CATALYTIC SYSTEMS FOR ETHANOL STEAM REFORMING

The development of a catalyst that is efficient at low temperatures, thereby preventing the formation of undesired by-products, is the most pressing research concern in this field. Various catalytic systems have been tested to use ethanol reforming in hydrogen production. The following discussion focuses on the ethanol steam-reforming performance of various catalytic systems.

2.4.1 Noble Metals

Noble metals such as Ru, Rh, Pd, Pt, Ir, Au on various supports are well-known for their high catalytic activity and have been studied extensively in terms of ethanol steam-reforming reactions (ESR). Breen et al. (2002) used Rh, Pd, and Pt on different supports. Rh has shown excellent activity with alumina as a support. In the ceria/zirconia-supported catalysts, the noble metals activity decreased in the order of Pt-loaded catalyst, Rh-loaded catalyst, Pd-loaded catalyst. Similar results were obtained by Liguras et al. (2003) as well with a catalyst having a metal content of 0–5 mass %.

Alternatively, Cavallaro et al. (2003) showed that deactivation of Rh/Al_2O_3 catalyst had occurred by metal sintering and coke formation. The use of Rh/Al_2O_3 as a reforming catalyst at 650◦C resulted in the formation of mainly CO_2, CH_4, CH_3CHO, and CO. A high conversion of ethanol was achieved at a gas hourly space velocity (GHSV) between 5000 h^{-1} and 80000 h^{-1}. The catalyst stability was also monitored with and without the presence of oxygen. The catalyst was more stable in the presence of O_2. The factors that can hinder coke formation are found to be operating at low temperatures, high Rh-loading, and high steam-to-ethanol molar ratio (Freni et al. 2002). Erdohelyi et al. (2006) performed a reforming reaction using Al_2O_3 and CeO_2-supported noble metal catalysts. It was found that water enhanced the stability of

ethoxide surface species formed by the dissociation of ethanol. Dehydration of ethanol to ethylene was noted on alumina-supported noble metal catalysts.

Among the noble metals on various supports, Rh is found to be the most active metal in the ethanol steam-reforming reactions. Table 2.2 shows the basic results of the selected studies on steam-reforming of ethanol using noble metal catalysts (Breen et al. 2002; Diagne et al. 2002; Erdohelyi et al. 2006; Frusteri et al. 2004b; Men et al. 2007; Romero-Sarria et al. 2008). However, the high cost and low availability of these noble metals is a major limiting factor in their use for hydrogen production via steam reforming.

Table 2.2 Noble metals used in ethanol steam-reforming

Active metal/support	Catalytic performance		Reference
	Ethanol conversion,%	H_2 selectivity,%	
Single metal/single support catalysts			
Rh/γ-Al_2O_3	100	~ 70	
Pt/γ-Al_2O_3	100	~ 45	Breen et al. (2002)
Pd/γ-Al_2O_3	100	~ 50	
Pd/MgO	10	70	Frusteri et al. (2004b)
Ru/CeO_2	> 90	57	Erdohelyi et al. (2006)
Rh/ZrO_2	100	~ 70	Diagne et al. (2002)
Single metal/mixed support catalysts			
Rh/CeO_2–ZrO_2	~ 100	~ 70	
Pt/CeO_2–ZrO_2	~ 100	~ 75	Breen et al. (2002)
Pd/CeO_2–ZrO_2	~ 100	~ 65	
Bimetallic/mixed support catalysts			
Rh–Co/CeO_2–ZrO_2	100	66	Romero-Sarria et al. (2008)
Rh–Ni/CeO_2–Al_2O_3	99.7	73.7	Men et al. (2007)

2.4.2 Non-Noble Metals

a) Cobalt- based catalyst

Cobalt-based catalysts were also extensively studied for ethanol-reforming. Llorca et al. (2002) studied the effect of low cobalt-loading (1 mass %) on different supports (γ-Al_2O_3, SiO_2, TiO_2, V_2O_5, ZnO, Sm_2O_3, and CeO_2). Cobalt-addition was found to positively influence the performances of several oxides in the catalytic production of hydrogen from ethanol, which was attributed to the ability of cobalt to promote C—C bond cleavage at temperatures as low as 400◦C. Batista et al. (2003) suggested that the Co_3O_4 and other CoO_x species interacting with Al_2O_3 or MgO were not active. The catalyst activity increased when the cobalt compounds were reduced to metallic cobalt.

Batista et al. (2004) studied the activity of cobalt on Al_2O_3 and SiO_2 carriers and suggested Co_3O_4 as the main phase of cobalt present in these systems. These catalysts showed a 70 % conversion of ethanol at 400◦C. An increase in ethanol conversion was observed with higher cobalt content. Kaddouri and Mazzocchia (2004) reported a high catalytic activity for both catalysts, Co/SiO_2 and Co/Al_2O_3, in steam-reforming of ethanol and concluded that the product distribution depended on the nature of the support as well as on the method of catalyst preparation.

A kinetic study of steam-reforming of ethanol using Co/Al_2O_3 catalysts was performed by Sahoo et al. (2007). The optimum operating conditions suggested for achieving maximum hydrogen production and minimum carbon monoxide and methane formation by steam-reforming of ethanol were a temperature of 773 K, a steam-to ethanol molar ratio of 3–5, and a contact time of 15–17 kg mol^{-1} s. In a comparative study conducted by Freni et al. (2003) on the catalytic performance of two metals, Ni and Co on MgO support, it was observed that Ni/MgO catalysts had greater activity and selectivity for hydrogen production than Co/MgO catalysts, owing to the greater possibility of metallic cobalt than metallic nickel to oxidise during the reaction.

The evolution of Co_3O_4 during ethanol steam reforming was investigated using XRD measurements by de la Peña O'Shea et al. (2007). Up to 275◦C, the presence of only Co_3O_4 crystalline phase was observed and, under these conditions, ethanol was dehydrogenated to acetaldehyde. Between 300 – 375◦C, the Co_3O_4 phase was found to be transformed into an admixture of Co_3O_4 and CoO. Above 375◦C, the catalyst became very active and selective for the ESR, with CH_4 as the only by-product. Auprêtre et al. (2002) showed the influence of the nature of the metal as well as the role of the support on catalytic activity. The activity of the catalyst in the steam-reforming reaction increased when the mobility of the –OH groups at the catalytic surface increased. The selectivity of the catalyst towards CO_2 decreased, resulting in a greater efficiency of the catalyst in water-gas shift reaction.

One important factor which determines the activity of the catalytic system is the extent of dispersion of the metal active phase on the support. Song et al. (2007) conducted H_2 chemisorptions on 10 mass % of cobalt supported on γ-Al_2O_3, TiO_2, and ZrO_2 . The authors concluded that an increase in the dispersion of cobalt increased the conversion of ethanol and the yield of hydrogen. The cobalt-dispersion was highest on ZrO_2, followed by γ-Al_2O_3 and TiO_2.

The effect of Fe, Ni, Cu, Cr, and Na (1 mass %) addition to the ZnO-supported Co (10 mass %) catalysts on the production of hydrogen in the steam-reforming of ethanol (ESR) and water-gas shift reaction (WGS) was studied by Casanovas et al. (2010). Catalysts promoted with Fe and Cr performed better in the ESR, and the sample promoted with Fe showed high activity to the WGS at low temperatures.

b) Copper- based catalyst

Some research groups consider copper to be a good candidate for ethanol steam-reforming. Copper is effective for dehydrogenation of ethanol because of its high ability to maintain the C—C bond (Chang et al. 2006). Nishiguchi et al. (2005) studied steam-reforming of ethanol on CuO/CeO_2 catalytic system. With copper catalysts, the main reaction products at temperatures below 300◦C were H_2 and

acetaldehyde. The formation of acetone occurred at 380◦C. The overall reaction is as follows:

$$2C_2H_5OH + H_2O \rightarrow CH_3COCH_3 + CO_2 + 4H_2 \quad (2.19)$$

In single metal copper-based catalysts, aggregation of copper on the surface of the support occurs at high temperature, causing a decline in activity of the catalyst. That is why in most cases copper catalysts are combined with other metals and they are discussed in the next section.

c) Nickel-based catalysts

Nickel-based catalysts are comparatively less expensive and widely used in the hydrogenation and steam reforming of hydrocarbons. Several research groups have carried out detailed investigations on catalysts having nickel on different supports.

1) Nickel catalysts with single support

Reforming reaction was carried out using various catalysts with Ni on La_2O_3, yttria-stabilized zirconia (YSZ), and MgO (Fatsikostas et al. 2002b). According to their observations, from among the different catalytic systems selected, Ni/La_2O_3 catalyst exhibited the highest activity in hydrogen production. The ESR activities of Ni/Y_2O_3 and Ni/La_2O_3 catalysts using nickel oxalate as precursor were investigated by Sun et al. (2005). It was found that the Ni/Y_2O_3 and Ni/La_2O_3 catalysts exhibited high activity in ethanol steam-reforming. In their study, Ni/Y_2O_3 exhibited comparatively lower activity in ethanol steam-reforming and hydrogen selectivity. However, both catalysts exhibited long term stability in the ethanol steam-reforming reaction.

Ni/MgO catalyst has been studied in steam reforming of ethanol by Freni et al. (2002). It was found that, because of the presence of the MgO support, there was a reduction in the amount of carbon decomposition on the catalyst. At higher temperatures (above 600◦C), nickel-based catalysts became more effective in ethanol steam-reforming giving H_2, CO, CO_2, and CH_4 as the main reaction products (Benito et al. 2007; Fatsikostas et al. 2002a; Fatsikostas & Verykios 2004)

Nickel–lanthanum composite oxides, LaNiO*x*, were used in steam-reforming of ethanol by Liu et al. (2010). The composite oxides were prepared by co precipitation– oxidation (PO) assisted by ultrasonic irradiation. The authors observed that the ethanol conversion reached completion at around 325◦C and the yield of hydrogen approached its highest value at about 375◦C. Investigations using other oxides as a support for Ni catalysts in the catalytic systems were performed by Yang et al. (2006). Even though all the catalysts achieved a complete conversion of ethanol, Ni/ZnO was found to give the best selectivity for hydrogen production compared with the other supported catalysts studied (Ni/La_2O_3 and Ni/MgO). Frusteri et al. (2004a) examined the effect of the addition of alkali (e.g. Li, Na, K) on the performance of Ni/MgO catalyst in bio-ethanol steam-reforming. Li and K enhanced the stability of Ni/MgO, mainly by diminishing Ni sintering.

A series of Ni catalysts supported on Al-SBA-15 was prepared and catalytic activity studies on ethanol steam-reforming were performed by Lindo et al. (2010). The authors found that the incorporation of Al atoms into the SBA-15 structure resulted in the formation of more acidic sites in the catalyst, an increase in size of the nickel species and stronger metal–support interaction between Ni and Al-SBA-15 carrier. With those catalysts containing a higher Al content, longer reaction time was required for ethanol conversion and Ni/Al-SBA-15 catalysts produced larger amounts of ethylene and coke, with slightly lower hydrogen selectivity than Ni/SBA-15. This was the consequence of ethanol dehydration on Ni/Al-SBA-15 acid sites, whereas the ethanol dehydrogenation mechanism predominated in Ni/SBA-15 catalyst.

2) Nickel catalysts with mixed support

Nickel catalysts with mixed oxide supports were also investigated in some reports (Coleman et al. 2009). Mg–Al mixed oxide-supported nickel catalysts were found to have high H_2 selectivity and improved catalyst stability. This preference was attributed to the higher nickel crystallite stability, reduced Ni interaction with the support, and lower carbon deposition. The performance of the catalyst varied with the Al and Mg content in the support. In the same year, Profeti et al. (2009) developed an alternative catalyst based on Ni/La_2O_3–Al_2O_3 promoted with noble metals for ethanol

steam-reforming. The presence of lanthanum dispersed on Al_2O_3 prevented the formation of the nickel aluminate in active phase.

2.4.3 Combined Metal-Based Catalysts

In the same year, Fierro et al. (2002) and Klouz et al. (2002) have investigated bimetallic based catalytic systems on SiO_2 support. The effect of reaction parameters (reaction temperature, H_2O: EtOH and O_2: EtOH molar ratios, etc.) were studied in detail as a part of the optimisation process to maximise hydrogen yield and CO_2 to CO molar ratio. The authors concluded that selectivity towards hydrogen increased with increasing H_2O: EtOH molar ratio in the feed. Moreover, the introduction of oxygen in the feed favored the production of hydrogen along with limiting the formation of methane and carbon deposits.

Cu–Ni–Zn–Al multi-component mixed metal oxide catalysts have been used by Velu et al. (2005) in oxidative steam-reforming of bio-ethanol. Dehydrogenation of ethanol to CH_3CHO was favored by a Cu-rich catalyst. The introduction of Ni resulted in the C—C bond cleavage and production of CO, CO_2, and CH_4. Bergamaschi and Carvalho (2008) investigated Cu/Ni bimetallic catalytic systems on zirconia and alumina microspheres for hydrogen production by ethanol steam-reforming prepared by the hydrolysis method. These authors concluded that Al_2O_3- supported catalysts were more active and selective in the production of hydrogen-rich gas than ZrO_2-supported catalysts. Vizcaíno et al. (2008) studied SiO_2- and γ-Al_2O_3-supported Cu–Ni. Although the use of copper reduced coke formation and facilitated the first step of the reaction mechanism, i.e. dehydration and dehydrogenation of ethanol, nickel was found to be a better choice for hydrogen production.

Ethanol steam-reforming was studied by Galetti et al. (2008) on Cu, Co, Zn, Al oxide with the addition of potassium. The activity was tested in a temperature range from 400◦C to 600◦C. The catalyst was found to be very active, giving complete ethanol conversion leading to high hydrogen selectivity (78 %). Ethanol conversion was observed to be complete at 400◦C with H_2 selectivity of 65 % with bimetallic Ni–Co on YSZ support for bio-ethanol steam-reforming. The addition of Co resulted in

inhibition of the dehydration reaction as well as methane production (Resini et al. 2008). Men et al. (2007) studied ethanol steam-reforming on Co, Ni, Rh, and Ru with catalyst supports like alumina, silica, magnesia, and zinc oxide. All these catalysts showed high selectivity in the formation of acetaldehyde and ethylene. The Rh-based catalyst was shown to be the most active with 80 % hydrogen selectivity at 600◦C reaction temperature. Rh/Ni/ceria catalytic systems containing 5 mass % Rh/10 mass % Ni and 15 mass % ceria on alumina showed a complete ethanol conversion at 650◦C for more than 100 hr test duration without any apparent deactivation.

2.4.4 Support Materials

Apart from the active metal catalyst, selecting a suitable support is an important which plays a crucial role in enhancing hydrogen production and ethanol conversion. The nature of the support used can strongly influence the catalytic performance of supported metal catalysts in the steam-reforming of ethanol, since it affects the dispersion and stability of the metal (Sánchez-Sánchez et al. 2007). Here we can further consider some commonly used support metal oxides.

a) Alumina – supported catalysts

Active aluminas are widely used in catalytic applications since they are not only excellent support materials, but active as catalysts as well. γ-alumina developed mesoporosity with specific areas between 50 and 300 m^2 g^{-1}. α-alumina is nonporous and has low surface area of around 3-5 m^2 g^{-1}. α-, γ-, and η- alumina are all used as support materials, the first one in applications where low surface areas are desired, as in partial oxidation reactions. The latter two, and especially γ-alumina, in applications where high surface areas and high thermal and mechanical stability are required.

One of the most prominent applications of γ- alumina as a support is in reforming processes. While α- alumina is not popular for reforming processes because of its low surface area. A comparison between γ-Al_2O_3 and α-Al_2O_3 on the ESR was conducted by Alberton et al. (2007a). They found that the activity for H_2 production over nickel on γ-Al_2O_3 was higher than on α-Al_2O_3. This was attributed to the higher

dispersion of the metal particles compared to the type of metal crystallites deposited on α-Al_2O_3.

b) Zirconia- supported catalysts

Zirconia is also a widely used support. Youn et al. (2008b) reported on the use of Ni catalysts on the zirconia support prepared by the incipient wetness impregnation method for the purpose of hydrogen production by auto-thermal reforming of ethanol. They compared the activity of this catalyst with the activity of a nickel catalyst with a commercial zirconia support. They found that all the Ni/ZrO_2 catalysts exhibited 100 % conversion of ethanol at 500◦C. The product distribution obtained with the Ni/ZrO_2 catalysts differed depending on the preparation method of zirconia. The increased hydrogen selectivity on sol-gel support was attributed to the formation of a pure tetragonal phase of zirconia as well as the high surface area attained.

In some studies, it was found that ZrO_2 provided a better dispersion of cobalt compared to γ- Al_2O_3. The addition of additives such as MgO and Y_2O_3 to ZrO_2 resulted in its structure becoming chemically and thermally stable (Benito et al. 2007; Breen et al. 2002; Song et al. 2007). In a study conducted by Srisiriwat et al. (2009b), it was reported that the addition of CeO_2 and/or ZrO_2 to nickel-based catalysts altered the properties of the catalyst by enhancing nickel dispersion and thus reducing nickel particle size. Other studies reported Ce-modified mesoporous zirconia (Zr–Ce-X, X = 0, 0.1, 0.3, 0.5, 0.7, and 0.9) supports prepared by means of a sol-gel template method (Youn et al. 2008a). They used 20 mass % Ni on the Zr–Ce-X support by the incipient wetness impregnation method for hydrogen production by auto-thermal reforming of ethanol. Complete conversion of ethanol was attained at 500◦C. The product distribution obtained with various catalytic systems differed depending upon the Ce-to-Zr molar ratio. Ni/Zr–Ce-0.7 showed the best catalytic performance in hydrogen production. Biswas and Kunzru (2007) investigated hydrogen production using Ni/$Ce_{1-x}Zr_xO_2$ (x = 0, 0.26, 0.59, 0.84, and 1) catalysts prepared by co-precipitation and incipient wetness impregnation techniques. Ni/$Ce_{0.74}Zr_{0.26}O_2$ catalyst with 30 mass % metal-loading exhibited high catalytic activity and hydrogen selectivity.

c) Ceria-supported catalysts

Hydrogen production from the steam-reforming reactions of ethanol was also reported on ceria-supported Ir, Co, and Ni catalysts (Zhang et al. 2006). The Ir/CeO_2 catalyst was significantly more active and selective in hydrogen production, and the superior catalytic performance was attributed to the intimate contact between the Ir particles and ceria. CeO_2 has the ability to promote CO oxidation and water-gas shift reaction (Diagne et al. 2002). In nickel oxide catalysts, a high degree of dispersion was achieved by Sun et al. (2010) who observed that simultaneous dehydrogenation of ethanol and water molecules on multi-active sites was possible. This catalyst of special morphology exhibited very good stability at a low temperature (at 350◦C)-ESR along with high H_2 selectivity and CO elimination.

2.4.5 Method of Preparation

The activity of a catalyst is directly affected by the preparation method, the type of precursor used, the calcination temperature, and the reduction procedure adopted. The preparation method affects the structural characteristics of catalysts and their performance. Aupretre et al. (2005) reported a substantial variation in the catalyst activity depending upon the type of metal precursor used in the catalyst preparation. Kaddouri and Mazzocchia (2004) studied the effect of the method of preparation adopted for the catalyst on the final product distribution of the catalytic reaction studied. Incipient wetness impregnation, the sol-gel template method, and a combination of both were used to prepare Co/SiO_2 and $Co/\gamma\text{-}Al_2O_3$ catalysts. They found that the combination of both methods provided better catalytic systems in terms of performance in hydrogen production on Co/SiO_2.

It is important to note that, most of the catalytic systems used in ethanol steam-reforming to produce hydrogen were prepared by impregnation method with different precursors. The sol-gel technique is significant for catalyst preparation because of the high thermal stability and resistance to catalyst deactivation exhibited by the resulting catalytic systems.

2.5 CATALYST CHARACTERIZATION

The reasons for characterizing catalysts are to identify catalytic properties such as bulk metal loading, surface area, crystalline phase, metal-support interaction which responsible on catalyst dispersion, and also to determine the catalyst characteristics responsible for catalyst performance. Brief description of some characteristic techniques is shown in the next sections.

2.5.1 X-Ray Diffraction (XRD) Studies

The XRD patterns recorded to investigate the species present in the catalysts, and to estimate the crystallite size. The X-ray powder diffraction (XRD) measurements normally carried out using a Bruker X-ray diffractometer, with copper (Cu) as an X-ray source. The crystallite size obtained by using Scherrer formula (Equation 2.19).

$$D = \frac{(K\lambda)}{\beta \cos\theta} \tag{2.19}$$

where,

D Particle size of the sample (nm),

K Constant, 1,

λ Wavelength usually for Cu Kα radiation,

β Width of diffraction line at full width half maximum (FWHM) in radian, and

θ The angle between the incident and diffracted beams.

2.5.2 Temperature-Programmed Reduction (TPR)

Temperature-programmed reduction (TPR) is a widely used tool for the characterization of metal oxides, mixed metal oxides, and metal oxides dispersed on a support. The TPR method yields quantitative information of the reducibility of the oxide surface. Another important reason for conducting TPR is to examine the interaction between the metal species and the support. TPR is a method in which a reducing gas mixture (typically hydrogen diluted in argon or nitrogen) flows over the sample. A thermal conductivity detector (TCD) is used to measure changes in the

thermal conductivity of the gas stream. A unit of temperature programmed reduction shown in Figure 2.2.

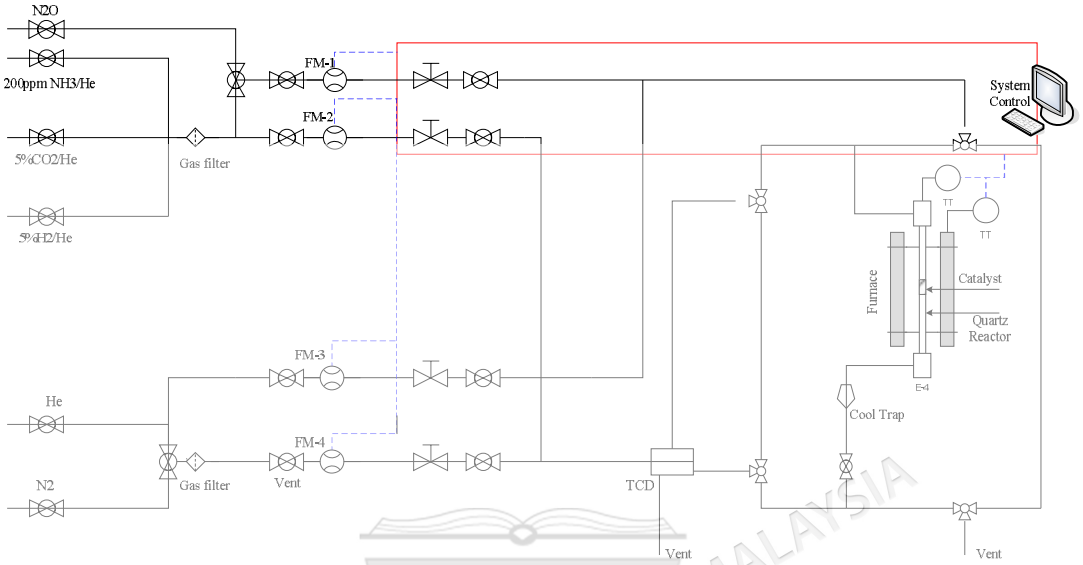

Figure 2.2 A unit of temperature programmed reduction (TPR)

Source: Nouri and Amran 2010

2.5.3 Scan Electron Microscope (SEM)

Scanning electron microscopes (SEM) are widely used to study the morphology and composition of physical materials on a nanometer scale. SEM imaging is usually carried out by scanning an electron probe over the specimen. Thus, both the morphology and topography of the specimen can be obtained using high- or low-resolution images with a great depth of field. An X-ray beam strikes the sample, and the electrons are ejected from or bounced off the surface. These electrons are then used to form an image, which can be viewed on a computer screen or as a digital image for later computer analysis.

Galetti et al. (2008) performed SEM imaging on fresh and used catalysts. In the SEM micrographs, the fresh samples showed particles with different morphologies. After reforming at different reaction temperatures, SEM observation indicated the presence of coke filaments on the catalyst surface. Other researchers

determined the chemical composition of the catalyst using SEM-EDX analysis (Youn et al. 2009), concluding that the catalyst composition of each metal was in a good agreement with the theoretical values.

2.5.4 (BET) Surface Area, Pore Volume and Pore Size Distribution

Measuring of surface area and pore size are performed by adsorption and condensation of nitrogen gas. One adsorbed nitrogen molecule occupies an area of surface comparable to its cross sectional area of 0.162 nm^2. So that, the internal surface area is measured by the number of nitrogen molecules adsorbed. The average pore diameters and the volume of pores were calculated from the desorption data using the Barret–Joyner– Halenda (BJH) method.

Brunauer, Emmett, and Teller proposed the following BET equation (Equation 2.20). This equation assumed that, the nitrogen molecules adsorbed at the monolayer coverage.

$$\frac{P}{(P_O - P)\mathrm{V}} = \frac{1}{\mathrm{V_M}C} + \frac{(C-1)P}{C\mathrm{V_M}P_O} \tag{2.20}$$

where,

P Gas pressure,

P_O Saturation pressure of adsorbed gas,

V Volume of adsorbed gas at pressure P,

$\mathrm{V_M}$ Volume of adsorbed gas in monolayer, and

C Constant.

2.6 REASONS FOR CHOOSING THE CATALYTIC SYSTEM COMPONENTS

To propose an optimized catalytic system for hydrogen production via ethanol steam reforming, numerous factors must be taken into account, such as the type of active metal catalyst, the type of catalyst support, the precursor used, the method of catalyst

preparation, and the reaction conditions (e.g., water-to-ethanol molar ratio, temperature, etc.).

Catalysts containing active metals, such as nickel and rhodium, have been observed to be very active in ethanol conversion and hydrogen selectivity. Rh and Ni are found to be the most suitable active metals to split C–C bonds, which may be due to the fact that ethanol adsorption on the metal surface produces ethoxide species that lead to an intermediate, resulting, in turn, to the cleavage of carbon bonds (Descorme et al. 2000; Idriss 2004; Raskó et al. 2004). However, the high cost and low availability of noble metals is a major limiting factor in their use in hydrogen production via steam reforming. Ru is the least expensive noble metal, but it is found to be active in ethanol dehydration, which causes the formation of ethylene, considered to be the main source of coke.

Nickel is considered the best choice for hydrogen production via catalytic steam reforming of ethanol because of its low cost, high activity in ethanol decomposition by breaking the bonds of ethanol (the C–C, O–H, and C–H bonds), and high activity in hydrogenation and dehydrogenation reactions. γ-Al_2O_3 is chosen as support in this study because it is cheap and has high surface area and high thermal stability.

2.7 APPLICATION OF STATISTICAL DESIGN FOR OPTIMIZATION EXPERIMENTS

Several research groups have investigated the effects of reaction parameters, such as steam-to-carbon (S/C) molar ratio, reaction temperature, feed flow rate, and space time, on hydrogen production by applying a wide range of operating conditions (Aupretre et al. 2005; Benito et al. 2005; Mas et al. 2006; Ni et al. 2007; Rabenstein et al. 2008). However, all these studies used the traditional procedure (one variable at a time), varying one parameter while keeping other variables constant, assuming there is no interaction between the process variables. Furthermore, the interaction effect between process variables is not taken in consideration, such that the correct optimum conditions are not achieved (Ghafari et al. 2009).

For the above reasons, the statistical design of the optimization experiments should be used widely in chemical and chemical engineering processes. The statistical technique was established to study empirical relationships in terms of empirical models, screening factors to determine which ones are important to explain process variations. Larentis et al. (2001) optimized the combined process of partial methane oxidation and carbon dioxide reforming. Factorial experimental design was applied in their work to obtain the optimum conversion of methane and maximum selectivity of synthesis gas. They concluded that independent variables can be optimized to obtain the best values of the responses.

Wu et al. (2002) used central composite design and response surface methodology to build a mathematical model and to optimize the mechanical properties that affect the calcination conditions of the catalyst. They concluded that the central composite design and response surface methodology can be used in the optimization process and in the mathematical modeling of the mechanical properties of solid catalysts. Other researchers used response surface methods to examine the relationships among one or more response variables and a set of quantitative experimental variables or factors (Frišták et al. 2012; Kandananond 2010; Kong et al. 2010; Monyanon et al. 2012; Sasikumar & Viruthagiri 2008).

2.8 ARTIFICIAL NEURAL NETWORK APPROACH

In recent years, new modeling methods such as artificial neural network (ANN) based modeling approach, have widened the perspective for developing empirical models. The relations between catalytic performances (such as catalyst selectivity and reactant conversion) and reaction parameters can be expressed effectively on the basis of the properties of ANN (Adib et al. 2013). ANN can be used as a predictor for any process and multi-objective function systems. Moreover, ANNs can be effectively applied to typical modeling methods, particularly to nonlinear systems.

2.8.1 Application of Artificial Neural Networks in Catalyst

The use of neural networks in the area of catalysis was reviewed by several researchers. Omata et al. (2005) developed Co-supported catalyst for the oxidation of CO using the ANN technique. The loading of Co and the preparation conditions of the Co-supported catalyst were optimized by using ANN. Three years later, Umegaki et al. (2008) developed an alternative high performance Cu-based catalyst for oxidative steam reforming of methanol using ANN. The trained ANN model predicts the performance of many catalysts. Based on the estimated data, they found the best conditions for catalyst composition and preparation conditions. The optimum Cu–Pr–Ti catalyst was Cu/Pr/Ti = 58/16/26, calcination temperature = 623 K, and total metal salt concentration in preparation step = 1 M.

The basic principles of ANN were explained by Holeňa and Baerns (2003). They applied multilayer perceptrons to data on catalyst composition and catalytic results in the oxidative dehydrogenation of propane to propene. By using such networks, they established relationships between the composition and the performance of a catalyst. A method based on ANN was developed to simulate the relations between catalyst components and catalytic performance, as proposed in a previous research (Huang et al. 2003). A multi-trained design strategy was applied to the catalyst design. They concluded that the new method was highly efficient and universal.

Recently, Adib et al. (2013) demonstrated the applicability of ANN models to predict the molar percentage of CH_4, CO_2, and CO in the Fischer–Tropsch process of natural gas in the presence of a Co/Al_2O_3 catalyst. Three input parameters were used, including temperature, pressure, and reaction time. Correlation coefficients for the CH_4, CO_2, and CO were 0.94, 0.93, and 0.96, respectively. The authors also argued that operation time has a significant effect on the molar percentage of CH_4 as a desired product with respect to other operational parameters. They concluded that an ANN is a reliable and highly accurate estimation method that can be used to predict the output composition of the Fischer–Tropsch synthesis. Other successful implementations of the ANN technique have been reported in the field of catalysis (Ahari et al. 2011;

Alamolhoda et al. 2012; Günay et al. 2012; Izadkhah et al. 2012; Khajeh-Hosseini-Dalasm et al. 2011). Table 2.3 higlights the studies used artificial neural network tools in the catalyst applications.

Table 2.3 Application of ANN in catalyst field

Catalyst type	Application	Prep. Meth.	ANN application	References
Pt/Al_2O_3	CO oxidation	IMP	The effects of preparation and operational variables on CO conversion were modelled	(Günay & Yildirim 2010)
$Co/SiO_2–Al_2O_3$	Fischer–Tropsch synthesis	IMP, CP	To find the reaction conditions for achieving an optimal selectivity	(Sharma et al. 1998)
$Ni/\alpha\text{-}\gamma\ Al_2O_3$	Oxidative reforming of methane	IMP	To find effective additives for Ni/Al_2O_3 for oxidative reforming of methane	(Omata et al. 2008)
$Pt–CeO_2/Al_2O_3$	water gas shift reaction	IMP	The experimental results were modelled using modular neural networks	(Günay et al. 2012)
$Co/SrCO_3$	preferential oxidation of CO	IMP	Virtual screening of additives to a $Co/SrCO_3$ catalyst for preferential oxidation of CO	(Omata et al. 2007)
Co (III)/Al_2O_3	Fischer–Tropsch synthesis	PT	ANN used to predict the molar percentage of CH_4, CO_2 and CO in the Fischer–Tropsch process of natural gas.	(Adib et al. 2013)
Au based catalysts	CO oxidation	-	Reaction rate was modelled as a function of catalyst preparation and operational variables by using neural networks.	(Günay & Yildirim 2013a)
$Na–W–Mn/SiO_2$	Oxidative Coupling of Methane	IMP	Optimization of OCM reactions over $Na–W–Mn/SiO_2$ catalyst using artificial neural network	(Sadeghzadeh Ahari et al. 2013)
Au/Al_2O_3	preferential CO oxidation	IMP	The experimental data for the CO oxidation over promoted Au/Al_2O_3 was analyzed using modular neural networks	(Günay & Yildirim 2013b)
KOH	biodiesel production from soybean oil	-	The optimized operational conditions for biodiesel production from soybean oil and application of artificial neural networks for estimation of the biodiesel yield	(Moradi et al. 2013)

CHAPTER III

METHODOLOGY

3.1 INTRODUCTION

This chapter introduces the thermodynamics equations applied to investigate the thermodynamic conditions for ethanol reforming reactions. Then, the preparation and characterization procedure of Ni/Al_2O_3 catalyst are described. The process description and experimental set-up are also discussed in this chapter. Finally, all the considerations regarding of building empirical and artificial neural network models are highlighted. Figure 3.1 shows how the flow chart of the study is carried out.

The first aim of this study is to determine the effects of temperature, pressure, and reactant molar ratio of the ethanol conversion and production of gaseous products (H_2, CO, CO_2, and CH_4). Two thermodynamics approaches were used to trigger an ethanol steam-reforming reaction. The first approach, which is based on the equilibrium constants (Kp), was used to study the effect of temperature, pressure, and the molar ratio on ethanol conversion. The minimization of the Gibbs free energy method was used to study the effect of temperature, pressure, and molar ratio on gaseous product yields.

Second and third aims are to synthesize, characterize, and evaluate the performance of Ni/Al_2O_3 catalysts. Three preparation methods were used: precipitation, impregnation, and sol gel. Catalyst characterization was performed to determine the relationship between the characteristics and the performance of a catalyst. Catalyst performance was evaluated using criteria of H_2 production and ethanol conversion.

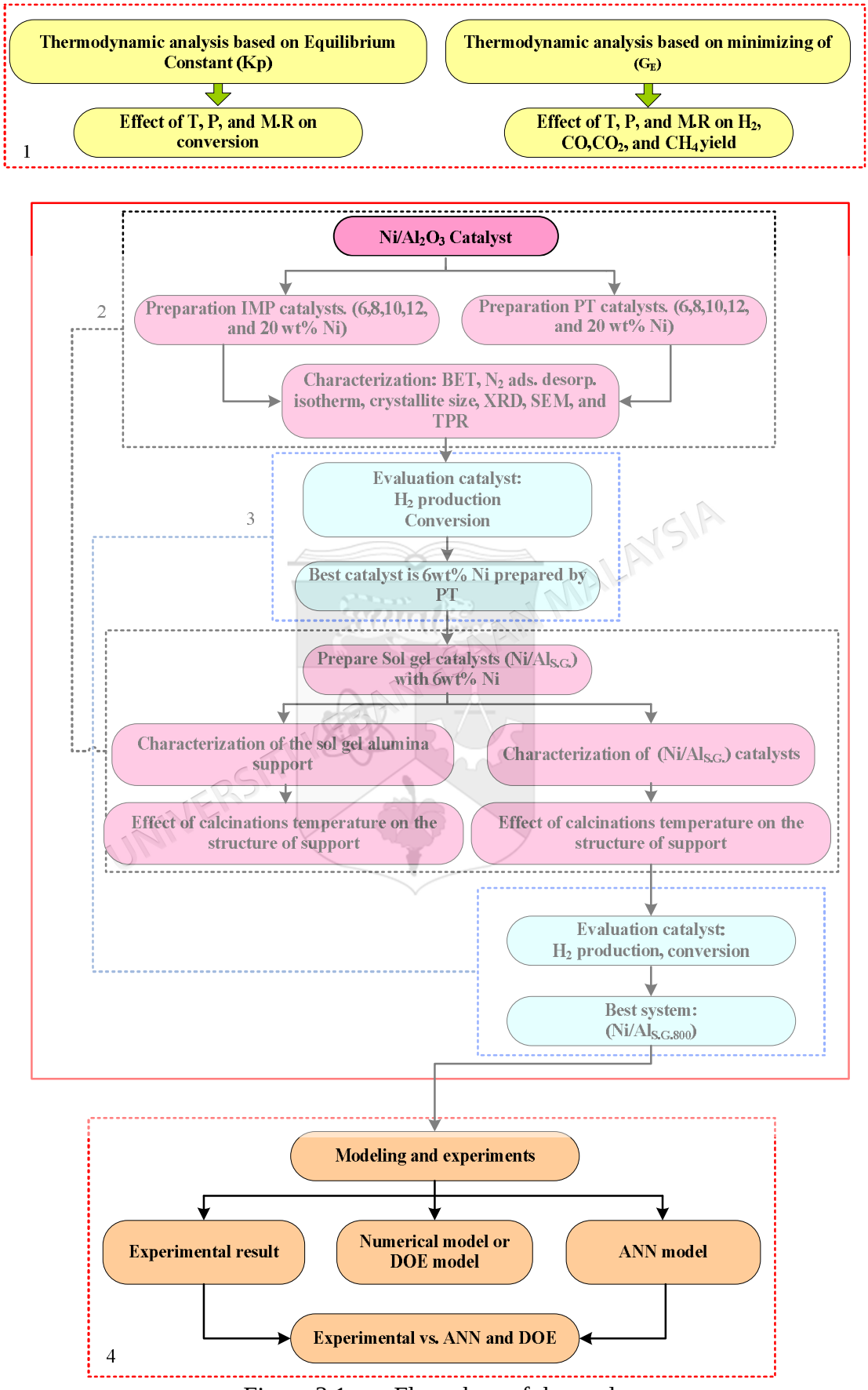

Figure 3.1 Flow chart of the study

After selecting the best Ni/Al_2O_3 catalyst conditions for ethanol steam-reforming reaction, the next aim was to optimize the reaction parameters using a numerical model and to develop an integrated system capable of predicting H_2, CO yields, and ethanol conversion by using ANN model. Results of both models were compared with experimental results. The succeeding sections describe in detail the methods and equations used to perform each objective.

3.2 THERMODYNAMICS CONSIDERATIONS

All thermodynamic calculations and equations used are highlighted in this section. These equations were applied to study the effect of reaction parameters, like temperature, pressure, and molar ratio of the reactants, on the ethanol-reforming process from a thermodynamic perspective. Ethanol conversion and H_2, CO,CO_2, and CH_4 yields are theoretically estimated.

The range of operating conditions covered for thermodynamic analysis is reported in Table 3.1. The reason of choosing this range of operating conditions, because it is expected that the significant effect of these parameters on ethanol steam reforming occurs within this rang, at less from experemintal prespective. Details of the thermodynamic calculations are enumerated in Appendix A.

Table 3.1 Range of operating conditions used for thermodynamics calculations

Variable	Value
Temperature, K	300-900
Pressure, atm	1-50
Water to ethanol molar ratio	3-12

3.2.1 Thermodynamics Calculation Based on Equilibrium Constant (Kp)

A basic thermodynamic analysis was performed based on the reforming reaction:

$$C_2H_5OH + 3H_2O \rightarrow 6H_2 + 2CO_2 \quad (3.1)$$

The thermodynamic equilibrium constant (Kp) was calculated at different values of temperature by obtaining the enthalpy values of each species and Gibb's free energy. Then ethanol conversion was calculated.

a) Standard property change of the reaction

Values for ΔA, ΔB, ΔC, and ΔD for the ethanol reforming reaction were first determined.The meaning of Δ is indicated by the following Equations:

$$\Delta = 6 * (H_2) + 2 * (CO_2) - (C_2H_5OH) - 3 * (H_2O) \quad (3.2)$$

$$\Delta A = \sum V_i \, A_i \quad (3.3)$$

where, V_i is the stoichiometric number of species *i*, and A_i is a constant for a chemical formula of species *i*.

Values of $\Delta H^O_{298.}$, and $\Delta G^O_{298.}$ are found through the heat of formation and Gibbs energy of formation for the reactants and the products as described below.

$$\Delta H^O_{298} = \sum V_i \, \Delta H^O_{fprod.} - \sum V_i \, \Delta H^O_{freact.} \quad (3.4)$$

$$\Delta G^O_{298} = \sum V_i \, \Delta G^O_{fprod.} - \sum V_i \, \Delta G^O_{freact.} \quad (3.5)$$

where, $\Delta H^O_{freact.}$ and $\Delta H^O_{fprod.}$ are standard enthalpies of formation of reactants and products, while $\Delta G^O_{freact.}$ and $\Delta G^O_{fprod.}$ are standard Gibbs energy of formation of reactants and products. Constants, heat formation, and Gibbs formation data are tabulated in Appendix A.

b) Equilibrium constant (Kp)

The equilibrium constant (Kp) can be calculated as a function of temperature as follow:

$$ln(K_P) = -\frac{\Delta G^O}{RT} \tag{3.6}$$

The term $\frac{\Delta G^O}{RT}$ in above equation can be expressed as the following:

$$\frac{\Delta G^O}{RT} = \frac{\Delta G^O_{298} - \Delta H^O_{298}}{RT_O} + \frac{\Delta H^O_{298}}{RT} + \frac{1}{T}\int_{T_O}^{T} \frac{\Delta Cp^o}{R}\, dT - \int_{T_O}^{T} \frac{\Delta Cp^o}{R}\frac{dT}{T} \tag{3.7}$$

where, *To* and *T* are the standard and reaction temperature respectively, $\Delta H^O_{298.}$, $\Delta G^O_{298.}$, are the standard enthalpy and free Gibbs energy change, *R* is the gas constant, and Cp^o is the standard heat capacity. The two integrals in Equation (3.7) are calculated based on the following Equations:

$$MCPH = \int_{T_O}^{T} \frac{\Delta Cp^o}{R}\, dT = \Delta A T_O(\tau - 1) + \frac{\Delta B}{2} T_O^2(\tau^2 - 1)\, T_O^3(\tau^3 - 1)\frac{\Delta D}{T_O}\left(\frac{\tau - 1}{\tau}\right) \tag{3.8}$$

$$\begin{aligned} MCPS &= \int_{T_O}^{T} \frac{\Delta Cp^o}{R}\frac{dT}{T} \\ &= \Delta A ln\tau \left[\Delta B T_O + \left(\Delta C T_O^2 + \frac{\Delta D}{\tau^2 T_O^2}\right)\left(\frac{\tau + 1}{2}\right)\right](\tau - 1) \end{aligned} \tag{3.9}$$

where, *MCPH* and MCPS are functions of the Equations (3.8) and (3.9), respectively. The two functions are solved using MATLAB software version 7.11.0 (R2010b).

c) Relation between equilibrium constant and composition

The relation between the equilibrium constant and the composition of reaction species are given in the following Equation:

$$\prod_i (y_i \phi_i)^{V_i} = \left(\frac{P}{P_o}\right)^{-V} K_P \tag{3.10}$$

with,

$$V = \sum_i V_i$$

where, $\emptyset_i$ is the fugacity coefficient of species i, y_i is the mole fraction of species i, P_o and P are the standard and operating pressure respectively, K_P is the reaction equilibrium constant, and V_i is the stoichiometric number of species i.

Equation (3.10) was used to evaluate the effect of composition in the calculation of equilibrium constant. Considering that the behavior of equilibrium mixture is ideal $\emptyset_i$= 1. Equation (3.10) can be simplified as follows:

$$(y_1\emptyset_1)^{V_1}(y_2\emptyset_2)^{V_2}(y_3\emptyset_3)^{V_3}(y_4\emptyset_4)^{V_4} = \left(\frac{P}{P_O}\right)^{-V} K_P \tag{3.11}$$

For an ideal mixture $\emptyset_i$ = 1, P = 1 bar, Equation (3.11) becomes as follows

$$(y_{C2H5OH})^{-1}(y_{H2O})^{-3}(y_{CO2})^{2}(y_{H2})^{6} = (1)^{-4}K_P \tag{3.12}$$

Further simplified, Equation (3.12) becomes as follows:

$$\frac{(y_{CO2})^{2}(y_{H2})^{6}}{(y_{C2H5OH})^{1}(y_{H2O})^{3}} = (1)^{-4}K_P \tag{3.13}$$

In order to calculate the mole fraction of species i, Equation (3.14) implied.

$$y_i = \frac{n_i o + V_i \varepsilon}{no + V\varepsilon} \tag{3.14}$$

where,

V_i Stoichiometric number of species i,

V Total stoichometric of all species,

y_i Mole fraction of species i,

$n_i o$ Initial moles of species i,

no Total number of moles, and

ε Reaction coordinate.

3.2.2 Thermodynamics Calculation Based on Minimization of Gibbs Free Energy

This method used to solve the equilibrium composition through minimization of the total Gibbs energy of the system. First a formula relates the j elements in our system to the species *i* was introduced in Equation (3.15).

$$\sum_{i=1}^{m} n_i \beta_{ij} = b_j \quad j = 1, 2 \ldots l \tag{3.15}$$

where,

n_i The number of moles of species *i*, *i* = 1, 2 ...m,

β_{ij} Formula coefficient matrix, and

b_j All elements that are present in the system, e.g., C, H, O,.

The Gibbs energy of the system as described in Equation (3.16) can be formulated as:

$$G = \sum_{i=1}^{m} \mu_i n_i \tag{3.16}$$

where,

G Gibbs energy,

μ_i Chemical potential of species *i*, and

n_i Moles of species *i*.

The aim is to calculate the different values of n_i which minimizes the Gibbs energy function. In order to do that, Gibbs energy function (Equation 3.16) will be subjected to the constraint function (Equation 3.15) by the introduction of the Lagrangian multiplier,λ_j.

$$G' = \sum_{i=1}^{m} \mu_i n_i + \sum_{j=1}^{l} \lambda_j \left(\sum_{i=1}^{m} n_i \beta_{ij} - b_j \right) \tag{3.17}$$

To find the composition at which this function is a minimized, set its derivative with respect to n_i to zero as follow:

$$\left(\frac{\partial G'}{\partial n_i}\right) = 0 = \mu_i + \sum_{j=1}^{l} \lambda_j \beta_{ij} \tag{3.18}$$

The phase expression for the chemical potential for an ideal gas described in Equation (3.19) as follow:

$$\mu_i = G_i^o + RTln\frac{\hat{f_i}}{f_i^o} \tag{3.19}$$

$$\frac{\hat{f_i}}{f_i^o} = y_i p = \frac{n_i}{n} p \tag{3.20}$$

where,

G_i^o Standard Gibbs energy of species *i*,

$\hat{f_i}$ Fugacity of reaction species *i* in real equilibrium mixture,

f_i^o Standard state fugacity at 1 bar, and

p Reaction pressure.

Equation (3.19) become,

$$\mu_i = G_i^o + RTlny_i p \tag{3.21}$$

Substitution Equation (3.21) into Equation (3.18),

$$G_i^o + RTlny_i p + \sum_{j=1}^{l} \lambda_j \beta_{ij} = 0 \tag{3.22}$$

Substitute the Gibbs energy of formation for the standard Gibbs energy of species *i* in Equation (3.21).

$$\Delta G_i^f + RT ln y_i p + \sum_{j=1}^{l} \lambda_j \beta_{ij} = 0 \tag{3.23}$$

Equations (3.18) and (3.23) represent a set of equations that can be solved for the unknown y_i and λ_j.

First formulate the coefficient matrix and the factor b for a 6:1 H_2O:C_2H_5OH (as an example) inlet feed molar ratio as follows:

$$\begin{matrix} Species \\ C_2H_5OH \\ H_2O \\ H_2 \\ CO \\ CO_2 \\ CH_4 \end{matrix} \begin{bmatrix} C & H & O \\ 2 & 6 & 1 \\ 0 & 2 & 1 \\ 0 & 2 & 0 \\ 1 & 0 & 1 \\ 1 & 0 & 2 \\ 1 & 4 & 0 \end{bmatrix} \quad \text{and} \quad \begin{matrix} b_c = 2 \\ b_H = 22 \\ b_O = 7 \end{matrix}$$

Equation (3.15) gives:

$$\begin{pmatrix} n_{C_2H_5OH} & n_{H_2O} & n_{H_2} & n_{CO} & n_{CO_2} & n_{CH_4} \end{pmatrix} \begin{bmatrix} C & H & O \\ 2 & 6 & 1 \\ 0 & 2 & 1 \\ 0 & 2 & 0 \\ 1 & 0 & 1 \\ 1 & 0 & 2 \\ 1 & 4 & 0 \end{bmatrix} = [2 \quad 22 \quad 7]$$

This can be written as three coupled equations:

$$2n_{C_2H_5OH} + n_{CH_4} + n_{CO} + n_{CO_2} = 2 \tag{3.24}$$

$$6n_{C_2H_5OH} + 2n_{H_2O} + 2n_{H_2} + 4n_{CH_4} = 22 \tag{3.25}$$

$$n_{C_2H_5OH} + n_{H_2O} + n_{CO} + 2n_{CO_2} = 7 \tag{3.26}$$

Equation (3.23) can be written for each of the N=6 species as:

$$\Delta G^{o}_{f,C_2H_5OH} + RTln\frac{n_{C_2H_5OH}}{n_T} + 2\lambda_C + 6\lambda_H + \lambda O = 0 \quad (3.27)$$

$$\Delta G^{o}_{f,H_2O} + RTln\frac{n_{H_2O}}{n_T} + 2\lambda_H + \lambda O = 0 \quad (3.28)$$

$$\Delta G^{o}_{f,H_2} + RTln\frac{n_{H_2}}{n_T} + 2\lambda_H = 0 \quad (3.29)$$

$$\Delta G^{o}_{f,CO} + RTln\frac{n_{CO}}{n_T} + \lambda_C + \lambda O = 0 \quad (3.30)$$

$$\Delta G^{o}_{f,CO_2} + RTln\frac{n_{CO_2}}{n_T} + \lambda_C + 2\lambda O = 0 \quad (3.31)$$

$$\Delta G^{o}_{f,CH_4} + RTln\frac{n_{CH_4}}{n_T} + \lambda_C + 4\lambda_H = 0 \quad (3.32)$$

where,

$$n_T = n_{C_2H_5OH} + n_{H_2O} + n_{H_2} + n_{CO} + n_{CO_2} + n_{CH_4}$$

This set of equations was solved by Newton-Raphson root finder using Thermo Solver software. The following section highlights the solving of multiple chemical reaction equilibrium by Thermo Solver software.

Thermo Solver is a thermodynamics software program designed to be both easy to use and useful in that it permits the user to make chemical engineering thermodynamic calculations. The main menu for the program is shown in Figure 3.2. A number of sub-programs can be selected. The chemical reaction equilibrium solver is one of the sub-programs used to find the number of moles and gas mole fraction of each species at equilibrium via a minimization technique. The solver window is shown in Figure 3.3. Any number of species may be included in the system. The initial number of moles must be specified for each species, and if it's not available from the database, then the Gibbs' energy of formation must also be specified.

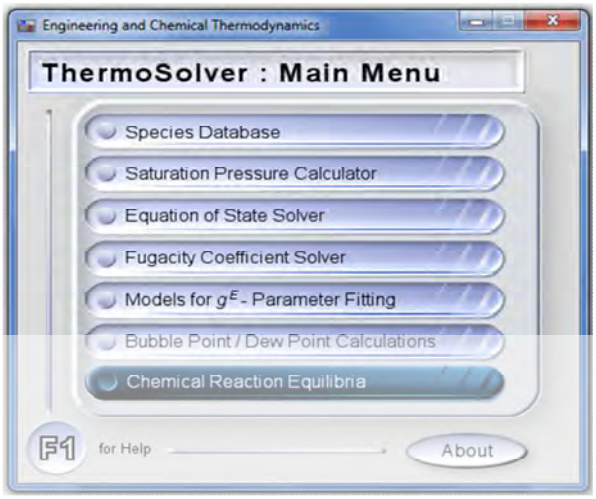

Figure 3.2 Thermo Solver main menu

An option allows the fugacity coefficients to either be set to unity or to the Peng- Robinson pure species $\emptyset_i$.

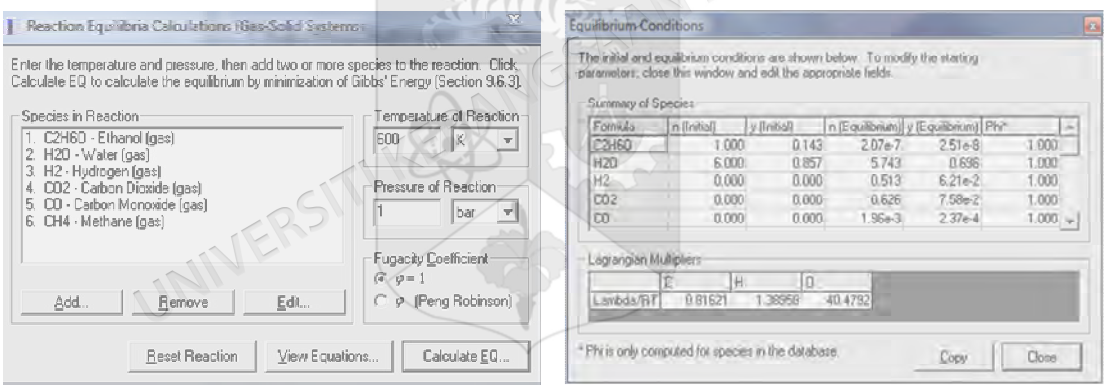

(a) (b)

Figure 3.3 a) Multiple chemical reaction equilibrium solver, b) Equilibrium conditions for the specified system

3.3 CATALYST PREPARATION

Catalysts were prepared using three different catalyst preparation techniques, namely, impregnation, precipitation, and sol gel. Commercial alumina was used as a support for the catalysts prepared by impregnation and precipitation procedures. The alumina support was prepared in our laboratory using the sol-gel technique and was used to prepare the nickel catalyst.

For impregnation and precipitation, five catalysts were prepared for each method by varying the nickel content. The sol-gel technique was used to prepare the alumina support. The calcination temperature of sol-gel-made alumina was changed to achieve higher catalyst performance in hydrogen production. The following sections list all chemicals, equipment, and methods used for the preparation of the catalyst.

3.3.1 Chemicals and Equipments Used

Table 3.2 shows the chemicals used in the catalyst preparation and their corresponding molecular weights. The purity levels and purposes of the chemicals used in the catalyst preparation are also included. Table 3.3 lists the equipment used in the catalyst preparation. For safety purposes, the preparation was conducted in a chemical fume hood.

Table 3.2 Chemicals used in catalyst preparation

Chemicals	Molecular Weight,($gmol^{-1}$)	Purity	Purpose
Nickel nitrate hexahydrate ($Ni(NO_3)_2.6H_2O$), Scharlau	290	98%	Catalyst preparation (precursor)
Aluminum sec butoxide $Al[OCH(CH_3)C_2H_5]_3$, Aldrich	246	97%	Catalyst preparation (precursor)
γ-alumina (Al_2O_3), Alfa Aesar	102	96%	Preparation of catalyst (catalyst supporter)
Sodium Carbonate (Na_2CO_3),	106	>99%	Catalyst preparation (precipitation agent)
Ethanol (C_2H_5OH)	46	>99%	Raw material for the reaction Solvent in catalyst preparation
Nitric Acid (HNO_3)	63	>90%	Catalyst preparation
Copper nitrate trihydrate, Scharlau, $Cu(NO_3).3H_2O$	241	99%	Catalyst preparation (precursor)

Table 3.3 List of equipments and instruments used

Equipment	Specification or Purpose
Filter Paper	Qualitative, circles, 150mm, Whatman
Beakers	100 ml, 500 ml, and 100 ml
Funnel	500 ml
Graduated Volumetric Cylinders	10 ml, 100 ml, and 1000 ml
Laboratory Balance	Model (XB 220A)
Stand	Rod and Base
Clamp	To hold the funnel
Magnetic Stirrer Hot Plate	Model (HARMONT HTS-1003)
Mechanical Stirrer	For vigorous stirring
Drying Oven	Thermo Electron Corporation (Heraeus)
Mortar and Pestle	For grinding the catalyst
Sample Bottles	To keep the prepared samples
Centrifuge	ROTEK Instruments
Furnace	(Thermo Concept) Max. Temp. 1100 ^oC
Volume pipette	100µm – 1000µm

3.3.2 Impregnation (IMP)

Ni/Al_2O_3 catalysts were prepared by using the impregnation method with Ni loadings of 6, 8, 10, 12, and 20 wt%. Aqueous solutions that contain the required weight percentages of the metal nitrate precursor solution (nickel nitrate hexahydrate, Scharlau, 98%) were treated with Al_2O_3 as the support (the commercialized alumina was γ-Al_2O_3, which was obtained from Alfa Aesar, 96%) at 80 ℃ until dry. The solution was further dried for 12 hr at 120 ℃ in an oven and calcined in a furnace at 550 ℃ for 5 hr. Figure 3.4 shows the steps of impregnation method.

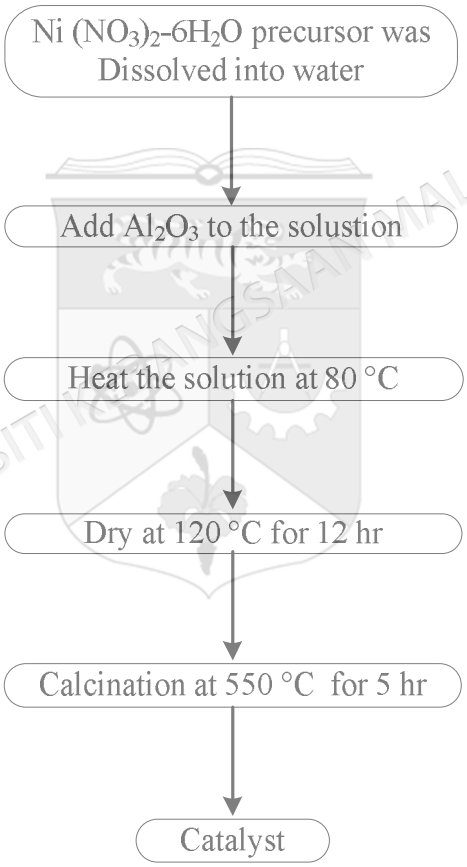

Figure 3.4 Preparation scheme of impregnation catalysts

3.3.3 Precipitation (PT)

As depicted in Figure 3.5, the precipitation procedure was performed by adding a solution that contains sodium carbonate and alumina to an aqueous solution with the required weight percentage of nickel nitrate hexahydrate [Ni $(NO_3)_2$-$6H_2O$]. Sodium

carbonate solution was added to induce complete precipitation of the nickel nitrate solution. The resulting slurry was then aged under vigorous stirring for 24 hr to completely precipitate of the metal nickel on the support. After filtering, the precipitate was dried at 80 ℃ for 12 hr and washed several times with distilled water to remove anions, which may be present in the solution. Finally, the obtained solids were dried at 120 ℃ for 12 hr in air and then calcined at 550 ℃ for 5 hr.

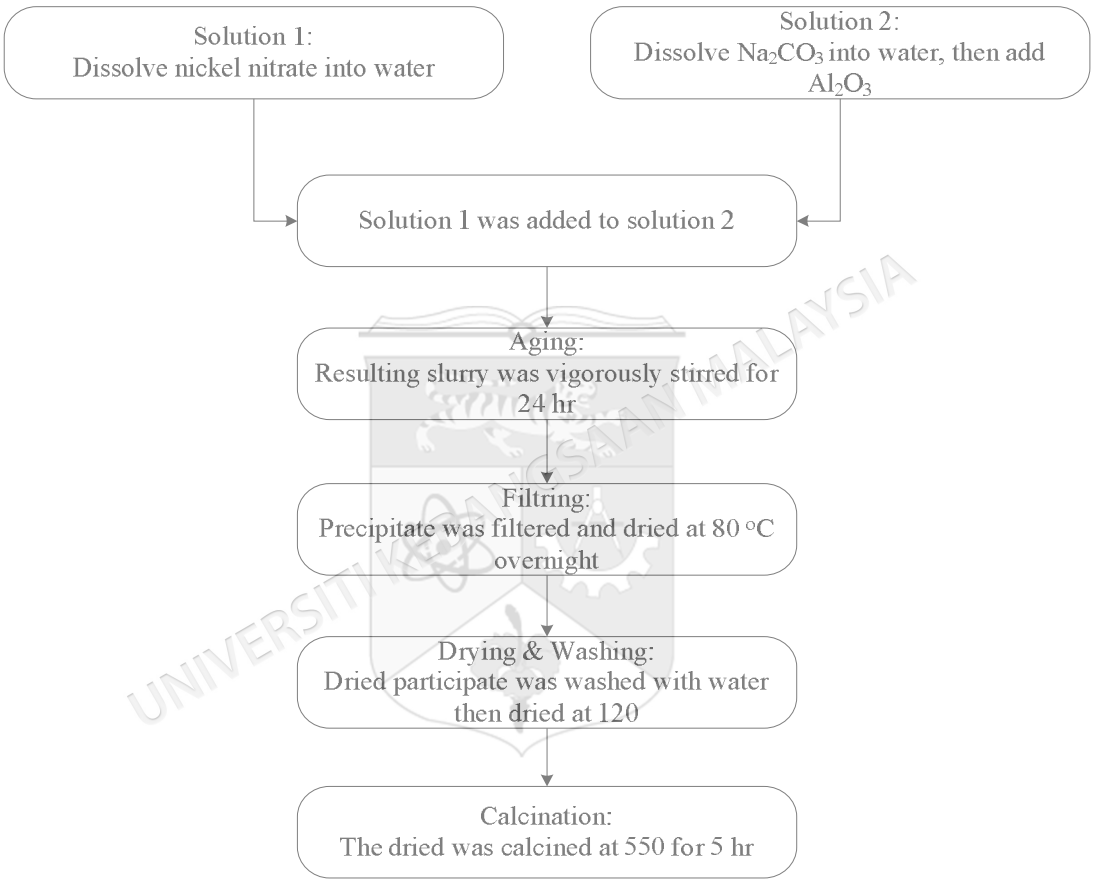

Figure 3.5 Preparation scheme of precipitation catalysts

3.3.4 Sol Gel (S.G.)

Sol gel made alumina support ($Al_{S.G.}$) was prepared (Figure 3.6). To prepare 20g of Al_2O_3 xerogel, 96g of precursor (aluminium sec- butoxide, Sigma–Aldrich) was dissolved in 828ml of ethyl alcohol under constant stirring at 80 ^oC (solution 1). 1.37ml of HNO_3 and 4.12ml of distilled water which was diluted with 549ml of ethyl alcohol (solution 2) were then mixed with solution 1. This mixture was fixed at 80 ^oC to form the sol. After cooling the sol, a transparent gel was obtained by slowly

dropping 8.23 ml of distilled water and 68.66ml of ethyl alcohol into the sol. Then, the alumina gel was covered and kept for one day before it was dried overnight. The solid formed was calcined at different values of temperatures to obtain the alumina sol gel. This support was denoted as $Al_{S.G.T}$, where T is the support calcinations temperature (varied from 600 °C to 1000 °C at an interval of 100 °C).

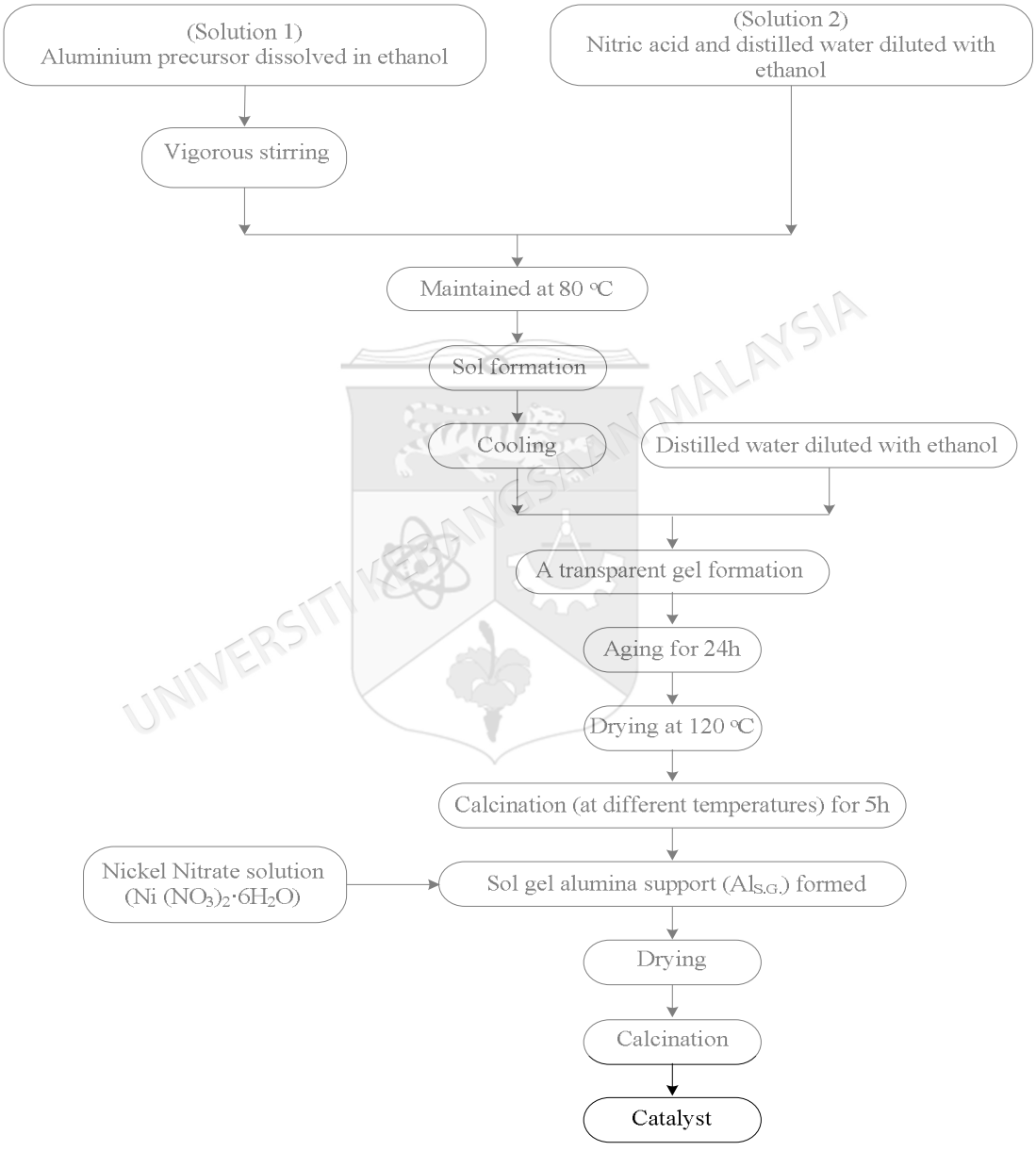

Figure 3.6 Preparation scheme of sol gel alumina support and catalyst

Nickel catalysts supported on alumina xerogel supports were synthesized by impregnating amount of (Ni $(NO_3)_2 \cdot 6H_2O$, Sigma–Aldrich) on the supports. The

supported nickel catalysts were denoted as $Ni/Al_{S.G.T}$ (T = 600, 700, 800, 900, and 1000 °C). The nickel content in all samples was fixed at 6 wt %.

3.3.5 Composition of Catalysts

The descriptions and elemental compositions of prepared catalysts are shown in Table 3.4. Symbols IMP, and PT, indicate impregnation, and precipitation synthesis methods, respectively. Numbers represent the percentage loading while the symbols represent the method of catalyst preparation. For instance, 8IMP indicates a catalyst with 8%Ni loading prepared by impregnation synthesis method.

Table 3.4 Name and chemical composition of catalysts

Method of preparation	Catalyst	Ni (wt %)	O (wt %)	Al (wt %)
Impregnation	6IMP	6	44.3	49.7
	8IMP	8	43.3	48.7
	10IMP	10	42.4	47.6
	12IMP	12	41.4	46.6
	20IMP	20	37.7	42.3
Precipitation	6PT	6	44.3	49.7
	8PT	8	43.3	48.7
	10PT	10	42.4	47.6
	12PT	12	41.4	46.6
	20PT	20	37.7	42.3

3.4 CATALYST CHARACTERIZATION

Characterization of the catalyst was performed to denote the catalyst properties that are related to the catalyst activity. Catalyst characterization was carried using: (BET) surface area and crystallite size, pore volume and pore size distribution, N_2 adsorption desorption isotherm, Powder X-ray diffraction (XRD), Temperature programmed

reduction (TPR), Temperature Programmed Desorption (TPD), CHNS elemental analysis, and Scanning electron microscopy and mapping (SEM- EDX). The key information on these characterization techniques is shown in Table 3.5.

Table 3.5 Summary of catalyst characterization techniques and product analysis instrumentations

Technique	Key information
BET Surface Area and Crystallite size	To measure surface area, and crystallite size of the catalysts
Powder X-ray Diffraction (XRD)	To identify species present in the catalyst
Temperature Programmed Reduction (TPR)	To study the reduction behaviorof NiO To examine the interaction between the nickel species and the support
Temperature Programmed Desorption (TPD)	To determine the dispersion, particle size, and surface area of nickel
CHNS Elemental Analysis	To measure the amount of carbon deposited on the used catalyst surface
Scanning Electron Microscopy and Mapping (SEM- EDX)	To analyze the surface and the morphology
GC (Model SRI 8610C)	To identefy the gas product generally consisting of H_2, N_2, CO, CO_2, and CH_4
GC-FID (7890A GC-system; Agilent Technologies, USA)	To determine the amount of ethanol out

3.4.1 BET Surface Area, Pore Volume, and Pore Size

(BET) surface areas of catalysts were measured by using a Micromeritics adsorption device (Model ASAP 2010, manufactured by Micromeritics Instruments Inc., Norcross, GA, USA) using N_2 gas (99.995% pure). Prior to analysis, each catalyst sample was enclosed in glass cell and evacuated or purged at 300°C for 1 hour in the inert gas to ensure that there was no adsorbed moisture and atmospheric gases such as CO_2 on the catalyst surface. Nitrogen adsorption-desorption isotherms were obtained by using the same instrument at boiling temperature of liquid nitrogen which is -195^{o}C.

3.4.2 Powder X-ray Diffraction (XRD)

X-ray diffraction (XRD) measurements of the samples were recorded for 2θ between 10° and 80° using a Bruker AXS D8 advance diffractometer that employs a scanning rate of 0.02° s^{-1} with Cu Kα radiation (λ=1.5406 Å). The working current and voltage of the X-ray tube were 40 mA and 40 kV, respectively. The crystallite sizes of the samples were obtained by using TOPAS software and the results were confirmed by Scherrer formula.

3.4.3 Temperature Programmed Reduction (TPR)

Temperature-programmed reduction (TPR) measurements were performed for all catalysts by using a Micromeritics instrument (Model, Autochem II 2920 manufactured by Quantachrome Corporation, FL, USA) connected to thermal conductivity detector (TCD). The temperature was elevated from 25 °C to 900 °C at a rate of 10 °C min^{-1}. For TPR analysis, a mixed stream of 5% H_2–N_2 mixture that was used as the carrier gas at a flow rate of 20 cm^3min^{-1} was passed on 0.03 g of catalyst sample.

3.4.4 Temperature Programmed Desorption (TPD)

H_2 temperature-programmed desorption (H-TPD) measurements were performed to determine the dispersion, particle size, and surface area of nickel. Initially the system was purged with pure argon (30 $mlmin^{-1}$) from room temperature to 900 °C for 1 hr. Before the chemisorptions measurements, the catalyst was treated with a mixed stream of carrier nitrogen (20 $mlmin^{-1}$) and argon (20 $mlmin^{-1}$) by elevating the temperature from 25 up to 900 °C for 3 hr to remove any impurities. After cooling down, Catalysts were reduced in situ with hydrogen at 400 ^oC for 1 hr. The samples were then cooled to room temperature under a flow of argon (30 $mlmin^{-1}$). The quantity of hydrogen uptake was measured by passing diluted hydrogen (5.1% hydrogen in argon) through the catalyst. Dispersion, surface area, and mean particle size of nickel were evaluated according to Equations (3.33), (3.34), and (3.35), respectively.

$$D_m = \frac{V_{chem.} \times SF \times MW}{c/100} \times 100 \quad (3.33)$$

$$S.A._m = V_{chem.} \times 6.02 \times 10^{23} \times SF \times \sigma_m \times 10^{-18} \quad (3.34)$$

$$d = \frac{6 \times c}{(S.A._m) \times \rho} \times 100 \quad (3.35)$$

where,

D_m Metal dispersion,

$V_{chem.}$ Chemisorption volume (mol g^{-1}),

SF Stoichiometry factor = 1,

MW Supported metal atomic weight,

c Supported metal weight, wt%,

$S.A._m$ Metal surface area (per g catalyst),

σ_m Supported metal cross section area = 0.0649 nm $atom^{-1}$,

d Mean particle diameter (nm), and

ρ Supported metal density.

3.4.5 Scanning Electron Microscopy and Energy Dispersive X-ray Spectroscopy (SEM-EDX)

Surface topography and morphology as well as catalyst dispersion were measured by using scanning electron microscopy and energy dispersive X-ray spectroscopy (SEM-EDX). Scanning electron micrographs were obtained by using a LEO 1450 VPSEM instrument operated with an acceleration voltage of 15 KV. The instrument was equipped with an energy-dispersive X-ray micro analyzer (Oxford Instruments, Model 7353 England) and a Si (Li) detector. Prior to the analysis, all samples were sputter coated with a thin layer of gold by using a vacuum sputter coater to avoid electrostatic charging before the samples were subjected to SEM.

3.5 EXPERIMENTAL SET UP AND PROCESS DESCRIPTION

Hydrogen production via ethanol steam reforming was performed on all prepared catalysts. The schematic diagram of the experimental set-up employed for the ethanol reforming reactions is presented in Figure 3.7. The reforming reaction was performed in a Pyrex glass tube reactor (internal diameter: 8 mm, length: 500 mm) at 400 °C under atmospheric pressure. The maximum working temperature allowable of the reactor is 500°C. Prior to the reaction, the catalyst was placed in the middle of the glass tube reactor and heated to 150 °C for 1 hr and then reduced for another 1 hr in situ under flowing H_2. The temperature inside the reactor was measured by using a thermocouple and controlled by temperature controller. The temperature reading error was within ±5 °C.

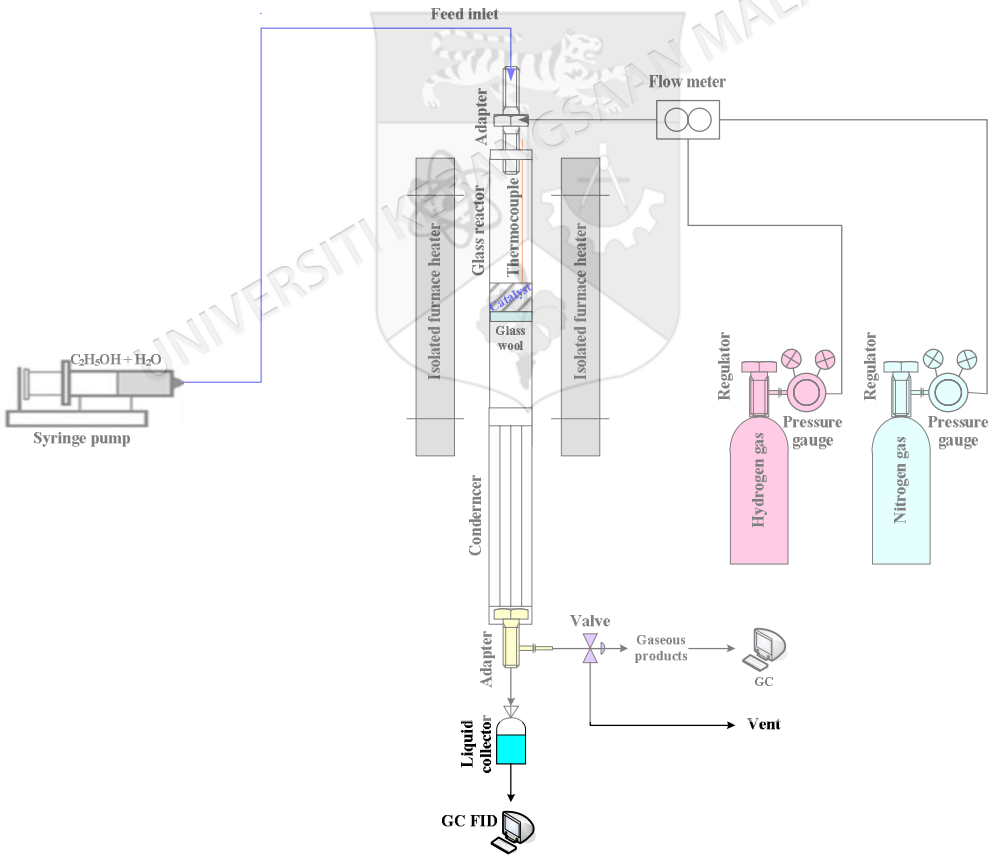

Figure 3.7 Schematic diagram of the experiment for the production of hydrogen by the reforming of ethanol

A mixture of liquid water and ethanol (molar ratio of 6:1) was subsequently introduced into the reactor containing 0.5 g of catalyst with a nitrogen carrier gas. The reactant mixture was fed to the reactor by using a syringe pump (Model NE-300) fixed at the required flow rate (0.1 ml min^{-1}). The flow rate of nitrogen entering the reactor was controlled by means of flow controller (Cole - Parmer 022-13-ST) and maintained at 30 ml mn^{-1}. The product stream was then cooled down by passing the stream through the condenser. The condensable liquid was separated from the gaseous species and collected in liquid collector before being sent to the GC for analysis. The gaseous product exits the bottom of the condenser was collected using a gas collection bag and send directly to GC for analysis.

Figure 3.8 shows the reactor assembly and the connections of all items. The reactor was installed in a particle laboratory at the Chemical Engineering Department of UKM. a) A glass wool (inert material) was gently inserted into the reactor column and held in the middle of the reactor tube. b) The specified amount of catalyst was placed on the glass wool by means of a small funnel. c) Then, the tube reactor was inserted into a double zone furnace at atmospheric pressure. d) The catalyst was heated up using a voltage regulator to remove any impurities, and the temperature inside the reactor was adjusted using a temperature controller. e) Hydrogen gas was passed through the reactor to reduce the catalyst. After the catalyst was reduced, reactants (water and ethanol) were mixed at the desired ratio in a small beaker and transferred into the syringe glass. The loaded syringe was then fixed on the holder by means of a syringe clamp. The flow rate of the reactants was adjusted using the keypad on the front panel of the pump. The reactants were then injected from the top of the reactor through an adapter with nitrogen gas as a carrier. The flow rate of nitrogen was controlled using a flow meter. Water from the tap was allowed to pass through a condenser directly after the reaction began to separate the gaseous and liquid products. For safety purposes, effluent gases were sent outside the lab using a valve after collecting each sample. A liquid collector was fixed under the condenser to collect the condensate. The liquid collected at the bottom of the separator was periodically sampled for analysis. A gas collection bag collected the gaseous product, which was sent to a gas chromatography (GC) system for analysis. Table 3.6 illustrates all the items used in the reactor assembly.

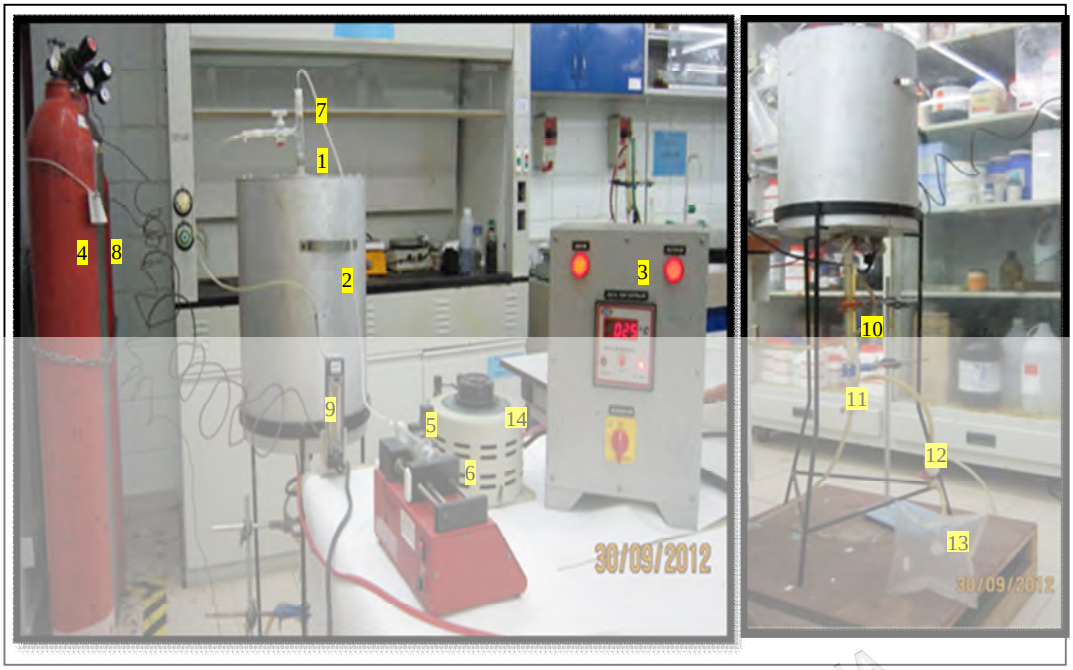

Figure 3.8 Photograph of the reactor assembly

Table 3.6 Items in the reactor assembly

Item	Description
1	Glass reactor
2	Double zone furnace
3	Temperature controller
4	Hydrogen gas cylinder
5	Syringe glass
6	Syringe clamp
7	Adapter
8	Nitrogen gas cylinder
9	Flow meter
10	Condenser
11	Liquid collector
12	Valve
13	Gas collection bag
14	Voltage regulator

3.6 PRODUCT ANALYSIS

Two types GC were used to analyze gas and liquid products. Analysis of the gaseous product stream was performed using a GC system (Model SRI 8610C) equipped with a molecular sieve, a silica gel column, and a thermal conductivity detector with helium as the carrier gas. The condensed liquids were collected every 1 h, and the sample was analyzed using a GC system (Supelco CO, Bellefonate, PA, USA) equipped with an Equity-1 capillary column (30 m × 0.32 mm × 0.1 μm film thickness) and a flame ionization detector (FID).

3.6.1 Gas Analysis

The gas products leaving the condenser were collected using a 1 L gas sampling bag manually injected into the GC. The collection of the sample occurred periodically. Two columns were used to separate the gas product generally consisting of H_2, N_2, CO, CO_2, and CH_4. Before injecting the samples in the column, a blank run was performed to purge any possible gases present in the column.

After cleaning, the sample was injected into a 10-port gas-sampling valve with a 1 ml sample loop in the heated valve oven and two columns in the temperature-programmable column oven. A 6 ft-long molecular sieve 13X packed column was used to separate H_2, nitrogen, CH_4, and CO, whereas the 6 ft-long silica gel-packed column was used to separate CO_2 gas and C_2–C_5 hydrocarbons. Helium was used as a carrier gas. The column oven temperature was controlled through a peak simple temperature program. The temperature program was utilized as shown in Figure 3.9.

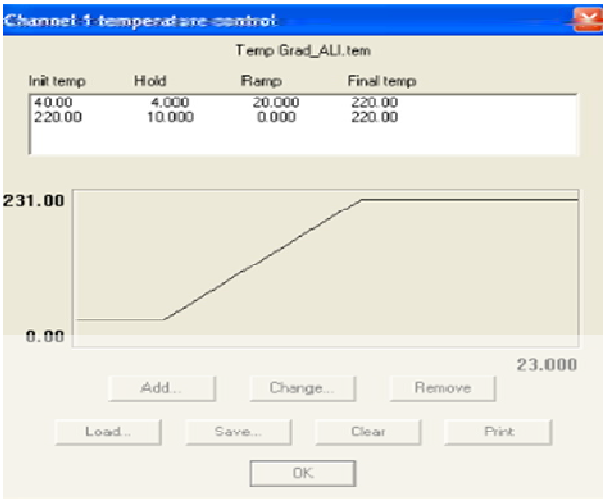

Figure 3.9 Temperature programe of GC gas analysis

3.6.2 Liquid Analysis

Liquid product was collected from the bottom of the separator and transferred into a 10 ml sample vial. The first ethanol standard was prepared using dichloromethane (DCM) as a solvent. The prepared standard was then injected into the GC to calibrate the column. To extract the liquid product from water, equivalent amounts of the liquid sample and the DCM were mixed and vortexes, and then sent to the centrifuge machine (ROTEK Instruments) to separate the water from the sample product. The two layers were generated, and a syringe was used to take the bottom product layer (ethanol + DCM). The liquid product was injected into the GC sample bottle after passing through a 0.2 µm filter. Subsequently, 1 µl of the prepared sample was injected into GC-FID (7890A GC-system; Agilent Technologies, Palo Alto, CA, USA). The sample was analyzed using a capillary column of 30 m length × 0.32 mm ID × 0.1 µm film thickness. The oven temperature was programmed to increase from 40 °C to 130 °C at a rate of 8 °C min^{-1}. The injector and detector were set at 250 °C and 280 °C respectively. Helium was used as a carrier gas and was set a flow rate of 1.5 ml min^{-1}.

3.7 EVALUATION OF CATALYST PERFORMANCE

The catalysts were evaluated for their activities in the ethanol steam reforming. The criteria used to evaluate catalyst performance included ethanol conversion, product selectivity, product yield, and ethanol conversion into gaseous products. Equations (3.36), (3.37), (3.8), and (3.39) were used to calculate ethanol conversion, product selectivity, product yield, and ethanol conversion into gases, respectively.

$$EtOH\ Conv. = \frac{F_{EtOH_{in}} - F_{EtOH_{out}}}{F_{EtOH_{in}}}\ x\ 100 \tag{3.36}$$

$$Product\ Selectivity = \frac{F_{i,out}}{\sum F_{i,out}}\ x\ 100 \tag{3.37}$$

$$Product\ yield = \frac{F_{i,out}}{F_{ETOH_{in}}} \tag{3.38}$$

$$E\text{tOH}\ Con.\ into\ gaseous = \frac{C\ atoms\ in\ the\ gas\ product}{Total\ C\ atoms\ in\ the\ feedstock}\ x\ 100 \tag{3.39}$$

where, $F_{ETOH_{in}}$ and $F_{ETOH_{out}}$ represent the molar flow rate of ethanol inlet and outlet of the reactor respectively, $F_{i,out}$ represents the molar flow rate of the product gas outlet of the reactor, and $\sum F_{i,out}$ represent total molar flow rate of the gaseous products.

3.8 STATISTICAL DESIGN

3.8.1 Definition

Statistically, design of experiment (DOE) is used to analyze the influence of separate and interacting factors, and to develop models that simulate the responses with a minimum number of experiments. There are a number of statistical methodologies

available for optimizing process parameters such as response surface methodology (RSM), Taguchi, and Mixture. RSM is used to examine the relationship between one or more response and a set of experimental variables. Its simplicity and high efficiency make RSM an optimization technique that can be commonly applied to optimize process variables in different applications. Moreover, RSM reduces the experimental trials needed to estimate the process variables. One of the efficient RSM useful tools is center composite design (CCD), which used to define the experimental conditions. The following are the basic concepts of experimental design:

1) Factor: Input variables whose levels are set by the experimenter,
2) Response: Output or dependent variables,
3) Interaction: The value of one factor affects the response of the system due to another factor,
4) Significance: A finding that a factor has a non-negligible effect on a response,
5) Determination Coefficient R^2: Statistical method that explains how much the experimental data is fit to the proposed model. In general, the higher the R^2, the better the model fits your data. R^2 has been always between 0 and 1, and
6) RSM plot: A surface plot displays a three-dimensional view that may provide a clearer picture of the response surface.

3.8.2 Implementation

The optimization of the reaction variables was carried out by a statistical design of experiment. After the best catalyst has been chosen, three independent variables, temperature (X_1), water–ethanol molar ratio (X_2), and liquid hourly space velocity (X_3) were verified based on the experimental design. The reason for choosing these three factors is because these conditions considered as the influential factors that effect on the performance of the catalyst (Yang et al. 2006). The CCD tool was implemented to investigate the influences of these operating factors on the hydrogen yield ($Y_{H_{2.Y}}$), ethanol conversion($Y_{ETOH_{Con.}}$), and carbon monoxide yield($Y_{CO.Y}$) in ethanol steam reforming reaction. Table 3.7 shows the three independent factors with their experimental ranges and the levels employed in this study. The center of the

design is coded as (0), and the upper and lower levels of the design are coded as (1) and (-1), respectively. The CCD of the independent variables is presented in Table 3.8. According to the CCD, 20 sets of runs were selected and each experiment was replicated twice. Standard deviations of the three observed responses are calculated based on the following Equation.

$$SD = \sqrt{\frac{\sum(x - \bar{x})^2}{N - 1}} \tag{3.40}$$

where,

SD Standard deviation,

x Each value in the dataset,

$\bar{x}$ The mean of all values in the dataset, and

N Number of values in the dataset.

Table 3.7 Coded values of variables selected for trials

Variables	Coding factor levels		
	-1	0	1
Temperature, X_1 (°C)	200	350	500
Water-ethanol ratio, X_2	3	13.5	24
Liquid hourly space velocity, X_3 (h^{-1})	0.125	0.5625	1

Table 3.8 Central composite experimental design

Run	Pt Type	Coded variables		
		X_1, (°C)	X_2	X_3, (h^{-1})
1	-1	200	13.5	0.5625
2	1	200	24	1
3	1	500	3	1
4	1	500	24	0.125
5	-1	350	13.5	1
6 C	0	350	13.5	0.5625
7	-1	350	3	0.5625
8	1	200	3	0.125
9 C	0	350	13.5	0.5625
10 C	0	350	13.5	0.5625
11	1	500	24	1
12	1	500	3	0.125
13 C	0	350	13.5	0.5625
14	-1	350	13.5	0.125
15 C	0	350	13.5	0.5625
16 C	0	350	13.5	0.5625
17	1	200	3	1
18	1	200	24	0.125
19	-1	350	24	0.5625
20	-1	500	13.5	0.5625

Note: C is the center point

The experimental design and statistical analysis were conducted using the Minitab software package (version 14.12.0). The experimental data were modeled and a second-order polynomial model (Equation 3.41) provided the predicted responses for each dependent variable ($Y_{H_{2,Y}}$, $Y_{ETOH_{Con.}}$, and$Y_{CO,Y}$). The observed experimental data were then compared with the data from the obtained models.

$$Y_i = \beta_0 + \sum_{j=1}^{3} \beta_j x_j + \sum_{j=1}^{3} \beta_{jj} x_j^2 + \sum_{i<j} \beta_{ij} x_i x_j \quad (3.41)$$

where, Y_i represents the response variables ($Y_{H_{2,Y}}$, $Y_{ETOH_{Con.}}$, and $Y_{CO,Y}$); β_0 is a constant; β_j, β_{jj}, and β_{ij} are the linear, quadratic, and interaction effect coefficients, respectively; and x_i and x_j are the input variables. For the three independent variables, the model represented is shown in Equation (3.42).

$$Y_i = \beta_0 + \beta_1 x_1 + \beta_2 x_2 + \beta_3 x_3 + \beta_{11} x_1^2 + \beta_{22} x_2^2 + \beta_{33} x_3^2 + \beta_{12} x_1 x_2 + \beta_{13} x_1 x_3 + \beta_{23} x_2 x_3 \quad (3.42)$$

The significance of the regression model was determined using an ANOVA with *p*-value less than 0.05. In addition, the coefficient of determination (R^2) was used to evaluate the performance of the model. In general, the higher the R^2, the better the model fits the data. A reduced model was obtained by eliminating the insignificant coefficients from the completed model. The influence of the three experimental variables on each response was explored using RSM plots.

Minitab also provides a command (Response Optimizer) that can identify the combination of input variable settings that optimize a set of responses. This command used after creating and analyzing the response surface design to provide an optimal condition for the process variables that maximized ethanol gasification and hydrogen yield and minimized carbon monoxide yield.

3.9 ARTIFICIAL NEURAL NETWORK DEFINITION

An artificial neural network (ANN) is a mathematical model for information processing based on a connectionist approach to computation. Also, artificial neural networks are a form of artificial intelligent technology. ANN like people learns by examples and it has strong learning ability for problems with nonlinear relations or very complicated relations between input and output dataset. It consists of a large

number of highly interconnected processing elements (neurons or nodes) to solve specific problems. The weight of each connecting line (W_{ij}) denotes the strength of the function between the two nodes.

The training method of the artificial neural network divided into steps: learning and recalling. The training start by inputting the actual information that the networks need in the learning phase, and then the networks will learn how to calculate desired results based on the iterative learning process. The two mentioned steps are briefly highlighted as follows:

3.9.1 Learning Process

During the learning phase, the initial training model is fed into the network to compute the desired result. The amount of error between the calculated result and target result are calculated. Based on the error amount, the values of the weights associated with each connection between neurons were adjusted by sending the error value back to the networks so that the error was minimized. Generally, Learning process used in neural network can be classified into two categories as follows:

a) Supervised Learning:

This is the most powerful technique to train the ANN. All the training data including input data and target result are inserted into the networks.

b) Unsupervised Learning:

In this instance, networks learn to adapt themselves without any external supervision. In other words, the outcome variable of interest is not observed. This means that the neural networks with unsupervised learning have no reference (Kohonen 2010).

3.9.2 Recalling or Testing

After learning step, the output tested result will be calculated by the artificial neural network according to the outcome of learning. Then, evaluation of the model can be done to investigate the performance of learning.

3.10 ANN IMPLEMENTATION

3.10.1 Basic Elements of ANN Model Building

ANN allows computers to learn from data and then properly predict new data (Bao & Intille 2004).The following subsections describe the methods and algorithms used to develop an integrated system capable to predict hydrogen yield using ANN models.

a) Multi-Layer Perceptron (MLP)

The multi-layer perception (MLP) neural network based on back propagation (BP) algorithm is used as a predictor. The MLP consists of a set of simple neurons called preceptrons, arranged in multiple layers and connected only in an adjacent layer by weight (Huang et al. 2009). The used type of MLP artificial neural network consists of three layers or groups, input layer, hidden layer, and the output layer (Figure 3.10). Each layer of these three layers has a number of neurons. The number of neurons in the input and output layers are equal to the number of input and output variables. Hidden layer can be one or more than one layer. The neurons activity in the hidden layer is determined by the activities of the input units and the weight on the connections between the input and the hidden units. The output performance depends on the activity of the hidden layer and the weights between the hidden and output layers (Adib et al. 2013).

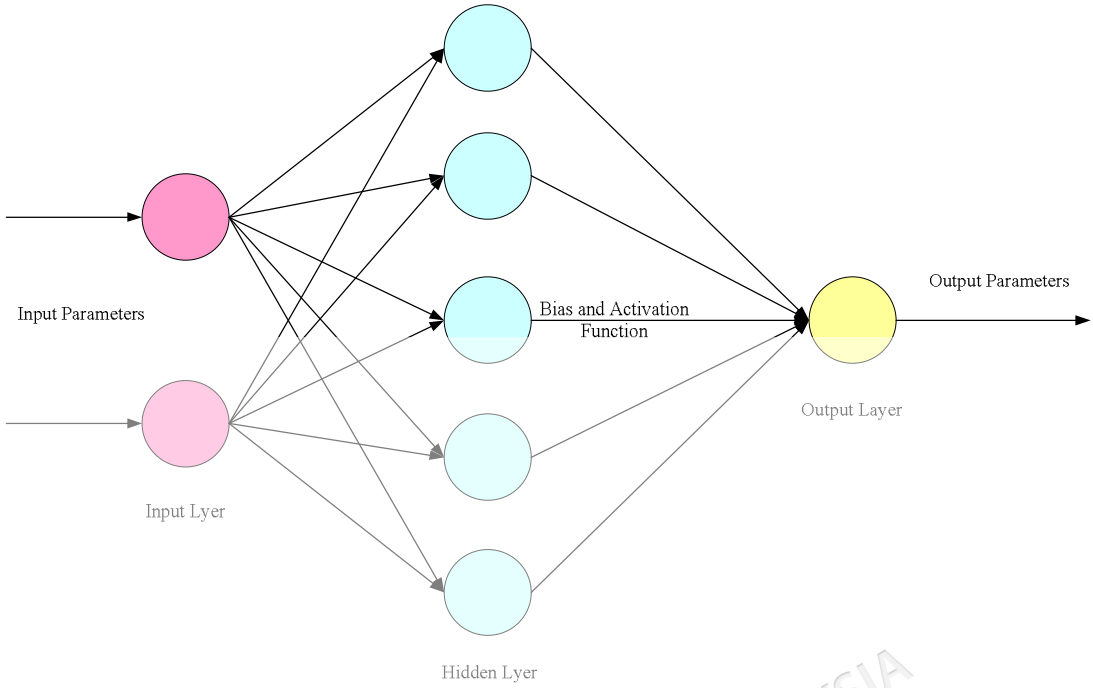

Figure 3.10 Basic structure of MLP neural network

Source: Adib et al. 2013

At the first, the input data of the each neuron (a_1, a_2, a_3) are multiplied by the corresponding weight functions that assigned to them (w_{j1}, w_{j2}, w_{j3}). Then the combined input c_j, forms as a summation of products of neurons and weight functions as shown in Equation (3.43) (Adib et al. 2013).

$$cj = a_1 w_{j1} + a_2 w_{j2} + a_3 w_{j3} \tag{3.43}$$

Each neuron in one layer has direct connections to the neurons of the subsequent layer by means of activation function (commonly a sigmoid function). Since we have more than one input and output in this research, the feed forward neural network process was set (MIMO) network structure.

b) Common transfer functions

Mjalli et al. (2007) reported that Log-sigmoid function is the most common type of the transfer functions used to construct neural networks. Furthermore, it is commonly used in back-propagation networks. Therefore, the log-sigmoid transfer function

(logsig) was used between the hidden layers and the output layer at all developed networks. The non-linear nature of this function enhances the performance of a neural network. Figure 3.11 shows common types of transfer functions used to construct neural network.

1) Gaussian

Gaussian or Radial basis transfer function (Radbas) is a neural transfer function calculates a layer's output from its net input. The output of this function is [0, 1].

$$a = exp\,(-n^2) \tag{3.44}$$

where, a is the radbas function, and n is the input/output data.

2) Gaussian Complement

Gaussian complement function reveals meaningful characteristics in the extremes of the data.

$$a = 1 - exp\,(-n^2) \tag{3.45}$$

3) Sin

The inputs must be scaled into [-1, 1] if this function has been used in the first hidden layer.

$$a = sin(n) \tag{3.46}$$

4) Purelin

Purelin is commonly the output layer transfer function.

$$a = f\,(n) = n \tag{3.47}$$

5) Log- Sigmoid

This function is useful for almost all neural network applications and maps the inputs into the [0, 1] range.

$$a = f\,(n) = \frac{1}{1 + exp(-n)} \tag{3.48}$$

6) Tangent sigmoid

Tangent logistic function maps the data to [-1, 1]. This function is mostly being used in hidden and output layers.

$$a = f\,(n) = \frac{2}{1 + exp(-n)} - 1 \tag{3.49}$$

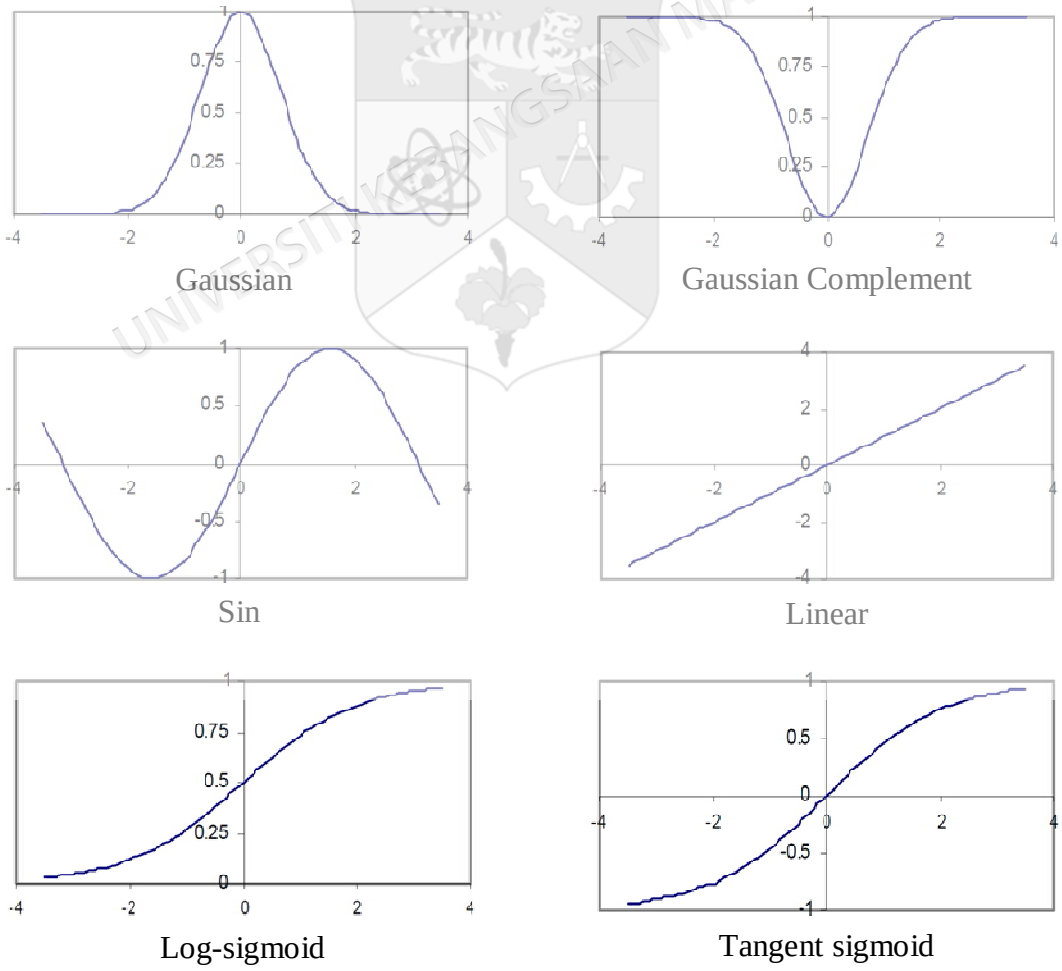

Figure 3.11 Common types of transfer functions

3.10.2 Description of Input & and Output Data

In the present study, MATLAB mathematical software version 7.11.0 (R2010b) was used as a tool to develop ANN models and predict the H_2 yields, CO yield, and ethanol conversion. For this purpose, experimental results were used to develop ANN prediction models. The method relies on the training part of the sample using feed-forward back-propagation learning. We aim to find the best model that can be used to produce a satisfactory prediction for H_2 yields, CO yield, and ethanol conversion. The datasets from experimental results were divided into input and output or target dataset. The input experimental variables were reaction temperature, the molar ratio of the reactants, and liquid hourly space velocity. The outputs were H_2 yield, ethanol conversion, and CO yield. Three-layer back-propagation neural network models were developed using 20 experimental data planned using central composite design as training data. The dataset was divided into training and testing subsets. Considering the smaller size of the dataset, 15% of the experimental data were used during the testing stage. Process inputs for neural network models were inconsistent based on their magnitudes. Thus, these input data were normalized within a consistent range [0 to 1] before introducing them to the input layer of the network to ensure that each data are given fair contribution in determining the network output. The data normalization method employed in this research is expressed in Equation (3.50).

$$Nor\_X = \frac{X_i}{max(X_i)} \tag{3.50}$$

where, Nor_X is the normalized data of the input and the output, X_i is the actual input /output before scaling (normalization), $max(X_i)$ is the maximum data, respectively.

The networks were trained using three different algorithms 1) Levenberg Marquardt Learning Algorithm (Trainlm), 2) Gradient descent w/momentum & adaptive backpropagation (Traingdx), 3) Scaled conjugate gradient backpropagation (Trainscg). Trial and error search method was applied to select the optimum topology of the model. The information was propagated forward to the output layer where the

output variable was calculated and compared to the actual value in order to generate a prediction error. The process of ANN modelling includes following steps:

1) Database collection,
2) Analysis and preprocessing of the data,
3) Design and training of the neural network,
4) Test of the trained network, and
5) Use of the trained NN for simulations and predictions.

3.11 ANN EVALUATION

The criteria used to evaluate ANN model performance included mean square error (MSE), and the efficiency (*Eff.*). Equations (3.51) and (3.52) were used to calculate (MSE) and (*Eff.)*, respectively.

$$MSE = \frac{1}{n}\sum_{i=1}^{n}\left(y_{Exp} - y_{ANN}\right)^2 \tag{3.51}$$

$$Eff = \frac{1 - MSE}{Var.} \tag{3.52}$$

$$Var = SD\left(y_{Exp}\right)^2 \tag{3.53}$$

where, y_{Exp} and y_{ANN} are vectors of an experimental and prediction value, respectively. *Var* and *SD* are the variance and standard deviation, respectively.

After appropriate input parameters for hydrogen prediction has been selected, the optimum number of neurons was searched in order to improve the predictive performance. Therefore, training algorithm and neuron number in the input layers were changed, while the transfer function, and number of neurons in the hidden layer were used as those used in the initial model.

Neurons numbers in the input layer were varied from [5 to 15] for the three training algorithms (*TrianLM, TrainScg, and TrainGdx*) tested, while numbers of neurons in the second hidden layer were kept constant at 4. The optimal number of neurons in the input layer was selected based on the minimum mean square error (MSE) and maximum efficiency in the testing stage. Neural network topologies of samples employed for the optimization of the neural network model are illustrated in Table 3.9.

Table 3.9 Neural network topologies of samples employed for the optimization of the neural network model

Training algorithms	Input layer	Hidden layer	Output layer	Activation functions
TrianLM	5	4	3	Log Sigmoid
TrianLM	10	4	3	Log Sigmoid
TrianLM	15	4	3	Log Sigmoid
TrainScg	5	4	3	Log Sigmoid
TrainScg	10	4	3	Log Sigmoid
TrainScg	15	4	3	Log Sigmoid
TrainGdx	5	4	3	Log Sigmoid
TrainGdx	10	4	3	Log Sigmoid
TrainGdx	15	4	3	Log Sigmoid

CHAPTER IV

RESULT AND DISCUSSION

This chapter is divided into three parts. The first part presents the thermodynamic calculations of ethanol steam reforming. The catalyst study to select the optimum catalyst system for H_2 production via ethanol reforming is described in the second part. The characterization of the physical and chemical properties of the catalyst was studied. The performance of the catalyst was evaluated in terms of H_2 yield and ethanol conversion. Building statistical and artificial neural network model capable to predict H_2 yield and ethanol conversion are then discussed in the last part of this chapter.

4.1 THERMODYNAMIC ANALYSIS

4.1.1 Effect of Ethanol-to-Water Molar Feed Ratio and Temperature on Ethanol Conversion

Figure 4.1 shows the thermodynamic conversions of ethanol as a function of temperature and ethanol-to-water molar feed ratio at atmospheric pressure. As expected for an endothermic reaction, increasing the temperature has a positive influence on ethanol conversion. That was obvious for temperature up to 500 K. Similar trend was observed regarding the effect of water to ethanol molar ratio. For example, at a value of water to ethanol molar feed ratio of 3, ethanol conversion increased significantly from 3.65% at 300 K to 97% at 500 K. Similarly, at a temperature of 400 K, ethanol conversion was increased from 40.63% at water to ethanol molar feed ratio of 3:1 to about 93% at water to ethanol molar feed ratio of 9:1.

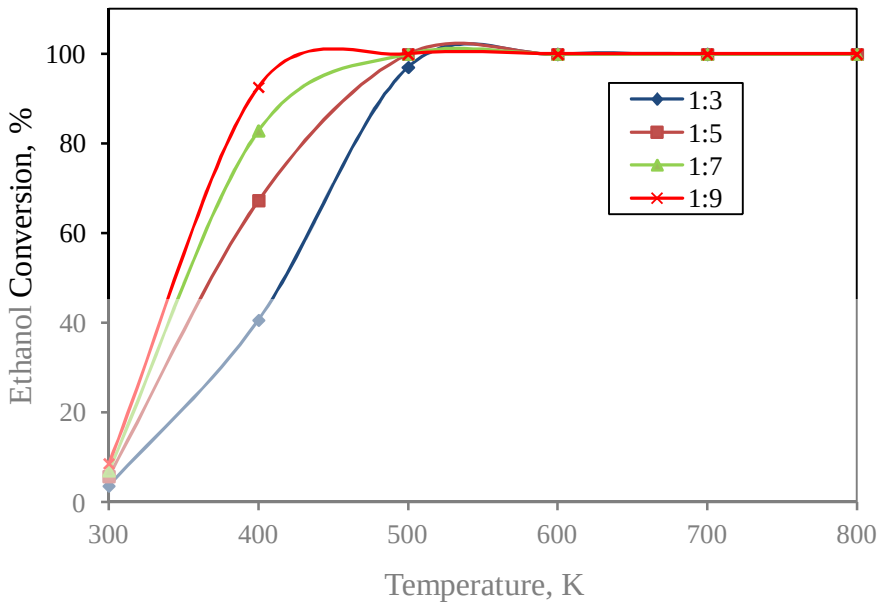

Figure 4.1 Thermodynamic effects of temperature and ethanol to water molar ratio on ethanol conversion at different reaction temperatures

As a result, approximately complete ethanol conversion was achieved as the temperature reached a value of 500 K at all values of ethanol-to-water molar feed ratio. At higher temperatures, ethanol-to-water molar feed ratio has no effect on ethanol conversion, which means that whatever the amount of water initially introduced, for $T > 500$ K, ethanol is completely converted. This may attributed to that, the excess of water added is being used for reforming other products such as acetaldehyde and methane. These results are similar to those reported in literature (Benito et al. 2005). This suggests that experiments should be conducted at temperatures above 500 K.

4.1.2 Effect of Pressure and Temperature on Ethanol Conversion

The effect of pressure on ethanol conversion with reaction temperature ranges from 300 K to 800 K is shown in Figure 4.2.

Given the difference in molar quantity between reactants and products, total pressure affects the equilibrium of ethanol steam reforming. The strongest effect of

pressure appears at low values of temperature ranges from 300 K to 600 K. Increase in pressure shifts the equilibrium to reactants. Within this temperature range, increasing pressure has a negative effect on ethanol conversion. For instance, at 400 K, ethanol conversion decreases from 41% at 1 atm to 7% at 50 atm. Similarly at 500 K, ethanol conversion decreases from 97% at 1 atm to 55% at 50 atm. For temperatures higher than 600 K, the pressure has no effect on ethanol conversion where all values of pressure show almost complete conversion of ethanol.

According to Le Chatelier's principle, when pressure apply on a system, the volume will decrease, so that, the particles will shift.to less moles of gas. This result was in good agreement with other published data noted by Lin et al. (2008). The thermodynamic calculation to obtain ethanol conversion based on equilibrium constants is shown in Appendix A-1.

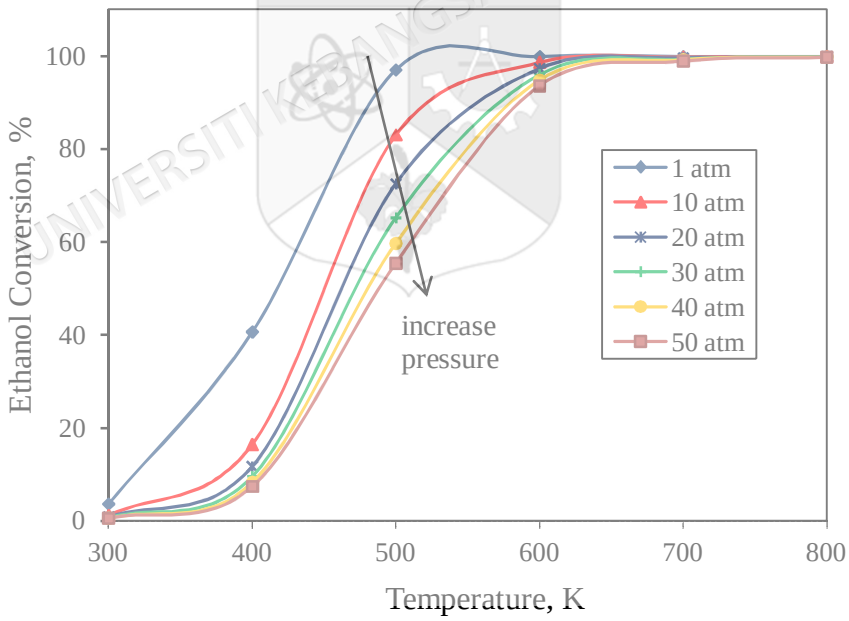

Figure 4.2 Thermodynamic effects of pressure and temperature on ethanol conversion at different temperatures

4.1.3 Effect of Temperature and Molar Ratio on Moles and Molar Fraction of Hydrogen

Figures 4.3 (a) and (b) depict the H_2 moles and molar fraction at different temperatures and ethanol-to-water molar ratios, respectively.

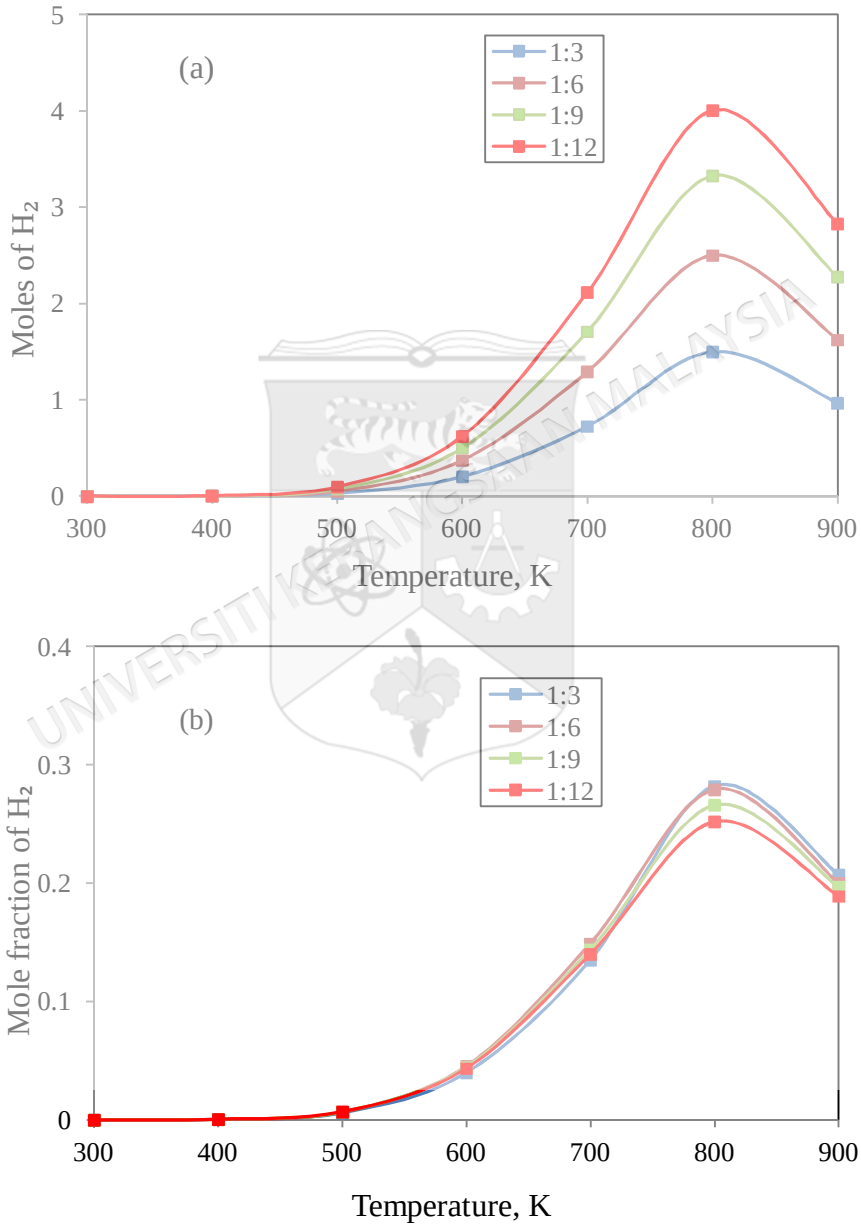

Figure 4.3 a) Hydrogen moles vs. temperature at different molar ratios at P =1 atm, b) Mole fraction of hydrogen vs. temperature at different molar ratios at P =1 atm

Low temperatures are found to be unsuitable for reaction based on H_2 yield. As shown in Figure 4.3 (a), the number of moles of H_2 increases with increasing temperature. Similarly, the number of moles of H_2 increases with increasing ethanol-to-water molar feed ratio. This increase can be attributed to the acceleration of water gas shift reaction (Equation 2.14), which converts CO to CO_2 and H_2 in the presence of water.

The effect of temperature and ethanol-to-water molar feed ratio on the molar fraction of H_2 is shown in Figure 4.3 (b). The molar fraction of H_2 is found to be higher in case of low ethanol-to-water molar feed ratio, which is clearly observed at higher temperature values because a large quantity of unreacted water exists in the product at high ethanol-to-water molar feed ratio. This amount of water diminishes the H_2 mole fraction, but not necessarily the amount of H_2. The largest amount of H_2 is obtained from excess water at all temperatures. The best conditions for H_2 production are obtained from excess amount of water, but the energy required to evaporate the excess water will be higher. These results shows similar trend exhibited by Adhikari et al. (2007) for glycerol steam reforming. They concluded that, the greatest quantity of hydrogen is produced at excess water at all temperatures.

4.1.4 Effect of Temperature and Molar Ratio on Moles and Molar Fraction of Methane

In addition to H_2, CH_4 is also produced in the case of H_2 production via ethanol steam reforming. Methane production occurs either by ethanol composition (Equation 2.10) or methanation reaction (reverse of Equation 2.7). However, CH_4 is an undesirable product because CH_4 competes with H_2. Figures 4.4 (a) and (b) show the CH_4 moles and molar fraction at different temperatures and ethanol-to-water molar ratios respectively. Figure 4.4 (a) shows that the production of CH_4 is thermodynamically favored at lower temperature in all values of ethanol-to-water molar feed ratio. Beyond 600 K, the moles of CH_4 decrease as the temperature and ethanol-to-water molar feed ratio increase. For instance, at a value of water to ethanol molar feed ratio of 3, methan production decreased significantly from 1.3 mol at 700 K to about 0.4 mol at 800 K. Similarly, at a temperature of 700 K, for example, moles of methan

were decreased from about 1.3 mol at water to ethanol molar feed ratio of 3:1 to about 1 mol at water to ethanol molar feed ratio of 12:1. This suggest that, the methanation reaction, is favored at higher water to ethanol molar feed ratio and lower temperatures (below 700 K).

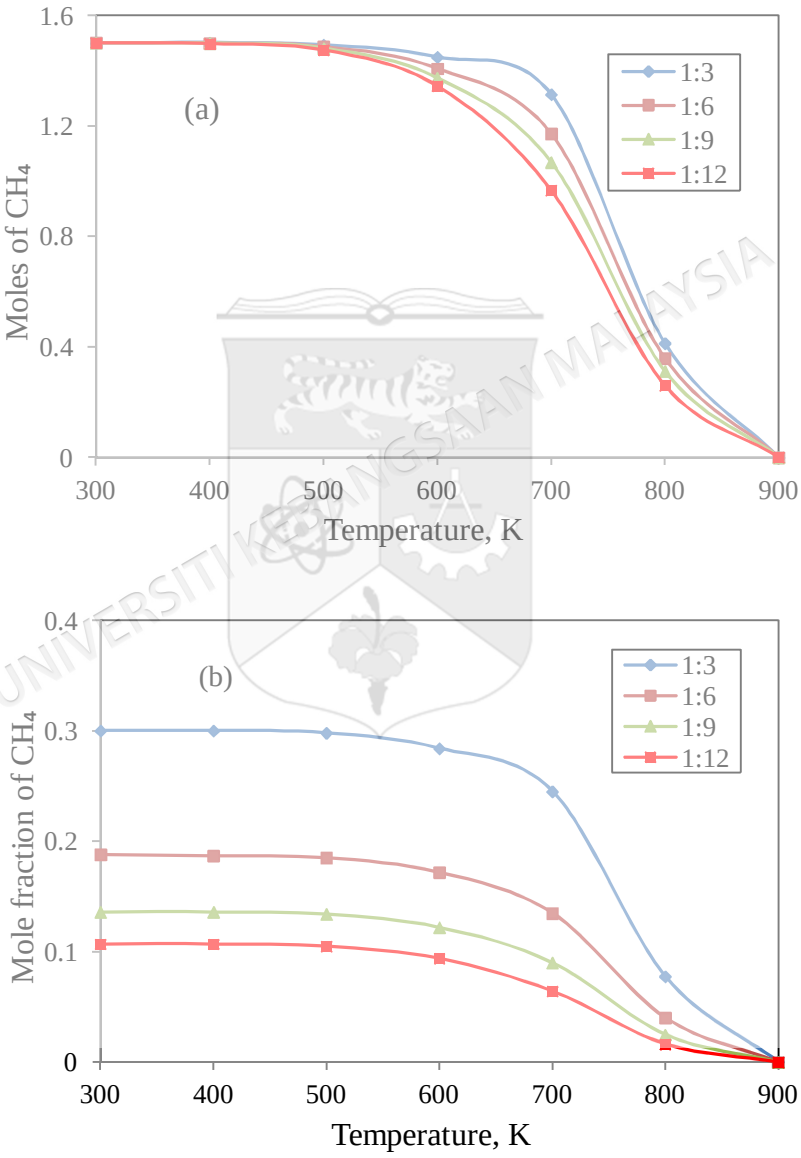

Figure 4.4 a) Methane moles vs. temperature at different molar ratios at P =1 atm, b) Mole fraction of methane vs. temperature at different molar ratios at P=1 atm

Figure 4.4 (b) shows a similar trend exhibited by the effect of temperature and ethanol-to-water molar feed ratio on the molar fraction of CH_4. Molar fraction of CH_4 also decreases with the increase in temperature and ethanol-to-water molar feed ratio. Therefore, reduction in the yield of CH_4 is obtained by the use of a higher ratio of water to ethanol in the feed. These results are similar to those reported in literature (Comas et al. 2004; García & Laborde 1991; Vasudeva et al. 1996). This would suggest that, in order to minimize CH_4 concentration in product stream, the reaction temperature should be high.

4.1.5 Effect of Temperature and Molar Ratio on Moles of Carbon Monoxide and Carbon Dioxide

Carbon monoxide and carbon dioxide are oxygenated compounds usually present in effluent gas and are considered as impurities. The mole numbers of CO and CO_2 at equilibrium against temperature at different ethanol-to-water molar feed ratios are presented in Figures 4.5 (a) and (b), respectively. Figure 4.5 (a) shows that the moles of CO increase with the decrease in ethanol-to-water molar feed ratio values but increase with the increase of temperature. Therefore, to reduce CO production, high ethanol-to-water molar feed ratios and low temperature are appropriate. However, the moles of CO_2 increase as temperature increases until the maximum value is reached at around 800 K, and then decrease at higher temperature values as shown in Figure 4.5 (b). These results show that at temperatures up to 800 K, a water–gas shift reaction is favored. For this reason, a number of H_2 moles increased significantly up to 800 K.

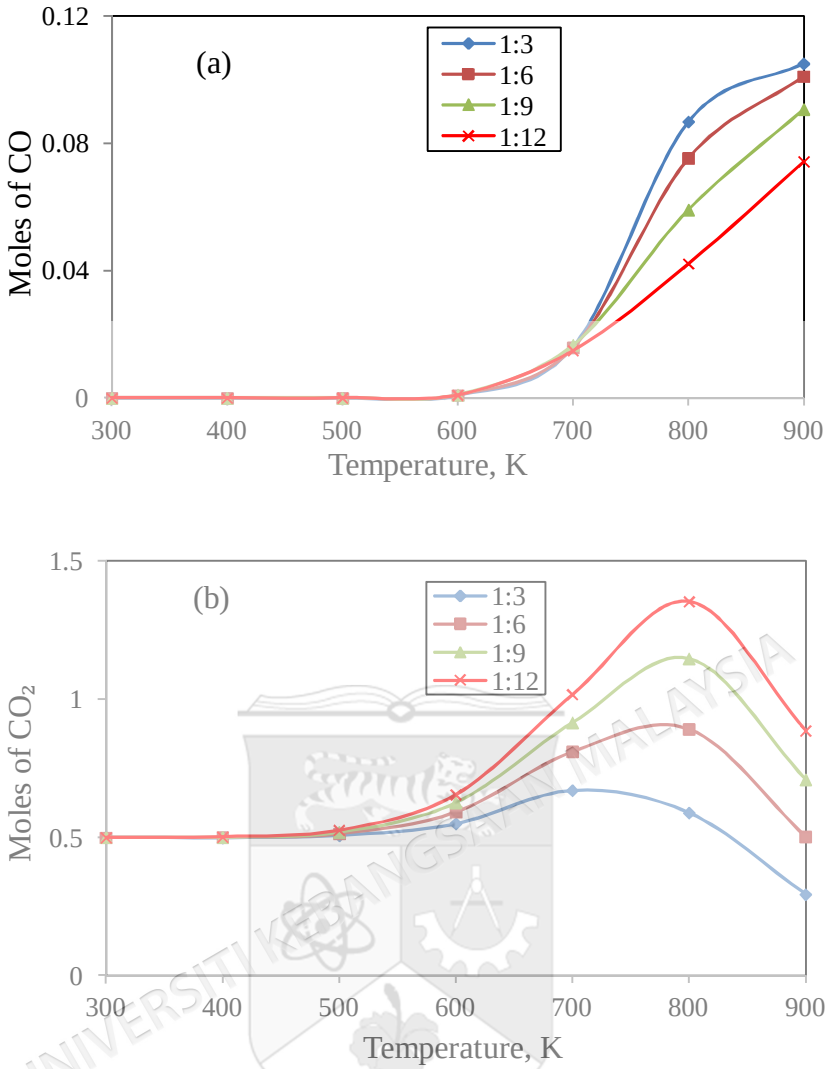

Figure 4.5 a) Carbon monoxide moles vs. temperature at different molar ratios at P=1 atm, b) Carbon dioxide moles vs. temperature at different molar ratios at P =1 atm

The moles of CO_2 also increase with the increase of water-to-water molar ratio because of the presence of a water–gas shift reaction that favored the production of CO_2 and H_2. Other publication studied hydrogen production via gelecyrol steam reforming shows that, the number of moles of CO_2 increase with increasing temperature also, till reach their maximum value at temperature of 850 K, and then decrease at higher temperature (Adhikari et al. 2007).

Figure 4.6 depicts the changes of equilibrium product moles by temperature for ethanol steam reforming of ethanol-to-water molar feed ratio of 1:12 and

atmospheric pressure. At low temperature, CH_4 and CO_2 are observed to occur the most with an insignificant amount of H_2 and almost no CO. As the temperature of the steam reforming increases, the H_2 amount increases, whereas the CH_4 content decreases concurrently. At higher temperature, the CO content increases. The increase in CO amount and decrease in CH_4 show that CO is mainly produced from the steam reforming of CH_4 (Equation 2.7) and reverse water–gas shift reactions. These results are in agreement with other published thermodynamic data obtained by (Rossi et al. 2009). The only difference is that, we use a wider temperature range, while in mentioned study the temperature values between 700 to 900 K.

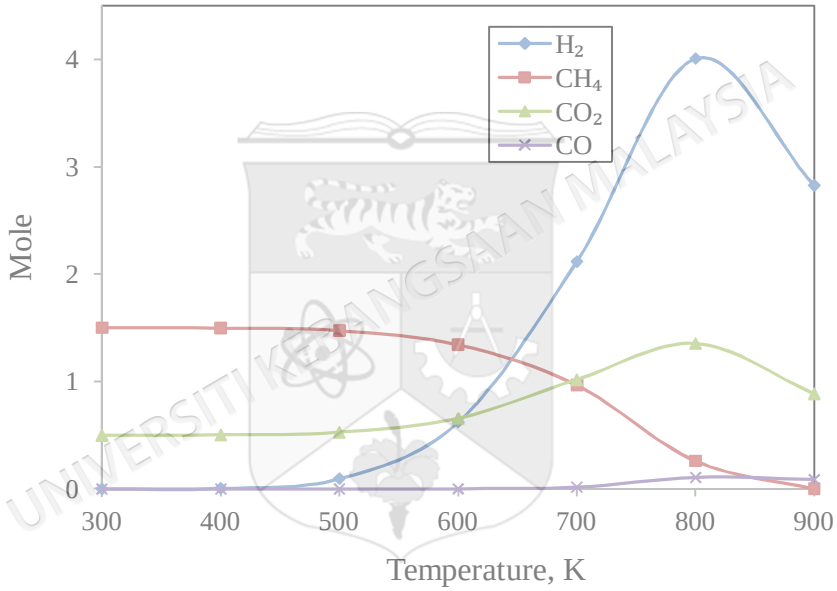

Figure 4.6 Product yields in mole for steam reforming of ethanol at ethanol to water molar feed ratio of 1:12 and atmospheric pressure

4.1.6 Effect of Pressure on Product Yields

The effect of pressure on H_2 and CH_4 yields with reaction temperature ranging from 300 K to 900 K is shown in Figures 4.7 (a) and (b) respectively. Pressure values from 1 atm to 30 atm were used.

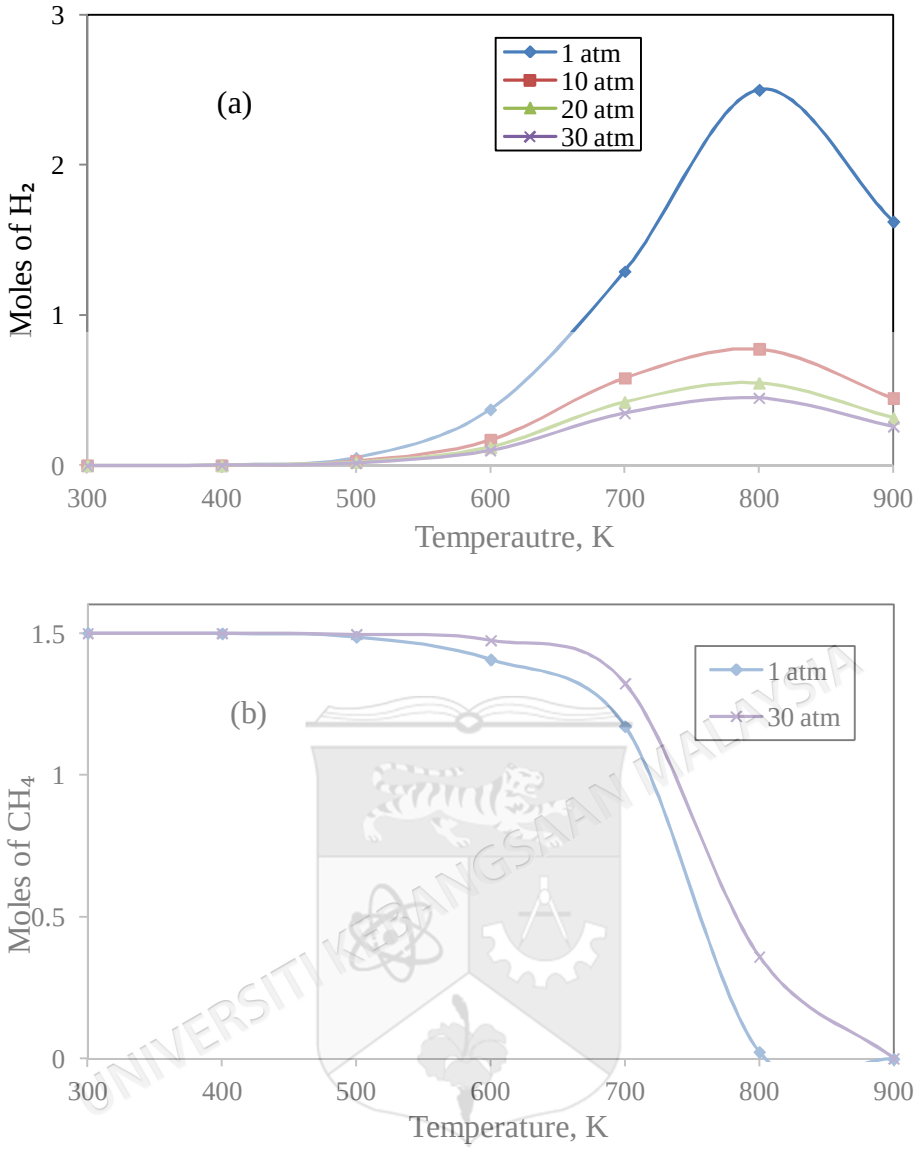

Figure 4.7 Thermodynamic effects of pressure on a) Hydrogen Moles, b) Methane moles produced at selected pressure

The significant effect of pressure on the production of H_2 and CH_4 yields occurs at higher temperature values, whereas low temperatures reduce the effect of pressure on both gases. As shown in Figure 4.7 (a), the number of moles of H_2 increases with decreasing pressure and increases with increasing temperature. This is because the reforming reaction of ethanol is affected significantly by the increase of pressure due to the difference between the number of moles in the product and reactant sides. The influence of pressure on the ethanol steam-reforming process is

found to be consistent with those of glycerol steam-reforming processes (Adhikari et al. 2007).

By contrast, higher pressure favors the production of CH_4, as shown in Figure 4.7 (b). At high temperature, the formation of CH_4 is greatly suppressed. However, the rapid decrease in H_2 production is accompanied by an increase in CH_4 moles, which indicates that the reaction is closely related to the methanation reaction.

Figures 4.8 (a) and (b) show the moles of CO and CO_2 at different reaction temperatures and pressures respectively. The amount of CO and CO_2 yields is presented as a function of pressure in the range of 1 to 30 atm. Increase of pressure has a negative effect on both gases, where the CO and CO_2 mole numbers decrease with increasing pressure. The strongest effect of pressure appears at temperature above 600 K for both gases. For example, as seen in Figure 4.8 (a), the increase of pressure from 1 to 10 atm causes a decrease in CO yield from 0.09 mol to less than 0.01 mol for T = 900 K, and from about 0.06 mol to less than 0.01 mol for T = 800 K. Similarly, as seen in Figure 4.8 (b), the increase of pressure from 1 to 10 atm causes a decrease in CO_2 yield from about 0.5 mol to 0.15 mol for T = 900 K, and from about 0.9 mol to 0.25 mol for T = 800 K. Overall, it can be said that the negative effect of pressure is small especially at higher pressure values (> 10 atm). Therefore, in order to decrease CO content, reaction temperature should be in the region where the pressure has insignificant effect on gas yield (< 700 K).

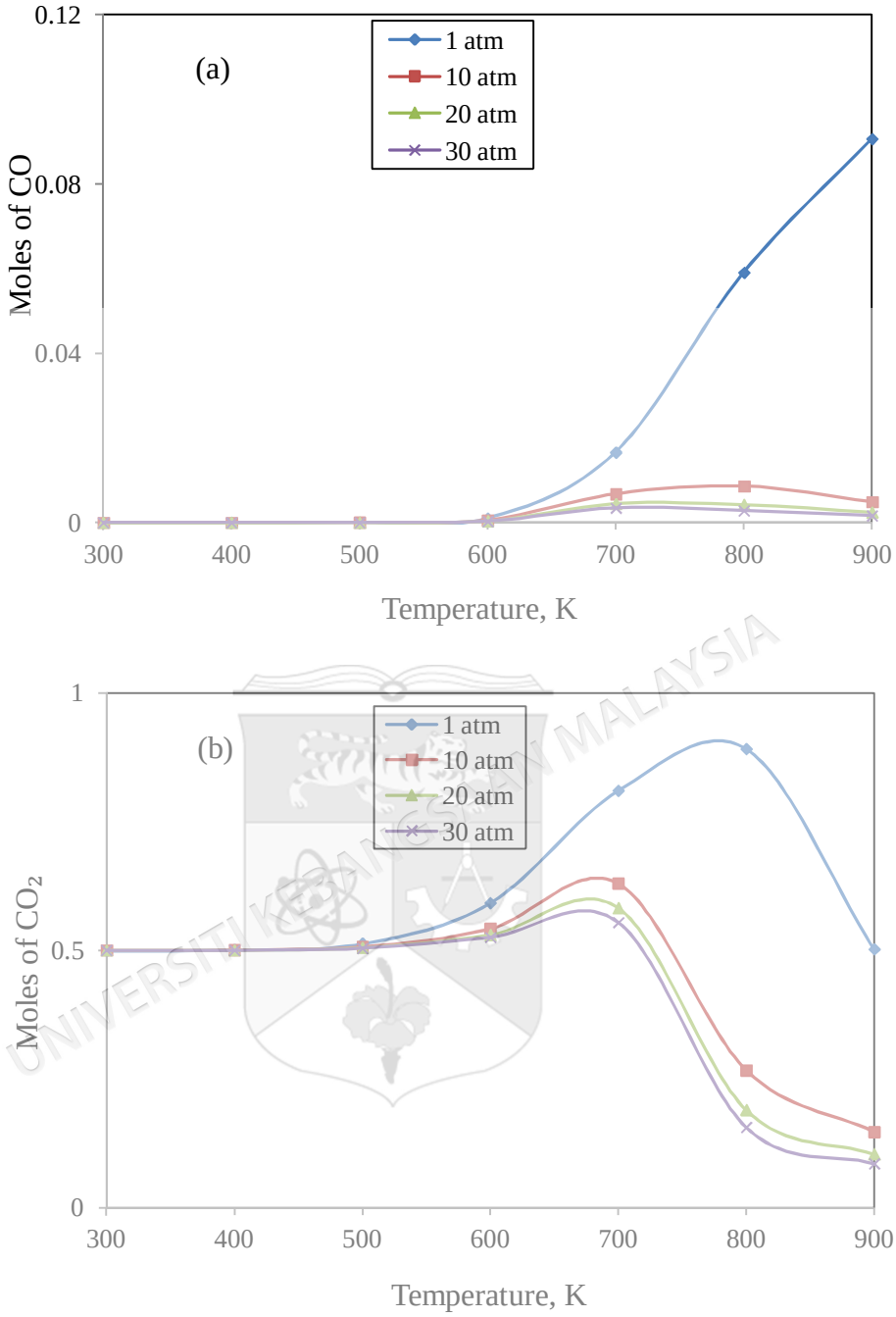

Figure 4.8 Thermodynamic effects of pressure on a) Carbon monoxide Moles, b) Carbon dioxide moles produced at selected pressure

4.1.7 Carbon Formation

Carbon is an undesirable substance that reduces H_2 formation and causes catalyst deactivation (Rossi et al. 2009). High temperatures that favor steam reforming to

produce H_2 can also be associated with the formation of carbon. Equations (2.12) and (2.13) can be a possible source of carbon formation (Rabenstein et al. 2008).

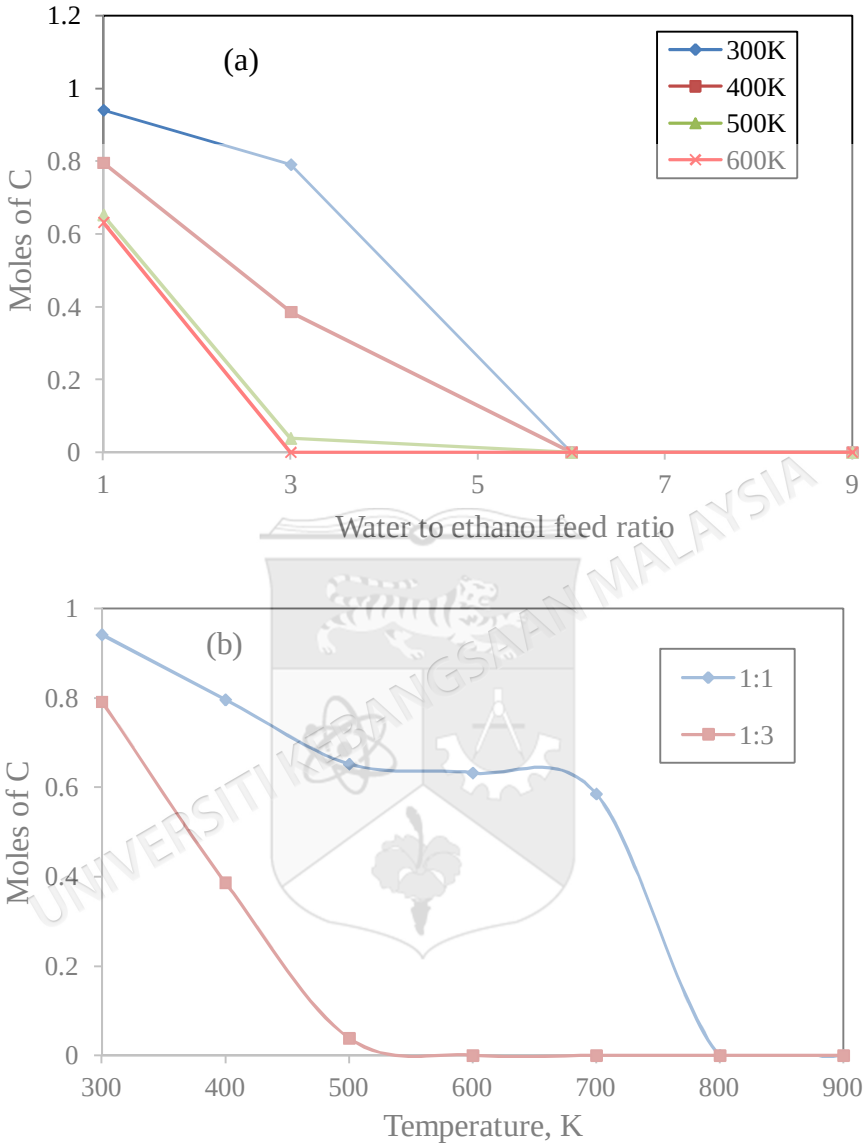

Figure 4.9 a) Moles of carbon formation at different ethanol to water molar feed ratios at selected temperatures at P =1 atm, b) Moles of carbon formation at different temperatures at selected ethanol to water molar feed ratios at P =1 atm

Figures 4.9 (a) and (b) show the carbon formation at different reaction temperatures and different ethanol-to-water molar feed ratios. At and above 800 K, no carbon is produced at any ethanol-to-water molar ratio value. At ethanol-to-water molar feed ratios of 1:6 and 1:9, carbon production was thermodynamically prevented

at any temperature value as shown in Figure 4.9 (a). In addition, increasing ethanol-to-water molar feed ratios from 1:1 to 1:3 significantly decreases carbon formation as shown in Figure 4.9 (b). Conversely, pressure has no effect on carbon formation as shown in Figure 4.10, where the amount and trend of carbon moles formed at P = 10 atm were exactly the same as in the case of 1 atm. Thermodynamic data regarding the minimization of the Gibbs free energy method are listed in Appendix A-3.

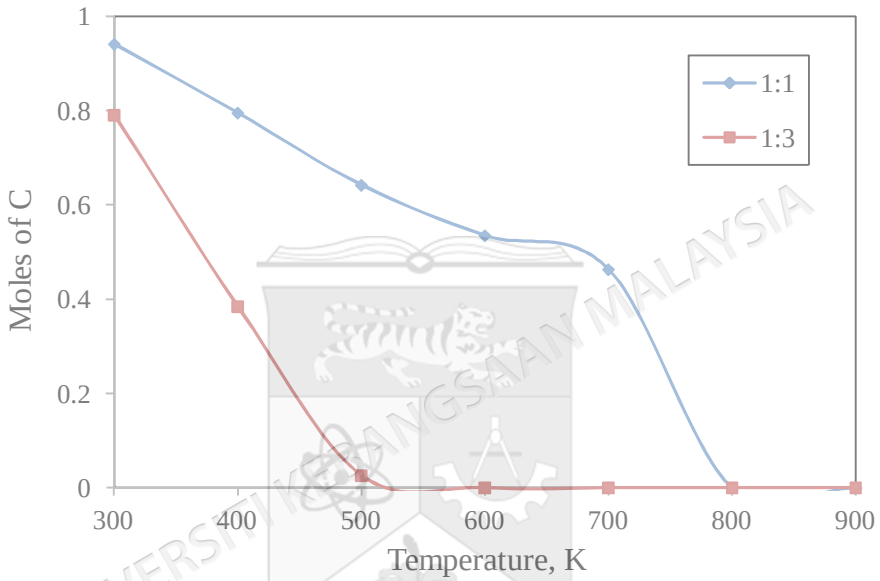

Figure 4.10 Moles of carbon formation at different temperatures at selected ethanol to water molar feed ratios at P =10 atm

4.1.8 Summary of Thermodynamics Analysis

A thermodynamic analysis for H_2 production by steam reforming of ethanol was performed. Thermodynamic ethanol conversion was calculated based on the equilibrium constants, and the number of moles of products was calculated based on minimizing the Gibbs free energy. The thermodynamic calculations show that ethanol conversion for temperatures equal or higher than 600 K can be completed at any value of pressure and molar ratio. H_2 yield is favored at high temperature, high ethanol-to-water molar feed ratio, and low pressure. By contrast, CH_4 formation is favored at low ethanol-to-water molar feed ratio, low temperature, and high pressure, and CO moles

are favored at high temperature, low ethanol-to-water molar feed ratio, and low pressure.

Seeking a high H_2 yield and a low CO yield is a contradiction because the reaction temperature should be sufficiently high to obtain a reasonable H_2 yield and as low as possible to obtain a low CO yield. Although this thermodynamic calculation indicates an advantage of conducting ethanol reformation at high temperature and high ethanol-to-water molar feed ratio because of the high level of H_2 formed, these conditions lead to an increase in energy requirement for water evaporation. Thus, experiments in this research were run under mild conditions of 673 K, 1 atm, and 6:1 water-to-ethanol molar ratio.

4.2 CATALYST CHARACTERIZATION

In this section, the characterization of catalysts covered all the catalysts prepared by both methods (impregnation and precipitation) to examine the relationship between its properties and catalytic performance. The Ni/Al_2O_3 catalysts were characterized using BET, crystallite size, N_2 adsorption desorption, XRD patterns, TPR, and SEM.

4.2.1 BET Surface Area and Crystallite Size

BET surface area analyses and crystallite size investigations were performed on all nickel loaded catalysts, as well as on the support. Results are provided in Table 4.1.

The commercial alumina support exhibited a higher surface area (138 m^2g^{-1}) than the IMP-synthesized catalysts. The BET surface area of the IMP-synthesized catalysts decreased from 119 to 102 m^2g^{-1} as the Ni content increased. A similar trend was observed with PT-synthesized catalysts where the surface area decreased from 154 to 136 m^2g^{-1}. The loss of surface area with increasing Ni loading was due to the plugging of some pores by excess nickel. The first three PT-synthesized catalysts (6PT, 8PT, and 10PT) exhibited higher surface areas than the support as a result of the leaching of Al from the matrix during treatment with Ni solution, resulting in

increased porosity. However, the surface area of certain catalysts (i.g. 6-10 IMP) were not significantly effected by varying Ni loading. That is may be due to the small differences between the values of Ni content, which only 2wt% increaments.

Table 4.1 Surface area and crystallite size of IMP and PT catalysts

Sample	BET, (m^2g^{-1})	Crystallite Size, (nm)	
		NiO	Al_2O_3
Al	138	-	11.32
6IMP	119	3.5	10.87
8IMP	118	4.0	10.49
10IMP	117	12.2	8.9
12IMP	103	13.5	7.6
20IMP	102	15.8	5.5
6PT	154	3.1	6.4
8PT	147	3.6	6.4
10PT	141	4.4	6.6
12PT	136	5.3	6.2
20PT	136	8.3	4.4

Figures 4.11 (a) and (b) show the nitrogen adsorption-desorption isotherms of the commercial alumina support, as well as isotherms for selected Ni-loaded catalysts prepared through the IMP and PT methods, respectively. All samples exhibited type-IV (IUPAC) curves, indicating the presence of a mesoporous material. The isotherms exhibited H4 hysteresis loops, which were indicative of narrow slit-like pores. This result is in a good agreement with other published data (Hernández et al. 2010). This study shows adsorption–desorption isotherms of 10% Ni-W/Al_2O_3 and 30%Ni-W/Al_2O_3 catalysts before the steam reforming reaction. The samples show type-IV (IUPAC) curves, pointing to the mesoporous material. In both preparation methods increases in nickel content resulted in a decrease in adsorbed gas, thereby giving evidence of a decrease in surface area.

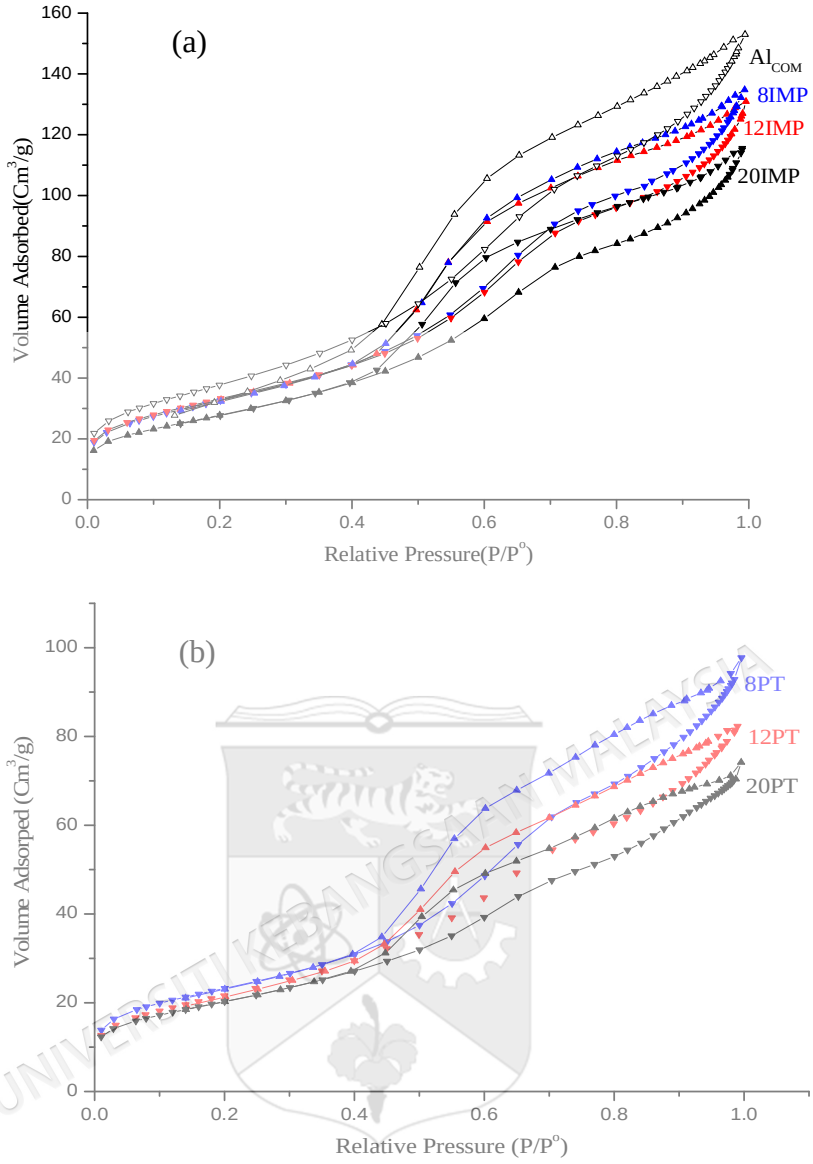

Figure 4.11 Nitrogen adsorption–desorption isotherms for support and catalysts a) Impregnation catalysts, b) Precipitation catalysts

4.2.2 Powder X-ray Diffraction (XRD)

The XRD patterns of the samples were recorded to investigate the chemical specie present in the catalysts. Figures 4.12 (a) and (b) show XRD patterns of the Ni/Al_2O_3 catalysts prepared with various metal loadings using both synthetic methods. The spectrum for the alumina support is also shown. This spectrum was used to identify the appearance of metal peaks in the catalyst. The alumina support and IMP catalyst patterns are shown in Figure 4.12 (a). The support exhibits the characteristic peaks of

γ-Al_2O_3 at 2θ values of 37.62°, 45.47°, and 67.09°. Additional peaks corresponding to a nickel oxide phase were observed. For samples with low Ni loading, the diffraction peaks of a NiO phase appear to be weak and broad. As Ni loading increased to 12IMP and 20IMP, the intensity of the peaks corresponding to the NiO phase increased significantly, indicating that large NiO particles are formed (Li et al. 2012). This finding was particularly evident in the 20IMP sample, where the NiO phase is identified by 2θ values at 37.2°, 43.3°, 62.8°, and 75.5° (Roh et al. 2003).

Figure 4.12 (b) presents similar NiO peaks with 2θ values of 37.25°, 43.25°, and 62.71° in catalysts prepared by using the PT method. These peaks are less intense than those observed in the IMP catalysts, indicating a high dispersion of metal species on the alumina surface. Although Na_2CO_3 was used for the synthesis of PT catalysts, the formation of nickel aluminum carbonate hydroxide ($Ni_2Al(CO_3)_2(OH)_3$ and $NiAl(CO_3)(OH)_3$) or nickel carbonate hydroxide hydrate ($Ni_2(CO_3)(OH)_2.4H_2O$) was not observed, which is consistent with previously published studies (Akande et al. 2005). These findings may be attributed to the removal of all CO_3^{-2} in the solution during washing and calcination treatment of the catalyst.

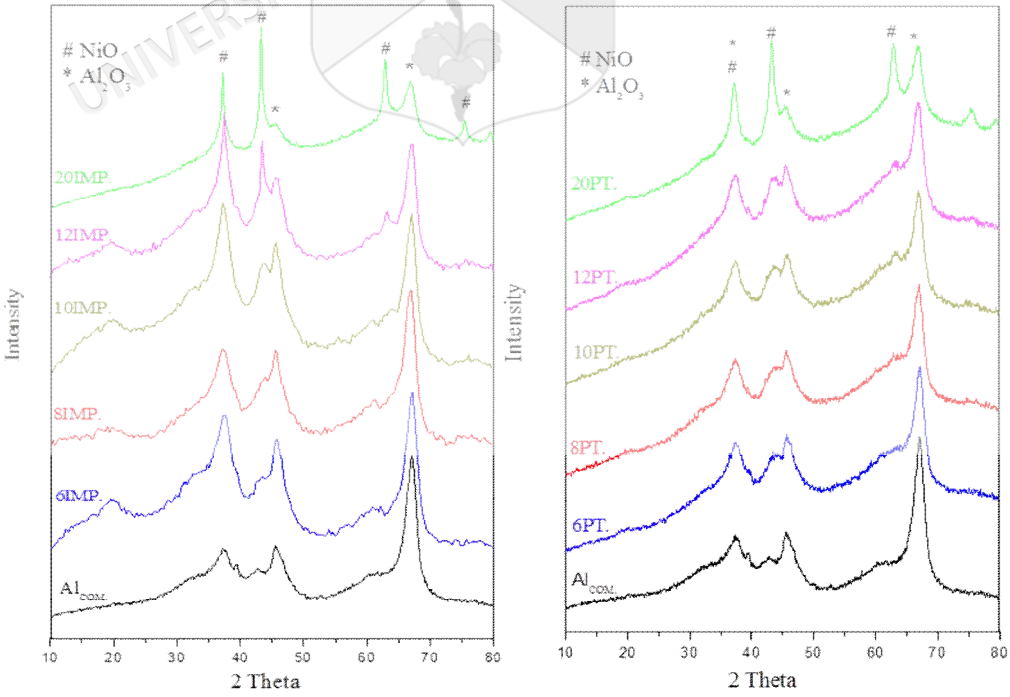

Figure 4.12 XRD patterns of the support and catalysts a) Impregnation catalysts, b) Precipitation catalysts

Crystallite size measurements for the Al_2O_3 supports and NiO species as a function of synthetic method and Ni loading are shown in Table 4.1. The crystallite sizes of the samples were obtained by using TOPAS software. Also, Sherrer equation was used to measure the crystallite size as a result confirmation. The most intense peaks, at 2θ values of 43° and 67°, were used to identify the NiO and Al_2O_3 phases, respectively. For the IMP-synthesized catalysts, the crystallite size of the NiO species ranged from 3.5 nm to 15.8 nm. The NiO crystallite size of these catalysts consistently increased with an increase of metal loading, but a remarkable increase in crystallite size was observed as the metal loading increased from 8 wt% to 10 wt%. The support does not have a uniform surface, as certain spots within the support are strongly bonded with the metal phases, making them stable. In contrast, other spots are weakly bonded with the metal phases; therefore, these species can collide and accumulate easily, forming large crystallites (Erhan Aksoylu & İlsenÖnsan 1997).

Though it is often difficult to explain the factors affecting metal dispersion, the reasoning above is a plausible reason for the relationship between crystallite size and metal content. The existence of larger particles on the surface of the catalyst is not favorable, as it causes nickel agglomeration and carbon formation on catalyst and further affects catalytic activity (Wigmans & Moulijn 1980). The PT method yielded crystallite sizes ranging from 3.1 nm to 8.3 nm; however, the NiO crystallite size increased linearly as Ni loading was increased. In addition, the NiO crystallite sizes obtained for the PT-synthesized catalysts were smaller than those of the IMP-synthesized catalysts. The formation of small crystallites led to high dispersion of the nickel species on the support surface, enhancing the catalytic behavior during steam reforming. For the PT-synthesized catalysts, the crystallite size exhibited a drastic reduction upon initial Ni incorporation but insignificant changes as the metal loading was increased. While no remarkable change in Al_2O_3 crystallite size was observed across all metal loadings of PT-synthesized catalysts, where values ranged from 6.6 nm to 4.4 nm, the Al_2O_3 particle sizes of IMP-synthesized catalysts decreased markedly as Ni loading increased.

4.2.3 Temperature Programmed Reduction Profiles (TPR)

Temperature-programmed reduction (TPR) measurements were performed with 30 mg of Ni/Al_2O_3 catalysts for various metal contents (Figures 4.13 (a) and (b)). TPR analysis allows the examination of the interaction between the nickel species and the support. According to previous studies (Li et al. 2006; Roh et al. 2003), Ni/Al_2O_3 catalysts have three types of reduction bands. The first band, attributed to the reduction of bulk NiO, appears approximately 400 °C, while the second band type, due to the reduction of bulk $NiAl_2O_4$, appears at approximately 800 °C. The third type appears in the range of 400 °C – 800 °C and is either the reduction of NiO strongly bonded with the carrier or the reduction of a surface nickel aluminate phase.

The main reduction peak for most catalysts was found approximately at 400 °C corresponding to the reduction of the NiO species supported on Al_2O_3. This reduction peak indicates minimal interaction with the Al_2O_3 supports (Rynkowski et al. 1993; Zieliński 1982). As reported elsewhere, the formation of strongly interacting NiO was observed in the region between 550 °C and 750 °C (Negrier et al. 2003). However, 6% Ni-doped alumina catalysts display additional reduction bands at 716 °C and 707 °C for 6IMP and 6PT, respectively, which may be attributed to the reduction of nickel oxide strongly interacting with the alumina support. The strong interaction between the nickel species and support in low nickel content catalysts may lead to a highly dispersed Ni species on the Al_2O_3 support surface, resulting in enhanced catalytic hydrogen production. When the amount of Ni increased, the reduction temperature shifted to the left (lower temperature). As more Ni occupies the support surface, the interaction between the metal and the carrier becomes weaker. At high Ni content, Ni phases may accumulate because of the weak interaction between the Ni and Al_2O_3, forming large particles that lead to the blockage of the pores of the support. The low-temperature peaks were attributed to the reduction of NiO not bound with the support, referring to it as "surface" nickel oxide (Rynkowski et al. 1993). The peak temperatures and corresponding species are summarized in Table 4.2.

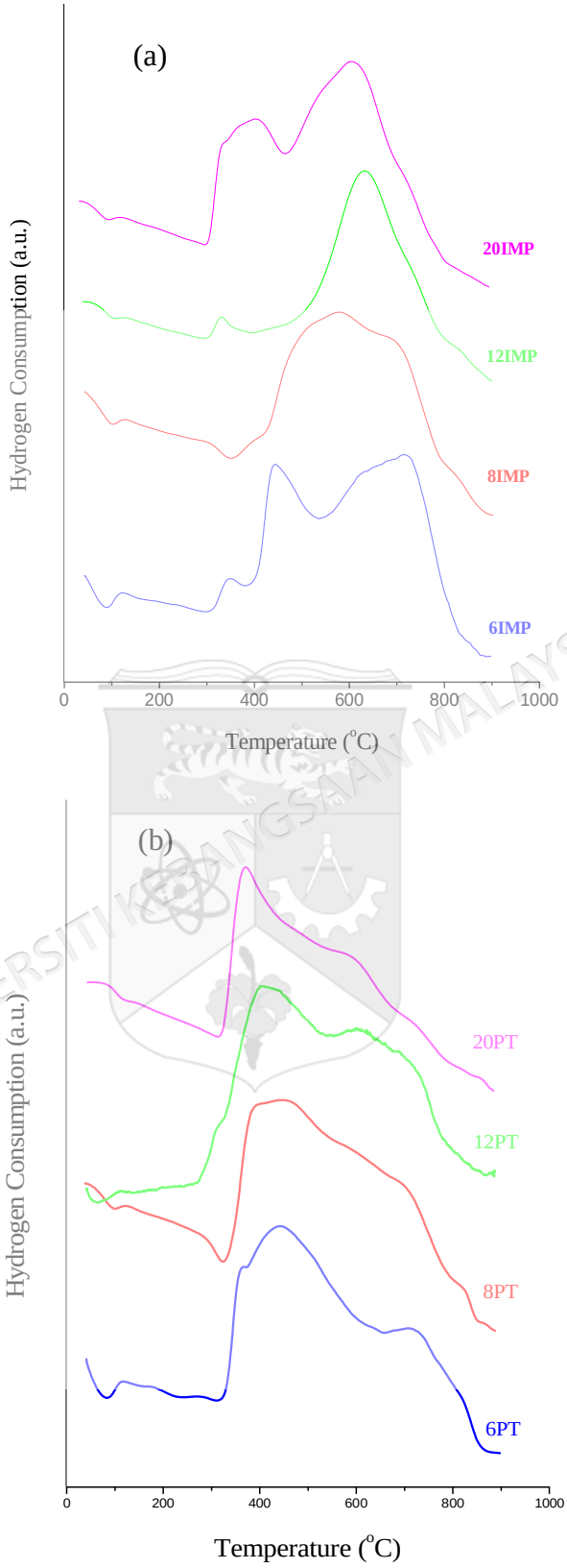

Figure 4.13 TPR profiles of a) Catalysts prepared by impregnation method, b) Catalysts prepared by precipitation method

Table 4.2 Summary of TPR analysis for Ni/Al_2O_3 catalysts

Catalysts name	Number of peaks	Peak temperature,^oC	Major reducible species
6IMP	3	348,441,716	Surface NiO, bulk NiO
8IMP	3	404,578,699	Bulk NiO
12IMP	2	328,632	Surface NiO, bulk NiO
20IMP	2	406,609	Bulk NiO
6PT	3	365,444,707	Surface NiO, bulk NiO
8PT	2	404,455	Bulk NiO
12PT	2	408,613	Bulk NiO
20PT	2	375,587	Surface NiO, bulk NiO,

4.2.4 Scanning Electron Microscopy (SEM-EDAX) Analysis

SEM techniques (Figures 4.14 and 4.15) were used to analyze the surface and morphology of selected samples of both PT and IMP synthetic methods, respectively.

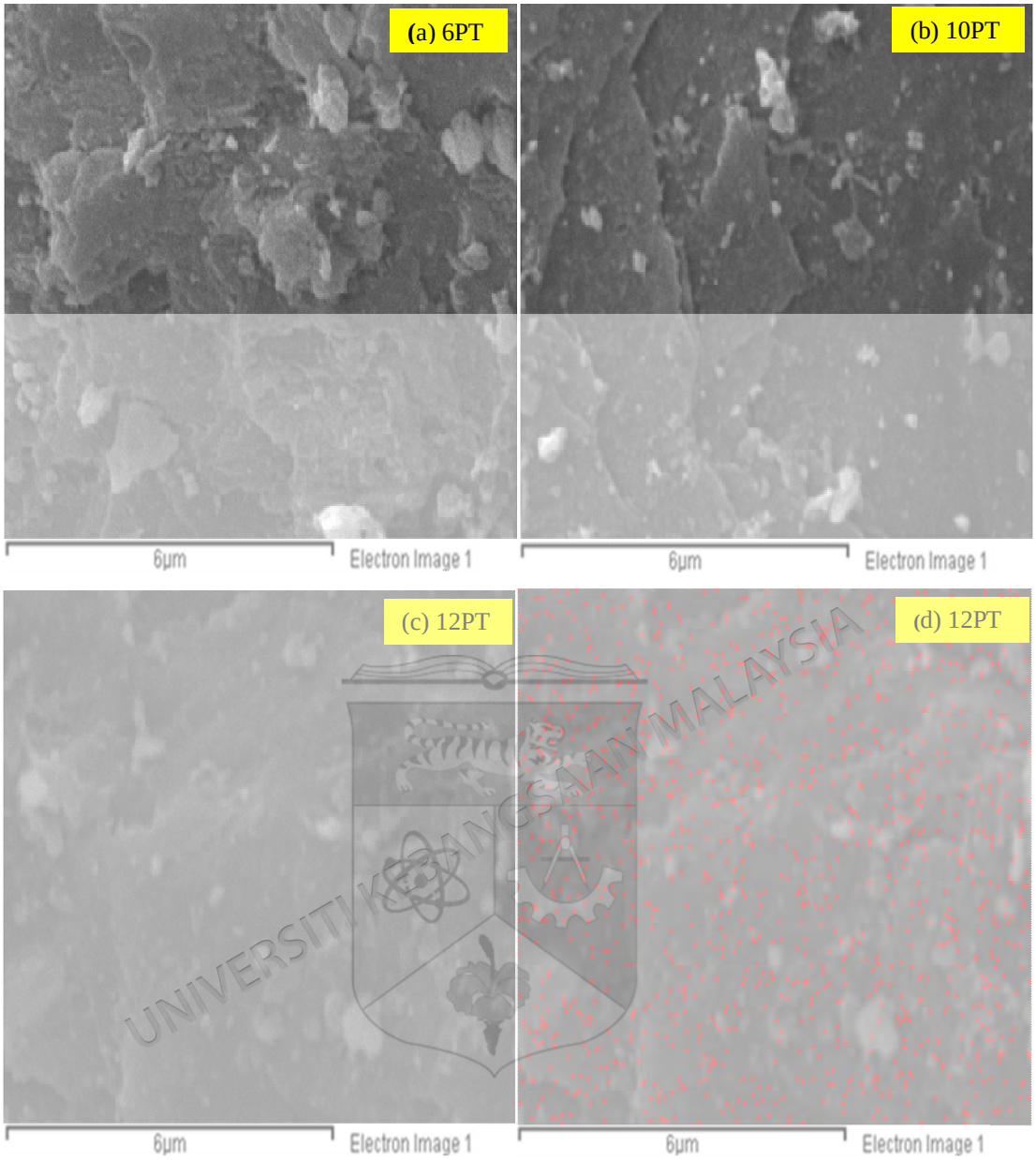

Figure 4.14 SEM micrographies and related EDX mapping of some fresh precipitation catalysts

SEM images of catalysts prepared by precipitation method (Figures 4.14 (a), (b), and (c)) revealed a surface with homogeneous morphology. EDX mapping of one sample (12PT) was employed to determine whether Ni particles are sufficiently dispersed on the catalyst support surface. As exhibited in Figure 4.14 (d), Ni particles (marked as red spots) covered the entire support surface of the catalyst, as is considered optimal for these catalytic systems. This uniform dispersion may have strengthened the catalysts and thereby enabled effective ethanol reformation.

Table 4.3 Theoretical and actual Ni loading on prepared catalysts

Catalyst	Precipitation Catalysts					Impregnation Catalysts				
	6PT	8PT	10PT	12PT	20PT	6IMP	8IMP	10IMP	12IMP	20IMP
Theoretical (Ni) wt %	6	8	10	12	20	6	8	10	12	20
Actual (Ni) wt %[a]	5.7	6.1	7.93	11.3	20.4	4.61	10.26	12.73	17.10	23.26

Note: a determined by EDX

In contrast, catalysts prepared by the impregnation method (Figures. 4.15 (a), (b), and (c)) exhibited morphologies, in which catalysts appeared to have wrinkled surfaces. In these catalysts, Ni particles were found to accumulate in specific zones on the surface (areas inside the circles), as shown in the EDAX mapping images (Figure 4.15 (d)). As a result of this accumulation, the Ni particles were insufficient to mask the support surface completely. The actual wt% of all Ni catalysts were determined and compared with theoretical values of Ni loading to prove the accumulation of Ni on the surface (Table 4.3). The theoretical and actual Ni loadings in the PT-synthesized catalysts followed the same trends at constant increments of the actual Ni loading. Actual Ni loading in the IMP-synthesized catalysts were higher than theoretical loading values, except for the 6IMP sample. Other studies have applied SEM analysis for supported nickel catalyst after use to investigate carbon deposition. The origin of carbon species was also observed. The studies show that large amount of filamentous carbon, as confirmed by EDS analysis (Alberton et al. 2007b; Souza et al. 2004).

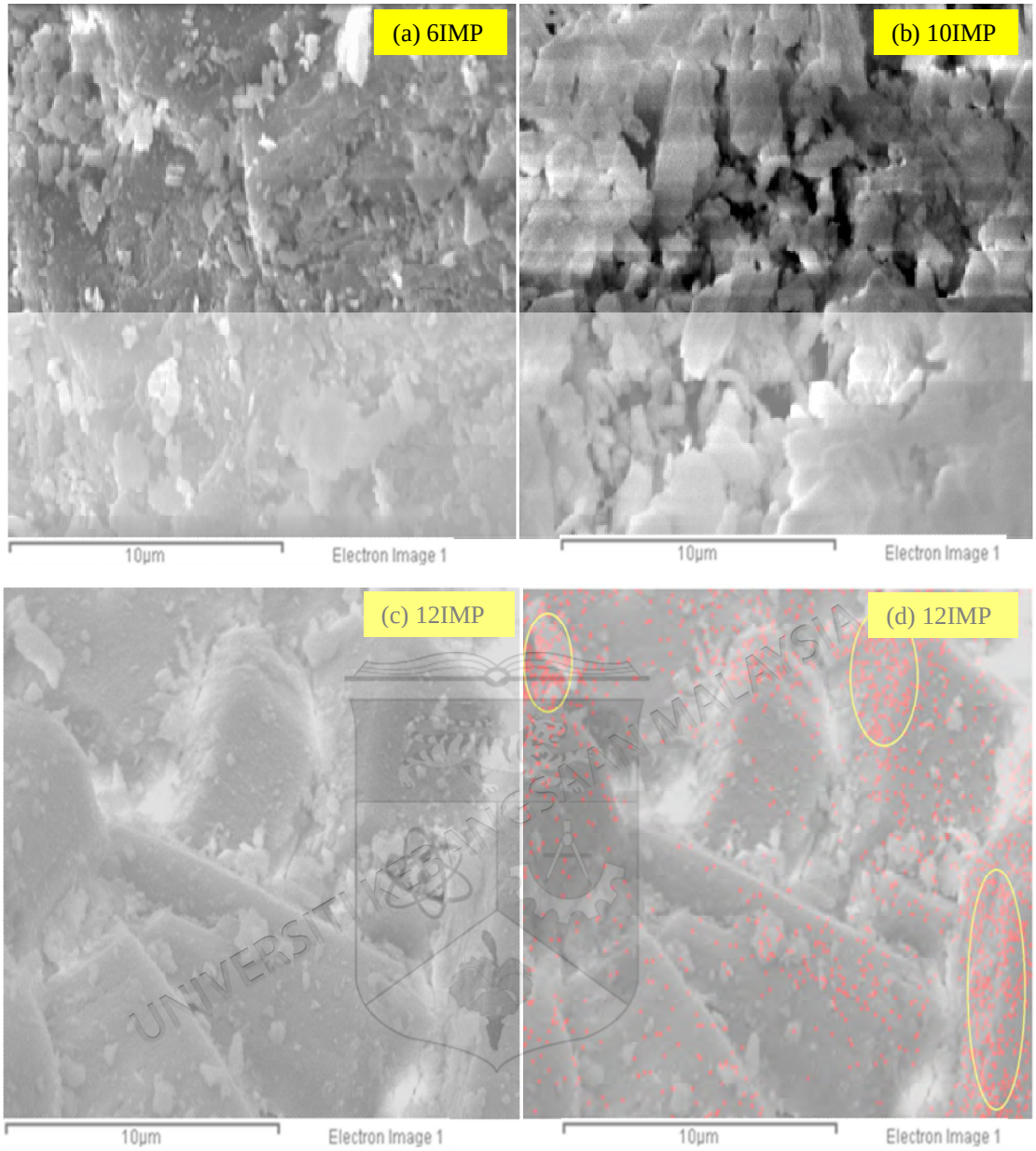

Figure 4.15 SEM micrographies and related EDX mapping of some fresh impregnation catalysts

4.3 CATALYTIC ACTIVITY

4.3.1 Ethanol Conversion and Product Selectivity over a 3-hr Reaction

All prepared catalysts were evaluated in terms of ethanol conversion at reaction temperature of 400 ^{o}C, water-to- ethanol feed ratio 6:1, and atmospheric pressure. Ethanol conversion was measured each half an hour continuously till 3hr reaction

time. Figure 4.16 shows the information on ethanol conversion (as defined in Equation 3.38) behaviour for impregnation method catalysts.

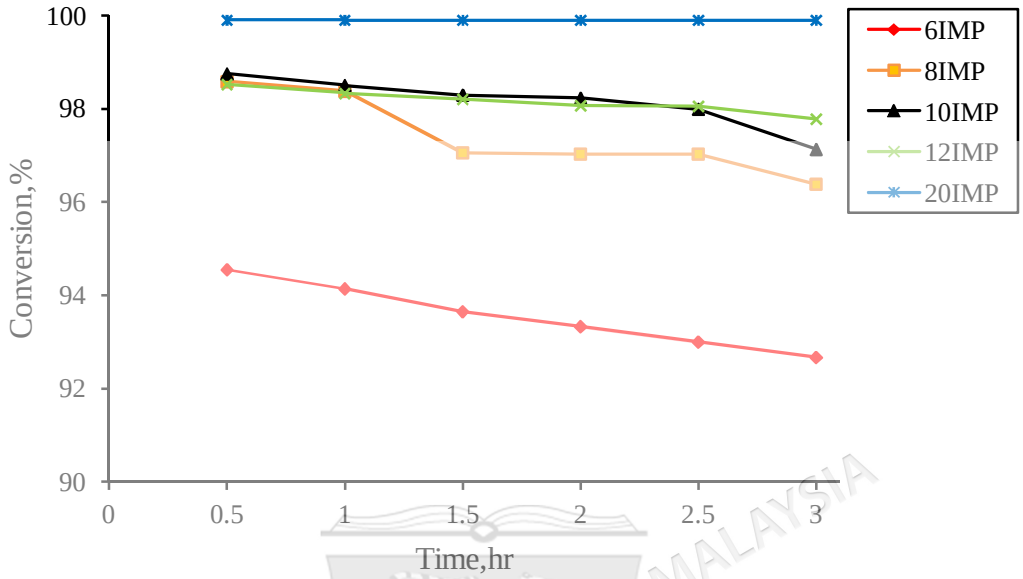

Figure 4.16 Conversion of ethanol as a function of time-on-stream (TOS) on catalyst prepared by impregnation method at a T = 400 °C, water-to-ethanol feed ratio of 6:1, and atmospheric pressure

In the first 30 minute of the reaction, it can be seen that except 6IMP (shows slightly lower activity in terms of ethanol conversion (94%)), all other catalysts exhibited a high conversion (98-100%) and this is because of the catalyst has initial high activity. 20IMP gave the complete and stable conversion for 3 hr. For other catalysts, slightly decrease in conversion with time was observed. For 6IMP conversion reaches its minimum of 92% in the end of the reaction. Fig.4.17 exhibited the result of ethanol conversions for precipitation method catalysts. Results showed similar trends to those observed by impregnation method catalysts. Here also all catalysts gave a high and stable conversion (98-100%) with lowest conversion over 6PT catalysts.

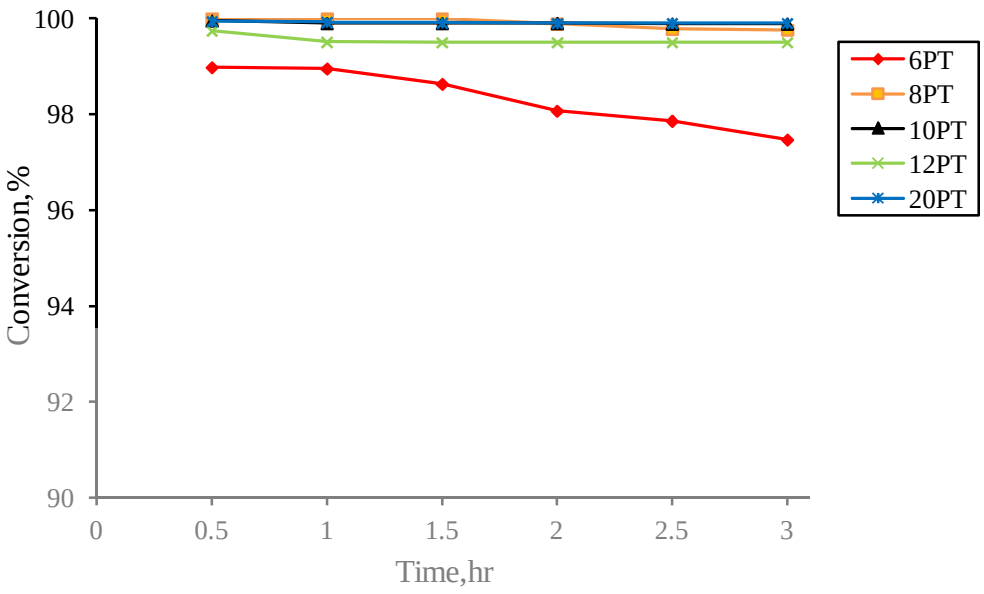

Figure 4.17 Conversion of ethanol as a function of time-on-stream (TOS) on catalyst prepared by precipitation method for 3 hr reaction at a T = 400 °C, water-to-ethanol feed ratio of 6:1, and atmospheric pressure

Ethanol conversions of the catalysts were compared after 3-hr runs to evaluate the effect of Ni loading on catalyst activity (Figure 4.18).

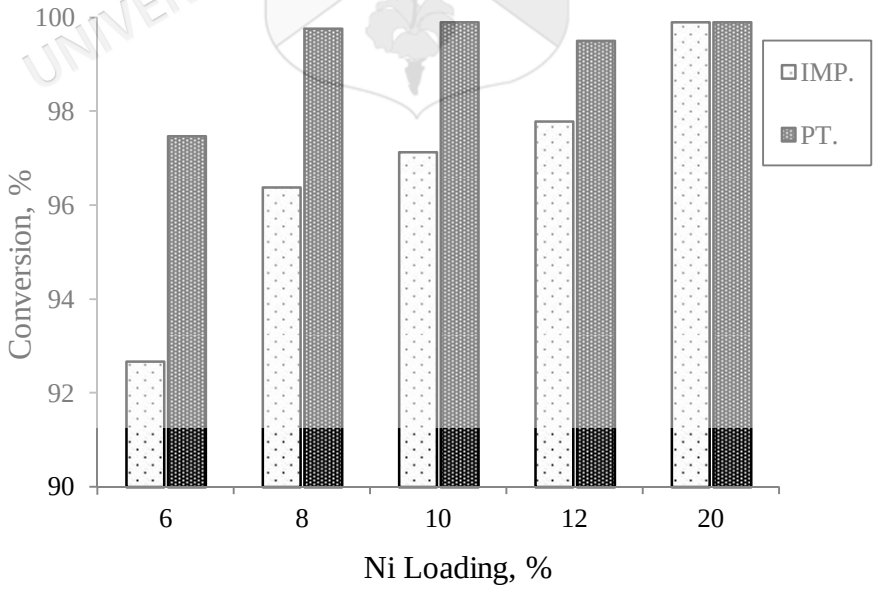

Figure 4.18 Comparison of ethanol conversion for impregnation and precipitation catalysts after 3 hr reaction at a T = 400 °C, water-to-ethanol feed ratio of 6:1, and atmospheric pressure

For the IMP-synthesized catalysts, conversion increased with Ni loading and reached complete conversion with a Ni loading of 20 wt%. For the PT-synthesized catalysts, the ethanol conversion did not change significantly with Ni loading (the values varied from 97.5% to a complete conversion). Ni loading had a trivial effect on ethanol conversion after 3 hr, at which time all catalysts prepared by either method yielded ethanol conversions between 92 and 100%.

The product selectivities of all of the catalysts after 3 hr, as defined in previous chapter (Equation 3.37), are presented in Tables 4.4 and 4.5 for IMP and PT synthesized catalysts, respectively. Data for H_2, CO_2, CH_4, and CO were obtained. Acetaldehyde and C_2 compounds were not detected.

Table 4.4 Product selectivity of IMP- synthesized catalysts after 3 hr reaction

Catalyst	Selectivity, (%)				CO/CO_2	H_2/CO
	H_2	CO	CO_2	CH_4		
6IMP	60.45	12.50	18.78	8.27	0.67	4.83
8IMP	62.22	11.5	17.42	8.86	0.66	5.41
10IMP	63.64	9.14	16.28	10.94	0.56	6.96
12IMP	56.01	12.71	19.48	11.80	0.65	4.40
20IMP	57.06	7.13	22.93	12.88	0.31	8.00

Table 4.5 Product selectivity of PT- synthesized catalysts after 3 hr reaction

Catalyst	Selectivity, (%)				CO/CO_2	H_2/CO
	H_2	CO	CO_2	CH_4		
6PT	64.13	4.00	24.14	7.73	0.16	16.03
8PT	62.03	3.82	23.49	10.66	0.16	16.23
10PT	61.67	3.96	25.47	8.90	0.15	15.57
12PT	60.32	8.47	19.87	11.34	0.42	7.12
20PT	56.89	7.30	23.79	12.02	0.30	7.79

For the IMP-synthesized catalysts (Table 4.4) H_2 selectivity slightly increased as Ni loading increased for the first three catalysts (6IMP, 8IMP, and 10IMP). The H_2 selectivity of 12IMP decreased to 56% as Ni loading increased, but this selectivity did not decrease below this level as Ni composition was further changed. A different trend was observed for the PT-synthesized catalysts (Table 4.5). As observed with the PT-catalysts, H_2 selectivity slightly decreased as Ni loading increased; however, these catalysts exhibited relatively high H_2 to CO ratios and low CO to CO_2 ratios compared to IMP-synthesized catalysts. These characteristics can be attributed to the catalytic acceleration of the water gas shift reaction. It was also observed that the H_2/CO ratio of PT-synthesized catalysts decreased with increasing Ni loading, while the CO/CO_2 ratio increased with increasing Ni loading. By comparing results in Table 4.5 with other published result (Srisiriwat et al. 2009b), it can observed that H_2/CO values obtained in this work is much larger than values in literature.

Ni content varies the dispersion behaviorof nickel particles on Al_2O_3 support, which will further affect the distribution of the product in steam reforming reactions. In both methods, it is interested to observe that, the presence of high Ni loading (12 and 20wt%) not only promote methane production but also increase the amount of carbon monoxide, especially in a case of PT-synthesized catalysts. It is expected that high content of nickel will not improve the catalytic performance because of their low surface area and large crystallites which will lead to poor dispersion of Ni species on the support and consequently will not improve the selectivity toward the desired product. This is in agreement with other published result, in which the authors observed that at law nickel content the dispersion was higher than that with higher nickel content and decreased gradually with content (Tsay & Chang 2000). Thus, catalysts with low Ni loading seemed to be more effective and feasible for hydrogen production from ethanol steam reforming with relatively low carbon monoxide emission.

4.3.2 Ethanol Conversion and Product Selectivity over an 8-hr Reaction

Figures 4.19 and 4.20 outline the ethanol conversions and product selectivities of catalysts prepared by PT and IMP methods, respectively with different Ni loading

over 8 hr. For both types of catalyst, no products other than H_2, CH_4, CO, and CO_2 were detected.

In terms of ethanol conversion and H_2 selectivity, PT-synthesized catalysts (Figure 4.19) were slightly more stable than IMP-synthesized catalysts (Figure 4.20). Changes in ethanol conversion with metal loading for PT-synthesized catalysts were insignificant, as all PT-catalysts exhibited almost complete conversion throughout the reaction. With IMP-synthesized catalysts, conversion increased with Ni loading and slightly decreased with time. For instance, in the case of the 6IMP, catalyst ethanol conversion decreased from 94% at the beginning of the reaction to approximately 89% after 8hr. Similar trends were observed in all IMP catalysts. The H_2 selectivity in all catalysts ranged from 55 to 65%. The H_2 selectivity of PT-synthesized catalysts was always above 60%, except for the 20PT catalyst, which showed a selectivity of approximately 56%. This reduction in H_2 selectivity with high nickel loading most likely results from the fact that high Ni loading leads to particle agglomeration, which is absent in the low Ni loading materials. This finding is in agreement with results reported by Tsay and Chang (2000) that show higher dispersion in catalysts of low Ni loading than those with high Ni loading and an overall decrease in dispersion with increasing Ni content. The small surface area and large Ni particles in catalysts of high Ni content may result in the blockage of carrier pores limiting the availability of active sites on the catalyst, thereby hindering selectivity and performance in steam reforming reactions (Li et al. 2012).

Although the CO selectivity remained unchanged throughout the reaction period for both methods, the amount of CO in the PT-synthesized catalysts was lower than the CO values in the IMP-synthesized catalysts, indicating that preparation method has a greater effect on CO selectivity than Ni loading. In contrast, the CO_2 values were higher in the PT-synthesized catalysts. These characteristics suggest that the water gas shift reaction might be responsible for the formation of CO_2 and the decrease in CO. Thus, the PT-synthesized catalysts are more attractive for use in the production of hydrogen by ethanol steam reforming. These results were similar to other published results, where PT and IMP preparation methods used for CO_2 methanation (Erhan Aksoylu & İlsenÖnsan 1997).

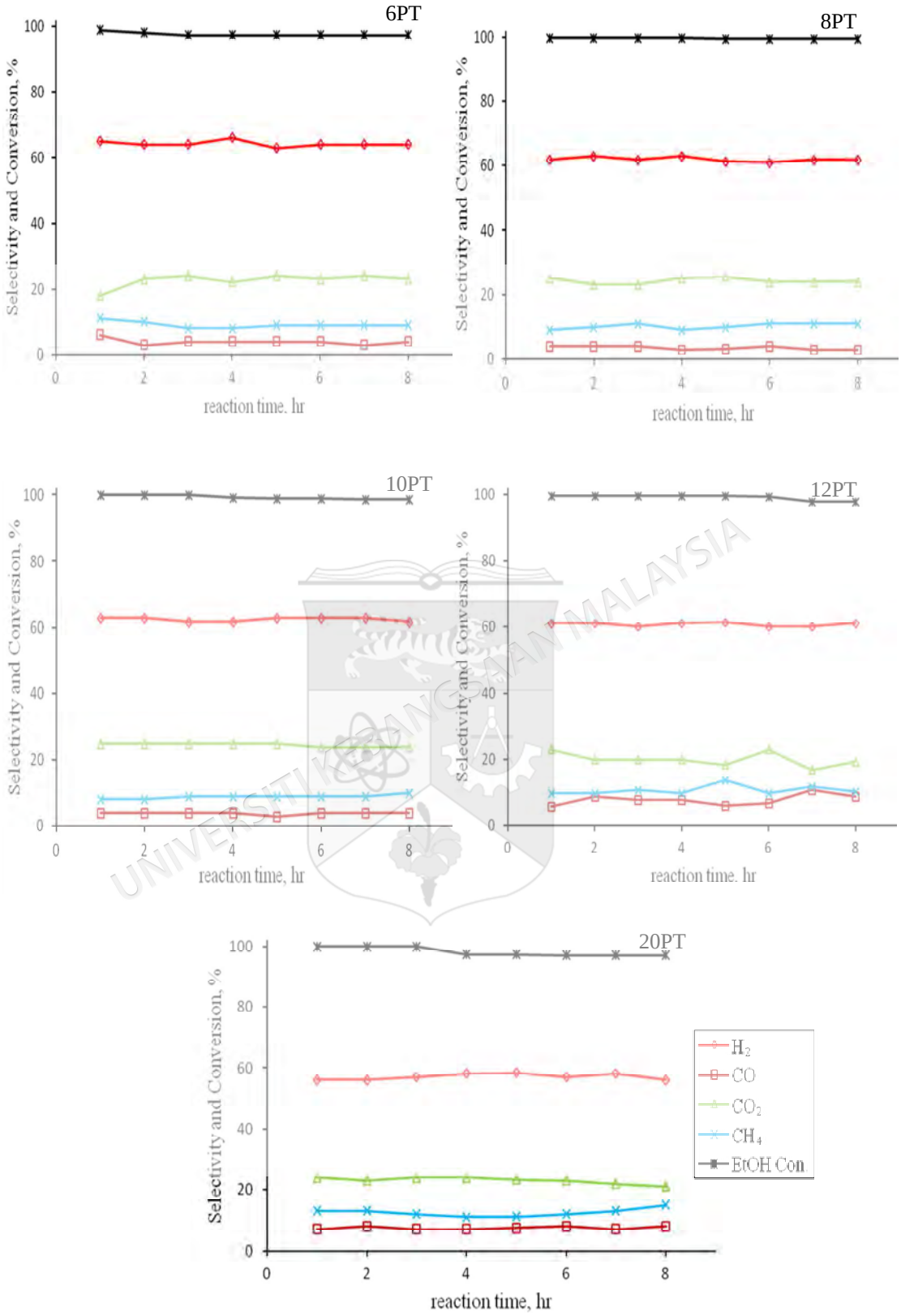

Figure 4.19 Ethanol conversion and product selectivity during 8-hr steam reforming of ethanol over precipitation catalysts

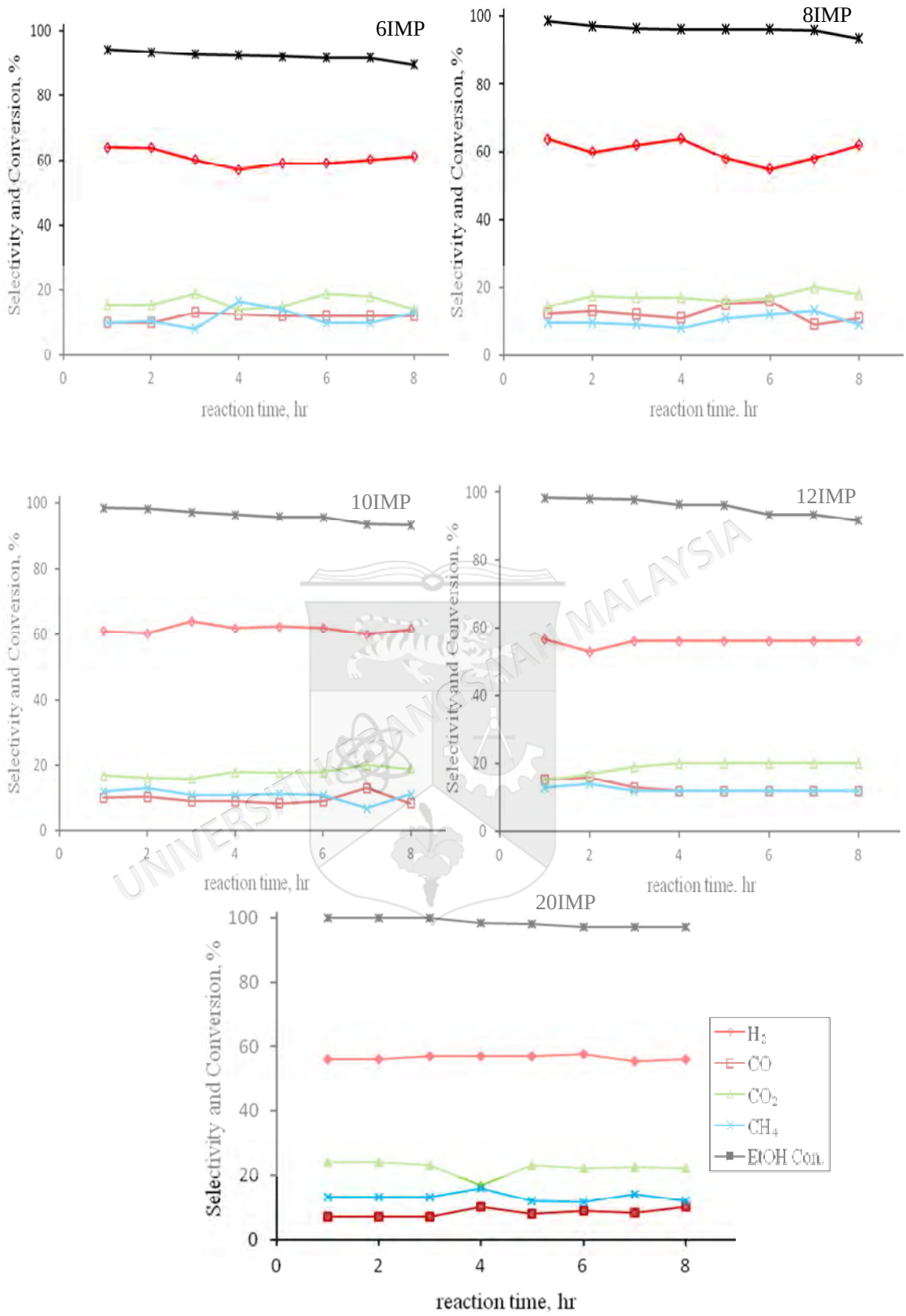

Figure 4.20 Ethanol conversion and product selectivity during 8-hr steam reforming of ethanol over impregnation catalysts

4.3.3 Ethanol Conversion into Gases After 8 hr Reaction

Ethanol conversion and ethanol conversion into gases products are shown in Table 4.6. Ethanol conversion into gases product was calculated based on Equation defined in previous chapter (3.39). Although the total ethanol conversion was high with all catalysts, conversion of ethanol into gases products did not exceed 90% except for 6PT. This could be due to the conversion of ethanol into other organic components.

Table 4.6 Ethanol conversion and conversion into gaseous after 8hr reaction

	Precipitation Catalysts					Impregnation Catalysts				
Catalyst	6PT	8PT	10PT	12PT	20PT	6IMP	8IMP	10IMP	12IMP	20IMP
$E\text{tOH}\ Con.$	97	99	99	98	97	89	93	93	92	91
$E\text{tOH}\ Con.$ into gases	94	79	62	75	62	78	66	61	74	87

4.3.4 Product Yield

The product yields (calculated based on Equation 3.38) of all of the catalysts were also evaluated. Figures 4.21 and 4.22 illustrate the variation in product yield as a function of Ni loading for the catalysts prepared by PT and IMP methods, respectively. For the PT-synthesized catalysts, the CO yield over catalysts with low Ni contents (6, 8, and 10PT) was low compared to those with higher Ni contents (12, and 20 PT), as shown in Figure 4.21. In contrast, CO_2 yields gradually decreased as the Ni loadings increased, indicating that the water gas shift reaction was favored at low Ni loadings. Similarly, CH_4 yields decreased from a maximum value of 0.51 mol per mol ethanol fed was observed for the catalyst of lowest loading to 0.34 mol per mol ethanol fed found with 10PT and all of the more heavily loaded catalysts. Generally, CO_2 yields were higher than CO yields for all PT-synthesized catalysts with the greatest difference observed with the 6PTcatalyst. The low CO yield and the high CO_2 yield indicate that steam reformation was accompanied by a water gas shift reaction. Moreover, the high methane yield indicates that these catalysts are notably active

toward methanation reactions. Similar trends was observed in other published result studied the effect of Ni laoding (10-25wt%) on catalyst acivity. The highest catalyst activity was observed over lowest Ni loading of 10wt% (Akande et al. 2005).

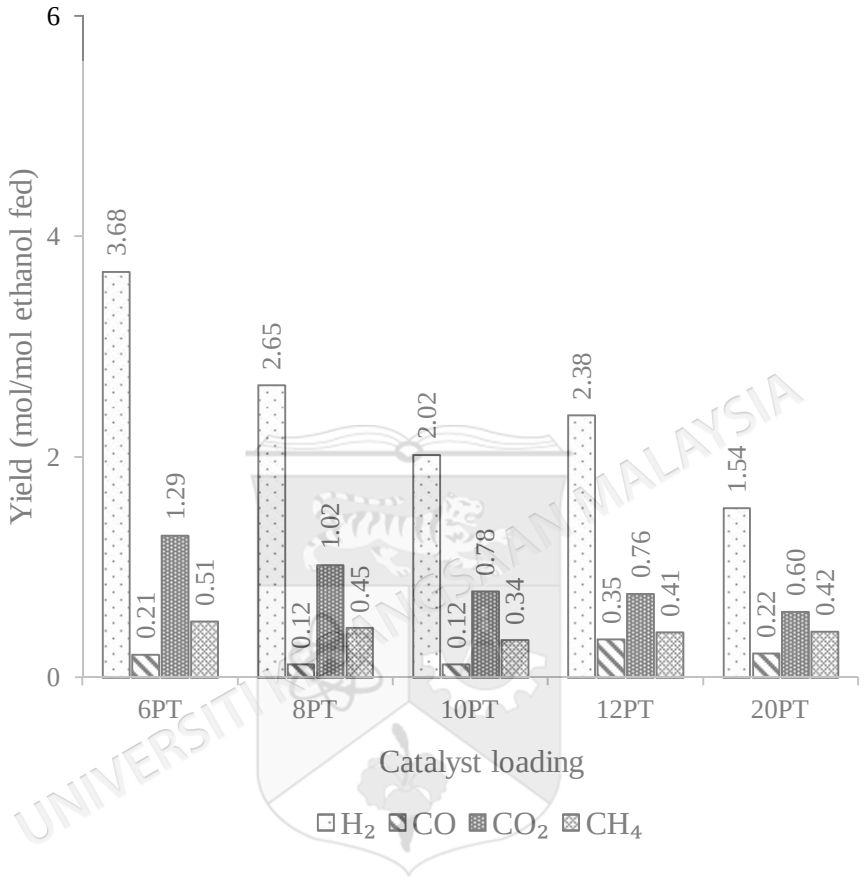

Figure 4.21 Effect of catalyst loading on the product yield for PT catalysts after 8 hr reaction

For IMP-synthesized catalysts (Figure 4.22), the CO_2 and CH_4 yields exhibited different trends than those found for the PT-synthesized catalysts. The yields of CO over IMP-synthesized catalysts were higher than CO yields over PT-synthesized catalysts. The PT-synthesized catalysts generally produced higher H_2 yields compared with the IMP-synthesized catalysts, except for 20PT, which showed lower yield than the 20IMP catalyst. The 6PT catalyst gave a yield that was not only higher than that of 6IMP but the highest among all catalysts. The high H_2 yield for the 6PT catalyst may be attributed to a combination of high surface area, small crystallite size and uniform dispersion of Ni particles on the support. This dispersion not only improves metal –

support interaction over the catalyst but also prevents metal agglomeration, resulting in excellent reformation of hydrocarbon intermediates. This was similar to other result observed that, at low nickel content, the small nickel crystallites exhibit no agglomeration, while at high nickel content, there was the existence of agglomeration due to the presence of significant nickel density (Tsay & Chang 2000).

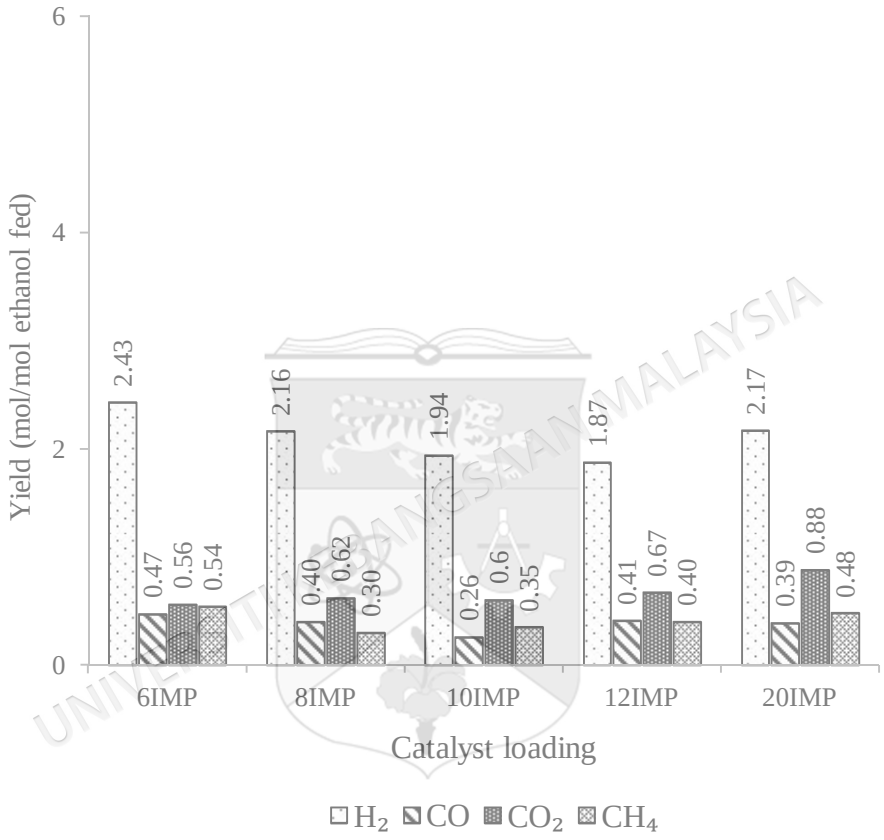

Figure 4.22 Effect of catalyst loading on the product yield for IMP catalysts after 8 hr reaction

The variation in H_2 yields with Ni loading for catalysts prepared by both methods were compared (Figure 4.23). Insignificant differences were found in H_2 yields for IMP-synthesized catalysts where H_2 yields ranged from 1.87 mol per mol ethanol fed to 2.43 mol per mol ethanol fed. These values indicate that Ni loading has almost no influence on product distribution. With PT-synthesized catalysts, the H_2 yield notably decreased as Ni content increased. Given that hydrogen production is the main scope of this study, 6PT was deemed the best catalyst, as it showed the highest

H_2 yield of 3.68 mol per mol ethanol fed and exhibited high, stable ethanol conversion. For these reasons, the 6PT catalyst was chosen for parameter optimization experiments.

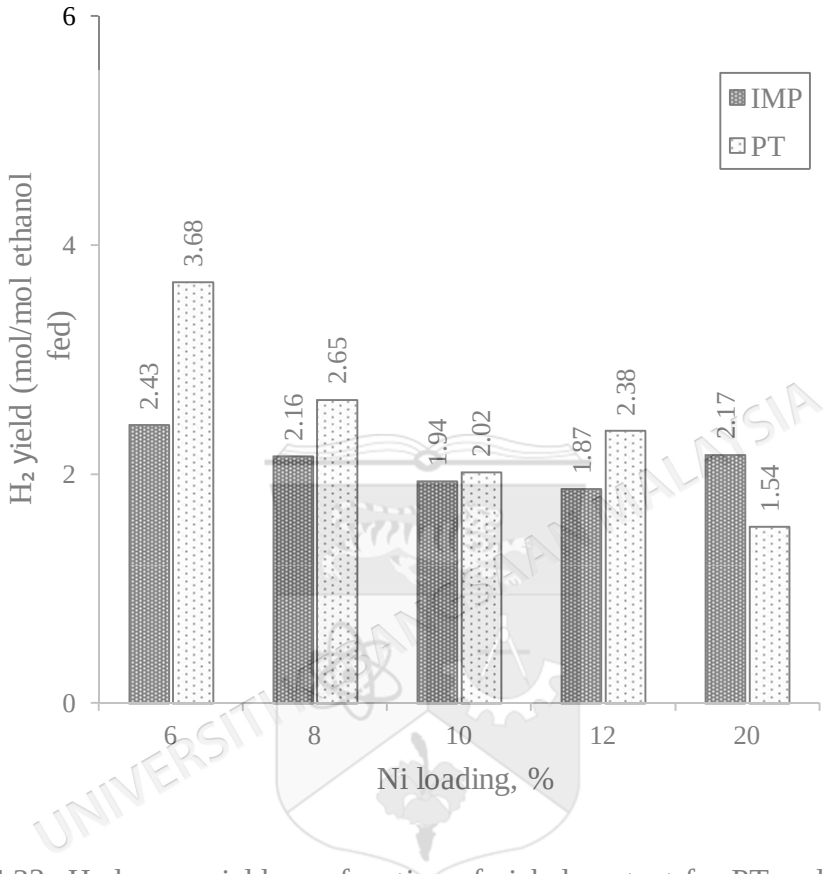

Figure 4.23 Hydrogen yield as a function of nickel content for PT and IMP methods at a T = 400 °C, water-to-ethanol feed ratio of 6:1, and atmospheric pressure

The XRD spectra of spent catalysts for PT and IMP catalysts are shown in Figures 4.24 (a) and (b), respectively. For catalysts with Ni loadings 6, 10, and12% in precipitation method, characteristic peaks of NiO and Al_2O_3 were observed. Peaks corresponding to Ni phase also start to appear at 10% loading. Moreover, the crystalline form of nickel appears on 20%loading. However, the disappearance of the peaks corresponding to nickel phase on 6PT catalyst could be due to interaction between the metal and the support in the reaction environment. In addition to these peaks, among all precipitation used catalysts, only small peak of carbon was observed on 20PT at 2θ values of 26^o. In contrast, peaks belong to carbon were observed in

catalysts prepared by impregnation method (10,12,and 20%) along with NiO, Al_2O_3, and Ni peaks as shown in Figure 4.24 (b). This could be a reason for the catalyst deactivation. Carbon deposits on the 12IMP catalyst could be very small or in an amorphous phase, and were thus not detectable as clear as other catalysts by XRD. It can be also noted that, no carbon peaks were detected on lowest nickel content catalysts (6IMP and 6PT). This may attributed to the high dispersion of the nickel particle which leads to high resistance of coke.

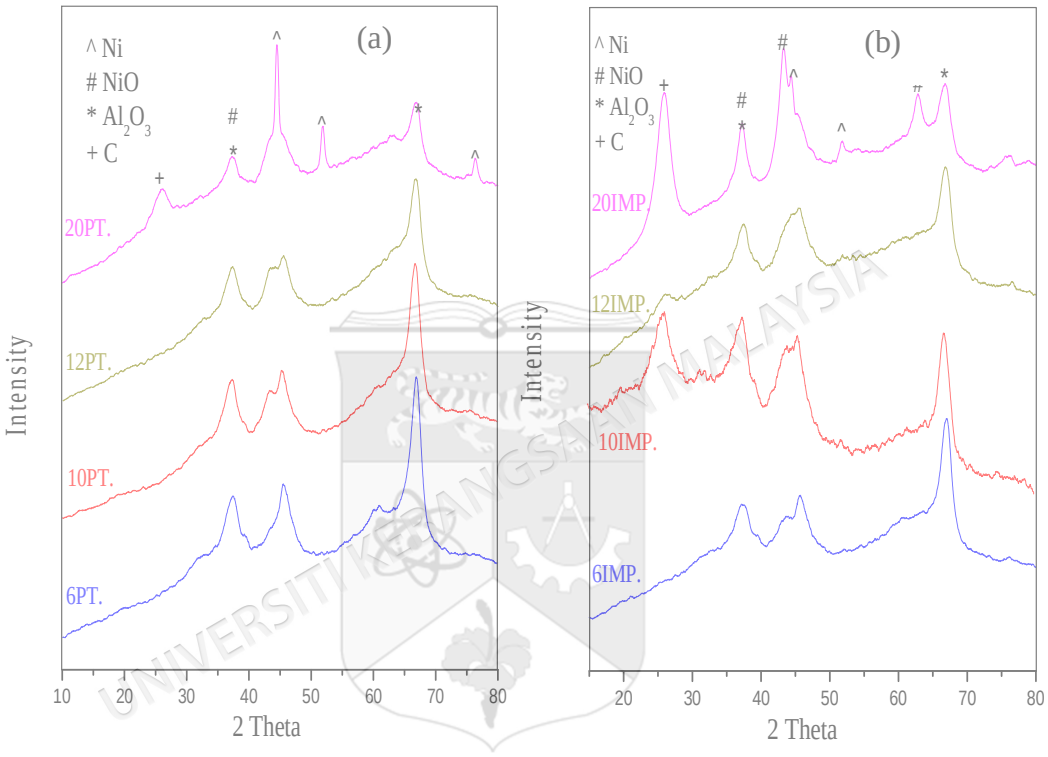

Figure 4.24 XRD spectra of spent catalysts for a) PT used catalysts b) IMP used catalysts

4.4 LOWER NICKEL LOADING EFFECT

In this section, lower nickel loading (2wt% and 4wt %) was tested in ethanol steam reforming in order to ensure the best nickel loading. Since 6PT was the best system, the comparison between 2wt%, 4wt%, and 6wt% prepared by precipitation method was investigated. The reaction conditions of temperature 400^{o}C, and water to ethanol molar ratio of 6 were used for steam reforming reaction. Based on previous studies of ethanol steam reforming where, the experimental data were collected after 8 hr or less

(Akande et al. 2005; Chang et al. 2006; Erdohelyi et al. 2006; Navarro et al. 2005; Sahoo et al. 2007; Srisiriwat et al. 2009a). Our product analysis was carried out after 8 hr reaction over all samples tested. The criteria used to evaluate the catalytic performance were ethanol conversion and hydrogen yield.

4.4.1 Ethanol Conversion and Hydrogen Yield for 2PT, 4PT and 6PT Catalysts

Figure 4.25 shows the ethanol conversion after 8hr reaction on 2PT, 4PT, and 6PT Catalysts. It is observed that, 6PT catalyst exhibited higher conversion than those over 2PT, 4PT catalysts. In terms of hydrogen yield, as shown in Figure 4.26, 2PT catalyst was the poorest catalyst among the three catalysts, where it showed the lowest H_2 yield of 1.26 mol/mol ethanol fed. As the metal loading increased up to 6PT, the ethanol conversion and hydrogen yield increase and that is due to the more number of active sites was available for the ethanol steam reforming reaction that resulted in higher conversion and hydrogen yield. In addition, 6PT exhibited highest CO_2 yield of 1.2 mol/mol ethanol fed, means that this catalyst favored water gas shift reaction more than the other two catalysts. For CO and CH_4 yields, 4PT catalyst exhibited a highest amount of both gases with values of 0.45 and 1.18 mol/mol ethanol fed, respectively.

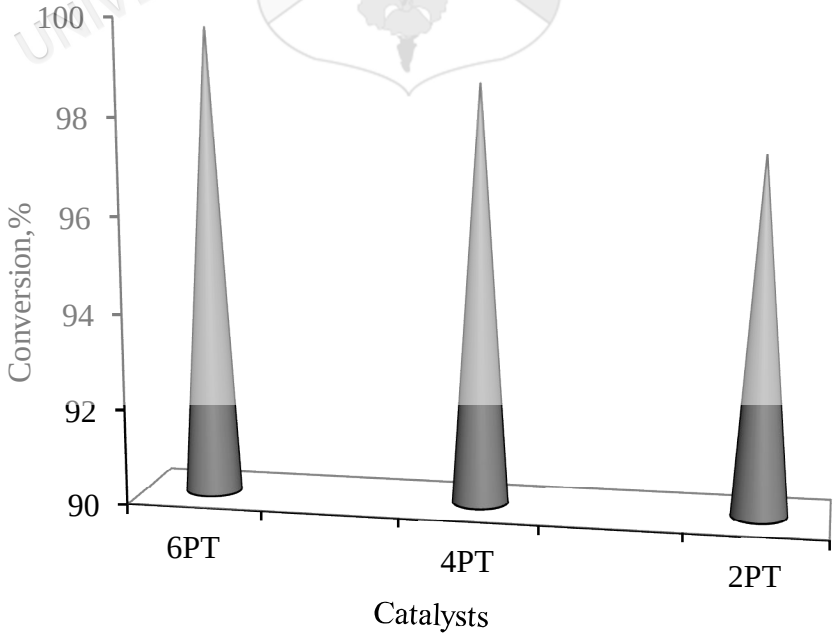

Figure 4.25 Effect of 6wt%, 4wt%, and 2wt% catalysts prepared by precipitation method on conversion of ethanol

Therefore, the catalyst with the nickel loading of 6wt% was selected to perform the reaction parameter optimization. Also this nickel loading was chosen to prepare sol gel catalysts.

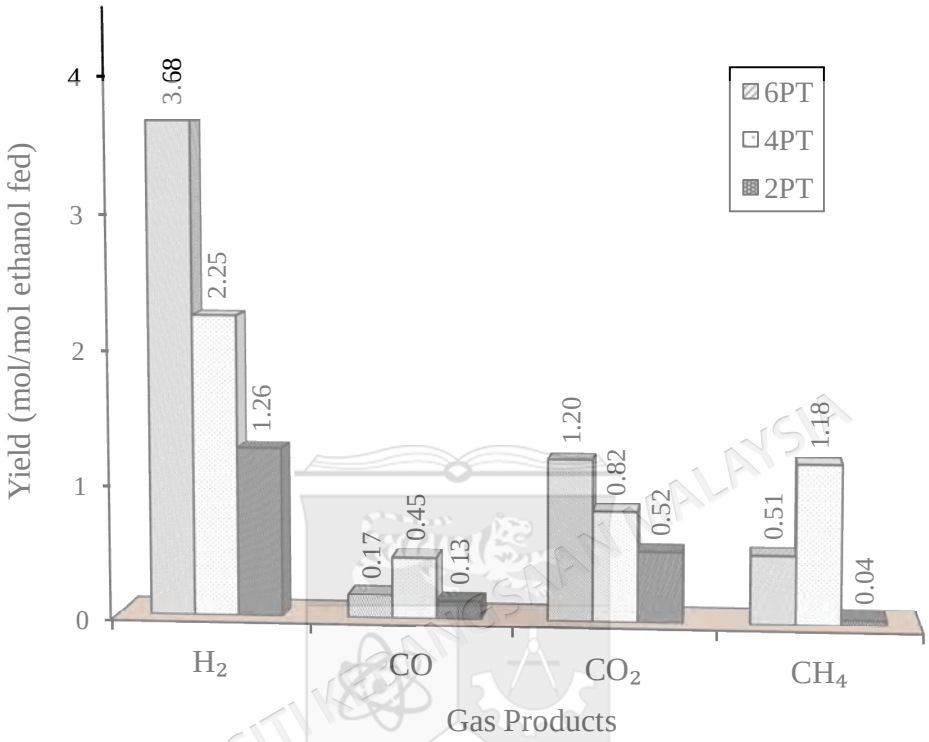

Figure 4.26 Effect of of 6wt%, 4wt%, and 2wt% catalysts on the product yield after 8 hr reaction

4.5 EFFECT OF REACTION VARIABLES

Reaction parameters were varied to study the effect of reaction variables on ethanol conversion and hydrogen selectivity. To achieve this goal, 6 wt% Ni-loaded alumina prepared via the PT method was employed.The reaction temperature, liquid hourly space velocity (LHSV), catalyst weight, and ethanol-to-water molar ratio were varied. The effects of these factors on conversion and selectivity were used to determine the best conditions for this present study.

4.5.1 Effect of Reaction Temperature

Reaction temperature was varied from 200 °C to 500 °C at an interval of 100 °C and the results are shown in Figure 4.27.

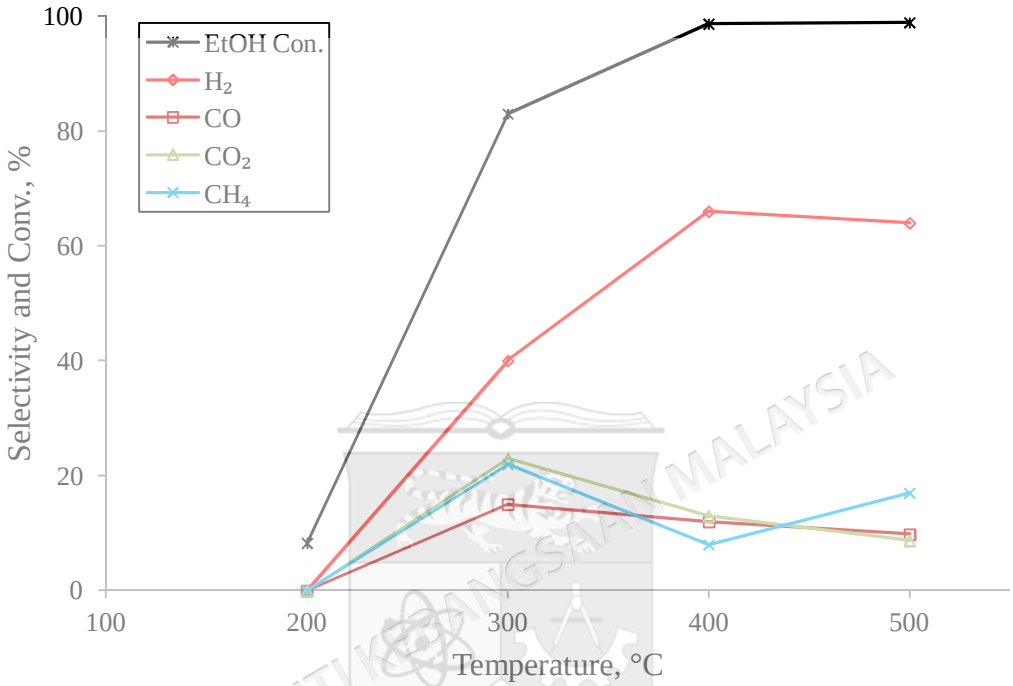

Figure 4.27 Effect of reaction temperature on Ethanol conversion and product selectivity

Low temperatures were found to be unsuitable for the reaction based on both ethanol conversion, as well as hydrogen selectivity. No notable gaseous product formation was observed at temperature of 200 °C, means that ethanol reforming reaction did not occur at this temperature and that is consistent with thermodynamic result. This is in a good agreement with other published study, where the conversion/selectivity/yield of H_2 vs. temperature curves show that ethanol conversion starts at above 300 °C (Resini et al. 2008). For temperatures of 300 °C and up, an appreciable amount of gaseous products was formed. Conversion increased drastically as the temperature was increased to 400 °C, and further increases in the temperature only served to enhance the ethanol conversion. Maximum conversion was observed at 500 °C, whereas hydrogen selectivity reached a maximum at 400 °C. Considering the

energy economy and hydrogen selectivity, a temperature of 400 ℃ was selected for further studies. The details of the full experiments of the ethanol conversion and product selectively versus the temperature are indicated in Table 4.7.

Table 4.7 Effect of temperature on Catalytic performance at different reaction time

Temperature, ^{o}C	Time, hr	Conversion, %	Selectivity, (%)			
			H_2	CO	CO_2	CH_4
200	1	9.75	-	-	-	-
200	2	9.04	-	-	-	-
200	3	8.27	-	-	-	-
300	1	84.11	42	14	25	19
300	2	83.01	38	16	24	22
300	3	83.00	40	15	23	22
400	1	98.98	64	13	14	9
400	2	98.95	64	12	14	10
400	3	98.63	66	12	14	8
500	1	99.67	63	10	12	15
500	2	99.36	62	10	12	16
500	3	98.91	64	10	09	17

4.5.2 Effect of Catalyst Weight

The catalyst dosage was varied from 0.25 to 2g, and the effect of such dosage on ethanol conversion and product selectivity was noted for 3hr reaction time as shown in Figure 4.28. In previous publications, the effect of catalyst weight on catalyst performance was measured through the change of residence time which is the amount of catalyst divided by the flow rate of the reactants (Aupretre et al. 2005; Fatsikostas et al. 2002b; Liguras et al. 2003). However, it is known that, increase the catalyst weight increase the residence time, so the change of residence time in this research was indirectly measured by changing

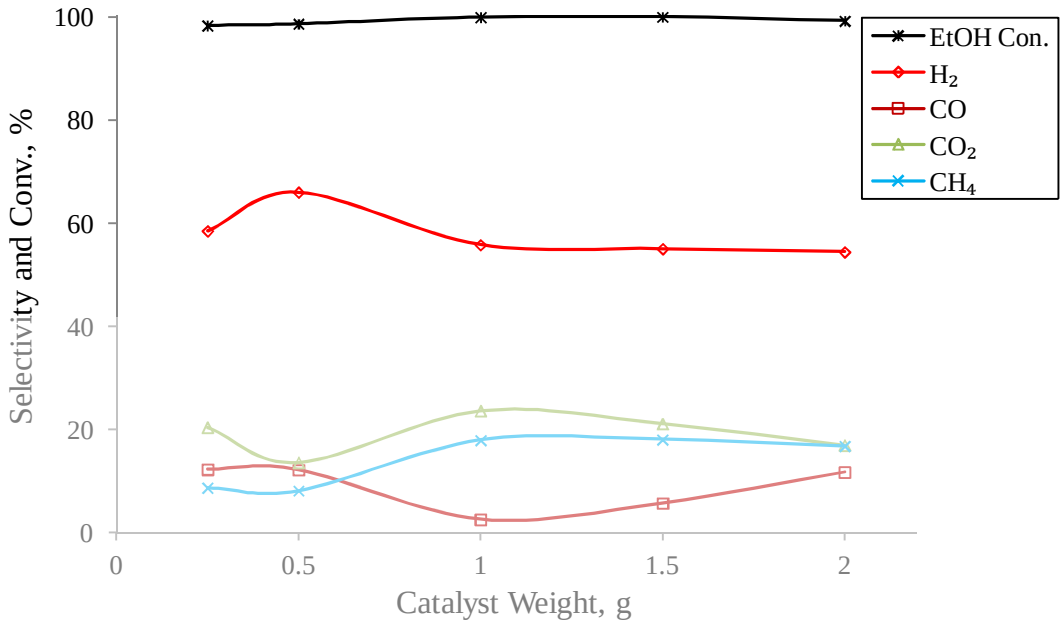

Figure 4.28 Effect of catalyst loading on ethanol conversion and product selectivity

Ethanol conversion was unaffected by the amount of catalysts, where all loadings gave almost complete ethanol conversion, whereas hydrogen selectivity was found to reach the maximum value at 66% of a catalyst dosage of 0.5 g under the selected conditions, suggesting that ethanol steam reforming reaction is the main reaction. As catalyst loading increases, hydrogen selectivity decrease to around 56% at 1g catalyst loading, accompanied by a decrease of the selectivity toward the formation of CO and by increase of the selectivity toward CO_2 and CH_4. At this catalyst loading of 1g, CO formation was found to be the least (3%) and CO_2 reached its highest value of 23%. This indicates that water gas shift reaction is the main reaction at this point. As the catalyst weight increase, hydrogen selectivity does not change significantly, while CO_2 and methane selectivity slightly decrease with increase in CO selectivity being observed. This increase in CO selectivity and a decrease in methane selectivity can be postulate that, CO is mainly produced from the steam reforming of methane and reverse water gas shift reactions. The details of the full experiment of the ethanol conversion and product selectively versus the catalyst loading are indicated in Table 4.8.

Table 4.8 Effect of catalyst weight on catalytic performance at different reaction time

Catalyst Weight, (g)	Time, hr	Conversion, %	Selectivity, (%)			
			H_2	CO	CO_2	CH_4
0.25	1	98.6	62	12	18	8
0.25	2	98.6	59	12	22	7
0.25	3	98.3	59	12	20	9
0.5	1	98.98	64	13	14	9
0.5	2	98.95	64	12	14	10
0.5	3	98.63	66	12	14	8
1	1	99.98	52	3	24	21
1	2	99.95	53	3	24	20
1	3	99.93	56	3	23	18
1.5	1	100	56	3	23	18
1.5	2	100	56	4	22	18
1.5	3	99.98	55	6	21	18
2	1	99.32	53	14	15	18
2	2	99.30	53	13	17	17
2	3	99.23	54	12	17	17

4.5.3 Effect of Liquid Hourly Space Velocity (LHSV)

The effect of Liquid Hourly Space Velocity (LHSV) on the catalytic performance was investigated, as illustrated in Figure 4.29. It is known that, increase the reactants flow rate increase the liquid hourly space velocity, so the change of LHSV was measured by changing the flow rate of the reactants.

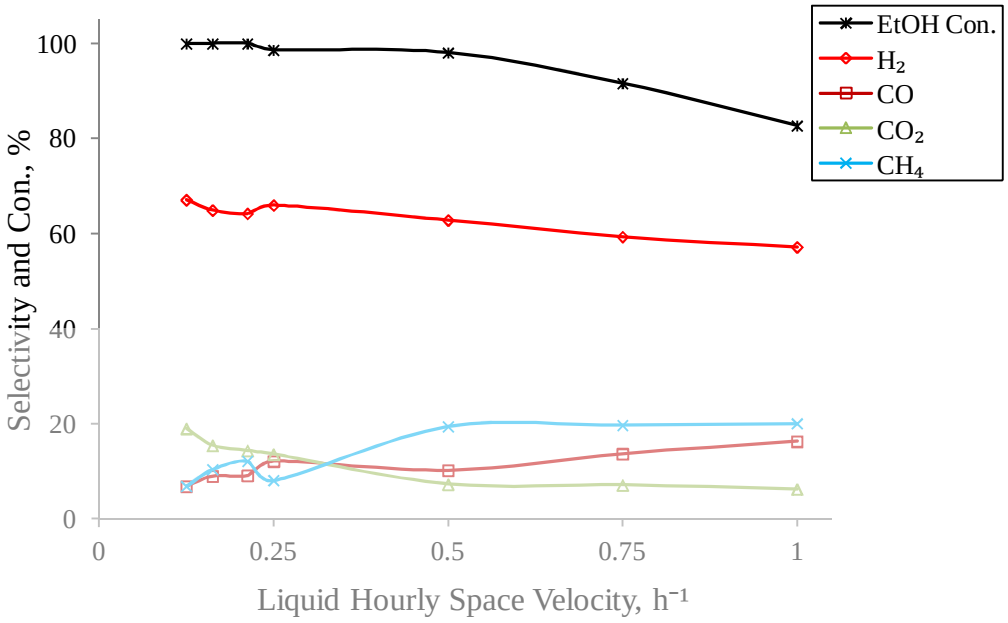

Figure 4.29 Effect of LHSV on ethanol conversion and product selectivity

The conversion was unaffected at LHSV values lower than 0.5 h^{-1}, where the conversion was almost complete. As LHSV values increased, the conversion decreased until reaching a minimum of 82% at 1 h^{-1}. A slight decrease in hydrogen selectivity also occurred with the increase in LHSV. In addition, an increase in LHSV increased the percentage selectivity of CO and decreased the selectivity of CO_2. The participation of water gas shift reaction was diminished with higher LHSV values. Because the concentration of methane increased with increasing LHSV values, the increase of CH_4 formation and decrease in H_2 selectivity are more likely due to the methanation reaction. This result was similar to other results was published (Yang et al. 2006; Zhang et al. 2009). Even though these mentioned studies used a higher liquid hourly space velocity range (5-25h^{-1}) than what we used in this research (0.125-1 h^{-1}), similar trend was observed. Table 4.9 shows the effect of LHSV on conversion and selectivity after each hour of the reaction.

Table 4.9 Effect of LHSV on catalytic performance at different reaction time

LHSV, h^{-1}	Time, hr	Conversion, %	Selectivity, (%)			
			H_2	CO	CO_2	CH_4
0.125	1	100	0.69	0.07	0.17	0.07
0.125	2	100	0.66	0.08	0.18	0.08
0.125	3	99.98	0.67	0.07	0.19	0.07
0.1625	1	100	0.64	0.09	0.15	0.12
0.1625	2	99.98	0.65	0.10	0.16	0.09
0.1625	3	99.98	0.65	0.09	0.15	0.11
0.2125	1	99.97	0.64	0.09	0.15	0.12
0.2125	2	99.97	0.64	0.09	0.15	0.12
0.2125	3	99.96	0.64	0.10	0.14	0.12
0.25	1	98.98	0.64	0.13	0.14	0.09
0.25	2	98.95	0.64	0.12	0.14	0.1
0.25	3	98.63	0.66	0.12	0.14	0.08
0.5	1	98.32	0.62	0.11	0.08	0.19
0.5	2	98.15	0.63	0.11	0.08	0.19
0.5	3	98.03	0.63	0.10	0.07	0.20
0.75	1	92.42	0.60	0.13	0.07	0.20
0.75	2	91.90	0.60	0.13	0.07	0.20
0.75	3	91.60	0.60	0.13	0.07	0.20
1	1	83.81	0.58	0.15	0.08	0.19
1	2	82.71	0.57	0.15	0.08	0.20
1	3	82.70	0.57	0.16	0.07	0.20

4.5.4 Effect of Water-to-Ethanol Molar Ratio

As Comas et al. (2004) reported in their previous work, the factor of water to ethanol molar ration has an influence on the product selcetivites of ethanol steam reforming. This parameter was further evaluated under broad water to ethanol molar ration ranged from 1:1 to 24:1 in certain interval as shown in Figure 4.30. Regardless of the volume of water introduced, no intermediate products (such as acetaldehyde and ethylene) were detected. Conversion was about 90% at a molar ratio of 1:1, whereas

the selectivity of H_2 was lower (53%) at lower molar ratios. Conversion was insignificantly affected at molar ratios of 6:1 and higher. Conversion reached its maximum at a molar ratio of 24:1. By increasing the water-to-ethanol molar ratio from 1:1 to 3:1, hydrogen selectivity slightly increased (from 53% to 56%). A further increase in the water-to-ethanol molar ratio improves the hydrogen selectivity, which reached 64% at a ratio 6:1. The increase in H_2 selectivity with increase water-to-ethanol molar ratio was ascribed to the large excess of water present which favours water gas shift (RWGS) (Freni et al. 2002). Hydrogen selectivity was insignificantly affected from a molar ratio of 6:1 onward.

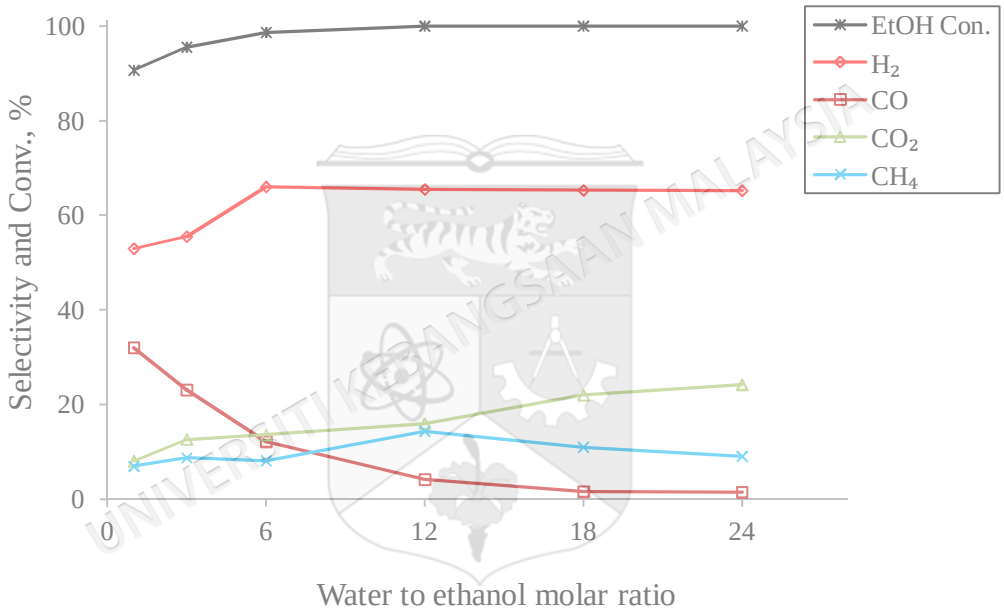

Figure 4.30 Effect of water-to-ethanol molar ratio on ethanol conversion and product selectivity

The percentage of CO was found to be considerable at lower molar ratios, reaching a maximum value of 32% at the lowest water-to-ethanol molar ratio and less than 10% at a molar ratio of 6:1. At a water-to-ethanol molar ratio of 24:1, the CO composition reaches its minimum at 1.5%. In contrast, the concentration of CO_2 in the outlet gas stream increased with the increase of the water-to-ethanol molar ratio. The concentration of methane increased with decreasing water content, reaching a maximum value of 15% at a water-to-ethanol ratio of 6:1 followed by a slight decrease as the ratio further decreased. Table 4.10 shows the full detailed experiments

at different reaction time. Only slightly difference in terms of conversion and selectivity was observed at different reaction time.

Based on these results, the following reaction conditions were selected for further studies: the water/ethanol molar ratio of 6, catalyst weight of 0.5g, and temperature of 400^{o}C. In addition, Ni content of 6% will be used for further studies.

Table 4.10 Effect of water to ethanol molar ratio on catalytic performance at different reaction time

Molar ratio	Time, hr	Conversion, %	Selectivity, (%)			
			H_2	CO	CO_2	CH_4
1:1	1	91.23	o.49	0.34	0.12	0.06
1:1	2	90.70	0.49	0.30	0.09	0.11
1:1	3	90.68	0.53	0.32	0.08	0.07
3:1	1	95.13	0.56	0.23	0.13	0.09
3:1	2	95.55	0.54	0.27	0.13	0.07
3:1	3	95.54	0.56	0.23	0.13	0.09
6:1	1	99.67	0.63	0.10	0.12	0.15
6:1	2	99.36	0.62	0.10	0.12	0.16
6:1	3	98.91	0.64	0.10	0.09	0.17
12:1	1	99.98	0.63	0.03	0.19	0.15
12:1	2	99.98	0.63	0.04	0.22	0.11
12:1	3	99.97	0.65	0.04	0.17	0.14
18:1	1	99.99	0.65	0.02	0.21	0.12
18:1	2	99.98	0.63	0.02	0.23	0.12
18:1	3	99.97	0.65	0.02	0.22	0.11
24:1	1	100	0.65	0.02	0.23	0.10
24:1	2	100	0.64	0.02	0.24	0.10
24:1	3	99.98	0.65	0.015	0.24	0.09

4.6 SOL GEL CATALYST SYSTEMS

Selected conditions were used for preparation of a catalyst system using sol gel made alumina. So far, nickel supported on sol gel made γ-alumina has not been applied in catalyst preparation for hydrogen production from ethanol steam reforming. Thus, this section focus on catalyst systems using sol gel made alumina as support instead of commercial alumina. The influence of calcinations temperature on the physical and chemical properties of the supports and catalysts are studied. The effects of calcinations temperature of the sol gel made alumina on catalytic performance are also investigated.

In order to evaluate the effect of calcinations temperature, alumina support was prepared by sol gel method and calcined at various temperatures. Then Ni /sol gel made alumina catalysts were then prepared by the impregnate a known amount of nickel precursor on the support. The effect of calcinations temperature of sol gel made alumina support on catalytic performance of Ni/$Al_{S.G.}$ catalysts was investigated in the following section.

4.6.1 Effect of Calcination Temperature on Supports Physical Properties

The physical properties of sol gel made alumina support ($Al_{S.G.}$) calcined at different temperatures ranging from 600 °C to 1000 °C were tested by N_2 adsorption–desorption isotherm determination (Figure 4.31).

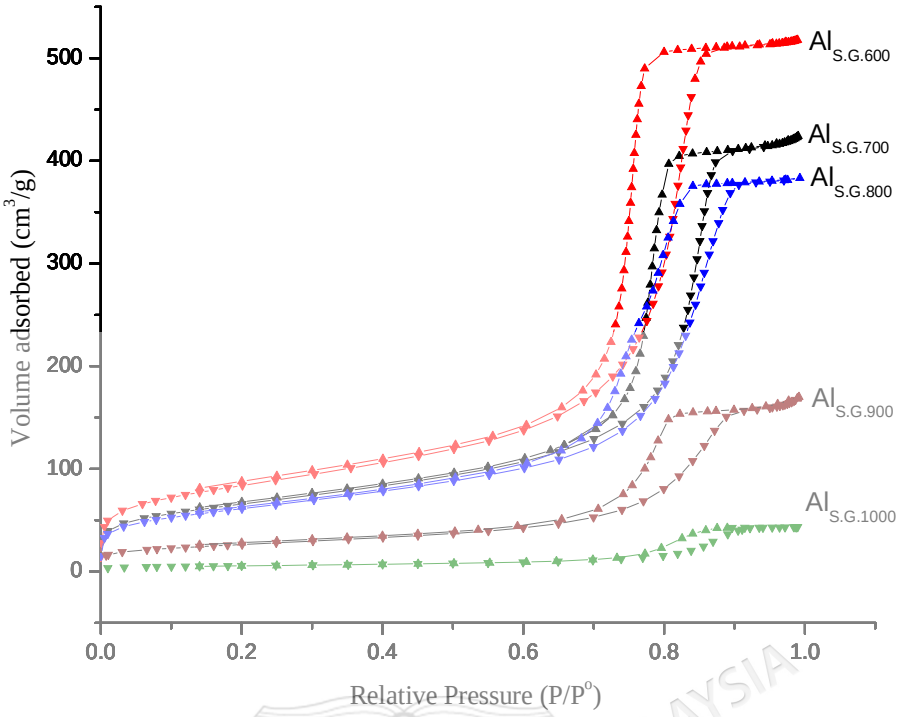

Figure 4.31 Nitrogen adsorption–desorption isotherms for sol gel alumina supports at different calcinations temperature

The samples exhibited type-IV (based on the International Union of Pure and Applied Chemistry (IUPAC)) curves, indicating the presence of a mesoporous material. Interestingly, the calcination temperature of the supports showed an influence on hysteresis loops. That is, the hysteresis loops shifted to lower relative pressure with decreasing calcination temperature. This result indicates that the pore size of $Al_{S.G.}$ increased with increasing calcination temperature. This is in agreement with other published result (Seo et al. 2009). This finding may be attributed to the development of pore texture with a relatively broad pore size distribution. Table 4.11 summarizes the physical properties of the $Al_{S.G.}$ supports.

Table 4.11 Physical properties of sol gel made alumina supports at different calcination temperatures

Catalyst name	BET, (m^2g^{-1})	Pore volume, (cm^3g^{-1})	Pore diameter, (nm)
$Al_{S.G.600}$	292	0.81	7.91
$Al_{S.G.700}$	230	0.67	8.46
$Al_{S.G.800}$	214	0.60	9.06
$Al_{S.G.900}$	92	0.27	9.10
$Al_{S.G.1000}$	19	0.07	10.18

The surface area of all prepared alumina supports decreased from 292 m^2 g^{-1} at 600 °C to 19 m^2 g^{-1} at 1000 °C. Similarly, pore volume decreased as the calcination temperature of the supports increased. Noticeably, the pore volume and surface area of the supports considerably declined at 1000 °C. By contrast, the pore diameter of $Al_{S.G.}$ increased with increasing calcination temperature. This result suggests that the physical properties of the $Al_{S.G.}$ supports were significantly influenced by calcination temperature which is agree with the data of previous studies (Burtin et al. 1987a; Chary et al. 2008).

4.6.2 Effect of Calcination Temperature on the Structure of the Supports and Supported Ni Catalysts

The effect of calcination temperature on the phase transformation and phases of the $Al_{S.G.}$ supports was tested by XRD measurements as illustrated in Figure 4.32 (a). The supports calcined at temperatures ranging from 600 °C to 800 °C showed similar diffraction peaks belonging to γ-alumina. However, the alumina supports calcined at 900 °C exhibited two mixed phases of alumina (γ and θ) because the alumina support transformed from γ- to θ-alumina at this calcination temperature. As expected, the support calcined at 1000 °C showed characteristic peaks corresponding to θ-alumina (Seo et al. 2008). However, the α-alumina phase was not detected at this temperature. The transformation of alumina phases occurs because of dehydroxylation and sintering reactions (Burtin et al. 1987a, 1987b), wherein the rate of these reactions varies by changing the calcination temperature of the support. Generally, the phase of γ-alumina can be detected at temperatures lower than or equal to 800 °C, whereas that

of θ-alumina appears at temperatures above 800 °C and becomes more intense at 1000 °C.

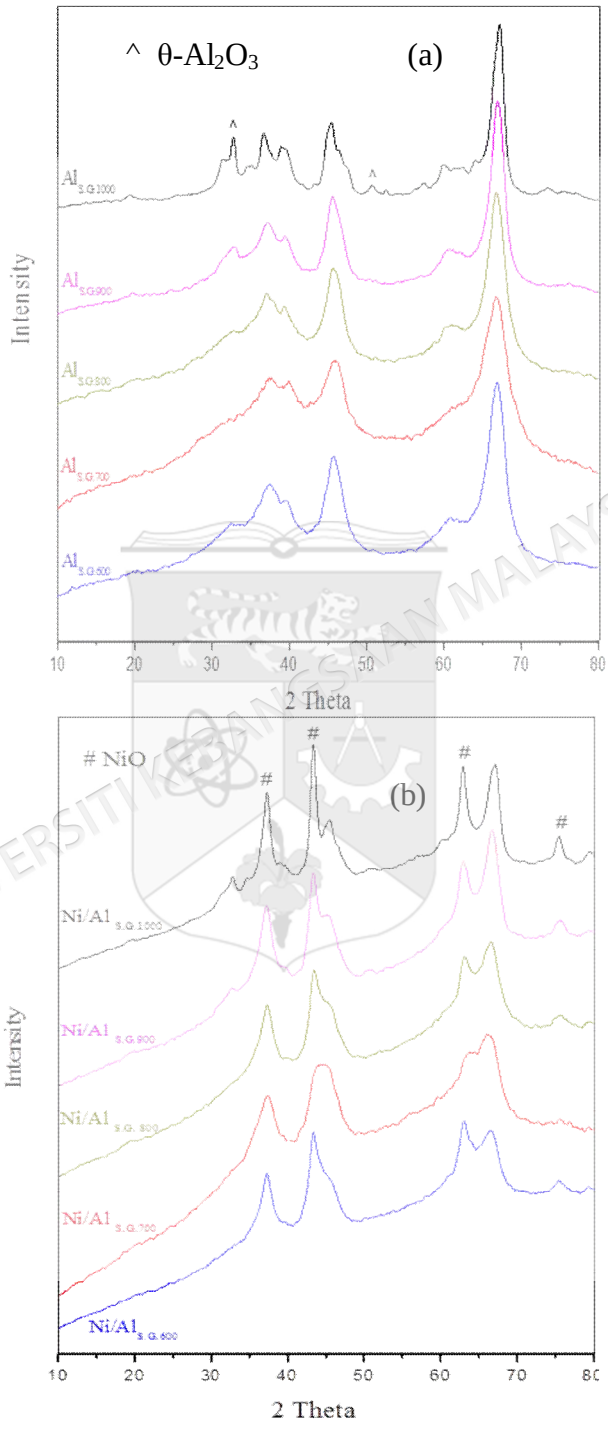

Figure 4.32 XRD patterns of a) Sol gel made alumina supports, b) Nickel catalysts supported on sol gel made alumina supports

The XRD diffraction peaks of the $Ni/Al_{S.G.}$ catalysts are shown in Figure 4.32 (b). All $Ni/Al_{S.G.}$ catalysts exhibited peaks belonging to nickel oxide (NiO). The diffraction peaks of NiO shifted to a higher angle as the calcination temperature of the support increased, as evidently observed in the $Ni/Al_{S.G1000}$ catalyst. The strong and narrow NiO peaks exhibited over the $Ni/Al_{S.G1000}$ catalyst can be ascribed to the weak interaction between Ni species and the $Al_{S.G.}$ supports. By contrast, the high surface area of the supports over the catalysts ($Ni/Al_{S.G600}$, $Ni/Al_{S.G700}$, and $Ni/Al_{S.G800}$) enhanced the incorporation of alumina cation into the NiO lattice.

4.6.3 Metal – Support Interaction

The TPR profiles of the $Ni/Al_{S.G.}$ catalysts are shown in Figure 4.33 to study the metal–support interaction. Two zones of reduction peaks are presented. The first zone was in the range of 200 °C to 370 °C, which was observed in the $Ni/Al_{S.G600}$, $Ni/Al_{S.G700,}$ and $Ni/Al_{S.G1000}$ samples. These reduction peaks correspond to the reduction of the NiO species which has minimal or no interaction with the Al_2O_3 supports, referring to it as "surface NiO" (Rynkowski et al. 1993; Zieliński 1982). These authors conclude that, the low-temperature reduction peaks were due to the reduction of NiO not interacted with the Al_2O_3 support, referring to it as "free" nickel oxide. The other zone of reduction peaks was observed in all samples and located in the range of 450 °C to about 800 °C, which may be attributed to the strong interaction of NiO and alumina support.

Notably, as the calcination temperature of the support increased ($Ni/Al_{S.G600}$, $Ni/Al_{S.G700}$, and $Ni/Al_{S.G800}$), the reduction bands shifted to higher temperature values until they reached a maximum value of 644 °C over the $Ni/Al_{S.G800}$ catalyst. As a result, more NiO species were embedded more deeply in the Al_2O_3 lattice, thereby strengthening the interaction between the metal oxide and the carrier. This strong interaction promotes the distribution of the NiO species on the catalyst, which will further affect the steam reforming reaction. A further increase in the calcination temperature of the support beyond 800 °C ($Ni/Al_{S.G900}$ and $Ni/Al_{S.G1000}$) caused reduction bands to start to shift to lower temperature values. Consequently, more NiO species were located on the support surface, which indicates weaker interaction

between the metal and the carrier as it caused nickel agglomeration and further affected the activity of the catalyst. Interestingly, bands belonging to Ni aluminate were not observed on all the examined catalysts, which coincide well with the XRD results. Other work done by Seo et al. (2008) to correlate the catalytic activity and selectivity of $Ni/Al_{S.G.}$ catalyst for steam reforming of natural gas and concluded that the support calcined at 900 °C gave the strongest metal - support interaction, while our support shown strongest interaction at support calcined temperature of 800 °C.

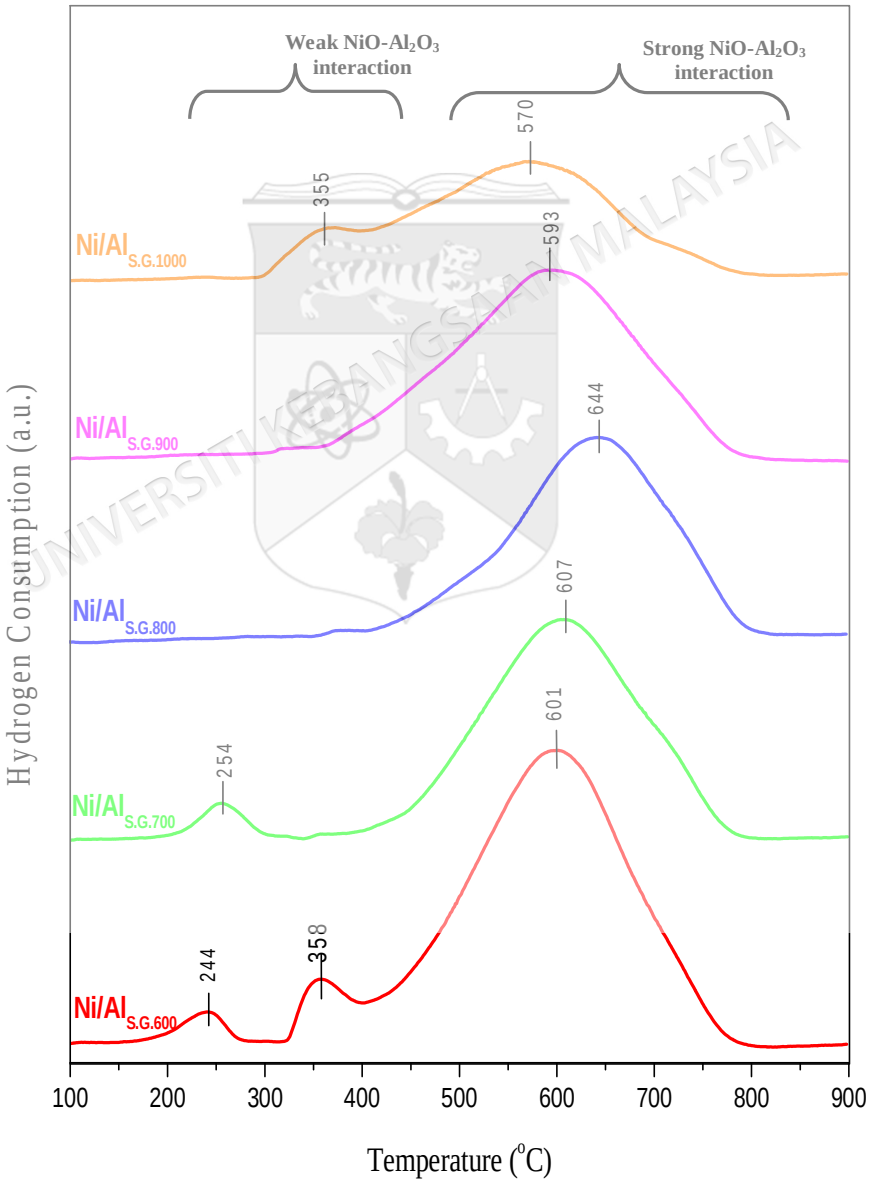

Figure 4.33 Temperature-programmed reduction (TPR) profiles of nickel/sol gel alumina catalysts

4.6.4 Hydrogen Chemisorption Measurements

The amount of H_2 uptake, and dispersion, surface area, and mean particle size of nickel were determined through chemisorption measurements, as shown in Table 4.12. As a result of hydrogen chemisorption, the amount of hydrogen uptake over the $Ni/Al_{S.G600}$, $Ni/Al_{S.G700}$, and $Ni/Al_{S.G800}$ catalysts increased as the calcination temperature increased. Furthermore, an increase in calcination temperature ($Ni/Al_{S.G900}$, $Ni/Al_{S.G1000}$) led to a decrease in hydrogen uptake. The trend in the dispersion and surface area of nickel is proportional to the amount of hydrogen uptake. As a result, the dispersion and surface area of nickel increased in the following order: $Ni/Al_{S.G600} < Ni/Al_{S.G700} < Ni/Al_{S.G1000} < Ni/Al_{S.G900} < Ni/Al_{S.G800}$, whereas the mean particle size values of nickel decreased. These results are also supported by TPR experiments, as shown in Figure 4.33. Hydrogen chemisorption measurements were conducted over $Ni/Al_2O_3–ZrO_2$ catalyst by other research group, studying hydrogen production by steam reforming of liquefied natural gas (Seo et al. 2009). Among the catalysts tested, Ni/AZ1000 catalyst with the strongest interaction between nickel species and AZ support exhibited the largest amount of hydrogen uptake, the highest nickel dispersion, and highest nickel surface area.

Table 4.12 Results for hydrogen chemisorptions measurements

Catalyst name	H_2 uptake, ($\mu mol\ g^{-1}$)	Ni dispersion, (%) *	Ni surface area, ($m^2 g^{-1}$) *	Mean particle diameter, (nm)
$Ni/Al_{S.G.600}$	45	4.40	1.75	22.9
$Ni/Al_{S.G.700}$	254	24.8	9.90	4.1
$Ni/Al_{S.G.800}$	566	55.4	22.1	1.8
$Ni/Al_{S.G.900}$	489	47.8	19.1	2.1
$Ni/Al_{S.G.1000}$	310	30.3	12.1	3.3

Note: * means $H/Ni_{atom} = 1$ was assumed

4.6.5 Steam Reforming of Ethanol over the Supported Ni Catalysts

The ethanol conversion and hydrogen yield over the Ni/$Al_{S.G.}$ catalysts in the ethanol reforming reaction as a function of the calcination temperature of $Al_{S.G.}$ are shown in Figure 4.34.

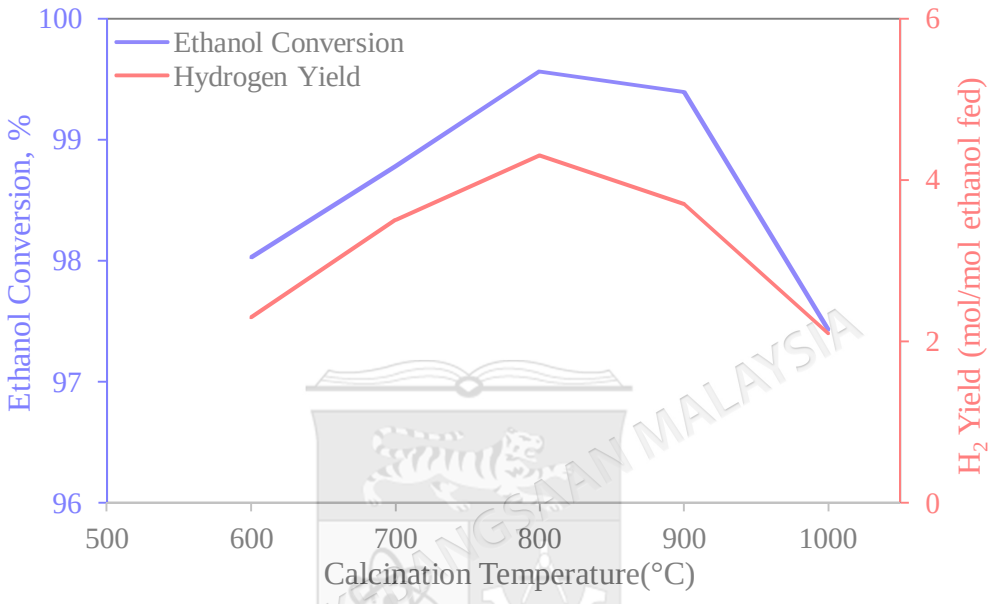

Figure 4.34 Ethanol conversion and hydrogen yield over Ni/sol gel made alumina catalysts in the steam reforming of ethanol, plotted as a function of calcinations temperature of the support

Both ethanol conversion and hydrogen yield were significantly affected by the calcination temperature of the $Al_{S.G.}$ supports. As depicted in Figure 4.34, the increase in both ethanol conversion and hydrogen yield was in the following order: Ni/$Al_{S.G1000}$ < Ni/$Al_{S.G600}$ < Ni/$Al_{S.G700}$ < Ni/$Al_{S.G900}$ < Ni/$Al_{S.G800}$. Among all the evaluated catalysts, the Ni/$Al_{S.G800}$ catalyst exhibited the best catalytic performance. The high performance of the Ni/$Al_{S.G800}$ catalyst may be due to its physical and chemical characteristics (Chang et al. 2006). Although the surface area and pore volume of the supports of the Ni/$Al_{S.G600}$ and Ni/$Al_{S.G700}$ catalysts were higher than those of the Ni/$Al_{S.G800}$ catalyst (Table 4.11), the Ni species in the Ni/$Al_{S.G800}$ catalyst interacted strongly with the alumina support (Figure 4.33). This strong metal–support interaction over the Ni/$Al_{S.G800}$ catalyst not only improves the dispersion and surface area of

nickel but also prevents metal agglomeration (Table 4.12). As a result, the number of active sites that can facilitate a reaction increased because of high metal dispersion. Consequently, this will enhance catalytic behaviour during the steam reforming reaction. Moreover, high dispersion of metal particles on the $Ni/Al_{S.G800}$ catalyst could exhibit high resistance toward carbon formation. An attempt has been done by Seo et al. (2008) to correlate the catalytic activity and selectivity of $Ni/Al_{S.G.}$ catalyst for steam reforming of natural gas and concluded that the support calcined at 900 °C is the most active system for hydrogen production, while our catalyst system shown highest selectivity and activity at calcined temperature of 800 °C.

Catalyst deactivation was tested by evaluating the deposited carbon on the used samples to compare the performance of each catalyst after 8 hr reaction. CHNS elemental analyses were performed to detect the quantity of carbon deposited on the used samples, as shown in Table 4.13. All samples contain only trace amounts of carbon. Therefore, catalyst deactivation by carbon deposition can be inferred to have an insignificant effect on catalytic activity after an 8 hr run.

Table 4.13 Carbon deposited on the used catalysts after 8 hr reaction

Catalyst name	Amount of carbon deposition, (wt %)
$Ni/Al_{S.G.600}$	0.26
$Ni/Al_{S.G.700}$	0.20
$Ni/Al_{S.G.800}$	0.14
$Ni/Al_{S.G.900}$	0.11
$Ni/Al_{S.G.1000}$	0.68

4.6.6 Effect of Calcinations Temperature of the Support on Product Yield

Figure 4.35 exhibited gaseous product yields over Ni/Al sol gel catalysts in the steam reforming of ethanol as a function of calcinations temperature of the alumina support.

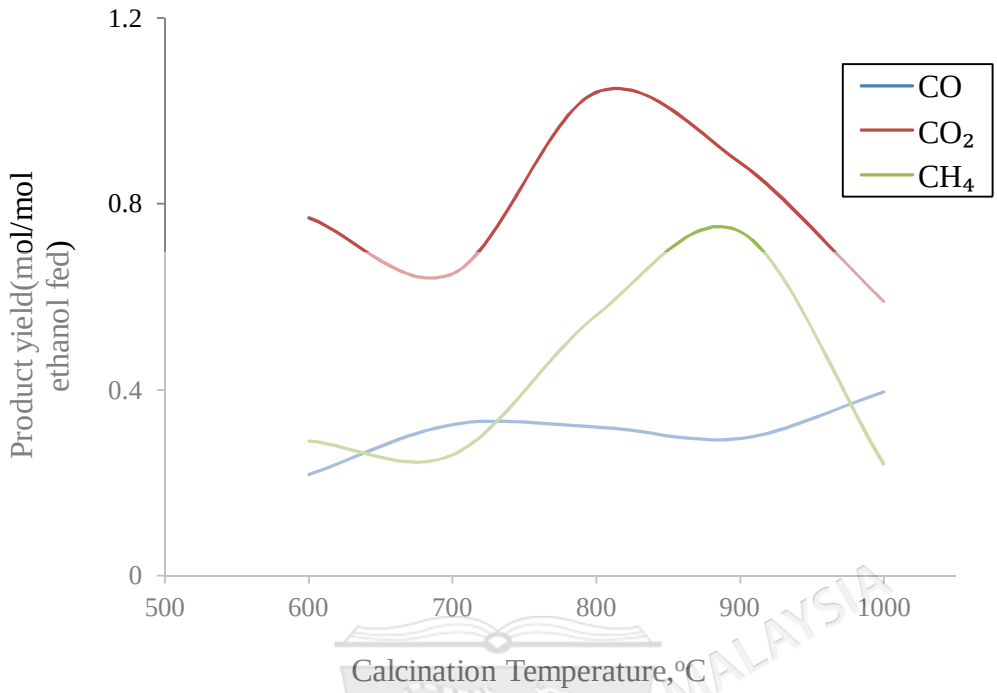

Figure 4.35 Product yield over Ni/sol gel made alumina catalysts in the steam reforming of ethanol, plotted as a function of calcinations temperature of the support

It is observed that the yield of CO slightly increases from 0.218 mol/mol ethanol fed over $Ni/Al_{S.G600}$ catalyst to 0.325 mol/mol ethanol fed over $Ni/Al_{S.G700}$. All catalysts exhibit insignificant change except over $Ni/Al_{S.G1000}$, after which the CO yield remain nearly constant before it increase to around 0.4 mol/mol ethanol fed over $Ni/Al_{S.G1000}$ catalyst. In contrast CO_2 yield, reach its maximum value of 1.04 mol/mol ethanol fed over $Ni/Al_{S.G800}$, means that water gas shift reaction was favored at this specific calcined temperature. Then CO_2 yield decline as calcinations temperature of the sol gel support increase till rich its minimum value of 0.59 mol/mol ethanol fed over $Ni/Al_{S.G1000}$. This decrease in CO_2 yield and slightly increase in CO yield means that, reverse water gas shift reaction was favored in the direction of increasing the calcinations temperature of the support above 800°C (Seo et al. 2009).

Since $Ni/Al_{S.G800}$ catalyst exhibited the best catalytic activity in terms of hydrogen yield, it was chosen to optimize the reaction conditions and to develop an

integrated system capable to predict hydrogen yield and ethanol conversion using empirical and artificial neural network (ANN) models.

4.7 PROPOSED REACTION MECHANISM

A possible reaction pathway for ethanol steam reforming over a catalyst is proposed. The reaction pathway for ethanol steam reforming over Ni catalyst was divided and simplified into four steps. Each step represents deferent reaction mechanism. Formation and decomposition of acetaldehyde, methane reforming, and water gas shift reaction are the main reactions will be discussed.

Ethanol dehydrogenation yields hydrogen and acetaldehyde which is illustrated in Figure 4.36.

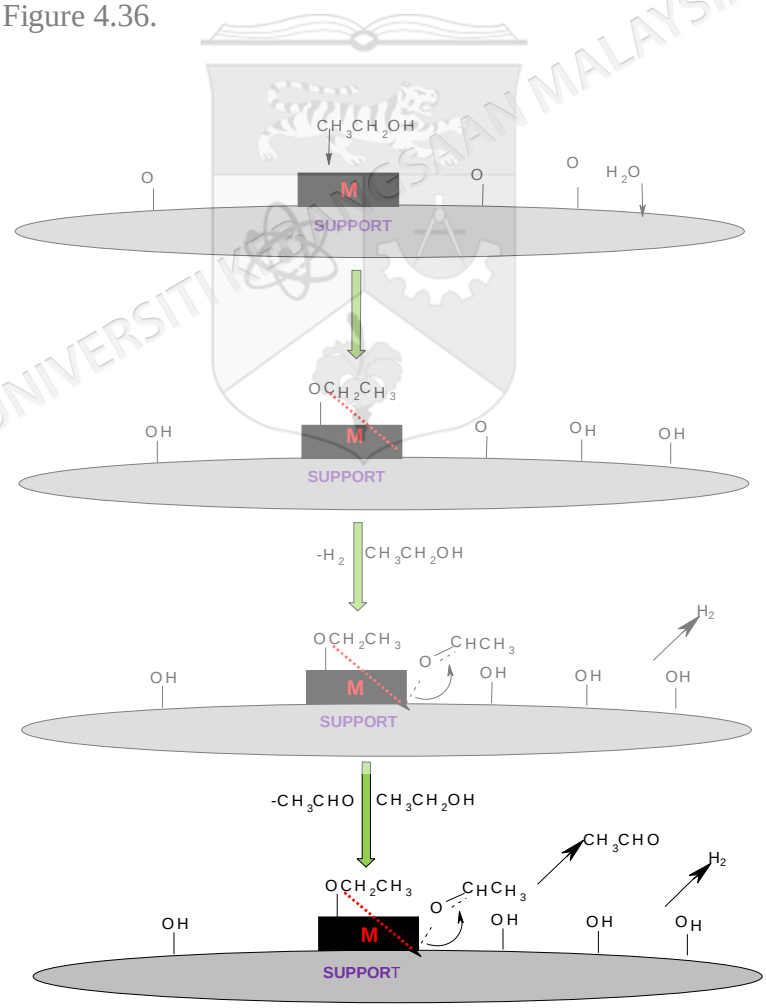

Figure 4.36 Schematic representation of a plausible mechanism for the formation of acetaldehyde and hydrogen by dehydrogenation of ethanol

The adsorption of ethanol is suggested to occur on the active metal site and form ethoxide species, whereas water is chemisorbed on the support to form hydroxyl groups. The H released from ethanol either combine with the oxygen present on the surface of the support and form OH groups or combine with H in H_2O molecule to form H_2. The formation of acetaldehyde occurs by abstract another H atom from the ethoxide at the metal and support interface.

Figure 4.37 presents the schematic representation of acetaldehyde decomposition that leads to the formation of methane and carbon monoxide through breaking the C-C bond by the metal.

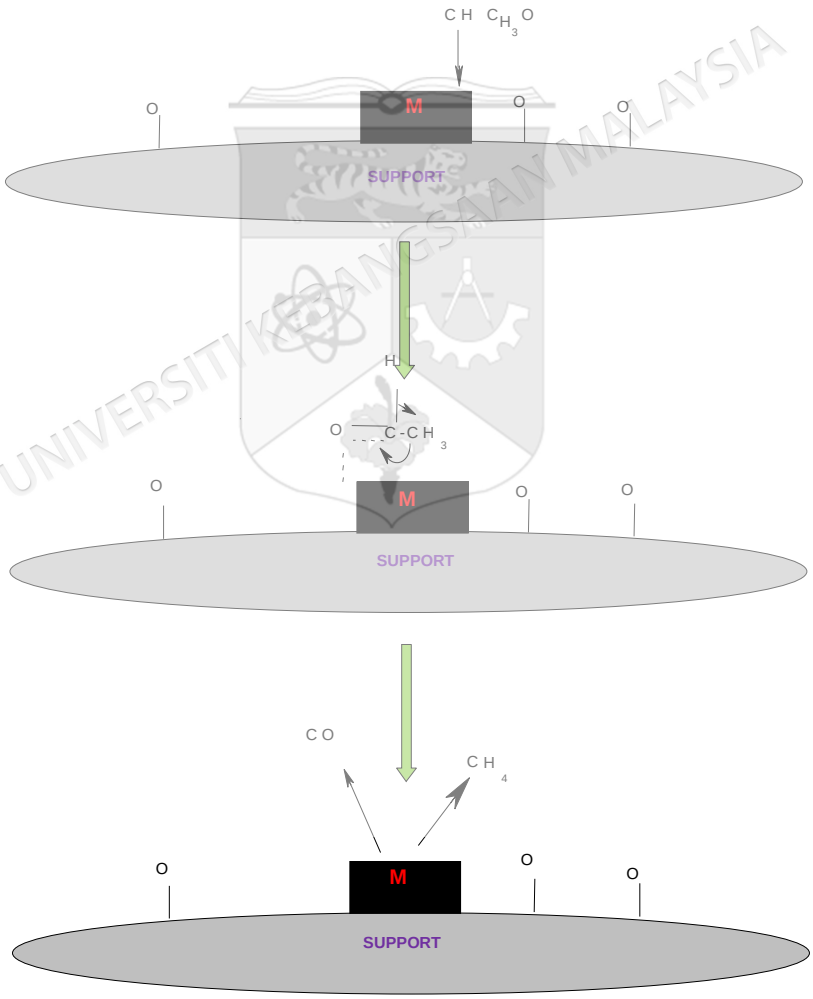

Figure 4.37 Schematic representation detailing the decomposition of acetaldehyde to form methane and carbon monoxide

Methane is reformed with steam in the next reaction step to obtain hydrogen and carbon monoxide, as given in Figure 4.38. Here also, water is adsorbed on the support whereas methane is captured by the metal to give H and CH_3. The methyl group will undergo oxidation through H subtraction and O addition to form formaldehyde intermediate which undergo to further oxidation.

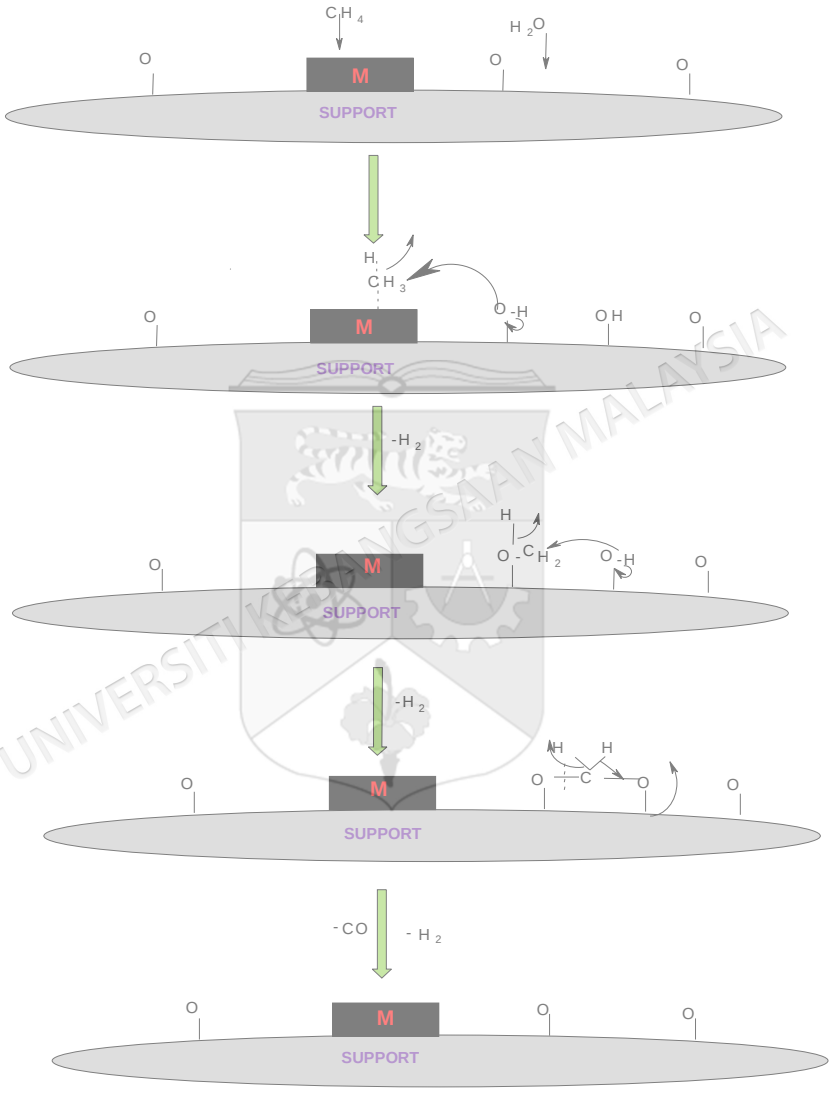

Figure 4.38 Schematic representation showing methane-reformation resulting in the formation of carbon monoxide and hydrogen

The last reaction step proposed in this mechanism is the water-gas shift reaction, which produces hydrogen and carbon dioxide (Figure 4.39). The oxygen-carbon species may further oxidize to obtain carbonate species, especially on supports

with high oxygen storage capacity, which can desorp as CO_2. The other undesirable products of the reaction are acetone, ethylene, coke, etc.

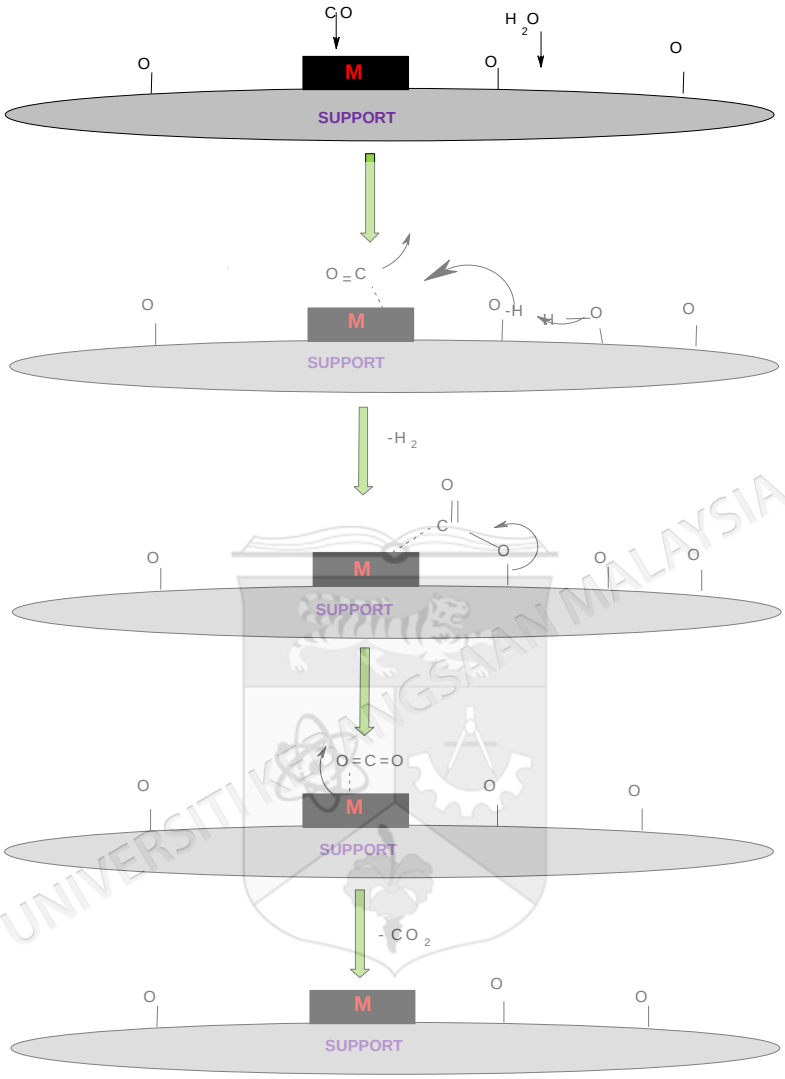

Figure 4.39 Schematic representation showing carbon monoxide adsorption and water-gas shift reaction on supported metal catalysts

4.8 EMPIRICAL MODEL OR (DOE) MODEL

Statistical design was used to optimize the influential factors that control hydrogen production via ethanol steam reforming. Hydrogen production via ethanol steam reforming was performed using $Ni/Al_{S.G800}$ catalyst. The optimization process was performed via RSM using central composite design (CCD) to evaluate the maximum

hydrogen yield ($Y_{H_{2.Y}}$) and ethanol gasification ($Y_{ETOH_{Con.}}$), and the minimum CO yield ($Y_{CO.Y}$). The influence of the three experimental variables and their interaction on each response was explored using RSM plots.

Two replicates of 20 sets of experiments were performed to investigate the influence of reaction temperature, ethanol to water molar ratio, and liquid hourly space velocity on hydrogen production during ethanol steam reforming. As indicated in chapter 3, lower, upper, and middle values of the mentioned independent variables were selected based on the values obtained from the literature (Chen et al. 2009; Rossi et al. 2009; Wang et al. 2009a). For the reforming temperature, the reaction performance was investigated at a wide range of temperature from 200 to 500 °C as reported elsewhere (Comas et al. 2004). Prior to the reaction, all runs were conducted under the same preheating and reduction procedure. Table 4.14 illustrates the experimental (observed) and predicted data obtained from the model for the three responses ($Y_{H_{2,Y}}$, $Y_{ETOH_{Con.}}$, and $Y_{CO,Y}$). Standard deviation values of the three observed responses are also shown in Table 4.14. Also, the first experimental result of each replicated experiments was recorded in the same table along with standard deviation values.

Table 4.14 Central composite design with observed and predicted values

No	Variables			$Y_{H_{2,Y}}$		$Y_{ETOH_{Con.}}$		$Y_{CO,Y}$	
	X_1	X_2	X_3	Observed	Predicted	Observed	Predicted	Observed	Predicted
1	200	13.5	0.56	0.54±0.028	0.94	26±0.70	25	0.18±0.03	0.17
2	200	24	1	0.89±0.018	0.71	25±0.70	26	0.15±0.003	0.10
3	500	3	1	2.1±0.99	2.7	80±2.12	73	0.42±0.029	0.40
4	500	24	0.12	4.8±0.07	4.69	81±0.70	78	0.21±0.009	0.21
5	350	13.5	1	2.7±0.21	2.63	61±2.1	57	0.17±0.015	0.20
6C	350	13.5	0.56	2.8±0.14	2.61	58±4.24	56	0.23±0.001	0.23
7	350	3	0.56	1.5±0.42	1.35	45±3.53	37	0.28±0.004	0.17
8	200	3	0.12	0.0±0.00	0.008	0.0±0.00	1	0.00±0.00	0.03
9C	350	13.5	0.56	2.6±0.07	2.61	59±17.67	56	0.22±0.003	0.23
10C	350	13.5	0.56	2.7±0.14	2.61	61±2.1	56	0.23±0.001	0.23
11	500	24	1	4.8±0.49	4.72	79±1.41	80	0.21±0.003	0.19
12	500	3	0.12	2.4±0.21	2.67	65±3.5	71	0.38±0.077	0.39
13C	350	13.5	0.56	2.7±0.28	2.61	45±5.65	56	0.26±0.071	0.23
14	350	13.5	0.12	2.9±0.14	2.60	65±3.5	55	0.33±0.008	0.21
15C	350	13.5	0.56	2.6±0.00	2.61	54±1.4	56	0.22±0.076	0.23
16C	350	13.5	0.56	2.5±0.07	2.61	58±1.41	56	0.22±0.078	0.23
17	200	3	1	0.0±0.00	0.023	0.0±0.00	3	0.00±0.00	0.00
18	200	24	0.12	0.89±0.017	0.681	24±0.71	24	0.10±0.015	0.13
19	350	24	0.56	2.2±0.07	2.70	52±1.4	52	0.06±0.022	0.12
20	500	13.5	0.56	4.3±0.07	4.29	85±0.092	87	0.30±0.005	0.39

The estimated regression coefficients of reduced and nonreduced models with their corresponding *p*-values are shown in Tables 4.15 and 4.16, respectively. These tables also provide the R^2 and adjusted R^2 values, which were used to evaluate the goodness of fit of the regression model. ANOVA was conducted to identify the terms that significantly influenced the responses at a *p*-value less than 0.05. Tables 4.15 and 4.16 indicate that the most important terms are X_1, X_2, X_2^2, and X_1X_2, which represent the linear terms of temperature, molar ratio, quadratic term of molar ratio, and the interaction term of temperature and molar ratio, respectively. These terms significantly influenced the responses ($Y_{H_{2,Y}}$, $Y_{ETOH_{Con.}}$, and $Y_{CO,Y}$). Notably, the liquid

hourly space velocity (LHSV), representing X_3, had negligible influence on the responses when all the *p*-values were greater than 0.05. As shown in Tables 4.15 and 4.16, R^2 and adjusted R^2 for $Y_{H_{2,Y}}$ and $Y_{ETOH_{Con.}}$ indicated that the proposed model adequately fitted the experimental data. For$Y_{CO,Y}$, the R^2 and adjusted R^2 values of the regression model were quite low, which suggests the presence of other important parameters.

Table 4.15 Non-reduced model and coefficient parameters for the responses

Regression coefficient	Term	Non-reduced model					
		Estimated regression coefficient			*p*-value		
		$Y_{H_{2,Y}}$	$Y_{ETOH_{Con.}}$	$Y_{CO,Y}$	$Y_{H_{2,Y}}$	$Y_{ETOH_{Con.}}$	$Y_{CO,Y}$
Linear	X_1	0.011	0.328	-0.0003	0.005	0.000	0.65
	X_2	0.159	4.499	0.0335	0.000	0.000	0.000
	X_3	-1.25	-13.29	0.0836	0.133	0.451	0.66
Quadratic	X^2_1	-0.00	-0.0001	0.000002	0.381	0.206	0.052
	X^2_2	-0.005	-0.097	-0.0007	0.000	0.000	0.006
	X^2_3	1.131	13.1	-0.0926	0.072	0.32	0.51
Interaction	X_1X_2	0.0002	-0.002	-4.5×10^{-5}	0.000	0.011	0.000
	X_1X_3	0.0005	0.021	0.000067	0.593	0.333	0.78
	X_2X_3	-0.013	-0.503	-0.0012	0.371	0.124	0.72
R^2		0.969	0.956	0.765	-	-	-
Adjusted R^2		0.960	0.942	0.695	-	-	-

Table 4.16 Reduced model and coefficient parameters for the responses

Regression coefficient	Term	Reduced model					
		Estimated regression coefficient			*p*-value		
		$Y_{H_{2,Y}}$	$Y_{ETOH_{Con.}}$	$Y_{CO,Y}$	$Y_{H_{2,Y}}$	$Y_{ETOH_{Con.}}$	$Y_{CO,Y}$
	X_1	0.0083	0.2404	0.0013	0.000	0.000	0.000
Linear	X_2	0.1354	4.319	0.031	0.000	0.000	0.003
	X_3	0.0354	2.4	-0.013	0.803	0.437	0.70
	X_1^2	-	-	-	-	-	-
Quadratic	X_2^2	-0.0053	-0.101	-	0.000	0.000	-
	X_3^2	-	-	-	-	-	-
	X_1X_2	0.00021	-0.0025	-4.5×10^{-5}	0.000	0.013	0.00
Interaction	X_1X_3	-	-	-	-	-	-
	X_2X_3	-	-	-	-	-	-
R^2		0.965	0.947	0.666	-	-	-
Adjusted R^2		0.960	0.940	0.628	-	-	-

The high R^2 (0.965) for $Y_{H_{2,Y}}$ in Table 4.16 indicates that the proposed model can account for most of the observed variations. The high R^2 value of 0.947 and the small *p*-value ($p < 0.05$) for the $Y_{ETOH_{Con.}}$ indicated that the regression model had a good correlation between the independent variables and the response. However, Table 4.16 shows that the linear terms of X_1 and X_2, the quadratic term of X_2^2, and the interaction term of X_1X_2 significantly influenced both $Y_{H_{2,Y}}$ and $Y_{ETOH_{Con.}}$ with *p*-value less than 0.05. By contrast, $Y_{CO,Y}$ was mostly affected by the linear terms of X_1 and X_2 and the interaction term of X_1X_2.

The following second-order polynomial equations (Equations 4.15, 4.16, and 4.17) describing the relationship between the process variables and their predicted responses for all the three dependent variables ($Y_{H_{2,Y}}$, $Y_{ETOH_{Con.}}$, and $Y_{CO,Y}$,) were generated.

$$Y_{H_{2.Y}} = -2.16 + 0.0083(X_1) + 0.135(X_2) + 0.0354(X_3) - 0.0053(X_2)^2 + 0.00021(X_1)(X_2) \quad (4.15)$$

$$Y_{ETOH_{Con.}} = -57.8203 + 0.2404(X_1) + 4.3199(X_2) + 2.4(X_3) - 0.1011(X_2)^2 - 0.0025(X_1)(X_2) \quad (4.16)$$

$$Y_{CO.Y} = -0.22575 + 0.0013(X_1) + 0.031(X_2) - 0.013(X_3) - 0.000045(X_1)(X_2) \quad (4.17)$$

Equations 4.15 and 4.17 show that X_2 had the greatest influence on $Y_{H_{2,Y}}$ and $Y_{CO,Y}$. The terms X_3 and X_1 also affected $Y_{H_{2.Y}}$, but to a lesser extent than X_2. The interaction between X_1X_2 only slightly affected$Y_{H_{2.Y}}$. As shown in Equation 4.16, $Y_{ETOH_{Con.}}$ was mostly affected by the linear term of X_2, followed by X_3 and X_1. However, the quadratic term X_2^2 and the interaction term X_1X_2 had lower effect on $Y_{ETOH_{Con.}}$ than the linear terms.

4.8.1 Effect of Process Variables on the Responses

Figures 4.40 - 4.42 presents the 3D response surface plots of the relationships between the independent variables and $Y_{H_{2,Y}}$. The advantage of using response surface plots with two independent variables at a time is to enable the examination of the relation of the main and the interaction factors with the response. Figure 4.40 illustrates the effect of X_1 and X_2 on $Y_{H_{2.Y}}$. The surface plot shows that the highest hydrogen yield was obtained when both independent variables (X_1 and X_2) were high (interaction effect). This finding was in agreement with other data (Mas et al. 2006), which indicate that high temperatures and high water–ethanol ratios enhance H_2 production. On the other hand, Figure 4.41 shows that $Y_{H_{2,Y}}$ varied only with X_1, whereas X_3 had no effect on $Y_{H_{2,Y}}$.

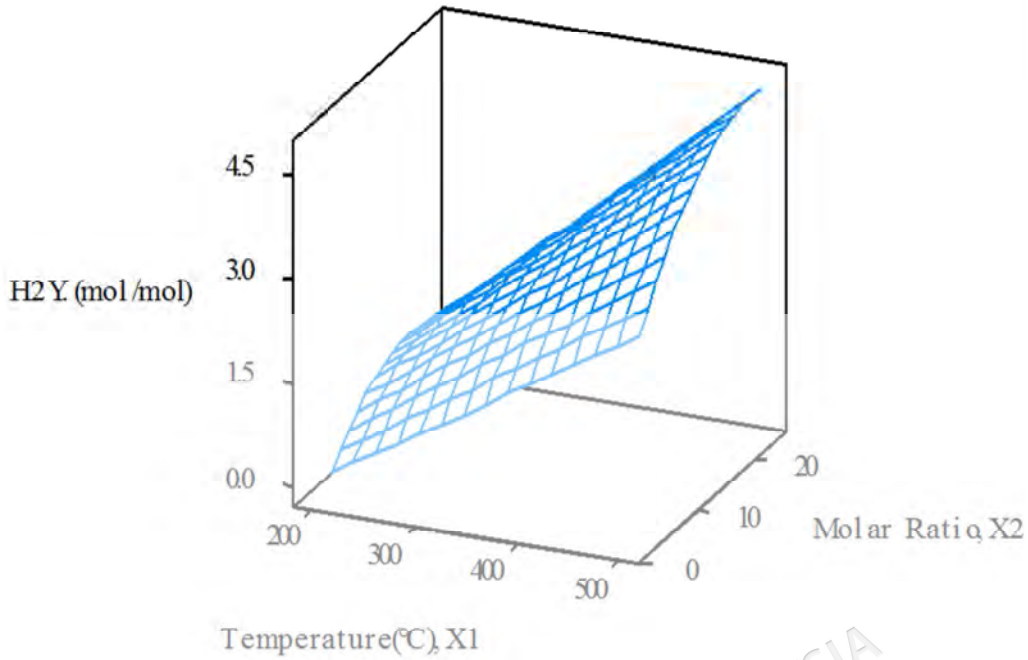

Figure 4.40 Interaction effects of temperature and molar ratio on hydrogen yield

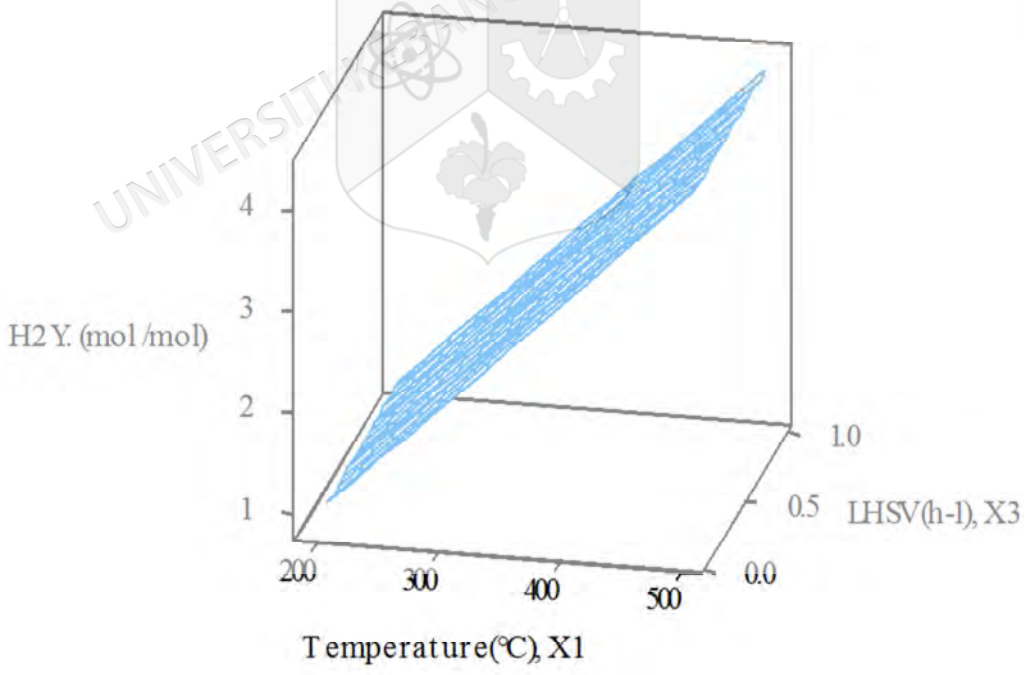

Figure 4.41 Interaction effects temperature and LHSV on hydrogen yield

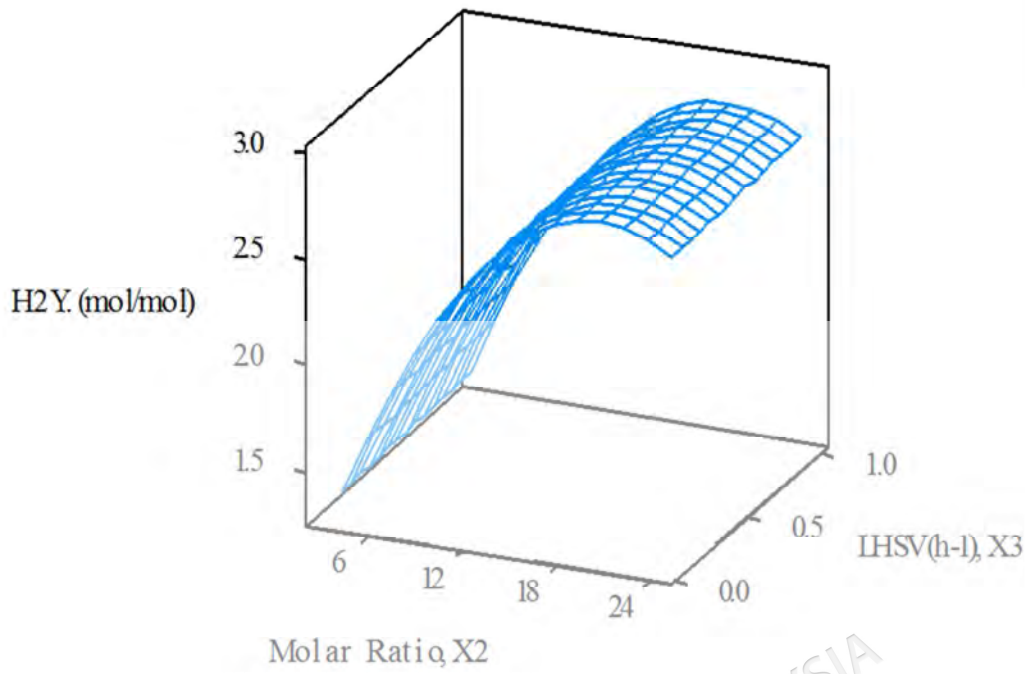

Figure 4.42 Interaction effects of molar ratio and LHSV on hydrogen yield

Figure 4.42 also shows that $Y_{H_{2,Y}}$ was significantly affected by X_2 up to 18, but was not significantly changed beyond this ratio. Generally, $Y_{H_{2,Y}}$ increased as X_1 and X_2 increased, which was expected because the steam reforming reaction is endothermic and positively affected by high temperature (Wang et al. 2009a).

The response surface in Figures 4.43 - 4.45 illustrate the interaction influence of varying temperature and water to ethanol molar ratio, temperature and liquid hourly space velocity, and water to ethanol molar ratio and liquid hourly space velocity on ethanol conversion into gaseous product, respectively. Figures 4.43 and 4.44 indicated that the $Y_{ETOH_{Con.}}$ is significantly increased as the X_1 increase. From Figure 4.43, the orientation of the principal axes of the surface plot indicated that the interaction between X_1 and X_2 had significantly affected the $Y_{ETOH_{Con.}}$, and the optimum values of both the variables were existed in the area experimentally explored. It is also noted that, the interaction effect between X_1 and X_2 on $Y_{ETOH_{Con.}}$ shown in Figure 4.43 is higher than that between X_1 and X_3 shown in Figure 4.44, where the X_3 variable had no effect on the $Y_{ETOH_{Con.}}$. Figure 4.45 shows that the $Y_{ETOH_{Con.}}$ is influenced significantly by the X_2 variable (Chen et al. 2009), especially at low and medium

levels, meanwhile the X_3 variable had lower effect on the $Y_{ETOH_{Con.}}$. Therefore, at constant value of X_2, the $Y_{ETOH_{Con.}}$ was slightly increased as X_3 increase. Generally, ethanol conversion and hydrogen yield were increased as the temperature and molar ratio were increased, which make sense since the steam reforming reaction is endothermic and it is favour at high temperature. It is also observed that the ethanol conversion into gaseous and hydrogen yield are varied insignificantly with the LHSV range taken in this study.

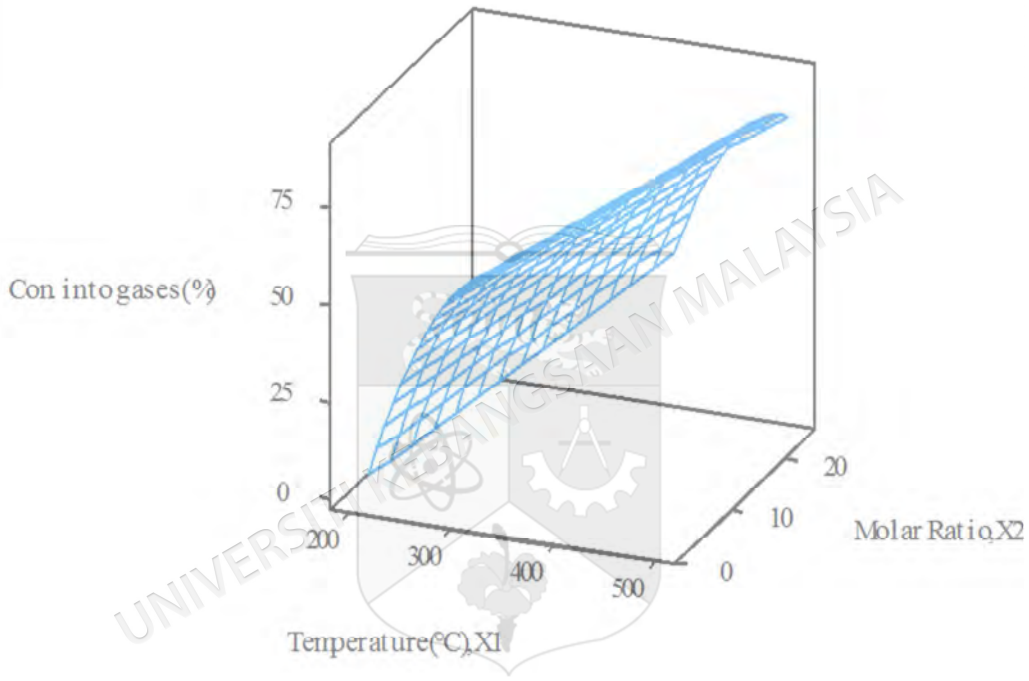

Figure 4.43 Interaction effects of temperature and molar ratio on ethanol gasification

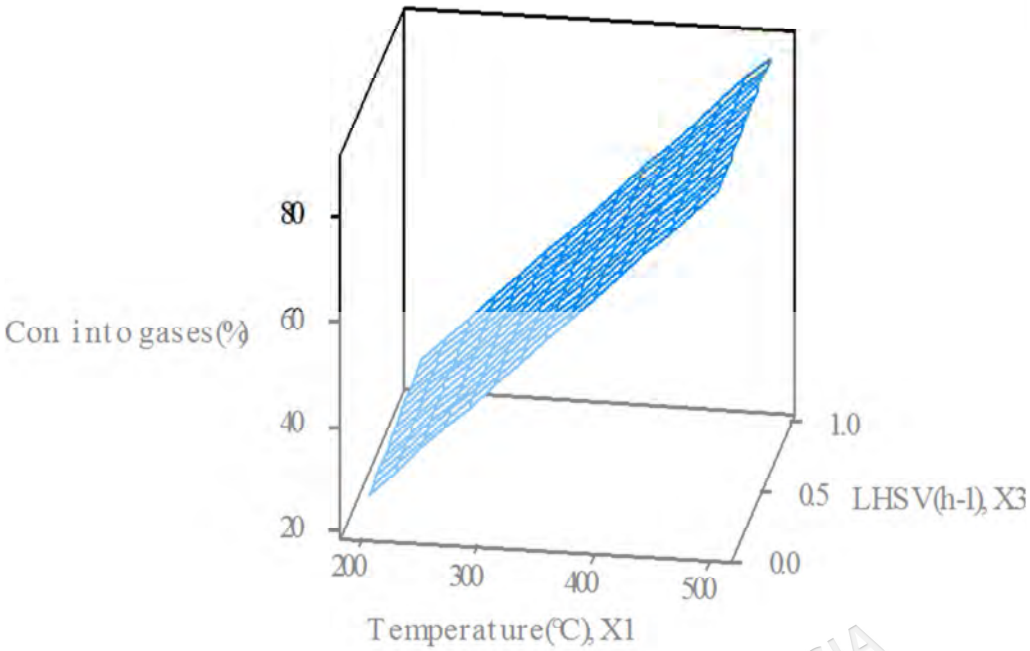

Figure 4.44 Interaction effects of temperature and LHSV on ethanol gasification

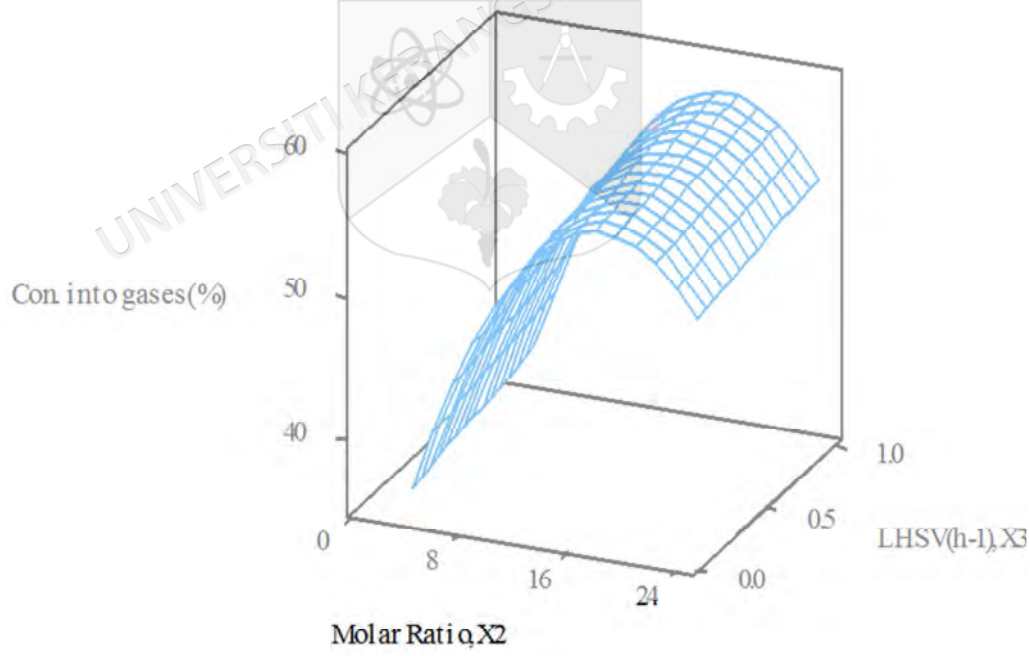

Figure 4.45 Interaction effects of molar ratio and LHSV on ethanol gasification

Response surface plots describing the effects of the main and the interaction variables on $Y_{CO,Y}$ are shown in Figures 4.46 - 4.48. The effect of the interaction between X_1 and X_2 on $Y_{CO,Y}$ is illustrated in Figure 4.46. $Y_{CO,Y}$ decreased as X_2

increased at high X_1 values, but it did not exceed 0.18 mol/mol for all values of X_2 at low X_1 values. The surface plot also shows that the lowest $Y_{CO,Y}$ was obtained at the lowest X_1 value. Figure 4.47 shows that the $Y_{CO,Y}$ values significantly varied with high X_1 values, whereas the variation in X_3 values had no effect on $Y_{CO,Y}$. At a constant X_1, $Y_{CO,Y}$ significantly varied with X_2. Figure 4.48 shows that the lowest $Y_{CO,Y}$ was obtained at high X_2 levels. However, the low $Y_{CO,Y}$ at high X_2 can be attributed to the acceleration of the water gas shift reaction caused by the catalyst.

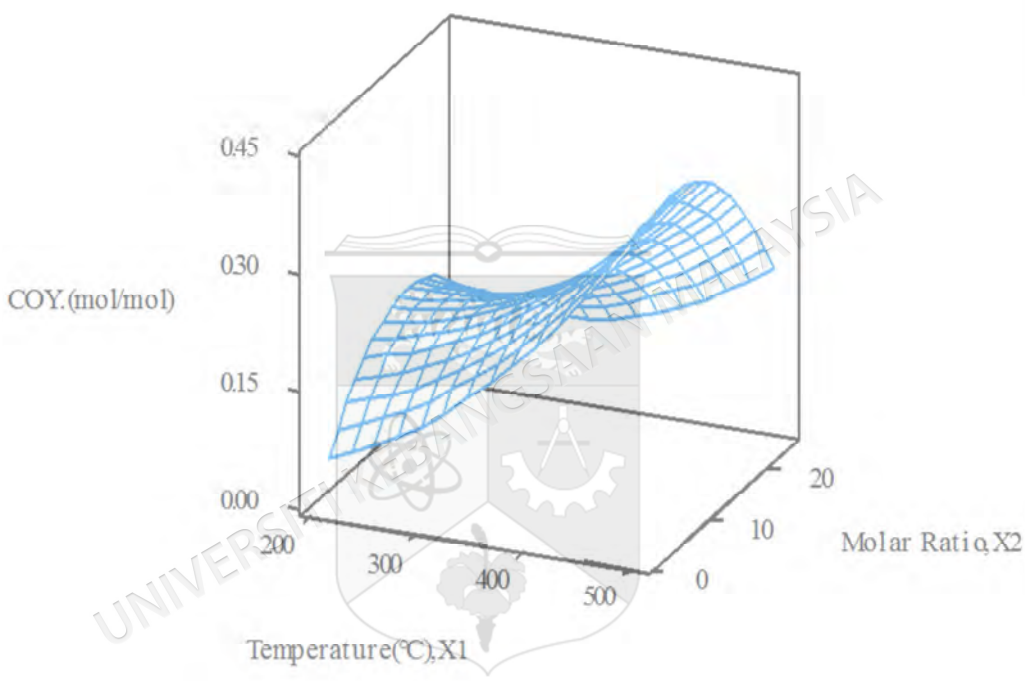

Figure 4.46 Interaction effects of temperature and molar ratio on CO yield

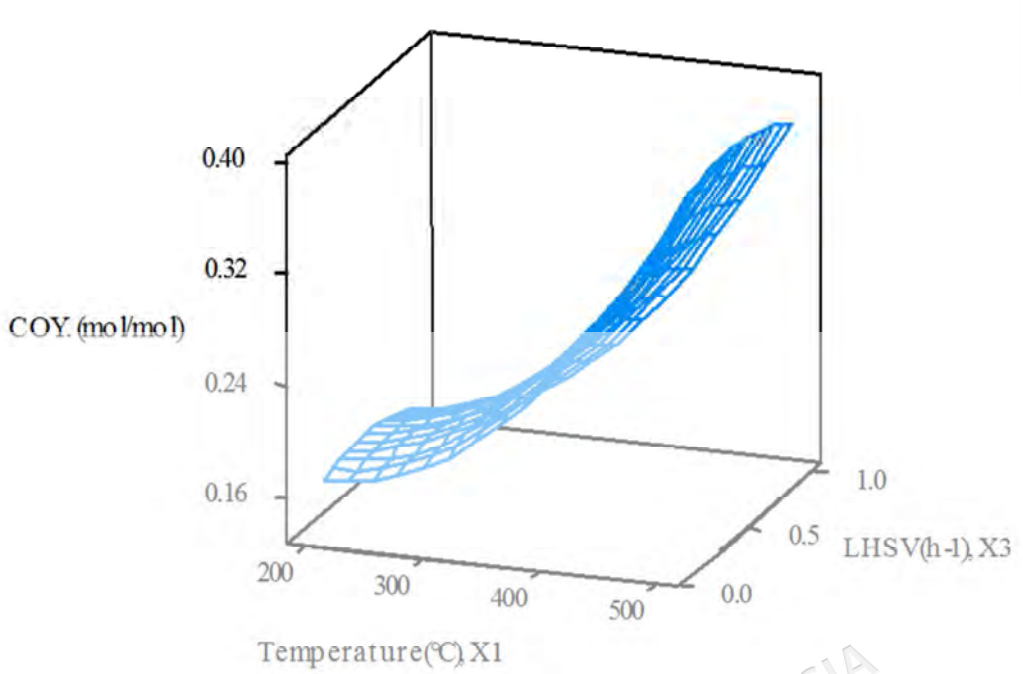

Figure 4.47 Interaction effects of temperature and LHSV on CO yield

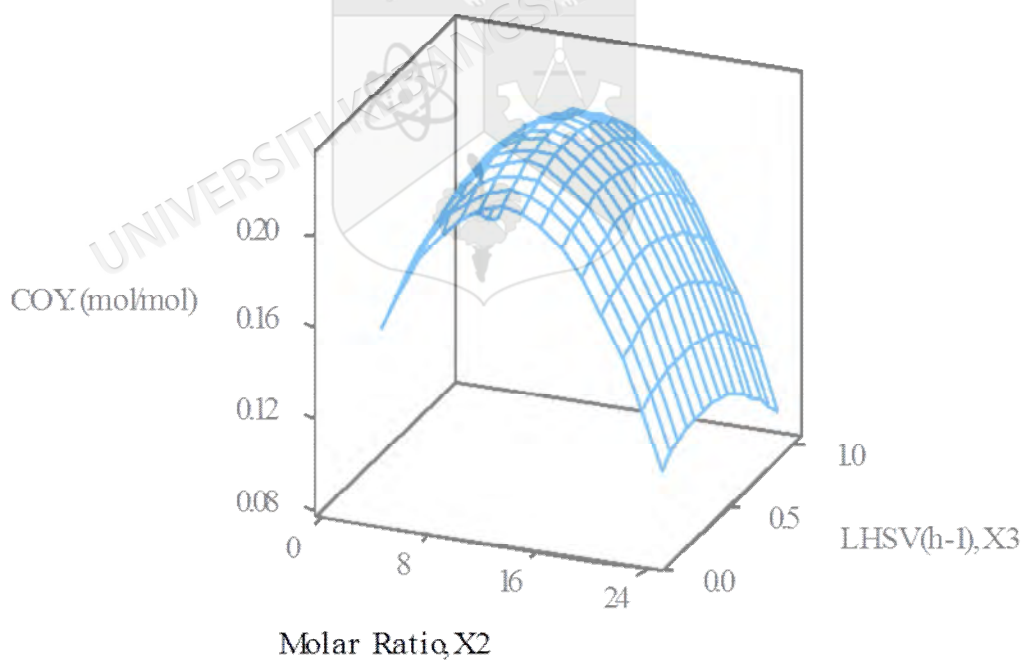

Figure 4.48 Interaction effects of molar ratio and LHSV on CO yield

4.8.2 Response Optimization

The optimum levels of the three independent variables, namely, temperature, water–ethanol molar ratio, and liquid hourly space velocity were determined using the response optimizer. The optimum conditions that maximized ethanol gasification and hydrogen yield and minimized carbon monoxide yield were a temperature of 500 °C, a water–ethanol molar ratio of 20, and a liquid hourly space velocity of 0.72 h^{-1}. Applying these optimum conditions resulted in hydrogen yield of 4.7 mol/mol of ethanol, an ethanol gasification rate of 85%, and a carbon monoxide yield of 0.25 mol/mol of ethanol. Other publication applied the same optimization tools to investigate optimization conditions of methanol steam reforming over a Au/CuO–CeO_2 catalyst (Monyanon et al. 2012). The optimized conditions for complete methanol conversion over 5wt% Au/CuO–CeO_2 catalysts were found to be an operating temperature of ~295 °C to ~307 °C and an S/M ratio of ~1.82 to 2.00 with good empirical-theoritical agreement.

4.9 ANN MODELLING OF HYDROGEN PREDICTION SYSTEM

The objective of this section is to develop an integrated system capable to predict hydrogen yield, ethanol conversion, and carbon monoxide yield using ANN models. Therefore, the experimental results were trained and tested before the predictive accuracy of the developed models is evaluated.

The dataset were divided into training and testing subsets. A three-layer back-propagation neural network models were developed using 20 experiments data as training data. 15% of the experiments were used in testing stage. Before training, input data were normalized before introducing them to the input layer. Then the data were trained by three different algorithms and the optimum number of neurons was searched in order to improve the predictive performance. Mean square error (MSE) and the efficiency (*Eff.*) were both used to evaluate the ANN model performance.

4.9.1 Input & Output Data

Figures 4.49 (a) and (b) show the input and output data respectively before normalization. Figure 4.49 (a) explain the three input parameters. Input 1 refers to the temperature which varies from 200-500 ^{o}C. Input 2 shows the molar ratio which vary from 1-24.while input 3 refer to the liquid hourly space velocity which is vary from 0-1h^{-1}. Outputs 1, 2, and 3 in Figure 4.49 (b) refer to H_2 yield, CO yield, and ethanol conversion into gaseous product, respectively. It is clearly seen that the magnitudes of the input and output variables are inconsistent. Thus, these data were normalized within a consistent range (0 to 1) before introducing them to the input layer of the network to ensure that each data is given fair contribution in determining the network output. Data after normalization for the input and output variables are shown in Figures 4.49 (c) and (d), respectively.

Similar study with different input parameters was conducted by Akande et al. (2005) using artificial neural network (ANN) approach to design an optimum Ni/Al_2O_3 catalyst for the production of hydrogen by the catalytic reforming of crude ethanol. These authors investigate the inter-relationships between catalyst-preparation methods, nickel loading, catalyst characteristics and catalyst performance. The optimal hydrogen yield was 4.4 mol%, and the associated crude-ethanol conversion and H_2 selectivity for the optimal hydrogen yield were 79.6 and 91.4 mol%, respectively. The optimal catalyst was the one prepared by the CP method with the optimal nickel loading of 12.4wt% and an optimal aluminum composition of 42.5 wt%.

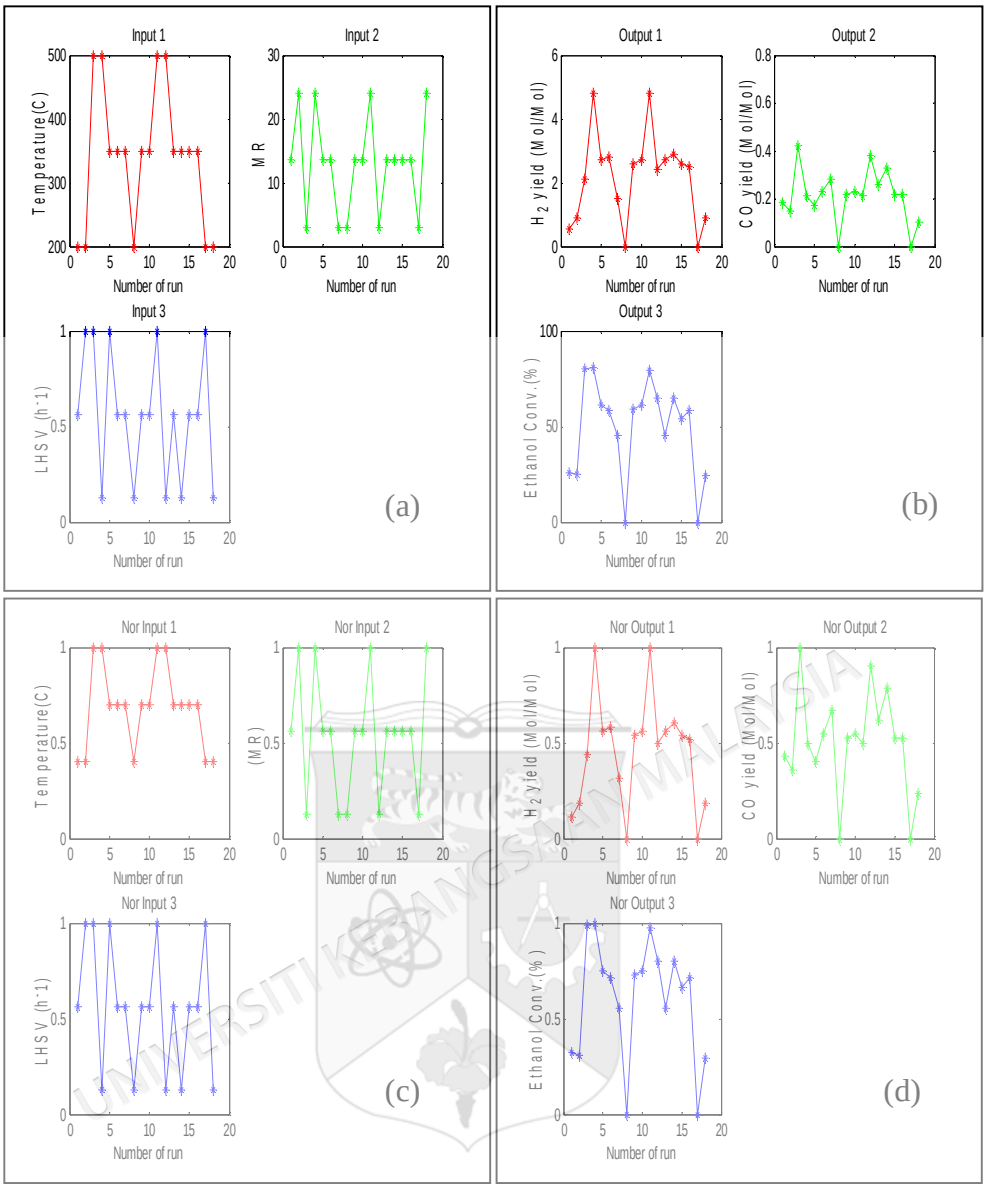

Figure 4.49 a) Input data before normalization, b) Output data before normalization, c) Input data after normalization, d) Output data after normalization

4.9.2 ANN Topology Selection

In order to gain high performance of ANN model, the best ANN tobology have to be obtained (Serra et al. 2003). The training process for the neural network is stopped only when the mean squared error falls below 0.0001 and the neural network have architecture of [5 4 3], [10 4 3], and [15 4 3] with the three deferent algorithms (trainlm, traingdx, and trainscg) are examined at all the trials. Tables 4.17 - 4.22 show the performance to optimize the best ANN design to model the three outputs. The

criteria used to obtain the best ANN design based on efficiency and MSE of each model in the training and testing stage. While other publication used the determination coefficient (R^2), root mean square error analysis (RMSE) and mean squared normalized error (MSE) to evaluate the performance of the ANN (Ninchuewong et al. 2013). As it seen, models were trained using different training algorithm with different number of nodes in the input layer. It was found that using of 5 neurons in the input layer, 4 neurons in the hidden layer, and 3 neurons in the output layer using trainlm as a training algorithm (shown in bold type) provided minimum average MSE (0.0073) of the three outputs in the testing stage and highest average efficiency (0.903) of the three outputs, the performance of the neural network valid when dealing with new data.

Table 4.17 ANN Design using *Trianlm* algorithm in training stage

Neurons per layer	Training stage					
	Mean square error (MSE)			Efficiency		
	H_2	CO	ETOH	H_2	CO	ETOH
Trainlm[5 4 3]*	**0.00047**	**0.00045**	**0.0047**	**0.9947**	**0.9944**	**0.9947**
Trainlm[10 4 3]	0.0038	0.00046	0.00038	0.9953	0.9942	0.9953
Trainlm[15 4 3]	0.00017	0.00075	0.00017	0.9979	0.9907	0.9979

Table 4.18 ANN Design using *Trianscg* algorithm in training stage

Neurons per layer	Training stage					
	Mean square error (MSE)			Efficiency		
	H_2	CO	ETOH	H_2	CO	ETOH
Trainscg [5 4 3]	0.00052	0.00071	0.00052	0.9935	0.9911	0.9935
Trainscg[10 4 3]	0.00047	0.00063	0.00047	0.99417	0.9922	0.9941
Trainscg [15 4 3]	0.00053	0.00058	0.00053	0.9934	0.9928	0.9934

Table 4.19 ANN Design using *Triangdx* algorithm in training stage

Neurons per layer	Training stage					
	Mean square error (MSE)			Efficiency		
	H_2	CO	ETOH	H_2	CO	ETOH
Traingdx [5 4 3]	0.0251	0.0323	0.02518	0.6911	0.6035	0.6911
Traingdx [10 4 3]	0.0284	0.0354	0.0284	0.65166	0.5656	0.65166
Traingdx [15 4 3]	0.0081	0.0082	0.00812	0.9002	0.8993	0.90029

Table 4.20 ANN Design using *Trianlm* algorithm in testing stage

Neurons per layer	Testing stage					
	Mean square error (MSE)			Efficiency		
	H_2	CO	ETOH	H_2	CO	ETOH
Trainlm[5 4 3]*	**0.00705**	**0.011**	**0.00387**	**0.9146**	**0.8410**	**0.9546**
Trainlm[10 4 3]	0.0122	0.0092	0.0077	0.8518	0.8664	0.9091
Trainlm[15 4 3]	0.01495	0.00408	0.00976	0.8189	0.9411	0.8859

Table 4.21 ANN Design using *Trianscg* algorithm in testing stage

Neurons per layer	Testing stage					
	Mean square error (MSE)			Efficiency		
	H_2	CO	ETOH	H_2	CO	ETOH
Trainscg [5 4 3]	0.0134	0.00586	0.0079	0.8372	0.9155	0.9065
Trainscg[10 4 3]	0.01439	0.00907	0.00925	0.8257	0.8693	0.8918
Trainscg [15 4 3]	0.0141	0.00327	0.0079	0.8292	0.9528	0.9076

Table 4.22 ANN Design using *Triangdx* algorithm in testing stage

Neurons per layer	Testing stage					
	Mean square error (MSE)			Efficiency		
	H_2	CO	ETOH	H_2	CO	ETOH
Traingdx [5 4 3]	0.0319	0.02919	0.03218	0.61307	0.5797	0.6239
Traingdx [10 4 3]	0.0306	0.0457	0.01995	0.6286	0.34107	0.7668
Traingdx [15 4 3]	0.0076	0.0173	0.00913	0.9070	0.7498	0.8932

4.9.3 Training Stage

After selection of the best ANN topology, all the training procedure of the ANN was empirically set with maximum Mean -Squared Error (MSE) at 10e-3. The training process was carried out of 10000 epochs. A three-layer back-propagation neural network was built by using the MATLAB Version 7.11.0.584 (R2010b) neural network toolbox to predict the three outputs (H_2 yield, CO yield, and Ethanol conversion). The performance of the ANN is evaluated by the mean square error (MSE) and the efficiency, which show the accuracy of the target output toward the predicted output by the trained ANN (Draper & Smith 1998). By trial and error, an architecture consisting with 5 nodes in the input layer, 4 nodes in the middle layer, and 3 nodes in the output layer was found to provide good performance. The transfer function used for all nodes was a log-sigmoidal transfer function 'logsig', and to train the neural network 'trainlm' were selected as indicted in the above table (Table 4.17).

a) Data prior training

Here, in total of 16 samples at each input (Temperature, molar ratio, and LHSV) present as the full set of input samples are passed through the neural network prior to training to recognize the outputs. Note that the neural network does not match the desired targets very well as we can see in the Fig 4.50. The blue colour specifies the target plot and the red colour specify the neural network.

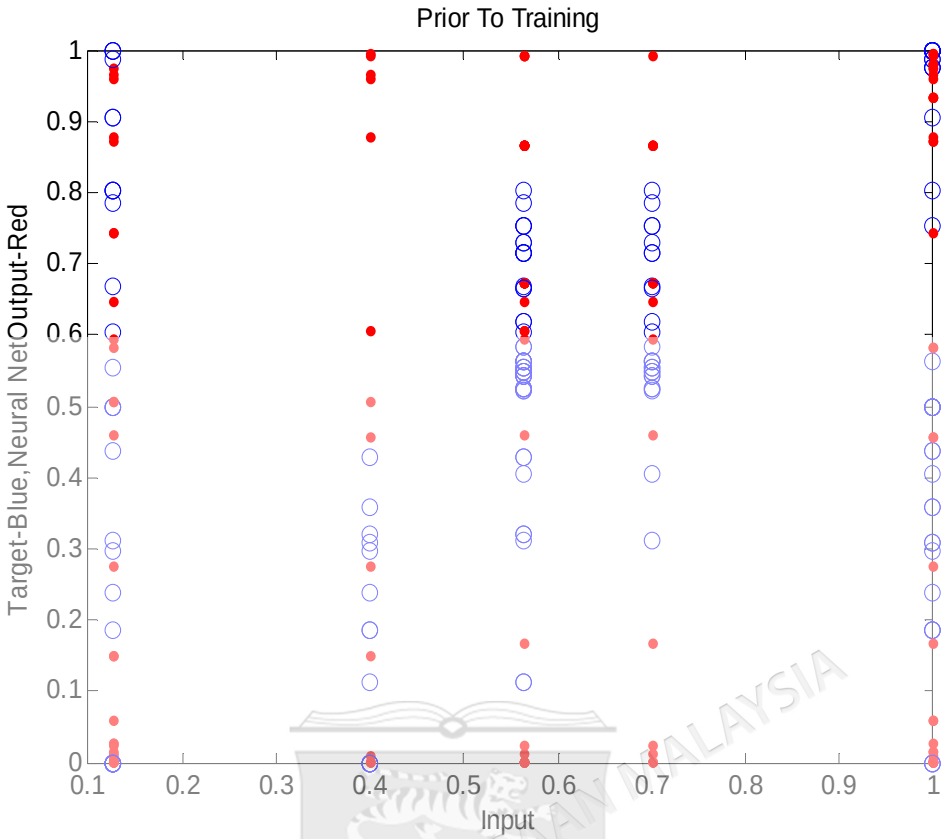

Figure 4.50 Dataset distributions before training the ANN model

b) Training error

The full set of input samples was passed through the neural network to compute the mean squared error function. Each such pass is called epoch**,** and it can be can seen graphically, at 47 epochs reach the goal of error (10^{-3}) with the performance 0.00096. The training took 4.8270 second to reach the error. The error is calculated by subtracting the output from input. Furthermore, the linear training regression (R= 0.99414) is obtained between the network outputs and the corresponding targets during the training stage as shown in Figure 4.51. .

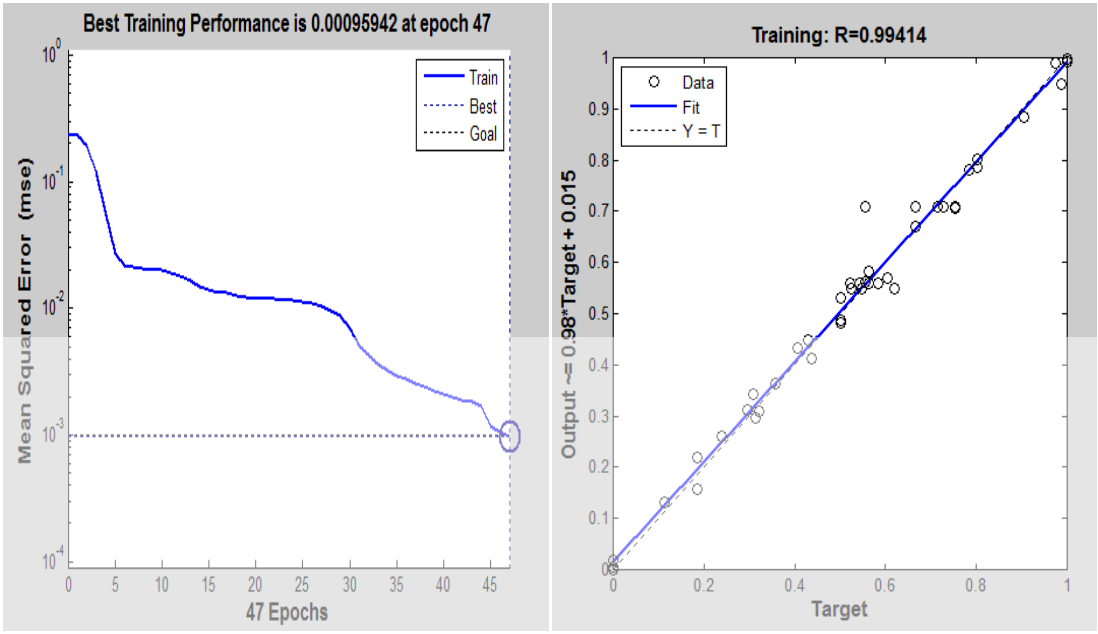

Figure 4.51 Iterations curve and linear regression analysis between the network outputs and the corresponding targets during training stage

c) Neural network output versus targets

After some training we see the network performs very well. Where, the neural network output versus targets match perfectly as shown in Figure 4.52.

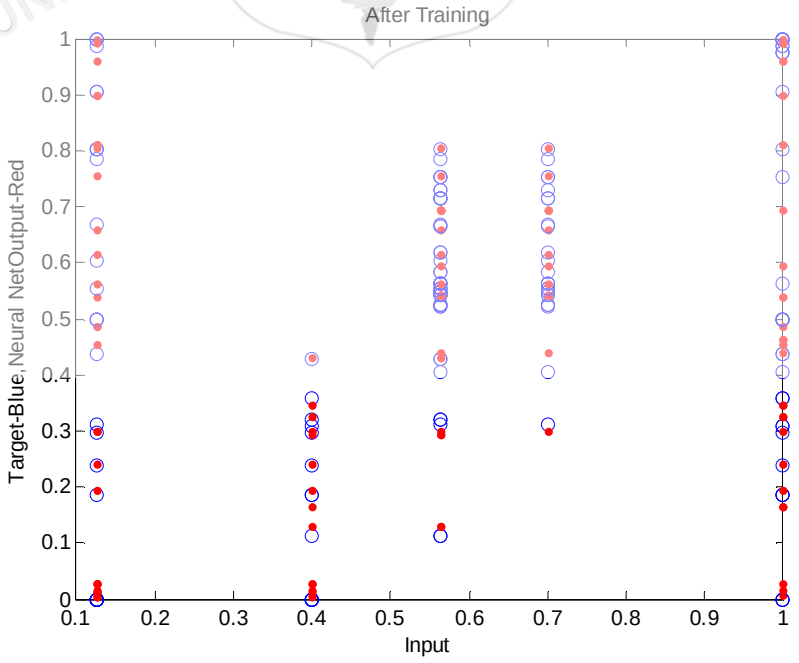

Figure 4.52 Dataset distributions after training the ANN model

4.9.4 Testing Stage

Here, in total of 20 samples entire training/testing, ANN back propagation with topology [5 4 3] and trainlm was used to the accuracy of each output. Figure 4.53 shows the experimental value versus predicted values from neural network model developed. The simulation data results are summarized in Appendix E.

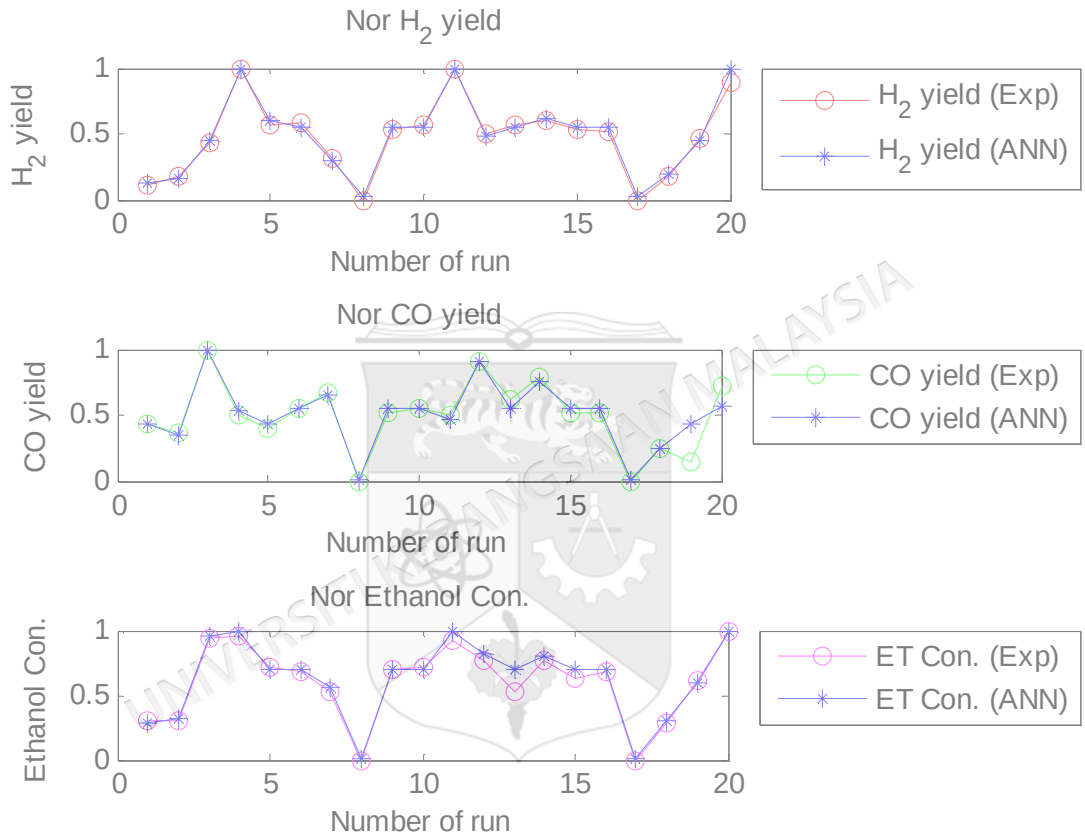

Figure 4.53 ANN predicted and observed data for the three outputs

It is clearly shown from Figure above that developed model can represent the process to predict the outputs (H_2, CO, and ethanol conversion) quite satisfactorily, with model efficiency higher than 0.90 and MSE lower than 0.0045 as shown in Table 4.23. MSE obtained in this studt was lower comparing with similar study conducted to design an optimum Ni/Al_2O_3 catalyst for the production of hydrogen (Akande et al. 2005), and that is a sign for a good performance of the ANN in this study.

Table 4.23 MSE and efficiency value examined in the testing stage

Outputs	MSE	Efficiency
H_2	0.00293	0.9645
CO	0.00437	0.937
ETOH Conv.	0.00278	0.9675

4.9.5 Experimental versus ANN and Numerical (DOE) Models

Figures 4.54 show the experimental value versus predicted value from numerical model and ANN developed model. It is clearly shown that both developed models can represent the process quite satisfactorily because both model approaches, efficiency coefficients were high. However, the neural network efficiency for neural network was slightly higher than numerical model. This measurement result is summarized in Table E-2 (Appendix E), where all the values of the experimental and the predicted models values are recorded. Appendix H explain the system prototype design and its constructed to facilitate the user prediction of the H_2 yield, CO yield, and ethanol conversion and via ethanol steam reforming. It can be conclude that, Empirical modelling and ANN modelling can be used to represent this reaction. However, ANN modelling is slightly more appropriate in predicting the output than empirical modelling. This result was in a good agreement with other published data to investigate carbon dioxide reforming of methane to syngas using response surface methodology and artificial neural network (Saidina Amin et al. 2012).

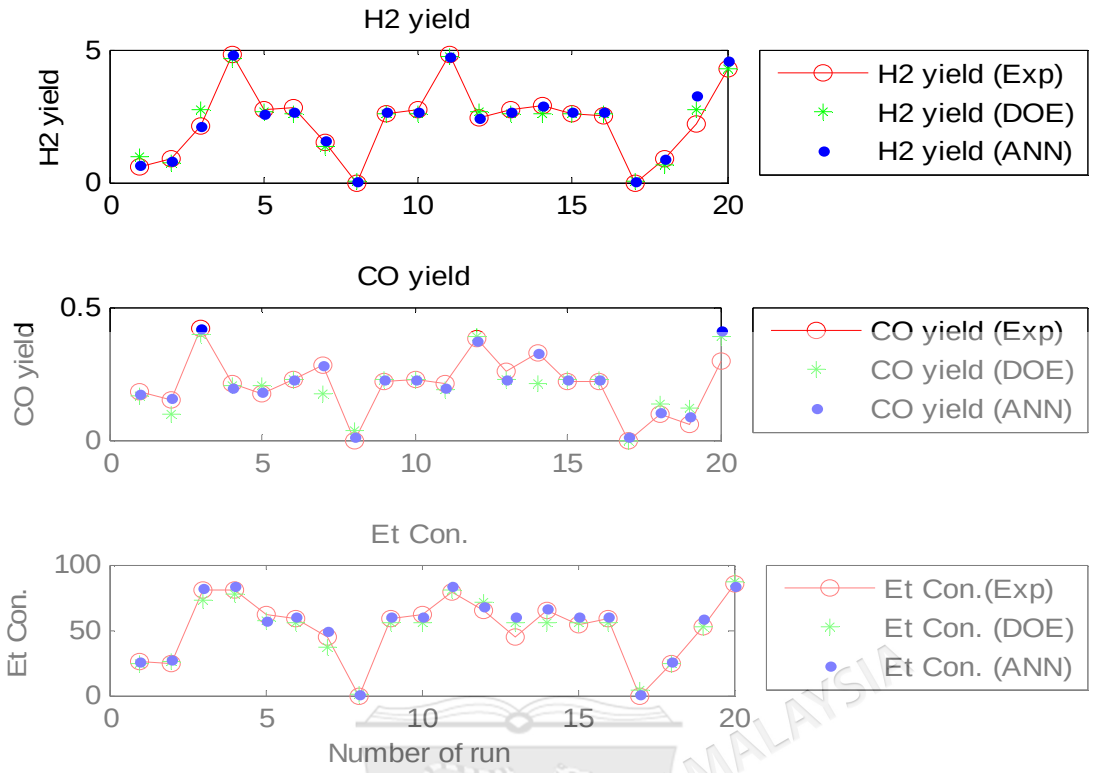

Figure 4.54 Eexperimental values of the outputs versus both ANN and numerical (DOE) model predicted values

CHAPTER V

CONCLUSIONS AND RECOMMENDATIONS

5.1 CONCLUSIONS

This work presented the practicality of catalytic ethanol reforming for H_2 production using Ni/Al_2O_3 as a catalyst. Before reforming reaction, thermodynamic equilibrium analysis was performed in the following variable ranges: pressure, 1 atm to 50 atm; temperature, 300 K to 900 K; and water-to-ethanol feed ratio, 3:1 to 12:1. Thermodynamic results show that ethanol conversion can be completed for temperatures equal to or higher than 600 K at any value of pressure and molar ratio. Conditions of high temperature, high ethanol-to-water molar feed ratio, and low pressure are preferred for H_2 production. By contrast, CH_4 formation is favored at low ethanol-to-water molar feed ratio, low temperature, and high pressure. Thermodynamic CO formation is favored at high temperature, low ethanol-to-water molar feed ratio, and low pressure. To conclude, thermodynamic analysis indicates an advantage of conducting ethanol reforming at high temperature and high ethanol-to-water molar feed ratio because of the high level of H_2 formed; these conditions lead to an increase in energy requirement.

A catalyst study was performed to investigate the performance of Ni as an active metal supported by γ-Al_2O_3. Two series of catalysts with various Ni loadings (6, 8, 10, 12, and 20 wt%) were prepared by impregnation (IMP) and precipitation (PT) methods and were tested in ethanol-reforming reaction. The catalysts in both methods exhibited only NiO species as evidenced from the XRD and TPR patterns. The increase of Ni content in both methods leads to a decrease in the surface area of the catalyst and poor dispersion of the Ni species over the Al_2O_3 support. High Ni

loading leads to the formation of large particles that can cause partial blockage of pores on the support and limit the active sites available for steam reforming. For both synthesis methods, ethanol conversion did not vary significantly with changes in Ni loading. Based on the H_2 yield, the lowest metal loading (6 wt%) resulted in the best performance in the catalysts prepared by both methods. The best system, 6 PT, yielded the highest amount of H_2 and was accompanied by a low CO/CO_2 ratio, as well as stable activity for a continuous period of 8 hr. These results were attributed to the small crystallite size present in catalysts of low Ni loading, which facilitates the high, uniform dispersion of the metal particles on the support surface. Although the CO selectivity was insignificantly changed with Ni loading for both methods, the amount of CO in the PT-synthesized catalysts was lower than the CO values in the IMP-synthesized catalysts, indicating that preparation method has greater effect on CO selectivity than Ni loading. High water-to-ethanol molar ratios enhance the conversion of CO to CO_2 through the water–gas shift reaction, but a very high water-to-ethanol molar ratio is not recommended because energy is needed to evaporate the water. In addition, the increase in LHSV within the range from 0.1 h^{-1} to 1 h^{-1} resulted in the decrease of both ethanol conversion and H_2 selectivity and an increase in CO selectivity.

Sol-gel-made alumina supports were prepared in our laboratory for Ni catalysts and were calcined at different temperatures. A series of Ni/AlS.G. catalysts was synthesized by an impregnation procedure and then tested for H_2 production via ethanol steam reforming. The physical properties of sol-gel-made alumina supports were significantly influenced by the calcination temperature. The structure of AlS.G. was converted from γ-alumina (from 600 °C to 800 °C) to a mixed phase between γ- and θ-alumina (at 900 °C) and then to θ-alumina (at 1,000 °C). The influence of calcination temperature of the AlS.G. supports on the activity of the Ni/AlS.G. catalysts was also studied. The increase in both ethanol conversion and H_2 yield was organized in the following order: $Ni/Al_{S.G800}$>$Ni/Al_{s.G900}$>$Ni/Al_{S.G700}$> $Ni/Al_{S.G600}$> $Ni/Al_{S.G1000}$. $Ni/Al_{S.G800}$ exhibited the best catalyst activity in terms of H_2 yield and ethanol conversion. The strong metal–support interaction of the $Ni/Al_{S.G800}$ catalyst enhanced the dispersion and surface area of Ni while reducing the mean particle size values, thereby resulting in high catalytic performance in terms of H_2 yield.

Statistical approach using response surface methodology and central composite design were employed to optimize the process variables. The H_2 yield, ethanol gasification, and CO yield were optimized, and the effects of temperature, water-to-ethanol molar ratio, and liquid hourly space velocity variations as independent variables were analyzed through statistical analysis. A second-order polynomial model was used to verify the linear and quadratic effects of the process variables and their linear and quadratic interaction. The interaction and quadratic terms had a lower effect than the linear terms. According to the reduced models, temperature and water-to-ethanol molar ratio significantly affect the responses. The optimum values for the independent variables were as follows: temperature = 500 °C, water-to-ethanol molar ratio = 20 and liquid hourly space velocity = 0.72 h^{-1}. These conditions result in an ethanol gasification rate of 85%, an H_2 yield of 4.7 mol/mol of ethanol, and CO yield of 0.25 mol/mol of ethanol.

An integrated system capable of predicting H_2 yield, ethanol conversion, and CO yield was developed using a multilayer ANN model. Experimental data used to build the ANN model were similar to the data used in the statistical approach. The study considered the effect of temperature, water-to-ethanol molar ratio, and LHSV as ANN inputs on H_2 yield, ethanol gasification, and CO yield as outputs. The performance of the ANN model was verified, demonstrating the effectiveness with a significant efficiency of 0.91, 0.84, and 0.95 for H_2, CO, and ethanol, respectively. A comparison of the ANN model with the statistical model showed that the ANN model provides a slightly better fit to the experimental data.

5.2 RECOMMENDATIONS

Recommendations on the study of ethanol steam forming for future work are listed as follows.

1) Modification of catalyst support by using Al_2O_3-ZrO_2 mixed oxides should be investigated; this is because ZrO_2 enhance the coking resistance and increase

the active nickel surface area, resulting in high catalytic performance steam reforming reaction.

2) Evaluation of catalyst durability for longer duration tests under steam reforming conditions should be attempted.

3) Crude ethanol produced from fermentation process should be tested because the water content in the bio-ethanol is within the water-to-ethanol molar ratio range used in literature. In addition, other organic compounds may accompany the bio-ethanol in the fermentation broth (such as maltose and lactic acid). Fuels other than ethanol should be analyzed as well, for example, glycerol, which is a by-product from biodiesel production.

4) Optimization of process variables should be studied in a wider range to develop a model capable of predicting H_2 more accurately and efficiently.

5) Genetic algorithm, a powerful optimization algorithm with the ANN model, is required to optimize process variables in further studies.

REFERENCES

Adhikari, S., Fernando, S., Gwaltney, S. R., Filip To, S. D., Mark Bricka, R., Steele, P. H. & Haryanto, A. 2007. A thermodynamic analysis of hydrogen production by steam reforming of glycerol. *International Journal of Hydrogen Energy* 32(14): 2875-2880.

Adib, H., Haghbakhsh, R., Saidi, M., Takassi, M. A., Sharifi, F., Koolivand, M., Rahimpour, M. R. & Keshtkari, S. 2013. Modeling and optimization of Fischer–Tropsch synthesis in the presence of Co (III)/Al_2O_3 catalyst using artificial neural networks and genetic algorithm. *Journal of Natural Gas Science and Engineering* 10(0): 14-24.

Ahari, J. S., Sadeghi, M. T. & Pashne, S. Z. 2011. Optimization of OCM reaction conditions over Na–W–Mn/SiO_2 catalyst at elevated pressure. *Journal of the Taiwan Institute of Chemical Engineers* 42(5): 751-759.

Akande, A. J., Idem, R. O. & Dalai, A. K. 2005. Synthesis, characterization and performance evaluation of Ni/Al_2O_3 catalysts for reforming of crude ethanol for hydrogen production. *Applied Catalysis A: General* 287(2): 159-175.

Alamolhoda, S., Kazemeini, M., Zaherian, A. & Zakerinasab, M. R. 2012. Reaction kinetics determination and neural networks modeling of methanol dehydration over nano γ-Al_2O_3 catalyst. *Journal of Industrial and Engineering Chemistry* 18(6): 2059-2068.

Alberton, A. L., Souza, M. M. V. M. & Schmal, M. 2007b. Carbon formation and its influence on ethanol steam reforming over Ni/Al_2O_3 catalysts. *Catalysis Today* 123(1-4): 257-264.

Aupretre, Fabien Descorme, Claude Duprez & Daniel. 2001. Catalytic steam reforming : Use for on-board hydrogen production from hydrocarbons or alcohols. *Annales de Chimie Science des Matériaux* 26(4): 93-106.

Aupretre, Fabien Descorme, Claude Duprez, Daniel Casanave, Dominique Uzio & Denis. 2005. Ethanol steam reforming over $Mg_xNi_{1-x}Al_2O_3$ spinel oxide-supported Rh catalysts. *Journal of Catalysis* 233(2): 464-477.

Auprêtre, F., Descorme, C. & Duprez, D. 2002. Bio-ethanol catalytic steam reforming over supported metal catalysts. *Catalysis Communications* 3(6): 263-267.

Aupretre, F., Descorme, C. & Duprez, D. 2004. Hydrogen production for fuel cells from the catalytic ethanol steam reforming. *Topics in Catalysis* 30-31: 487-492.

Bao, L. & Intille, S. 2004. Activity Recognition from User-Annotated Acceleration Data

Pervasive Computing. Dlm. Ferscha, A. & Mattern, F. (pnyt.). 3001. hlm. 1-17. Springer Berlin / Heidelberg.

Batista, M. S., Santos, R. K. S., Assaf, E. M., Assaf, J. M. & Ticianelli, E. A. 2003. Characterization of the activity and stability of supported cobalt catalysts for the steam reforming of ethanol. *Journal of Power Sources* 124(1): 99-103.

Batista, M. S., Santos, R. K. S., Assaf, E. M., Assaf, J. M. & Ticianelli, E. A. 2004. High efficiency steam reforming of ethanol by cobalt-based catalysts. *Journal of Power Sources* 134(1): 27-32.

Benito, M., Padilla, R., Rodríguez, L., Sanz, J. L. & Daza, L. 2007. Zirconia supported catalysts for bioethanol steam reforming: Effect of active phase and zirconia structure. *Journal of Power Sources* 169(1): 167-176.

Benito, M., Sanz, J. L., Isabel, R., Padilla, R., Arjona, R. & Daza, L. 2005. Bio-ethanol steam reforming: Insights on the mechanism for hydrogen production. *Journal of Power Sources* 151: 11-17.

Bergamaschi, V. S. & Carvalho, F. M. S. 2008. Hydrogen production by ethanol steam reforming over Cu and Ni catalysts supported on ZrO_2 and Al_2O_3 microspheres. Materials Science Forum. 591-593**:** 734-739.

Biswas, P. & Kunzru, D. 2007. Steam reforming of ethanol for production of hydrogen over Ni/CeO–ZrO catalyst: Effect of support and metal loading. *International Journal of Hydrogen Energy* 32(8): 969-980.

Breen, J. P., Burch, R. & Coleman, H. M. 2002. Metal-catalysed steam reforming of ethanol in the production of hydrogen for fuel cell applications. *Applied Catalysis B: Environmental* 39(1): 65-74.

Burtin, P., Brunelle, J. P., Pijolat, M. & Soustelle, M. 1987a. Influence of surface area and additives on the thermal stability of transition alumina catalyst supports. I: Kinetic data. *Applied Catalysis* 34(0): 225-238.

Burtin, P., Brunelle, J. P., Pijolat, M. & Soustelle, M. 1987b. Influence of surface area and additives on the thermal stability of transition alumina catalyst supports. II: Kinetic model and interpretation. *Applied Catalysis* 34(0): 239-254.

Casanovas, A., Roig, M., de Leitenburg, C., Trovarelli, A. & Llorca, J. 2010. Ethanol steam reforming and water gas shift over Co/ZnO catalytic honeycombs doped with Fe, Ni, Cu, Cr and Na. *International Journal of Hydrogen Energy* 35(15): 7690-7698.

Cavallaro, S., Chiodo, V., Freni, S., Mondello, N. & Frusteri, F. 2003. Performance of Rh/Al_2O_3 catalyst in the steam reforming of ethanol: H_2 production for MCFC. *Applied Catalysis A: General* 249(1): 119-128.

Cavallaro, S. & Freni, S. 1996. Ethanol steam reforming in a molten carbonate fuel cell. A preliminary kinetic investigation. *International Journal of Hydrogen Energy* 21(6): 465-469.

Chang, F.-W., Yang, H.-C., Roselin, L. S. & Kuo, W.-Y. 2006. Ethanol dehydrogenation over copper catalysts on rice husk ash prepared by ion exchange. *Applied Catalysis A: General* 304: 30-39.

Chary, K. V. R., Ramana Rao, P. V. & Venkat Rao, V. 2008. Catalytic functionalities of nickel supported on different polymorphs of alumina. *Catalysis Communications* 9(5): 886-893.

Chen, H., Zhang, T., Dou, B., Dupont, V., Williams, P., Ghadiri, M. & Ding, Y. 2009. Thermodynamic analyses of adsorption-enhanced steam reforming of glycerol for hydrogen production. *International Journal of Hydrogen Energy* 34(17): 7208-7222.

Chen, M.-N., Zhang, D.-Y., Thompson, L. T. & Ma, Z.-F. 2011. Catalytic properties of Ag promoted ZnO/Al_2O_3 catalysts for hydrogen production by steam reforming of ethanol. *International Journal of Hydrogen Energy* 36(13): 7516-7522.

Coleman, L. J. I., Epling, W., Hudgins, R. R. & Croiset, E. 2009. Ni/Mg-Al mixed oxide catalyst for the steam reforming of ethanol. *Applied Catalysis A: General* 363(1-2): 52-63.

Comas, J., Laborde, M. & Amadeo, N. 2004. Thermodynamic analysis of hydrogen production from ethanol using CaO as a CO_2 sorbent. *Journal of Power Sources* 138(1–2): 61-67.

de la Peña O'Shea, V. A., Homs, N., Pereira, E. B., Nafria, R. & Ramírez de la Piscina, P. 2007. X-ray diffraction study of Co_3O_4 activation under ethanol steam-reforming. *Catalysis Today* 126(1-2): 148-152.

Descorme, C., Madier, Y., Duprez, D. & Birchem, T. 2000. Surface mobility of oxygen species on mixed-oxides supported metals. Dlm. (pnyt.). Volume 130, Part 1. hlm. 347-352. Elsevier.

Diagne, C., Idriss, H. & Kiennemann, A. 2002. Hydrogen production by ethanol reforming over Rh/CeO_2-ZrO_2 catalysts. *Catalysis Communications* 3(12): 565-571.

Draper, N. R. & Smith, H. 1998. Applied regression analysis (wiley series in probability and statistics).

Dubey, P. K., Sinha, A. S. K., Talapatra, S., Koratkar, N., Ajayan, P. M. & Srivastava, O. N. 2010. Hydrogen generation by water electrolysis using carbon nanotube anode. *International Journal of Hydrogen Energy* 35(9): 3945-3950.

Erdohelyi, A., Raskó, J., Kecskés, T., Tóth, M., Dömök, M. & Baán, K. 2006. Hydrogen formation in ethanol reforming on supported noble metal catalysts. *Catalysis Today* 116(3): 367-376.

Erhan Aksoylu, A. & İlsenÖnsan, Z. 1997. Hydrogenation of carbon oxides using coprecipitated and impregnated Ni/Al_2O_3 catalysts. *Applied Catalysis A: General* 164(1): 1-11.

Fatsikostas, A. N., Kondarides, D. I. & Verykios, X. E. 2002b. Production of hydrogen for fuel cells by reformation of biomass-derived ethanol. *Catalysis Today* 75(1–4): 145-155.

Fatsikostas, A. N. & Verykios, X. E. 2004. Reaction network of steam reforming of ethanol over Ni-based catalysts. *Journal of Catalysis* 225(2): 439-452.

Fierro, V., Klouz, V., Akdim, O. & Mirodatos, C. 2002. Oxidative reforming of biomass derived ethanol for hydrogen production in fuel cell applications. *Catalysis Today* 75(1-4): 141-144.

Fishtik, I., Alexander, A., Datta, R. & Geana, D. 2000. A thermodynamic analysis of hydrogen production by steam reforming of ethanol via response reactions. *International Journal of Hydrogen Energy* 25(1): 31-45.

Freni, S., Cavallaro, S., Mondello, N., Spadaro, L. & Frusteri, F. 2002. Steam reforming of ethanol on Ni/MgO catalysts: H_2 production for MCFC. *Journal of Power Sources* 108(1-2): 53-57.

Freni, S., Cavallaro, S., Mondello, N., Spadaro, L. & Frusteri, F. 2003. Production of hydrogen for MC fuel cell by steam reforming of ethanol over MgO supported Ni and Co catalysts. *Catalysis Communications* 4(6): 259-268.

Freni, S., Maggio, G. & Cavallaro, S. 1996. Ethanol steam reforming in a molten carbonate fuel cell: a thermodynamic approach. *Journal of Power Sources* 62(1): 67-73.

Frišták, V., Remenárová, L. & Lesný, J. 2012. Response surface methodology as optimization tool in study of competitive effect of Ca^{2+} and Mg^{2+} ions in sorption process of Co^{2+} by dried activated sludge. *Journal of Microbiology, Biotechnology and Food Sciences* 1(5): 1235-1249.

Frusteri, F., Freni, S., Chiodo, V., Spadaro, L., Di Blasi, O., Bonura, G. & Cavallaro, S. 2004a. Steam reforming of bio-ethanol on alkali-doped Ni/MgO catalysts: hydrogen production for MC fuel cell. *Applied Catalysis A: General* 270(1-2): 1-7.

Frusteri, F., Freni, S., Spadaro, L., Chiodo, V., Bonura, G., Donato, S. & Cavallaro, S. 2004b. H2 production for MC fuel cell by steam reforming of ethanol over MgO supported Pd, Rh, Ni and Co catalysts. *Catalysis Communications* 5(10): 611-615.

Galetti, A. E., Gomez, M. F., Arrua, L. A., Marchi, A. J. & Abello, M. C. 2008. Study of CuCoZnAl oxide as catalyst for the hydrogen production from ethanol reforming. *Catalysis Communications* 9(6): 1201-1208.

García, E. Y. & Laborde, M. A. 1991. Hydrogen production by the steam reforming of ethanol: Thermodynamic analysis. *International Journal of Hydrogen Energy* 16(5): 307-312.

Ghafari, S., Aziz, H. A., Isa, M. H. & Zinatizadeh, A. A. 2009. Application of response surface methodology (RSM) to optimize coagulation–flocculation treatment of leachate using poly-aluminum chloride (PAC) and alum. *Journal of Hazardous Materials* 163(2–3): 650-656.

Günay, M. E., Akpinar, F., Onsan, Z. I. & Yildirim, R. 2012. Investigation of water gas-shift activity of Pt–MOx–CeO2/Al2O3 (M = K, Ni, Co) using modular artificial neural networks. *International Journal of Hydrogen Energy* 37(3): 2094-2102.

Günay, M. E. & Yildirim, R. 2010. Analysis of selective CO oxidation over promoted Pt/Al_2O_3 catalysts using modular neural networks: Combining preparation and operational variables. *Applied Catalysis A: General* 377(1–2): 174-180.

Günay, M. E. & Yildirim, R. 2013a. Developing global reaction rate model for CO oxidation over Au catalysts from past data in literature using artificial neural networks. *Applied Catalysis A: General* 468(0): 395-402.

Günay, M. E. & Yildirim, R. 2013b. Modeling preferential CO oxidation over promoted Au/Al_2O_3 catalysts using decision trees and modular neural networks. *Chemical Engineering Research and Design* 91(5): 874-882.

Hernández, I. P., Gochi-Ponce, Y., Contreras Larios, J. L. & Fernández, A. M. 2010. Steam reforming of ethanol over nickel-tungsten catalyst. *International Journal of Hydrogen Energy* 35(21): 12098-12104.

Holeňa, M. & Baerns, M. 2003. Feedforward neural networks in catalysis: A tool for the approximation of the dependency of yield on catalyst composition, and for knowledge extraction. *Catalysis Today* 81(3): 485-494.

Huang, C.-Y., Chen, L.-H., Chen, Y.-L. & Chang, F. M. 2009. Evaluating the process of a genetic algorithm to improve the back-propagation network: A Monte Carlo study. *Expert Systems with Applications* 36(2, Part 1): 1459-1465.

Huang, K., Zhan, X.-L., Chen, F.-Q. & Lü, D.-W. 2003. Catalyst design for methane oxidative coupling by using artificial neural network and hybrid genetic algorithm. *Chemical Engineering Science* 58(1): 81-87.

Idriss, H. 2004. Ethanol reactions over the surfaces of noble metal/cerium oxide catalysts. *Platinum Metals Review* 48(3): 105-115.

Ioannides, T. 2001. Thermodynamic analysis of ethanol processors for fuel cell applications. *Journal of Power Sources* 92(1-2): 17-25.

Izadkhah, B., Nabavi, S. R., Niaei, A., Salari, D., Mahmuodi Badiki, T. & Çaylak, N. 2012. Design and optimization of Bi-metallic Ag-ZSM5 catalysts for catalytic oxidation of volatile organic compounds. *Journal of Industrial and Engineering Chemistry* 18(6): 2083-2091.

Kaddouri, A. & Mazzocchia, C. 2004. A study of the influence of the synthesis conditions upon the catalytic properties of Co/SiO_2 or Co/Al_2O_3 catalysts used for ethanol steam reforming. *Catalysis Communications* 5(6): 339-345.

Kamarudin, S. K., Daud, W. R. W., Yaakub, Z., Misron, Z., Anuar, W. & Yusuf, N. N. A. N. 2009. Synthesis and optimization of future hydrogen energy infrastructure planning in Peninsular Malaysia. *International Journal of Hydrogen Energy* 34(5): 2077-2088.

Kandananond, K. 2010. Using the response surface method to optimize the turning process of AISI 12L14 steel. *Advances in Mechanical Engineering* 2010: 1-6.

Khajeh-Hosseini-Dalasm, N., Ahadian, S., Fushinobu, K., Okazaki, K. & Kawazoe, Y. 2011. Prediction and analysis of the cathode catalyst layer performance of proton exchange membrane fuel cells using artificial neural network and statistical methods. *Journal of Power Sources* 196(8): 3750-3756.

Klouz, V., Fierro, V., Denton, P., Katz, H., Lisse, J. P., Bouvot-Mauduit, S. & Mirodatos, C. 2002. Ethanol reforming for hydrogen production in a hybrid electric vehicle: process optimisation. *Journal of Power Sources* 105(1): 26-34.

Kohonen. 2010. Model Extremely Complex Functions, Neural Networks. http://www.statsoft.com/textbook/neural-networks/#index [June 15 2012].

Kong, K. W., Ismail, A., Tan, C. P. & Rajab, N. F. 2010. Optimization of oven drying conditions for lycopene content and lipophilic antioxidant capacity in a by-product of the pink guava puree industry using response surface methodology. *LWT - Food Science and Technology* 43(5): 729-735.

Larentis, A. L., de Resende, N. S., Salim, V. M. M. & Pinto, J. C. 2001. Modeling and optimization of the combined carbon dioxide reforming and partial oxidation of natural gas. *Applied Catalysis A: General* 215(1–2): 211-224.

Le Valant, A., Garron, A., Bion, N., Duprez, D. & Epron, F. 2011. Effect of higher alcohols on the performances of a $1\%Rh/MgAl_2O_4/Al_2O_3$ catalyst for hydrogen production by crude bioethanol steam reforming. *International Journal of Hydrogen Energy* 36(1): 311-318.

Levin, D. B. & Chahine, R. 2010. Challenges for renewable hydrogen production from biomass. *International Journal of Hydrogen Energy* 35(10): 4962-4969.

Li, G., Hu, L. & Hill, J. M. 2006. Comparison of reducibility and stability of alumina-supported Ni catalysts prepared by impregnation and co-precipitation. *Applied Catalysis A: General* 301(1): 16-24.

Li, Z., Hu, X., Zhang, L., Liu, S. & Lu, G. 2012. Steam reforming of acetic acid over Ni/ZrO_2 catalysts: Effects of nickel loading and particle size on product distribution and coke formation. *Applied Catalysis A: General* 417–418(0): 281-289.

Liguras, K., D., Kondarides, D. I. & Verykios, X. E. 2003. Production of hydrogen for fuel cells by steam reforming of ethanol over supported noble metal catalysts. *Applied Catalysis B: Environmental* 43(4): 345-354.

Lin, W.-H., Hsiao, C.-S. & Chang, H.-F. 2008. Effect of oxygen addition on the hydrogen production from ethanol steam reforming in a Pd–Ag membrane reactor. *Journal of Membrane Science* 322(2): 360-367.

Lindo, M., Vizcaíno, A. J., Calles, J. A. & Carrero, A. 2010. Ethanol steam reforming on Ni/Al-SBA-15 catalysts: Effect of the aluminium content. *International Journal of Hydrogen Energy* 35(11): 5895-5901.

Liu, J.-Y., Lee, C.-C., Wang, C.-H., Yeh, C.-T. & Wang, C.-B. 2010. Application of nickel–lanthanum composite oxide on the steam reforming of ethanol to produce hydrogen. *International Journal of Hydrogen Energy* 35(9): 4069-4075.

Llorca, J., Homs, N., Sales, J. & de la Piscina, P. R. 2002. Efficient Production of Hydrogen over Supported Cobalt Catalysts from Ethanol Steam Reforming. *Journal of Catalysis* 209(2): 306-317.

Mas, V., Kipreos, R., Amadeo, N. & Laborde, M. 2006. Thermodynamic analysis of ethanol/water system with the stoichiometric method. *International Journal of Hydrogen Energy* 31(1): 21-28.

Men, Y., Kolb, G., Zapf, R., Hessel, V. & Löwe, H. 2007. Ethanol Steam Reforming in a Microchannel Reactor. *Process Safety and Environmental Protection* 85(5): 413-418.

Mjalli, F. S., Al-Asheh, S. & Alfadala, H. E. 2007. Use of artificial neural network black-box modeling for the prediction of wastewater treatment plants performance. *Journal of Environmental Management* 83(3): 329-338.

Monyanon, S., Luengnaruemitchai, A. & Pongstabodee, S. 2012. Optimization of methanol steam reforming over a $Au/CuO–CeO_2$ catalyst by statistically designed experiments. *Fuel Processing Technology* 96(0): 160-168.

Moradi, G. R., Dehghani, S., Khosravian, F. & Arjmandzadeh, A. 2013. The optimized operational conditions for biodiesel production from soybean oil and application of artificial neural networks for estimation of the biodiesel yield. *Renewable Energy* 50(0): 915-920.

Navarro, R. M., Ã lvarez-Galvan, M. C., Sanchez-Sanchez, M. C., Rosa, F. & Fierro, J. L. G. 2005. Production of hydrogen by oxidative reforming of ethanol over Pt catalysts supported on Al_2O_3 modified with Ce and La. *Applied Catalysis B: Environmental* 55(4): 229-241.

Negrier, F., Marceau, É., Che, M. & de Caro, D. 2003. Role of ethylenediamine in the preparation of alumina-supported Ni catalysts from $[Ni(en)_2(H_2O)_2](NO_3)_2$: from solution properties to nickel particles. *Comptes Rendus Chimie* 6(2): 231-240.

Ni, M. L., Dennis Y. C. Leung & H., M. K. 2007. A review on reforming bio-ethanol for hydrogen production. *International Journal of Hydrogen Energy* 32(15): 3238-3247.

Ninchuewong, T., Tirawanichakul, S. & Tirawanichakul, Y. 2013. Empirical Model and Artificial Neural Network Model Approach for Air Dried Sheets (ADS) Rubber. *Advanced Materials Research* 622: 69-74.

Nishiguchi, T., Matsumoto, T., Kanai, H., Utani, K., Matsumura, Y., Shen, W.-J. & Imamura, S. 2005. Catalytic steam reforming of ethanol to produce hydrogen and acetone. *Applied Catalysis A: General* 279(1-2): 273-277.

Omata, K., Endo, Y., Ishii, H., Masuda, A. & Yamada, M. 2008. Effective additives of Ni/-Al2O3 catalyst at low methane conversion of oxidative reforming for syngas formation. *Applied Catalysis A: General* 351(1): 54-58.

Omata, K., Kobayashi, Y. & Yamada, M. 2005. Artificial neural network-aided development of supported Co catalyst for preferential oxidation of CO in excess hydrogen. *Catalysis Communications* 6(8): 563-567.

Omata, K., Kobayashi, Y. & Yamada, M. 2007. Artificial neural network aided virtual screening of additives to a Co/S_rCO_3 catalyst for preferential oxidation of CO in excess hydrogen. *Catalysis Communications* 8(1): 1-5.

Prins, M. J., Ptasinski, K. J. & Janssen, F. J. J. G. 2005. Exergetic optimisation of a production process of Fischer–Tropsch fuels from biomass. *Fuel Processing Technology* 86(4): 375-389.

Profeti, L. P. R., Dias, J. A. C., Assaf, J. M. & Assaf, E. M. 2009. Hydrogen production by steam reforming of ethanol over Ni-based catalysts promoted with noble metals. *Journal of Power Sources* 190(2): 525-533.

Rabenstein, Gerd Hacker & Viktor. 2008. Hydrogen for fuel cells from ethanol by steam-reforming, partial-oxidation and combined auto-thermal reforming: A thermodynamic analysis. *Journal of Power Sources* 185(2): 1293-1304.

Raskó, J., Hancz, A. & Erdohelyi, A. 2004. Surface species and gas phase products in steam reforming of ethanol on TiO_2 and Rh/TiO_2. *Applied Catalysis A: General* 269(1-2): 13-25.

Resini, C., Concepción Herrera Delgado, M., Presto, S., Alemany, L. J., Riani, P., Marazza, R., Ramis, G. & Busca, G. 2008. Yttria-stabilized zirconia (YSZ) supported Ni-Co alloys (precursor of SOFC anodes) as catalysts for the steam reforming of ethanol. *International Journal of Hydrogen Energy* 33(14): 3728-3735.

Rifkin, J. 2003. *The hydrogen economy: The creation of the worldwide energy web and the redistribution of power on earth*. JP Tarcher.

Roh, H.-S., Jun, K.-W. & Park, S.-E. 2003. Methane-reforming reactions over Ni/Ce-ZrO_2/θ-Al_2O_3 catalysts. *Applied Catalysis A: General* 251(2): 275-283.

Romero-Sarria, F., Vargas, J. C., Roger, A.-C. & Kiennemann, A. 2008. Hydrogen production by steam reforming of ethanol: Study of mixed oxide catalysts $Ce_2Zr_{1.5}Me_{0.5}O_8$: Comparison of Ni/Co and effect of Rh. *Catalysis Today* 133-135: 149-153.

Rossi, C. C. R. S., Alonso, C. G., Antunes, O. A. C., Guirardello, R. & Cardozo-Filho, L. 2009. Thermodynamic analysis of steam reforming of ethanol and glycerine for hydrogen production. *International Journal of Hydrogen Energy* 34(1): 323-332.

Rynkowski, J. M., Paryjczak, T. & Lenik, M. 1993. On the nature of oxidic nickel phases in NiO/γ-Al_2O_3 catalysts. *Applied Catalysis A: General* 106(1): 73-82.

Sadeghzadeh Ahari, J., Sadeghi, M. T., Zarrinpashne, S. & Irandoukht, A. 2013. Optimization of OCM reactions over Na–W–Mn/ SiO_2 catalyst at elevated pressure using artificial neural network and response surface methodology. *Scientia Iranica* 20(3): 617-625.

Sahoo, D. R., Vajpai, S. & Patel, S. P., K. K. 2007. Kinetic modeling of steam reforming of ethanol for the production of hydrogen over Co/Al_2O_3 catalyst. *Chemical Engineering Journal* 125(3): 139-147.

Saidina Amin, N. A., Mohd Yusof, K. & Isha, R. 2012. Carbon Dioxide Reforming of Methane to Syngas: Modeling Using Response Surface Methodology and Artificial Neural Network. *Jurnal Teknologi* 43(1): 15–30.

Sánchez-Sánchez, M. C., Navarro, R. M. & Fierro, J. L. G. 2007. Ethanol steam reforming over – (, La, Zr and Mg) catalysts: Influence of support on the hydrogen production. *International Journal of Hydrogen Energy* 32(10–11): 1462-1471.

Sasikumar, E. & Viruthagiri, T. 2008. Optimization of Process Conditions Using Response Surface Methodology (RSM) for Ethanol Production from Pretreated Sugarcane Bagasse: Kinetics and Modeling. *BioEnergy Research* 1(3-4): 239-247.

Seo, J. G., Youn, M. H., Park, S., Chung, J. S. & Song, I. K. 2009. Hydrogen production by steam reforming of liquefied natural gas (LNG) over Ni/Al_2O_3–ZrO_2 xerogel catalysts: Effect of calcination temperature of Al2O3–ZrO2 xerogel supports. *International Journal of Hydrogen Energy* 34(9): 3755-3763.

Seo, J. G., Youn, M. H., Park, S. & Song, I. K. 2008. Effect of calcination temperature of mesoporous alumina xerogel (AX) supports on hydrogen production by steam reforming of liquefied natural gas (LNG) over Ni/AX catalysts. *International Journal of Hydrogen Energy* 33(24): 7427-7434.

Serra, J. M., Corma, A., Chica, A., Argente, E. & Botti, V. 2003. Can artificial neural networks help the experimentation in catalysis? *Catalysis Today* 81(3): 393-403.

Sharma, B. K., Sharma, M. P., Kumar Roy, S., Kumar, S., Tendulkar, S. B., S. Tambe, S. & Kulkarni, B. D. 1998. Fischer–Tropsch synthesis with $Co/SiO_2–Al_2O_3$ catalyst and steady-state modeling using artificial neural networks. *Fuel* 77(15): 1763-1768.

Song, C. 2003. Overview of hydrogen production options for hydrogen energy development, fuel-cell fuel processing and mitigation of CO_2 emissions. *Proceeding of the Proceedings of 20th International Pittsburgh Coal Conference*, hlm. 15-19.

Song, H., Zhang, L., Watson, R. B., Braden, D. & Ozkan, U. S. 2007. Investigation of bio-ethanol steam reforming over cobalt-based catalysts. *Catalysis Today* 129(3-4): 346-354.

Souza, M. d. M. V. M., Clavé, L., Dubois, V., Perez, C. A. C. & Schmal, M. 2004. Activation of supported nickel catalysts for carbon dioxide reforming of methane. *Applied Catalysis A: General* 272(1–2): 133-139.

Srisiriwat, N., Therdthianwong, S. & Therdthianwong, A. 2009a. Oxidative steam reforming of ethanol over Ni/Al_2O_3 catalysts promoted by CeO_2, ZrO_2 and CeO_2-ZrO_2. *International Journal of Hydrogen Energy* 34(5): 2224-2234.

Srisiriwat, N., Therdthianwong, S. & Therdthianwong, A. 2009b. Oxidative steam reforming of ethanol over Ni/Al_2O_3 catalysts promoted by CeO_2, ZrO_2 and $CeO_2–ZrO_2$. *International Journal of Hydrogen Energy* 34(5): 2224-2234.

Sun, J., Qiu, X.-P., Wu, F. & Zhu, W.-T. 2005. H2 from steam reforming of ethanol at low temperature over Ni/Y_2O_3, Ni/La_2O_3 and Ni/Al_2O_3 catalysts for fuel-cell application. *International Journal of Hydrogen Energy* 30(4): 437-445.

Sun, J., Wang, Y., Li, J., Xiao, G., Zhang, L., Li, H., Cheng, Y., Sun, C., Cheng, Z., Dong, Z. & Chen, L. 2010. H_2 production from stable ethanol steam reforming over catalyst of NiO based on flowerlike CeO_2 microspheres. *International Journal of Hydrogen Energy* 35(7): 3087-3091.

Tanksale, A., Beltramini, J. N. & Lu, G. M. 2010. A review of catalytic hydrogen production processes from biomass. *Renewable and Sustainable Energy Reviews* 14(1): 166-182.

Tsay, M.-T. & Chang, F.-W. 2000. Characterization of rice husk ash-supported nickel catalysts prepared by ion exchange. *Applied Catalysis A: General* 203(1): 15-22.

Umegaki, T., Masuda, A., Omata, K. & Yamada, M. 2008. Development of a high performance Cu-based ternary oxide catalyst for oxidative steam reforming of methanol using an artificial neural network. *Applied Catalysis A: General* 351(2): 210-216.

Vaidya, P. D. & Rodrigues, A. E. 2006. Insight into steam reforming of ethanol to produce hydrogen for fuel cells. *Chemical Engineering Journal* 117(1): 39-49.

Vasudeva, K., Mitra, N., Umasankar, P. & Dhingra, S. C. 1996. Steam reforming of ethanol for hydrogen production: Thermodynamic analysis. *International Journal of Hydrogen Energy* 21(1): 13-18.

Velu, S., Suzuki, K., Vijayaraj, M., Barman, S. & Gopinath, C. S. 2005. In situ XPS investigations of $Cu_{1-x}Ni_xZnAl$-mixed metal oxide catalysts used in the oxidative steam reforming of bio-ethanol. *Applied Catalysis B: Environmental* 55(4): 287-299.

Vizcaíno, A. J., Arena, P., Baronetti, G., Carrero, A., Calles, J. A., Laborde, M. A. & Amadeo, N. 2008. Ethanol steam reforming on Ni/Al_2O_3 catalysts: Effect of Mg addition. *International Journal of Hydrogen Energy* 33(13): 3489-3492.

Wang, H., Wang, X., Li, M., Li, S., Wang, S. & Ma, X. 2009a. Thermodynamic analysis of hydrogen production from glycerol autothermal reforming. *International Journal of Hydrogen Energy* 34(14): 5683-5690.

Wang, Y., Wang, W., Hong, X., Li, Y. & Zhang, Z. 2009b. Yttrium-stabilized zirconia-promoted metallic nickel catalysts for the partial oxidation of methane to hydrogen. *International Journal of Hydrogen Energy* 34(5): 2252-2259.

Wigmans, T. & Moulijn, J. A. 1980. Activity and mechanism of CO methanation on activated carbon-supported nickel. *Journal of the Chemical Society, Chemical Communications* (4): 170-171.

Wu, D., Li, Y., Shi, Y., Fang, Z., Wu, D. & Chang, L. 2002. Effects of the calcination conditions on the mechanical properties of a $PCoMo/Al_2O_3$ hydrotreating catalyst. *Chemical Engineering Science* 57(17): 3495-3504.

Yang, Y., Ma, J. & Wu, F. 2006. Production of hydrogen by steam reforming of ethanol over a Ni/ZnO catalyst. *International Journal of Hydrogen Energy* 31(7): 877-882.

Youn, M. H., Seo, J. G., Cho, K. M., Park, S., Park, D. R., Jung, J. C. & Song, I. K. 2008a. Hydrogen production by auto-thermal reforming of ethanol over nickel catalysts supported on Ce-modified mesoporous zirconia: Effect of Ce/Zr molar ratio. *International Journal of Hydrogen Energy* 33(19): 5052-5059.

Youn, M. H., Seo, J. G., Park, S., Jung, J. C., Park, D. R. & Song, I. K. 2008b. Hydrogen production by auto-thermal reforming of ethanol over Ni catalysts supported on ZrO_2: Effect of preparation method of ZrO_2 support. *International Journal of Hydrogen Energy* 33(24): 7457-7463.

Youn, M. H., Seo, J. G., Park, S., Park, D. R., Jung, J. C., Kim, P. & Song, I. K. 2009. Hydrogen production by auto-thermal reforming of ethanol over Ni-Ti-Zr metal oxide catalysts. *Renewable Energy* 34(3): 731-735.

Zhang, B., Tang, X., Li, Y., Cai, W., Xu, Y. & Shen, W. 2006. Steam reforming of bio-ethanol for the production of hydrogen over ceria-supported Co, Ir and Ni catalysts. *Catalysis Communications* 7(6): 367-372.

Zhang, L., Li, W., Liu, J., Guo, C., Wang, Y. & Zhang, J. 2009. Ethanol steam reforming reactions over $Al_2O_3.SiO_2$-supported Ni–La catalysts. *Fuel* 88(3): 511-518.

Zieliński, J. 1982. Morphology of nickel/alumina catalysts. *Journal of Catalysis* 76(1): 157-163.

Zinoviev, S., Müller-Langer, F., Das , P., Bertero , N., Fornasiero , P., Kaltschmitt , M., Centi , G. & Miertus, S. 2010. Next-Generation Biofuels: Survey of Emerging Technologies and Sustainability Issues. *ChemSusChem* 3(10): 1106-1133.

APPENDIX A
THERMODYNAMIC ANALYSIS

A.1 Thermodynamic Analysis Based on Equilibrium Constant

$$C_2H_5OH + 3H_2O \rightarrow 6H_2 + 2CO_2 \quad \text{(A.1)}$$

Steps for calculation the thermodynamics ethanol conversion for ethanol steam reforming reaction are explained as follow:

Step 1 Calculation the Standard Property Change of the Reaction $\Delta H^O_{298.}$**, and** $\Delta G^O_{298.}$

Firstly is the determination of ΔA, ΔB, ΔC, and ΔD values for the ethanol reforming reaction. All constants, heat formation, and Gibbs formation data are tabulated below.

The meaning of Δ is indicated by the following Equations:

$$\Delta = 6 * (H_2) + 2 * (CO_2) - (C_2H_5OH) - 3 * (H_2O) \quad \text{(A.2)}$$

$$\Delta A = \sum V_i A_i \quad \text{(A.3)}$$

where, V_i is the stoichiometric coefficient, and A_i is a constant for a chemical formula

ΔA = (2*5.46) + (6*3.25) - 3.52 - (3*3.47) = 16.48

ΔB = $-19.72*10^{-3}$

ΔC = $6*10^{-6}$

ΔD = $-2.17*10^{5}$

Values of $\Delta H^O_{298.}$, and $\Delta G^O_{298.}$ are found through the following Equations:

$$\Delta H^O_{298} = \sum Vi\, \Delta H^O_{fprod.} - \sum Vi\, \Delta H^O_{freact.} \quad \text{(A.4)}$$

$$\Delta G^{O}_{298} = \sum Vi\, \Delta G^{O}_{fprod.} - \sum Vi\, \Delta G^{O}_{freact.} \quad \text{(A.5)}$$

Table A.1 Thermodynamic data

Component	A	B*10^3	C*10^6	D*10^{-5}
C_2H_5OH	3.52	20	-6.00	0.00
H_2O	3.47	1.45	0.00	0.12
H_2	3.25	0.42	0.00	.083
CO_2	5.46	1.05	0.00	-1.16

Table A.2 Standard enthalpies and Gibbs energies of formation

Component	ΔH_f, (Jmol^{-1})	ΔG_f, (Jmol^{-1})
C_2H_5OH	-235,100	-168,490
H_2O	-286,000	-237,000
H_2	0.00	0.00
CO_2	-393,509	-394,359

at, T= 700 K, using information in above Tables,

ΔH^{O}_{298} = 306,082 J/mol

ΔG^{O}_{298} = 90,772 J/mol

Step 2 Calculation of Equilibrium Constant (Kp)

The equilibrium constant (Kp) can be calculated as a function of temperature as follow:

$$ln(K_P) = -\frac{\Delta G^{O}}{RT} \quad \text{(A.6)}$$

The term $\frac{\Delta G^{O}}{RT}$ in above equation can be expressed as follow:

$$\frac{\Delta G^{O}}{RT} = \frac{\Delta G^{O}_{298} - \Delta H^{O}_{298}}{RT_O} + \frac{\Delta H^{O}_{298}}{RT} + \frac{1}{T}\int_{T_O}^{T} \frac{\Delta Cp^{o}}{R}\, dT - \int_{T_O}^{T} \frac{\Delta Cp^{o}}{R}\, \frac{dT}{T} \quad \text{(A.7)}$$

The two integrals in Equation (A.7) are calculated based on the following Equations:

$$MCPH = \int_{T_O}^{T} \frac{\Delta Cp^o}{R}\, dT = \Delta A T_O(\tau - 1) + \frac{\Delta B}{2} T_O^2(\tau^2 - 1)\, T_O^3(\tau^3 - 1)\frac{\Delta D}{T_O}\left(\frac{\tau - 1}{\tau}\right) \quad (A.8)$$

$$MCPS = \int_{T_O}^{T} \frac{\Delta Cp^o}{R}\, \frac{dT}{T} = \Delta A ln\tau \left[\Delta B T_O + \left(\Delta C T_O^2 + \frac{\Delta D}{\tau^2 T_O^2}\right)\left(\frac{\tau + 1}{2}\right)\right](\tau - 1) \quad (A.9)$$

The two functions are solved using MATLAB software and their values at all tested temperatures are shown in Table A.3.

at, T = 700 K $\tau = T/T_O$ = 700/298 = 2.3.

Table A.3 Values of functions determined to solve thermodynamic equations

T, K	MCPS	MCPH
300	13.3527	-1.3039
400	11.5828	642.936
500	9.5697	$1.44*10^3$
600	7.7570	$2.1428*10^3$
700	6.0679	$2.739*10^3$
800	4.4717	$3.234*10^3$

at, T = 700 K, $MCPS$ = 6.0679 and $MCPH$ = $2.739*10^3$ were obtained.

Substitution these values into Equation (A.7) for reaction temperature of 700 K and reference temperature of 298 K and solved by MATLAB give,

$\Delta G^O/RT$ = 34.2947, and Kp = $7.834*10^{14}$

Values of $\Delta G^o/RT$, and Kp at different temperatures are listed in Table A. 4.

Table A.4 Gibbs free energy and equilibrium constant at different reaction temperatures

T, K	$\Delta G^O/RT$	Kp
300	-23.1832	$8.5441*10^{-11}$
400	-1.8406	0.1587
500	15.688	$6.51*10^{6}$
600	26.7678	$4.217*10^{11}$
700	34.2947	$7.834*10^{14}$
800	39.6618	$1.678*10^{17}$

Step 3 Calculation of Ethanol Conversion

The appropriate expression is given in Equation (A.10) as follow:

$$\prod_i (y_i \phi_i)^{v_i} = \left(\frac{P}{P_o}\right)^{-v} K_P \quad \text{(A.10)}$$

where, $\emptyset_i$ is the fugacity coefficient of species *i*, y_i is the mole fraction of species *i*, P_o and *P* are the standard and operating pressure, respectively.

Equation (A.10) can be simplified as follow:

$$(y_1\emptyset_1)^{v_1}(y_2\emptyset_2)^{v_2}(y_3\emptyset_3)^{v_3}(y_4\emptyset_4)^{v_4} = \left(\frac{P}{P_O}\right)^{-V} K_P \quad \text{(A.11)}$$

For an ideal mixture $\emptyset_i$ = 1, *P* = 1 bar, Equation (A.11) become as follow:

$$(y_{C2H5OH})^{-1}(y_{H2O})^{-3}(y_{CO2})^{2}(y_{H2})^{6} = (1)^{-4}K_P \quad \text{(A.12)}$$

Further simplified, Equation (4.12) become

$$\frac{(y_{CO2})^{2}(y_{H2})^{6}}{(y_{C2H5OH})^{1}(y_{H2O})^{3}} = (1)^{-4}K_P \quad \text{(A.13)}$$

In order to calculate the mole fraction of the product mixture, Equation (A.14) applied

$$y_i = \frac{n_i o + v_i \varepsilon}{no + v\varepsilon} \tag{A.14}$$

where,

v_i Stoichiometric number of species *i*,

v Total stoichometric of all species,

y_i Mole fraction of species *i*,

$n_i o$ Initial moles of species *i*,

no Total number of moles, and

ε Reaction coordinate.

Table A.5 shows the stoichiometric number and initial moles of each species in the reaction as well as total stoichometric and total number of moles.

Table A.5 Stoichiometric number and initial moles of each species in the reaction

COMPONENT	v_i	$n_i o$
C_2H_5OH	-1	1
H_2O	-3	3
CO_2	2	0
H_2	6	0
	$v = 4$	$no = 4$

Apply the values presents in Table (A-5) in Equation (A.14) resulting,

$$y_{H_2} = \frac{6\varepsilon}{4 + 4\varepsilon} \qquad y_{CO_2} = \frac{2\varepsilon}{4 + 4\varepsilon}$$

$$y_{C2H5OH} = \frac{1 - \varepsilon}{4 + 4\varepsilon} \qquad y_{H2O} = \frac{3 - 3\varepsilon}{4 + 4\varepsilon}$$

Replacing these values in Equation (A.13) resulting the following Equation:

$$\frac{\left(\frac{2\varepsilon}{4 + 4\varepsilon}\right)^2 \left(\frac{6\varepsilon}{4 + 4\varepsilon}\right)^6}{\left(\frac{1 - \varepsilon}{4 + 4\varepsilon}\right)^1 \left(\frac{3 - 3\varepsilon}{4 + 4\varepsilon}\right)^3} = (1)^{-4} K_P \tag{A.15}$$

Equation (A.15) solved by MATLAB, however the codes used to solve the functions and tables are listed below:

Table A.6 Ethanol conversion at different temperatures and molar ratios

T, K	ETOH/H_2O molar ratio			
	1:3	1:5	1:7	1:9
300	3.65	5.79	7.06	8.67
400	40.63	47.61	82.84	92.58
500	97.00	98.58	99.34	99.56
600	99.9	99.9	99.9	99.9
700	99.9	99.9	99.9	99.9
800	99.9	99.9	99.9	99.9

Table A.7 Ethanol conversion at different temperatures and pressures

T, K	Pressure, atm					
	1	10	20	30	40	50
300	3.65	1.15	0.81	0.66	0.57	0.51
400	40.63	16.43	11.69	9.57	8.29	7.42
500	97.00	83	72.49	65.17	59.69	55.41
600	99.9	98.65	97.28	96.00	94.78	93.59
700	99.9	99.78	99.57	99.36	99.15	98.93
800	99.9	99.94	99.88	99.83	99.77	99.72

A.2 Code Matlab for Thermodynamic Calculations

```
MATLAB simulation
%%% MCPH function
clear all
clc

A=16.48;
To=298.15;
T=input ('please enetr T : =');
Block1=(A*To*(T/To-1));

B=-19.72e-3;
Block2=((B/2)*To^2*((T/To)^2-1));

C=6e-6;
Block3=((C/3)*To^3*((T/To)^3-1));

D=-2.17e5;
Block4=(D/To)*(((T/To)-1)/(T/To));

Result_MCPH=Block1+Block2+Block3+Block4
MCPS=  13.3527;
Result_H=87-(36815/T)-(1/T*(Result_MCPH))+MCPS

Result_K=exp(Result_H)



%%% MCPS Function
clear all
clc

A=16.48;
B=-19.72e-3;
C=6e-6;
D=-2.17e5;
To=298.15;
T=input ('please enetr T : =');
Block1=A*0.81;
Block2=(B*To);
Block3=(C*To^2);
Block4=D/((T/To)^2*To^2);
Block5=((T/To +1)/2);
Block6=((T/To)-1);

Result_MCPS=Block1+(Block2+(Block3+Block4)*(Block5))*(Block6)

Result_ICPS=Result_MCPS*log((T/To))


clear all
clc
syms x
Po=1;
P=input ('please enetr P : =');
K=input ('please enetr K : =');
v=input ('please enetr v : =');
A=(6*x/(6+4*x));
```

```
B=(2*x/(6+4*x));
C=(1-x)/(6+4*x);
D=(5-3*x)/(6+4*x);

f=(A^6*B^2)/(C*D^3)-((P/Po)^-v)*K
d=solve(f)
```

A.3 Thermodynamics Data Regarding Minimization of the Gibbs Free Energy Method

Table A.8 Thermodynamics data at 1 atm and 1:3 ethanol to water molar feed ratio

T/K	$\lambda_C/_{RT}$	$\lambda_H/_{RT}$	$\lambda_O/_{RT}$	n_{H_2}	n_{CO_2}	n_{CH_4}	n_{CO}
300	-1.19	5.71	81.28	0.00006	0.501	1.499	9.6E-11
400	-0.587	4.02	65.05	1.6E-03	0.499	1.501	7.E-08
500	-0.122	2.58	51.40	2.9E-02	0.507	1.493	2.E-05
600	0.113	1.63	42.52	0.203	0.55	1.449	9.6E-04
700	0.160	1.00	36.27	0.726	0.67	1.314	1.5E-02
800	0.793	0.633	31.46	1.501	0.589	0.414	7.4E-02
900	4.13	0.778	26.55	0.966	0.294	1.2E-03	4.2E-02

Table A.9 Thermodynamics data at 1 atm and 1:6 ethanol to water molar feed ratio

T/K	$\lambda_C/_{RT}$	$\lambda_H/_{RT}$	$\lambda_O/_{RT}$	n_{H_2}	n_{CO_2}	n_{CH_4}	n_{CO}
300	0.498	5.66	81.21	1.1E-04	0.499	1.501	9.7E-11
400	0.105	3.97	64.95	2.9E-03	0.501	1.499	6.4E-08
500	0.568	2.52	51.28	5.2E-02	0.513	1.487	1.9E-05
600	0.790	1.58	42.38	0.373	0.592	1.407	9.9E-04
700	0.837	0.974	36.08	1.292	0.81	1.172	1.7E-02
800	1.35	0.640	31.23	2.5	0.891	0.36	9.1E-02
900	4.54	0.793	26.35	1.623	0.502	1.2E-03	5.9E-02

Table A.10 Thermodynamics data at 1 atm and 1:9 ethanol to water molar feed ratio

T/K	$\lambda_C/_{RT}$	$\lambda_H/_{RT}$	$\lambda_O/_{RT}$	n_{H_2}	n_{CO_2}	n_{CH_4}	n_{CO}
300	-0.093	5.64	81.17	1.7E-04	0.5	1.5	1.2E-10
400	0.511	3.95	64.90	4.1E-03	0.501	1.499	6.1E-08
500	0.971	2.50	51.24	7.4E-02	0.519	1.481	1.8E-05
600	1.181	1.57	42.32	0.502	0.626	1.373	9.0E-04
700	1.236	0.978	35.98	1.709	0.915	1.069	1.6E-02
800	1.729	0.663	31.085	3.326	1.146	0.313	0.101
900	4.789	0.813	26.245	2.276	0.709	1.7E-03	7.5E-02

Table A.11 Thermodynamics data at 1 atm and 1:12 ethanol to water molar feed ratio

T/K	$\lambda_C/_{RT}$	$\lambda_H/_{RT}$	$\lambda_O/_{RT}$	n_{H_2}	n_{CO_2}	n_{CH_4}	n_{CO}
300	0.195	5.63	81.15	6.2E-05	0.499	1.501	8.5E-12
400	0.798	3.938	64.87	5.4E-03	0.502	1.498	6.2E-08
500	1.255	2.491	51.21	9.6E-02	0.526	1.474	1.8E-05
600	1.455	1.568	42.27	0.622	0.655	1.344	8.5E-04
700	1.527	0.990	35.90	2.116	1.017	0.967	1.6E-02
800	2.053	0.691	30.96	4.008	1.353	0.261	0.105
900	4.983	0.832	26.16	2.827	0.886	1.7E-03	8.7E-02

Table A.12 Thermodynamics data at 10 atm and 1:6 molar feed ratio

T/K	$\lambda_C/_{RT}$	$\lambda_H/_{RT}$	$\lambda_O/_{RT}$	n_{H_2}	n_{CO_2}	n_{CH_4}	n_{CO}
300	-0.47784	5.03082	79.5259	3.4E-05	0.5	1.5	3.1E-11
400	0.26125	2.93523	59.4334	2.3E-03	0.501	1.499	1.2E-07
500	0.66473	1.64445	47.3884	3.0E-02	0.507	1.493	1.8E-05
600	0.88721	0.77593	39.3537	0.171	0.542	1.457	5.5E-04
700	0.99937	0.17500	33.5927	0.583	0.63	1.321	6.8E-03
800	3.2661	-0.01337	28.6109	0.776	0.267	5.5E-03	8.6E-03
900	6.63259	0.24192	23.9158	0.45	0.147	1.2E-04	4.9E-03

Table A.13 Thermodynamics data at 20 atm and 1:6 ethanol to water molar feed ratio

T/K	$\lambda_C/_{RT}$	$\lambda_H/_{RT}$	$\lambda_O/_{RT}$	n_{H_2}	n_{CO_2}	n_{CH_4}	n_{CO}
300	-0.47784	4.85753	79.1793	2.4E-05	0.5	1.5	2.2E-11
400	0.26142	2.76187	59.0869	1.6E-03	0.5	1.5	8.6E-08
500	0.66688	1.47012	47.0426	2.1E-02	0.505	1.495	1.3E-05
600	0.89847	0.59695	39.0113	0.122	0.53	1.469	3.8E-04
700	1.04936	-0.01588	33.2552	0.422	0.582	1.332	4.4E-03
800	3.61874	-0.19817	28.2462	0.549	0.19	3.0E-02	4.3E-03
900	6.98447	0.06277	23.5574	0.318	0.104	8.2E-05	2.4E-03

Table A.14 Thermodynamics data at 30 atm and 1:6 ethanol to water molar feed ratio

T/K	$\lambda_C/_{RT}$	$\lambda_H/_{RT}$	$\lambda_O/_{RT}$	n_{H_2}	n_{CO_2}	n_{CH_4}	n_{CO}
300	-0.47784	4.75616	78.9766	2.0E-05	5.0E-01	1.5	1.8E-11
400	0.26149	2.66047	58.8842	1.3E-03	5.0E-01	1.5	7.1E-08
500	0.66784	1.36829	46.8402	1.7E-02	5.0E-01	1.496	1.1E-05
600	0.90361	0.49302	38.8105	0.10	5.3E-01	1.475	3.1E-04
700	1.08313	-0.12563	33.056	0.348	5.5E-01	1.323	3.5E-03
800	3.8245	-0.30462	28.0352	0.449	1.6E-01	2.5E-02	2.8E-03
900	7.18964	-0.04117	23.3495	0.26	8.6E-02	6.7E-05	1.6E-03

APPENDIX B
CATALYST PREPARATION AND CHARACTERIZATIONS

B.1 Calculation Procedure for Precipitation Method

(6%Ni/Al_2O_3) as an example

Solution 1

6 g Ni	94 g Al_2O_3
0.6 g	9.4 g

Ni $(NO3)_2.6H_2O$	Ni
290	58
??	0.6 g

Amount of nickel nitrate = 3g

For 0.05 M

0.05*290	1000 ml
3g	??

= 206 ml water

Step 1 Dissolve 3 g of nickel nitrate into 206 ml water

Solution 2

Take 0.25 M Na_2CO_3

0.25 *105.99	1000 ml water
??	100 ml

= 2.65 g Na_2CO_3

Step 2 Dissolve 2.65 g of Na_2CO_3 into 100 ml water, and then add 9.4 g Al_2O_3

Step 3 Solution 1 was added to solution 2

Step 3 Resulting slurry was vigorously stirred for 24 hr

Step 4 Precipitate was filtered and dried at 80 ^oC overnight

Step 5 Dried participate was washed with water then dried at 120

Step 6 The dried was calcined at 550 for 5 hr

B.2 Calculation Procedure for Sol gel Method

1- Amount of Aluminium precursor needed

$Al[OCH(CH_3)C_2H_5]_3$	Al_2O_3
2*246.32	102 g
??	20 g

Amount of aluminium sec butoxide needed

$$= \frac{20 * 2 * 246.32}{102} = 96.6\ g$$

2- Moles of Al needed

$$= \frac{20}{102} = 0.196\ mol$$

1 mole of Al_2O_3	2 mole of Al
0.169 mole of Al_2O_3	??

Moles of Al are equal to 0.169 *2 = 0.338 mole

3- Amount of ethanol needed

Mwt of aluminium precursor (aluminium sec butoxide) = 246 $ggmol^{-1}$

Moles of aluminium precursor (aluminium sec butoxide) = $\frac{\text{Wt of Al precorsor}}{Mwt\ of\ \text{Al precorsor}}$

$= {}^{96.9}/_{246} = 0.392\ mol$

In literature, 0.0284 mole of Al precursor Needs → 60 ml of ethanol

0.392 mole of Al precursor Needs → ??

Amount of ethanol needed

$= \frac{0.392 * 60}{0.0284} = 828.8\ ml\ of\ ethanol$

4- Amount of nitric acid needed

In literature, 0.0284 mole of Al precursor Needs → 0.1 ml of nitric acid

0.392 mole of Al precursor Needs → ??

Amount of nitric acid needed

$= \frac{0.392 * 0.1}{0.0284} = 1.37\ ml\ of\ ethanol$

5- Amount of distilled water needed

= 1.37 *3 = 4.119 ml of distilled water

6- Amount of ethanol needed

In literature, 0.0284 mole of Al precursor Needs → 40 ml of ethanol

0.392 mole of Al precursor Needs → ??

Amount of ethanol needed

$= \frac{0.392 * 40}{0.0284} = 549\ ml\ of\ ethanol$

<u>Solution for gel forming</u>

7- Amount of distilled water needed

In literature, 0.0284 mole of Al precursor Needs → 0.6 ml water

0.392 mole of Al precursor Needs → ??

Amount of distilled water needed for gel formation

$$= \frac{0.392 * 0.6}{0.0284} = 8.239\ ml$$

8- Amount of ethanol needed for gel formation

In literature, 0.6 ml distilled water $\xrightarrow{\text{Needs}}$ 5 ml of ethanol

8.239 ml distilled water $\xrightarrow{\text{Needs}}$??

Amount of ethanol needed

$$= \frac{8.239 * 5}{0.6} = 68.66\ ml$$

Procedure

Step 1 96.6 g of aluminium precursor (aluminium sec butoxide) was dissolved in 828 ml of ethanol at 80 ^{o}C.

Step 2 1.37 ml of nitric acid and 4.119 ml of distilled water that had been diluted with 549 ml of ethanol were then slowly added into the solution containing both precursors. The resulting solution was maintained at 80 ^{o}C for few minutes to obtain a clear sol. The sol was then cooled at room temperature.

Step 3 Transparent gel was formed within a few minutes by adding 8.23 ml of distilled water diluted with 68.66 ml of ethanol into the sol.

Step 4 After aging the gel for 24 h, it was dried over night at 120 ^{o}C.

Step 5 The resulting powder was calcined (at different values of temperature) for 5 h to yield Al_2O_3 xerogel support.

Step 6 Nickel catalysts supported on laboratory made Al_2O_3 were prepared by impregnating known amount of $(Ni(NO_3)_2.6H_2O$ on the support.

B.3 Calculation of Crystallite Size

a) Using TOPAS Software

The crystallite sizes of the samples were obtained by using TOPAS software. The most intense peaks at 2θ values of 43° and 67° were used to identify the NiO and Al_2O_3 phases, respectively, in determining the crystallite size. Figure B-1 shows the crystallite size of both Al_2O_3 and NiO on 10IMP sample using TOPAS software is one sample of the 20 PT sample. It's shown that the crystallite sizes of Al_2O_3 and NiO are 8.9 nm, and12.2nm, respectively at 2θ of 67° and 43°.

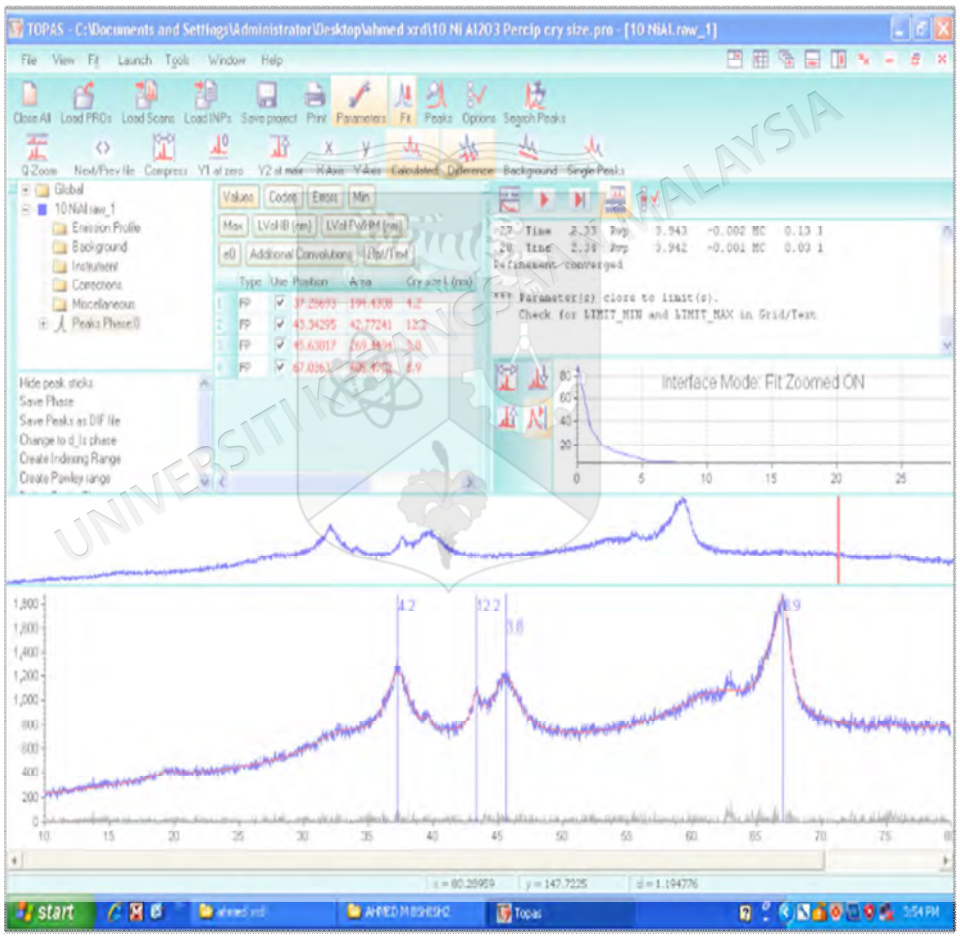

Figure B.1 Crystallite size of 10IMP sample by using TOPAS software

b) Using Scherrer Formula

To confirm the result obtained by the software, also Sherrer equation was used to measure the crystallite size. The following figures and calculation shows one sample calculation of the crystallite size. The same sample was taken for calculation. Here,

we take an example, how we obtain the crystallite size of Al_2O_3 by the Sherrer equation at peak 67° and compare the result with the corresponding result obtained by the software.

$$D = \frac{(K\lambda)}{\beta \cos\theta}$$

where,

D Particle size of the powder sample (nm),

K Constant, 1,

λ Wavelength usually for Cu Kα radiation,

β Width of diffraction line at full width half maximum (FWHM) in radian, and

θ The angle between the incident and diffracted beams.

As shown in the Figure B-2, at x= 67.12, y_1, and y_2 are obtained.

From Figure,

y_2= 16.1, and y_1= 6.3

Subtract y_1 from y_2, we get 9.8

Then, divide the result value by 2 and add to the y_1 becomes,

(9.8/2) + 6.3 = 11.2

At this value of 11.2, we get X_2, and X_1.

X_2= 67.74, and X_1 = 66.45.

- To find β which is the width of diffraction line at full width half maximum (FWHM) in radian, we subtract X_1 from X_2.

$\beta = X_2 - X_1$

β = 67.74- 66.45= 1.29 (radian)

Some calculation needed to convert β from radian to degree

$\beta = 1.29*3.14/180 = 0.02^o$

- To calculate the angle between the incident and diffracted beams (Cos θ), we do some calculation as follow.

Since, θ = X/2

Cos θ = Cos (X/2) = Cos (67.12/2)

= 0.8

Also, since the λ = 1.5406 A^o = 0.15406 nm, and the value of constant K is suppose to be between 0.9 -1, here K value chosen to be 1.

Then, the term $K\lambda$ in Sherrer formula is equal to (0.95*0.15406 = 0.1463).

Finally, by substation all above terms, β, ($K\lambda$), and Cos θ into Sherrer equation, the crystallite size of 10IMP sample was found.

$$D = \frac{0.15406}{0.022 * 0.8} = 8.75\, nm$$

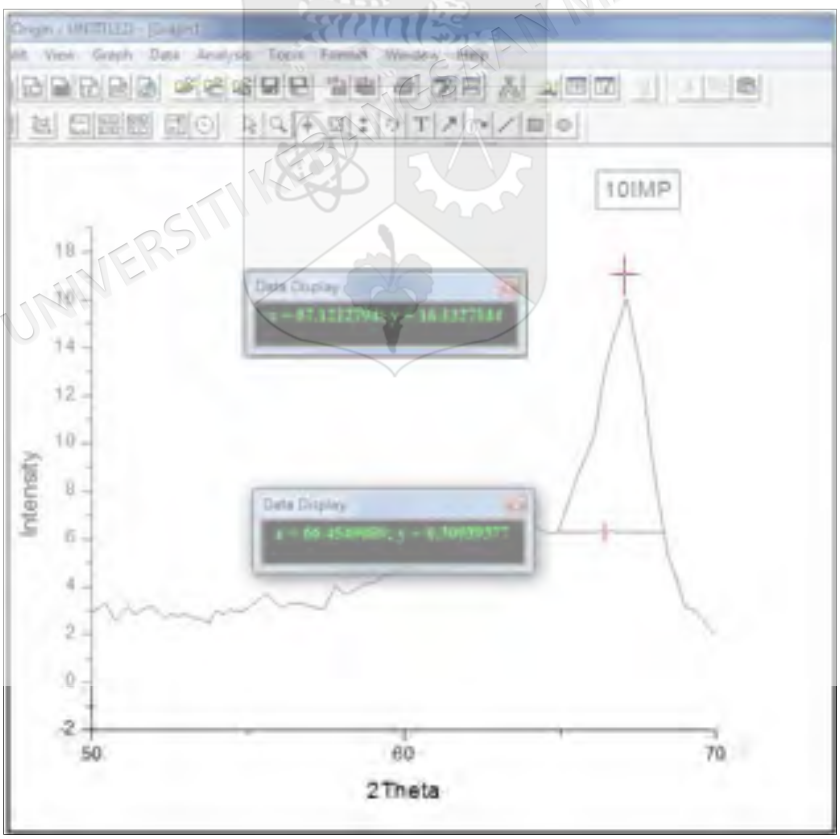

Figure B.2 Crystallite size of 10IMP sample by using Sherrer formula

For the first method, the particle size of Al_2O_3 was found to be 8.9nm. While by using Sherrer formula, the particle size was 8.75nm. It can conclude that, both method obtained similar value.

B.4 FTIR Profiles for Selected Samples

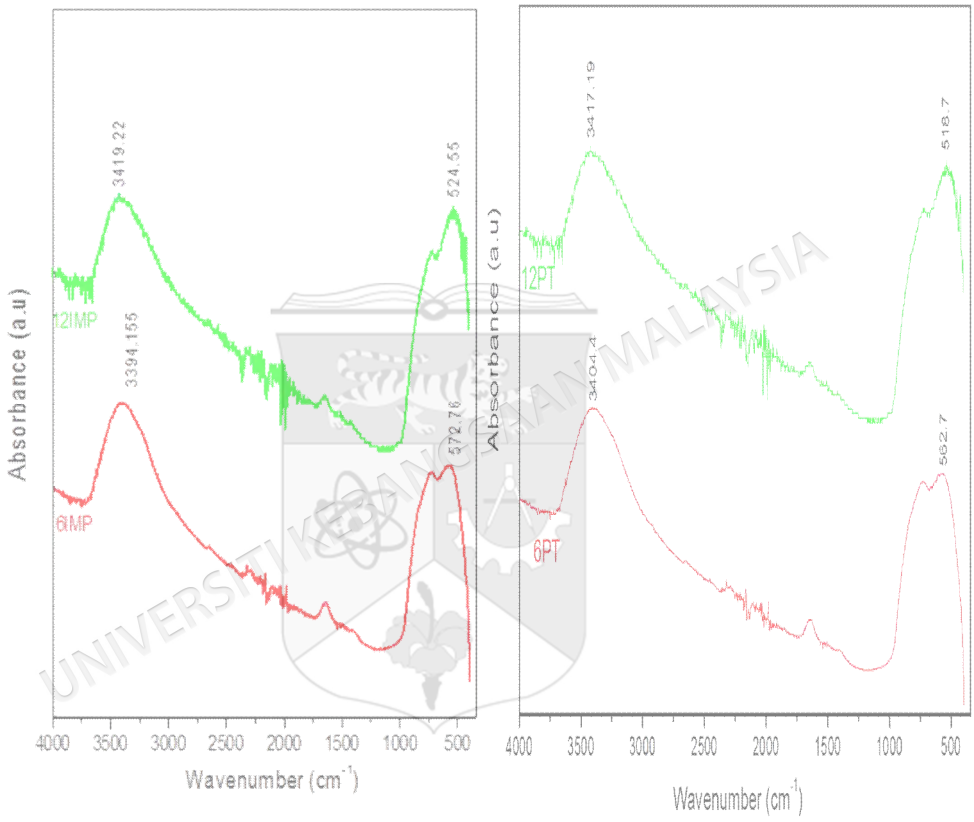

Figure B.3 FTIR spectra of selected IMP and PT catalysts

APPENDIX C
ETHANOL STANDARD

Table C.1 Ethanol standard preparation

ETHANOL STANDARD				
CON.(g l^{-1})	Density, (g ml^{-1})	ml l^{-1}	ml $100ml^{-1}$	ml $10ml^{-1}$
2	0.789	2.534854	0.253485	0.025349
4	0.789	5.069708	0.506971	0.050697
6	0.789	7.604563	0.760456	0.076046
8	0.789	10.13942	1.013942	0.101394
10	0.789	12.67427	1.267427	0.126743

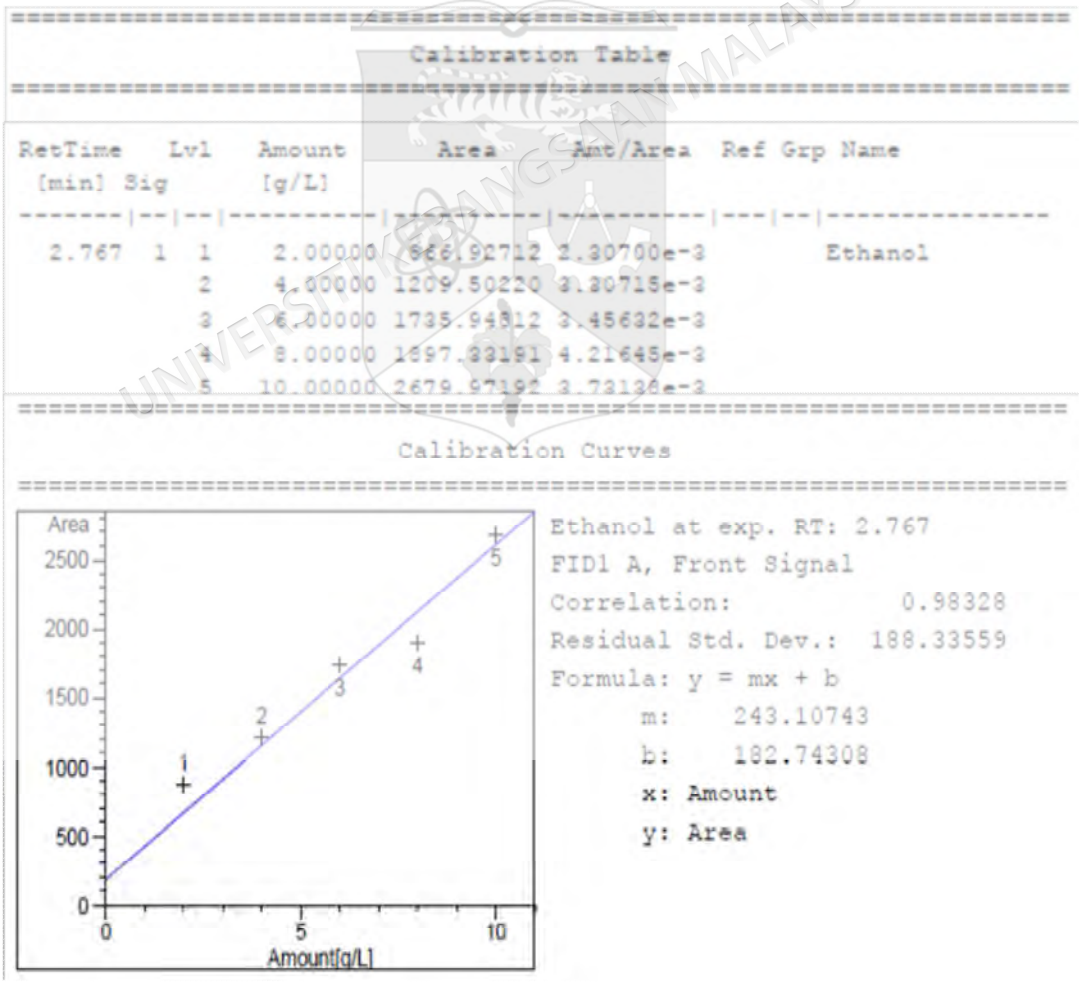

Calibration Table

RetTime [min]	Sig	Lvl	Amount [g/L]	Area	Amt/Area	Ref	Grp	Name
2.767	1	1	2.00000	866.92712	2.30700e-3			Ethanol
		2	4.00000	1209.50220	3.30718e-3			
		3	6.00000	1735.94812	3.45632e-3			
		4	8.00000	1897.33191	4.21648e-3			
		5	10.00000	2679.97192	3.73136e-3			

Calibration Curves

Ethanol at exp. RT: 2.767
FID1 A, Front Signal
Correlation: 0.98328
Residual Std. Dev.: 188.33559
Formula: y = mx + b
m: 243.10743
b: 182.74308
x: Amount
y: Area

Figure C.1 Calculation of ethanol standard

APPENDIX D
SELECTIVITY DATA FOR "PT" AND "IMP" CATALYSTS

Selectivity of the product gases was calculated base on the following equation:

$$Product\ Selectivity = \frac{F_{i,out}}{\sum F_{i,out}}\ x\ 100 \quad \text{(D.1)}$$

Table D.1 Calculation of the selectivity of the product gases for one sample

Comp.	GC Data	Yi	Total flow rate	Component flow rate out	Density	MW	Mole out	Selectivity
H_2	41.83	0.3	58.3657	17.5	0.00009	2	0.00078	0.63
CO	2.79	0.02		1.16	0.001165	28	4.86E-05	0.04
CO_2	15.21	0.12		7.00	0.00184	44	0.000293	0.23
CH_4	6.37	0.05		2.91	0.000668	16	0.000122	0.10
N_2	69.99	0.514		30				

$$F_T = \frac{F_{N2}}{Y_{N2}} \quad \text{(D.2)}$$

where,

F_T Total flow rate,

F_{N2} Nitrogen flow rate, and

Y_{N2} Nitrogen composition.

$$\text{Moles out} = \text{flow rate out (ml/min.)} * \text{Density/Mwt} \quad \text{(D.3)}$$

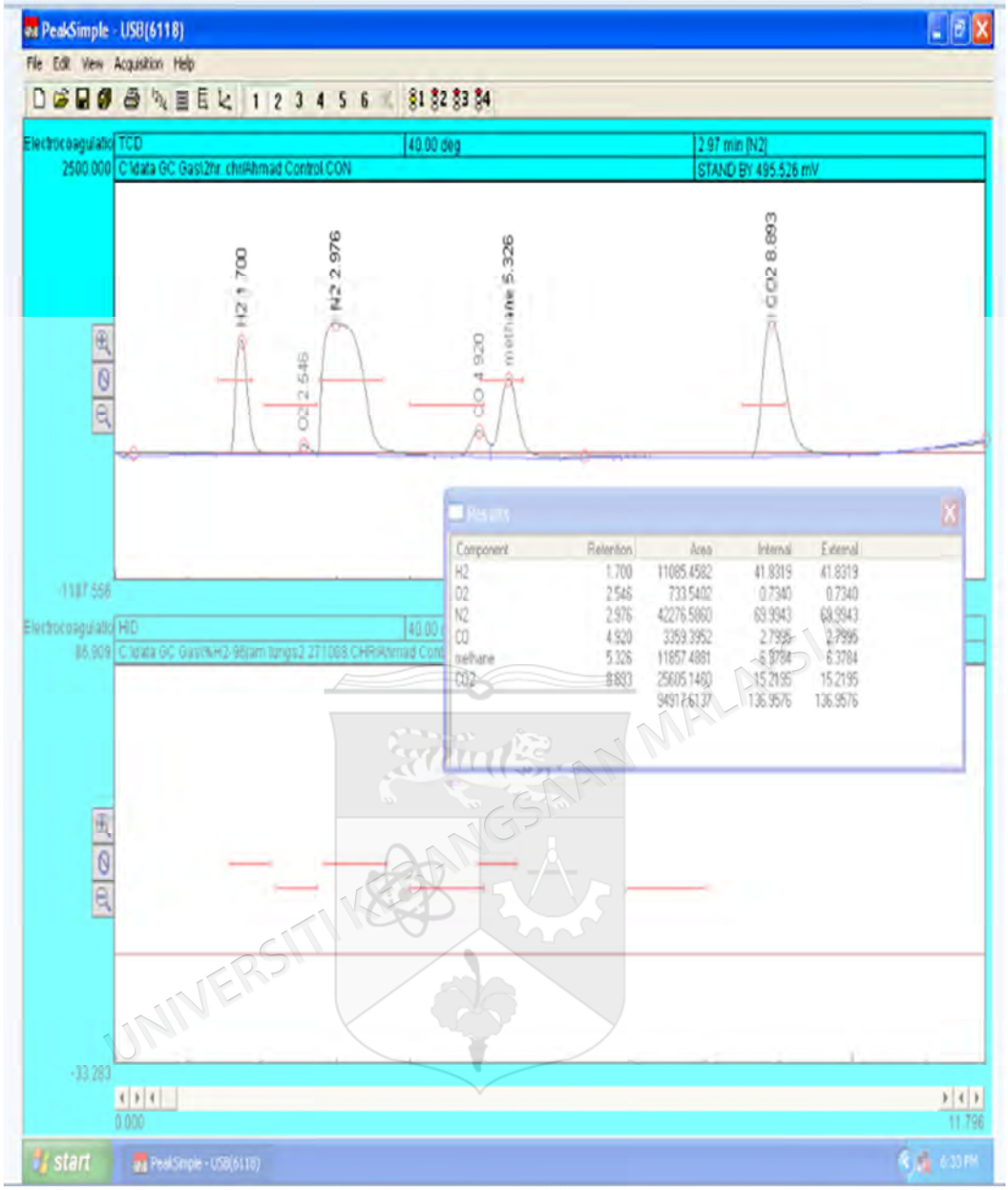

Figure D.1 GC result for the 8PT sample after 2 h reaction

Table D.2 Conversion and selectivity data for 6PT catalyst

Time,h / Comp.	1	2	3	4	5	6	7	8
H_2	0.65	0.64	0.64	0.66	0.63	0.64	0.64	0.64
CO	0.06	0.03	0.04	0.04	0.04	0.04	0.03	0.04
CO_2	0.18	0.23	0.24	0.22	0.24	0.23	0.24	0.23
CH_4	0.11	0.10	0.08	0.08	0.09	0.09	0.09	0.09
Conv.	0.98	0.98	0.97	0.97	0.97	0.97	0.97	0.97

Table D.3 Conversion and selectivity data for 8PT catalyst

Time,h / Comp.	1	2	3	4	5	6	7	8
H_2	0.62	0.63	0.62	0.63	0.61	0.615	0.62	0.62
CO	0.03	0.04	0.04	0.03	0.03	0.032	0.03	0.03
CO_2	0.25	0.23	0.23	0.25	0.25	0.24	0.24	0.24
CH_4	0.09	0.10	0.10	0.09	0.10	0.11	0.11	0.11
Conv.	1.00	1.00	1.00	1.00	0.99	0.99	0.99	0.99

Table D.4 Conversion and selectivity data for 10PT catalyst

Time,h / Comp.	1	2	3	4	5	6	7	8
H_2	0.63	0.63	0.62	0.62	0.62	0.63	0.63	0.62
CO	0.04	0.04	0.04	0.04	0.03	0.04	0.04	0.04
CO_2	0.25	0.25	0.25	0.25	0.25	0.24	0.24	0.24
CH_4	0.09	0.08	0.089	0.086	0.085	0.09	0.10	0.10
Conv.	1.00	1.00	1.00	0.99	0.99	0.99	0.99	0.99

Table D.5 Conversion and selectivity data for 12PT catalyst

Time,h / Comp.	1	2	3	4	5	6	7	8
H_2	0.61	0.61	0.60	0.61	0.61	0.60	0.60	0.61
CO	0.07	0.09	0.08	0.08	0.06	0.07	0.11	0.09
CO_2	0.23	0.20	0.20	0.20	0.18	0.23	0.17	0.19
CH_4	0.10	0.10	0.11	0.11	0.14	0.10	0.12	0.10
Conv.	1.00	0.99	0.99	0.99	0.99	0.99	0.98	0.98

Table D.6 Conversion and selectivity data for 20PT catalyst

Time,h / Comp.	1	2	3	4	5	6	7	8
H_2	0.56	0.56	0.57	0.58	0.58	0.57	0.58	0.56
CO	0.07	0.08	0.07	0.07	0.07	0.08	0.07	0.08
CO_2	0.24	0.23	0.24	0.24	0.23	0.23	0.22	0.22
CH_4	0.13	0.13	0.12	0.11	0.11	0.12	0.13	0.15
Conv.	1.00	1.00	1.00	0.97	0.97	0.97	0.97	0.97

Table D.7 Conversion and selectivity data for 6IMP catalyst

Time,h / Comp.	1	2	3	4	5	6	7	8
H_2	0.64	0.64	0.60	0.57	0.59	0.59	0.60	0.60
CO	0.10	0.10	0.13	0.12	0.12	0.12	0.12	0.11
CO_2	0.15	0.15	0.19	0.14	0.19	0.18	0.18	0.14
CH_4	0.10	0.12	0.08	0.17	0.14	0.10	010	0.13
Conv.	0.94	0.94	0.94	0.93	0.93	0.93	0.93	0.90

Table D.8 Conversion and selectivity data for 8IMP catalyst

Time,h / Comp.	1	2	3	4	5	6	7	8
H_2	0.64	0.60	0.62	0.64	0.58	0.56	0.58	0.62
CO	0.12	0.13	0.12	0.11	0.15	0.16	0.09	0.11
CO_2	0.14	0.17	0.17	0.17	0.16	0.17	0.20	0.18
CH_4	0.09	0.09	0.09	0.08	0.11	0.12	0.13	0.09
Conv.	0.99	0.98	0.97	0.96	0.96	0.96	0.96	0.93

Table D.9 Conversion and selectivity data for 10IMP catalyst

Time,h / Comp.	1	2	3	4	5	6	7	8
H_2	0.61	0.60	0.63	0.62	0.62	0.62	0.60	0.61
CO	0.11	0.10	0.09	0.09	0.08	0.09	0.13	0.08
CO_2	0.17	0.16	0.16	0.18	0.18	0.18	0.20	0.19
CH_4	0.12	0.13	0.11	0.12	0.11	0.11	0.07	0.11
Conv.	0.99	0.98	0.97	0.96	0.96	0.96	0.94	0.93

Table D.10 Conversion and selectivity data for 12IMP catalyst

Time,h / Comp.	1	2	3	4	5	6	7	8
H_2	0.57	0.53	0.56	0.56	0.56	0.56	0.56	0.56
CO	0.15	0.17	0.13	0.12	0.12	0.12	0.12	0.12
CO_2	0.15	0.17	0.19	0.20	0.20	0.20	0.20	0.20
CH_4	0.13	0.14	0.12	0.12	0.12	0.12	0.12	0.12
Conv.	0.99	0.98	0.98	0.96	0.96	0.93	0.93	0.92

Table D.11 Conversion and selectivity data for 20IMP catalyst

Time,h / Comp.	1	2	3	4	5	6	7	8
H_2	0.56	0.56	0.57	0.57	0.57	0.57	0.55	0.56
CO	0.07	0.07	0.07	0.10	0.08	0.08	0.08	0.10
CO_2	0.24	0.24	0.22	0.18	0.23	0.22	0.22	0.22
CH_4	0.13	0.13	0.13	0.16	0.12	0.12	0.14	0.12
Conv.	1.00	1.00	1.00	0.99	0.98	0.97	0.97	0.97

Some GC result

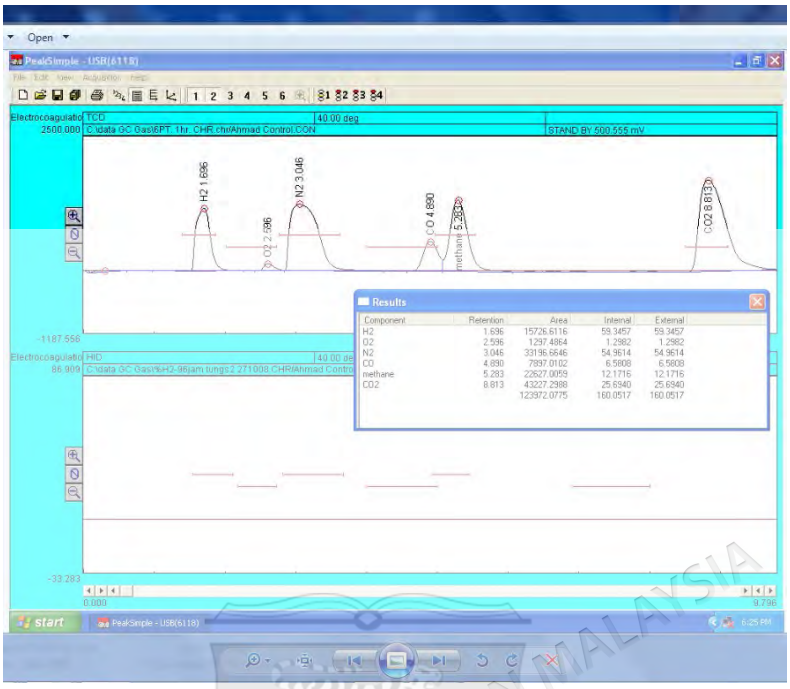

Figure D.2 GC result for the 6PT sample after 1h reaction

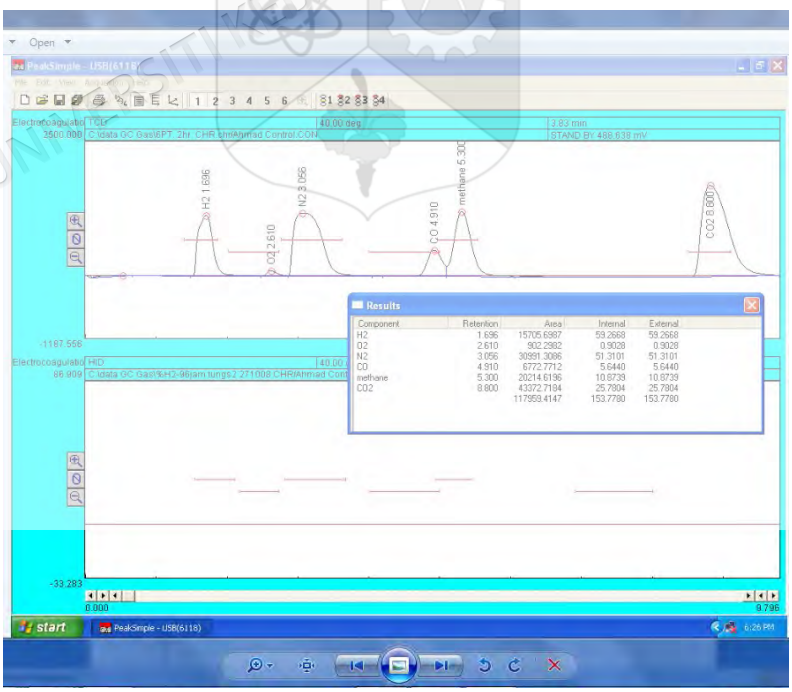

Figure D.3 GC result for the 6PT sample after 2 h reaction

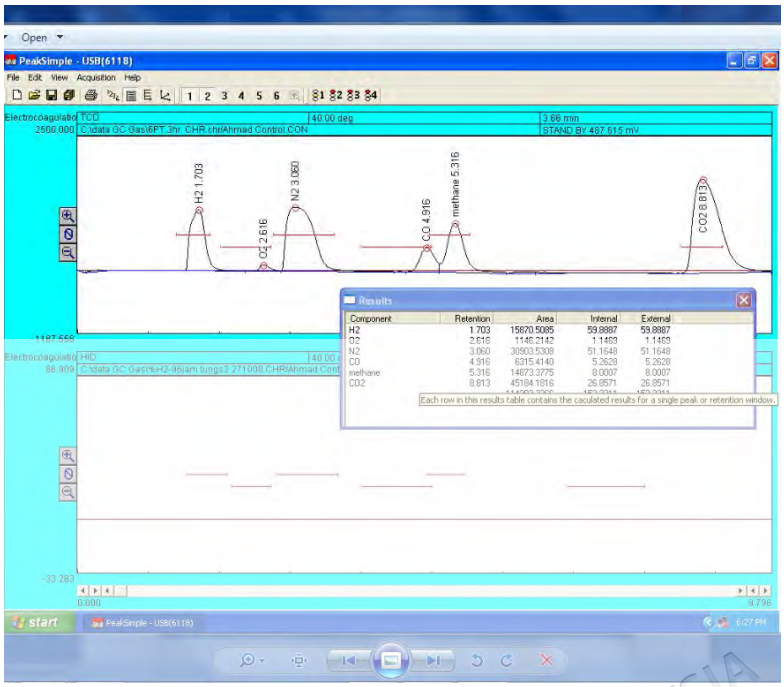

Figure D.4 GC result for the 6PT sample after 3 h reaction

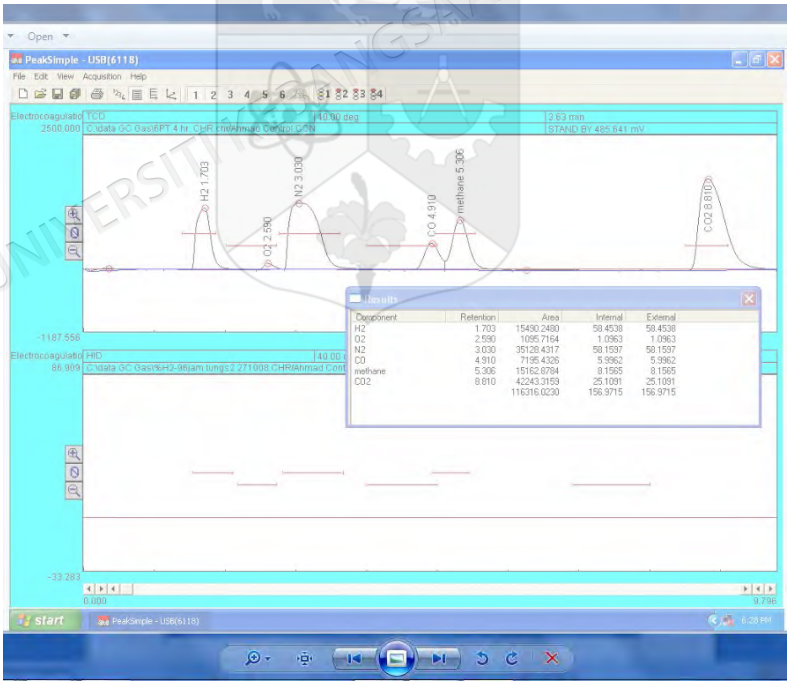

Figure D.5 GC result for the 6PT sample after 5 h reaction

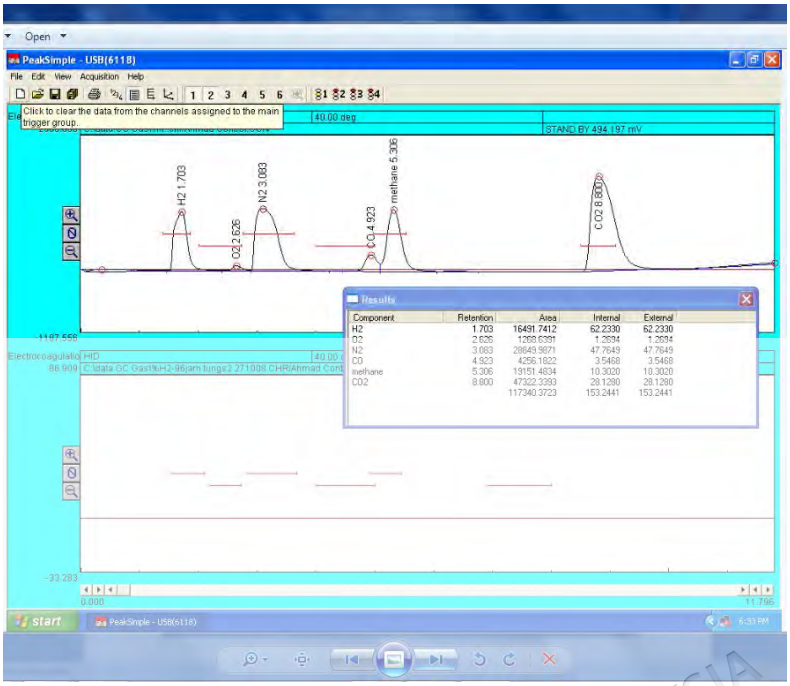

Figure D.6 GC result for the 8PT sample after 1 h reaction

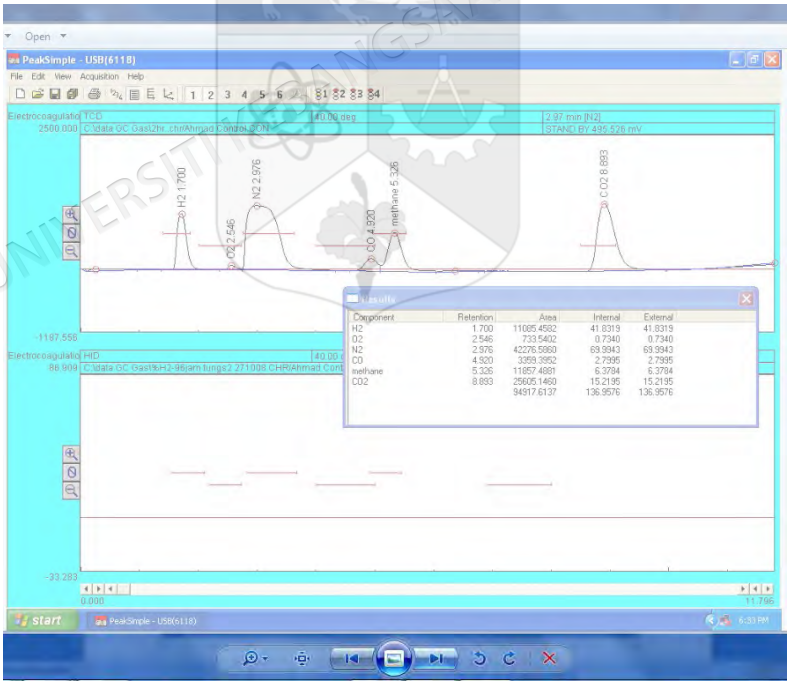

Figure D.7 GC result for the 8PT sample after 2 h reaction

Figure D.8 GC result for the 8PT sample after 3 h reaction

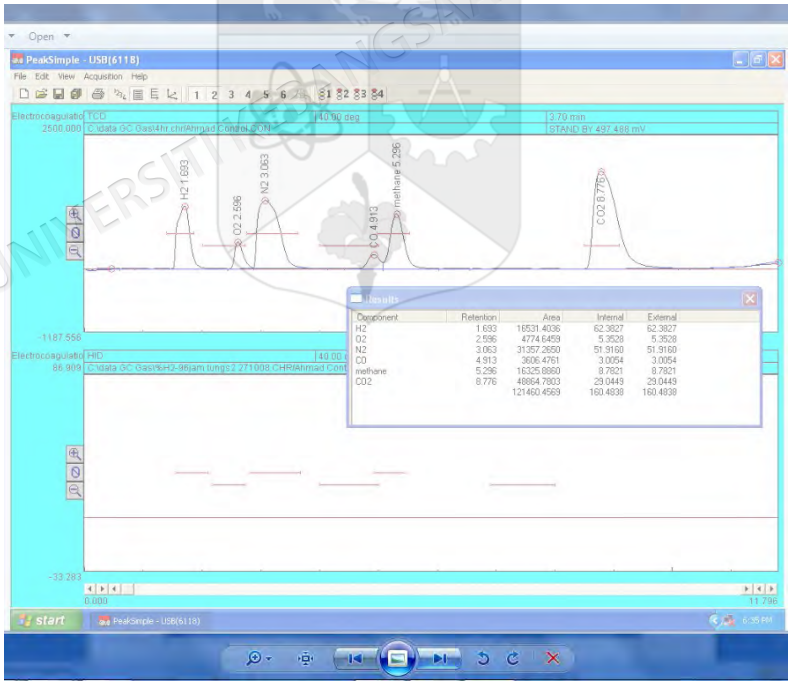

Figure D.9 GC result for the 8PT sample after 4 h reaction

Figure D.10 GC result for the 8PT sample after 5 h reaction

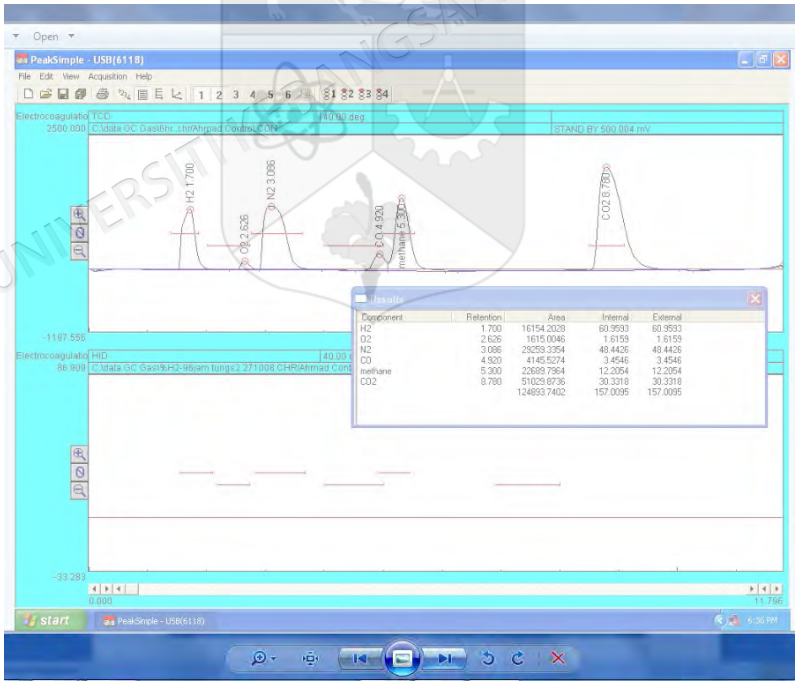

Figure D.11 GC result for the 8PT sample after 6 h reaction

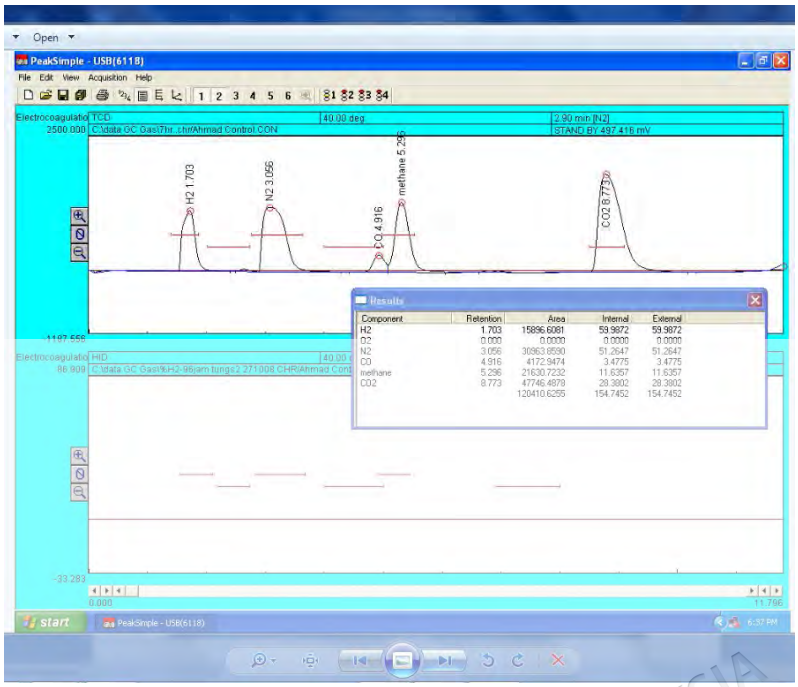

Figure D.12 GC result for the 8PT sample after 7 h reaction

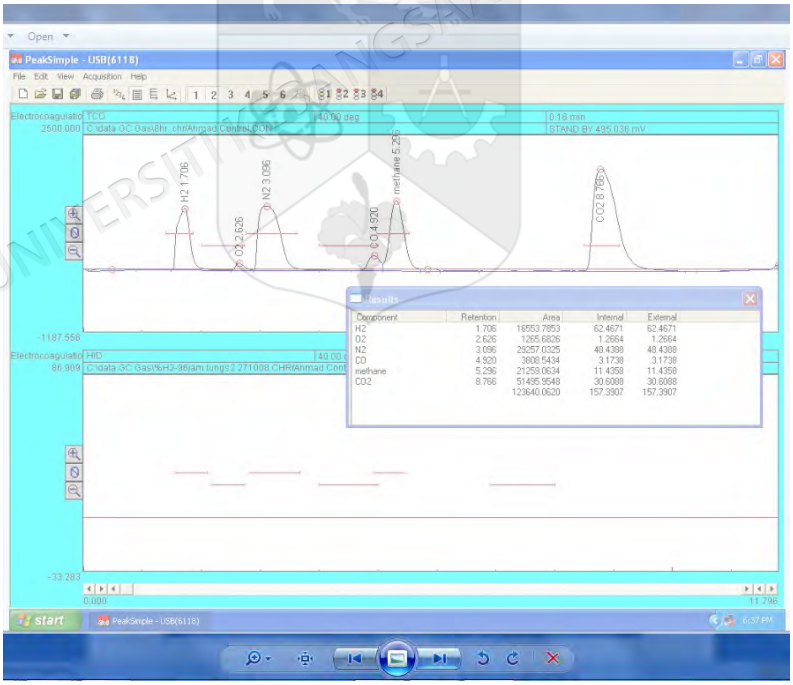

Figure D.13 GC result for the 8PT sample after 7 h reaction

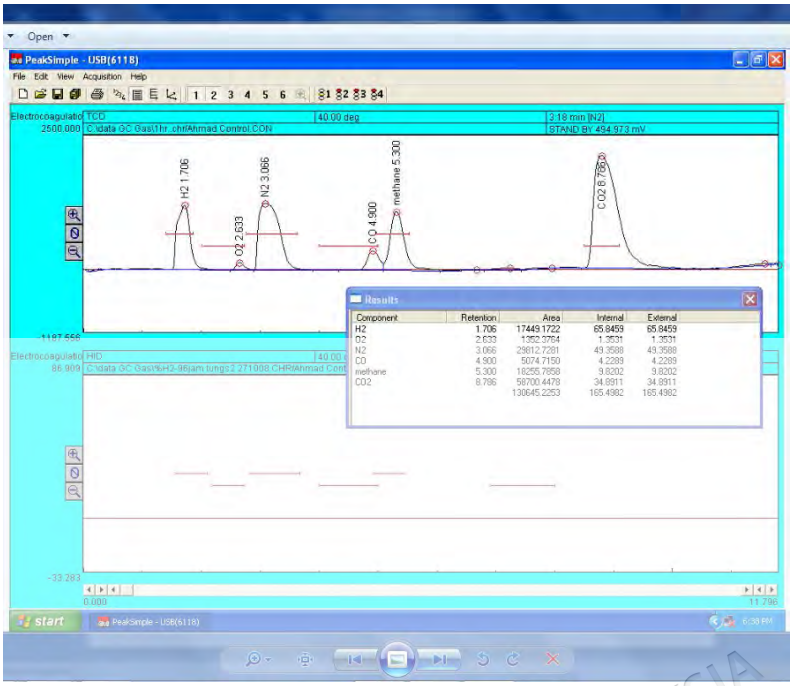

Figure D.14 GC result for the 10PT sample after 1 h reaction

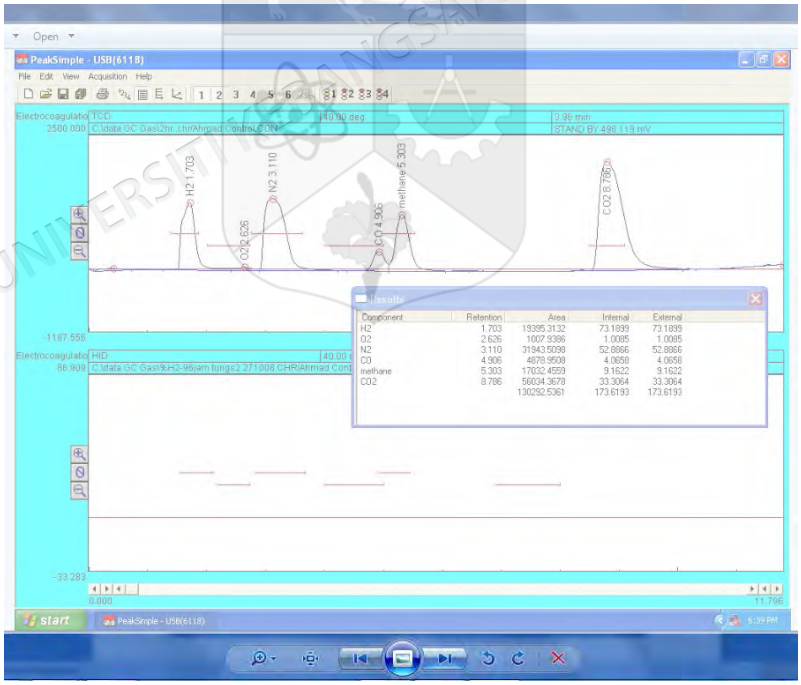

Figure D.15 GC result for the 10PT sample after 2 h reaction

Figure D.16 GC result for the 10PT sample after 3 h reaction

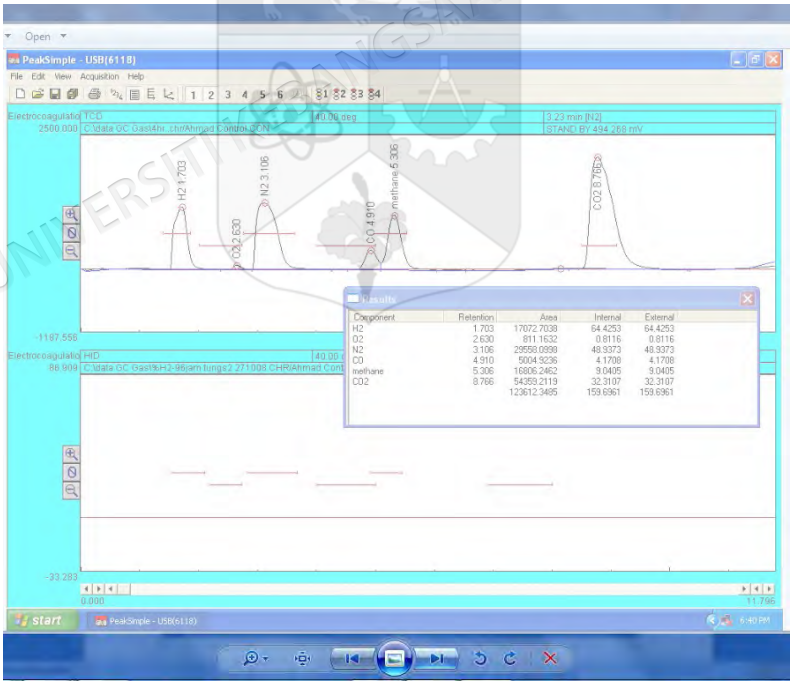

Figure D.17 GC result for the 10PT sample after 4 h reaction

Figure D.18 GC result for the 10PT sample after 5 h reaction

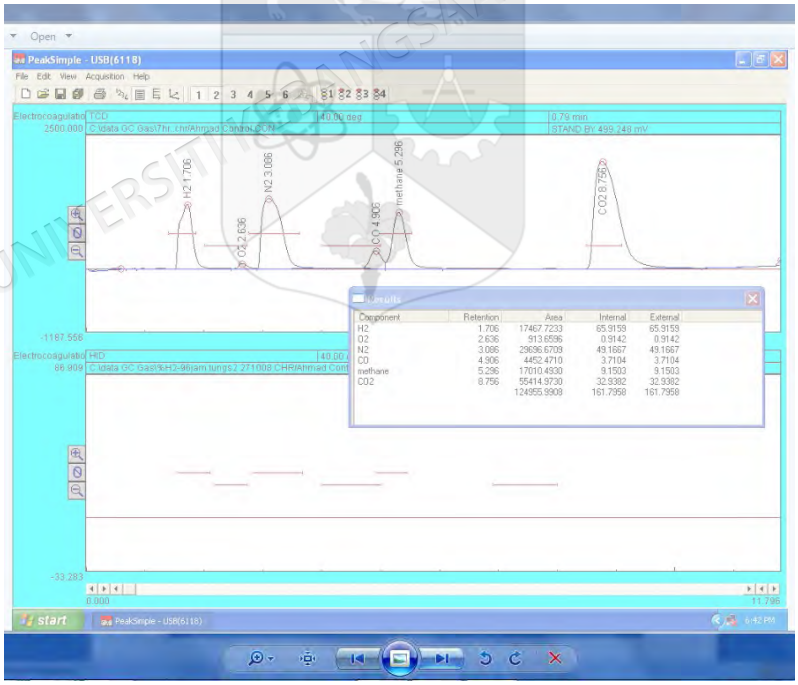

Figure D.19 GC result for the 10PT sample after 7 h reaction

APPENDIX E
EXPERIMENTAL DATA VERSUS PREDICTED DATA

Table E.1 Experimental value versus predicted value from ANN model

	($Y_{H2.Y}$)		($Y_{CO.Y}$)		($Y_{EtOH.Con.}$)	
Run	Obs. H_2 yield	Pred. H_2 yield	Obs. CO yield	Pred. CO yield	Obs. EtOH. Con.	Pred. EtOH. Con.
1	0.54	0.67301	0.18	0.173199	26	25.98547
2	0.89	0.819198	0.15	0.156441	25	28.11331
3	2.1	2.109891	0.42	0.419904	80	81.66909
4	4.8	4.77591	0.21	0.19832	81	83.93234
5	2.7	2.60986	0.17	0.181332	61	56.63784
6 (C)	2.8	2.683487	0.23	0.228066	58	60.07792
7	1.5	1.562822	0.28	0.280881	45	48.87216
8	0	4.19E-07	0	0.009225	0	0.000215
9 (C)	2.6	2.683487	0.22	0.228066	59	60.07792
10 (C)	2.7	2.683487	0.23	0.228066	61	60.07792
11	4.8	4.762337	0.21	0.199762	79	83.54344
12	2.4	2.41975	0.38	0.37667	65	67.57718
13 (C)	2.7	2.683487	0.26	0.228066	45	60.07792
14	2.9	2.854592	0.33	0.324757	65	67.14571
15 (C)	2.6	2.683487	0.22	0.228066	54	60.07792
16 (C)	2.5	2.683487	0.22	0.228066	58	60.07792
17	0	2.49E-07	0	0.007926	0	0.00014
18	0.89	0.897616	0.1	0.100907	24	25.55842
19	2.2	3.280706	0.06	0.087109	52	58.03678
20	4.3	4.586233	0.3	0.413296	85	83.69671

Table E.2 Experimental data versus predicted models values

Experimental result output			Numerical Model result output (N.M)			Neural Net work result output (ANN)		
H_2 yield	CO yield	ETOH. Con.	H_2 yield	CO yield	ETOH. Con.	H_2 yield	CO yield	ETOH. Con.
0.54	0.18	26	0.94	0.169	24.75	0.67301	0.173199	25.98547
0.89	0.15	25	0.71	0.1	26.088	0.819198	0.156441	28.11331
2.1	0.42	80	2.7	0.396	73.087	2.109891	0.419904	81.66909
4.8	0.21	81	4.69	0.205	78.113	4.77591	0.19832	83.93234
2.7	0.17	61	2.63	0.202	56.8	2.60986	0.181332	56.63784
2.8	0.23	58	2.61	0.226	55.75	2.683487	0.228066	60.07792
1.5	0.28	45	1.35	0.172	37.1	1.562822	0.280881	48.87216
0	0	0	0.008	0.032	1.112	4.19E-07	0.009225	0.000215
2.6	0.22	59	2.61	0.226	55.75	2.683487	0.228066	60.07792
2.7	0.23	61	2.61	0.226	55.75	2.683487	0.228066	60.07792
4.8	0.21	79	4.72	0.19	80.213	4.762337	0.199762	83.54344
2.4	0.38	65	2.67	0.388	70.988	2.41975	0.37667	67.57718
2.7	0.26	45	2.61	0.226	55.75	2.683487	0.228066	60.07792
2.9	0.33	65	2.6	0.214	54.7	2.854592	0.324757	67.14571
2.6	0.22	54	2.61	0.226	55.75	2.683487	0.228066	60.07792
2.5	0.22	58	2.61	0.226	55.75	2.683487	0.228066	60.07792
0	0	0	0.023	0	3.212	2.49E-07	0.007926	0.00014
0.89	0.1	24	0.681	0.132	23.988	0.897616	0.100907	25.55842
2.2	0.06	52	2.7	0.119	52.1	3.280706	0.087109	58.03678
4.3	0.3	85	4.29	0.392	86.75	4.586233	0.413296	83.69671

APPENDIX F
CALCULATION OF CONVERSION AND YIELD FOR ONE SAMPLE

Step by step calculation of conversion and yield. This result belongs to $Ni/Al_{S.G800}$ sample.

A. Ethanol Conversion

Sample 1

1- Ethanol IN

The flow rate of the reactants (ethanol and water) was equal to 0.1 ml/min. The total amount of reactants enters to the reactor after 8 hr reaction is calculated as follow:

$$= 0.1 \frac{ml}{min} * 480\ min = 48\ ml$$

Since the composition of ethanol is 0.35, the volume of ethanol enter the reactor after 8 h is

= 0.35* 48 = 16.8 ml.

Convert to mole, becomes 0.288 mol ethanol enter to the reactor.

2- Ethanol OUT

From the GC FID reading, we found the concentration of the ethanol out. As seen in the GC result (shown below), the concentration of ethanol is 1.59 g/l. We convert the unit to mol/l, since the molecular weight of ethanol is 46 g/mol.

$$= 1.59 \frac{g}{l} * \frac{mol}{46\ g} = 0.0345 \frac{mol}{l}$$

1000 ml ---------- 0.0345 mol

48 ml---------- ???

The amount of ethanol out calculated as follow:

$$= \frac{48 * 0.0345}{1000} = 0.001656\ mol$$

The conversion is [ethanol IN – ethanol OUT / ethanol IN]* 100

$$= \frac{0.288 - 0.001656}{0.288} * 100 = 99.42\ \%$$

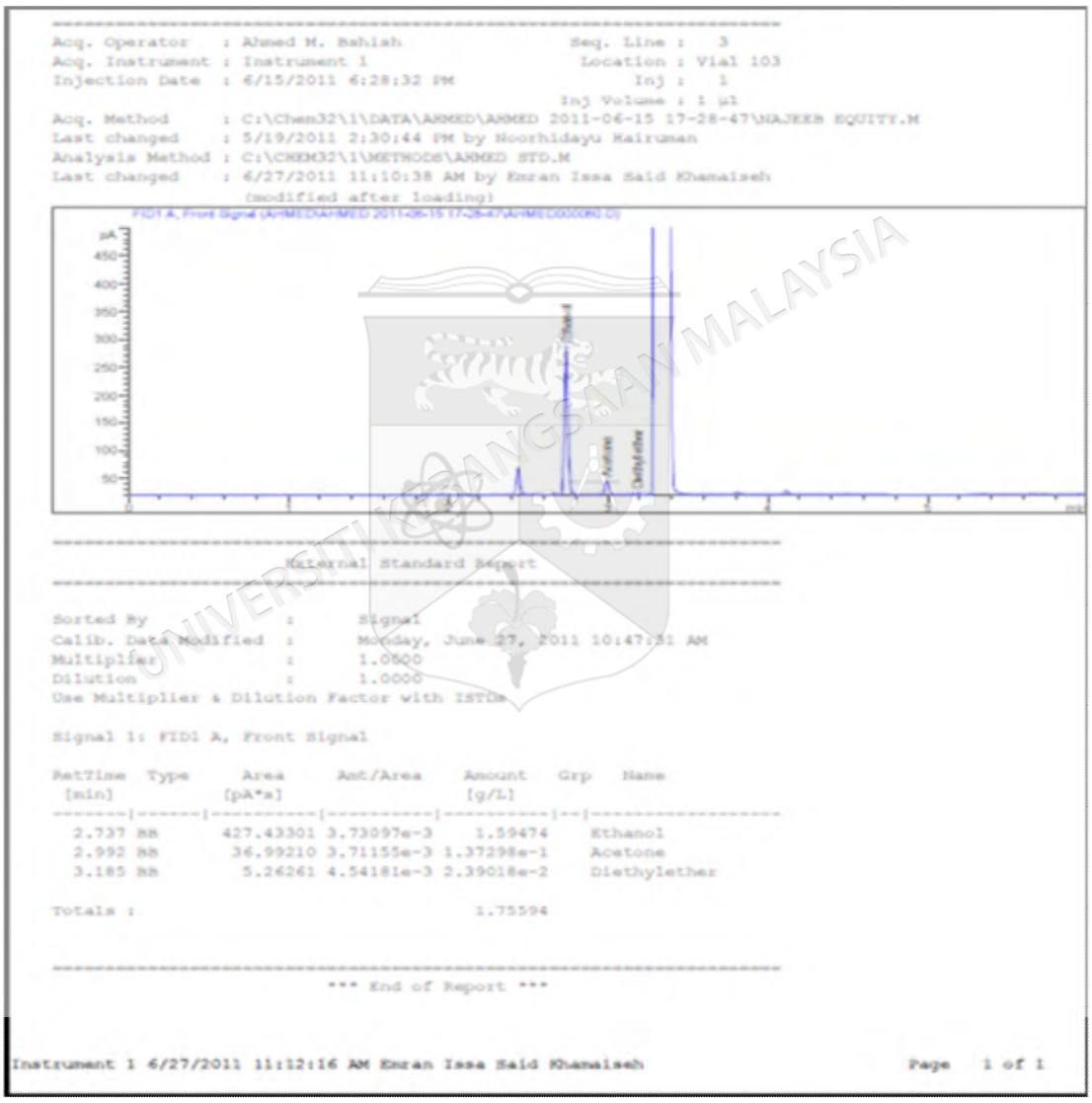

Acq. Operator : Ahmed M. Bahlah Seq. Line : 3
Acq. Instrument : Instrument 1 Location : Vial 103
Injection Date : 6/15/2011 6:28:32 PM Inj : 1
Inj Volume : 1 µl
Acq. Method : C:\Chem32\1\DATA\AHMED\AHMED 2011-06-15 17-28-47\NAJEEB EQUITY.M
Last changed : 5/19/2011 2:30:44 PM by Noorhidayu Hairuman
Analysis Method : C:\CHEM32\1\METHODS\AHMED STD.M
Last changed : 6/27/2011 11:10:38 AM by Emran Issa Said Khamaiseh
(modified after loading)

External Standard Report

Sorted By : Signal
Calib. Data Modified : Monday, June 27, 2011 10:47:31 AM
Multiplier : 1.0500
Dilution : 1.0000
Use Multiplier & Dilution Factor with ISTDs

Signal 1: FID1 A, Front Signal

RetTime [min]	Type	Area [pA*s]	Amt/Area	Amount [g/L]	Grp	Name
2.737	BB	427.43301	3.73097e-3	1.59474		Ethanol
2.992	BB	36.99210	3.71155e-3	1.37298e-1		Acetone
3.185	BB	5.26261	4.54181e-3	2.39018e-2		Diethylether

Totals : 1.75594

*** End of Report ***

Instrument 1 6/27/2011 11:12:16 AM Emran Issa Said Khamaiseh Page 1 of 1

Sample 2

From the below GC FID reading (0.957 g/l) for ethanol out, the conversion of the same sample is obtained by using the same procedure as above.

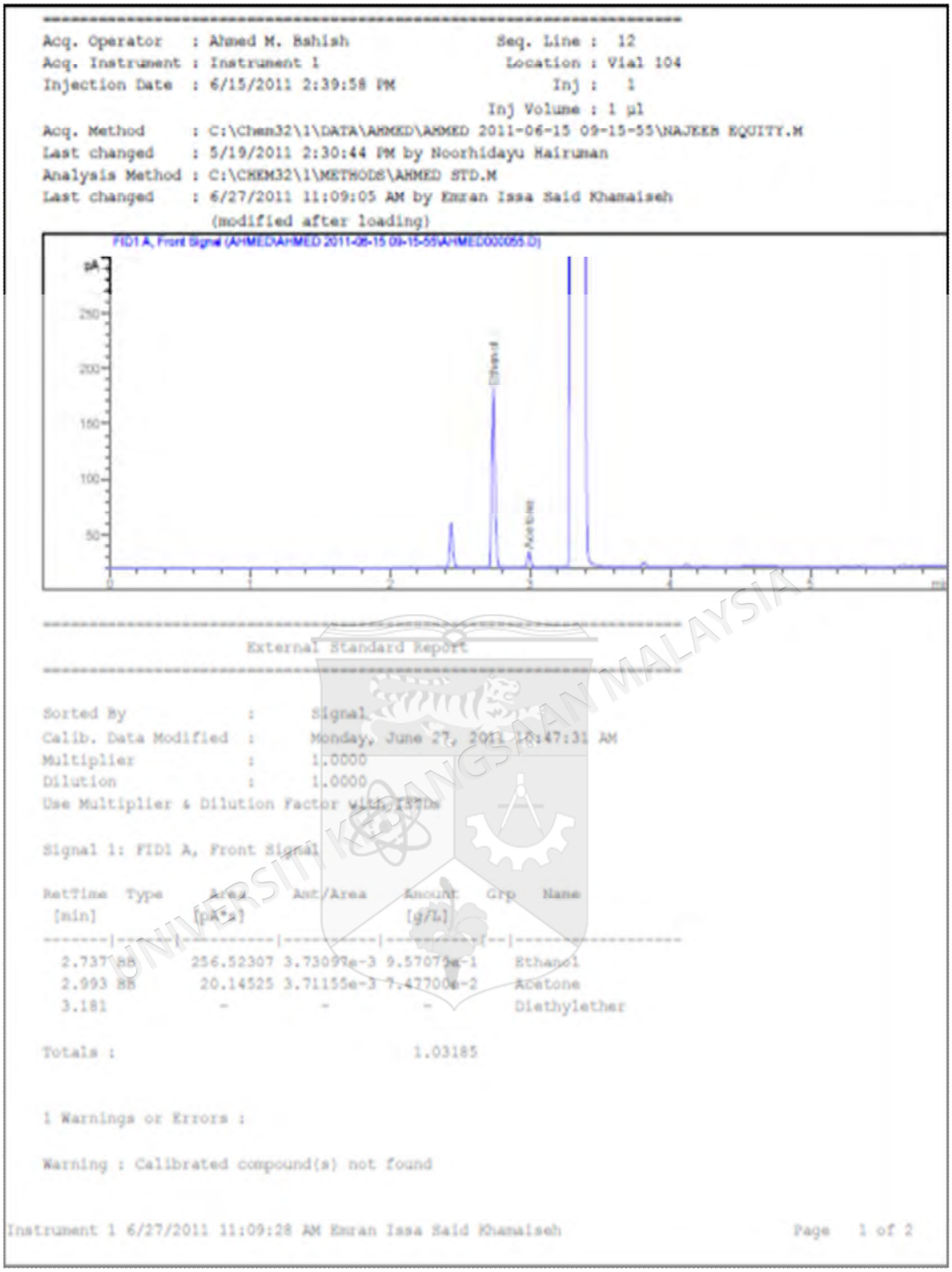

Acq. Operator : Ahmed M. Bshish Seq. Line : 12
Acq. Instrument : Instrument 1 Location : Vial 104
Injection Date : 6/15/2011 2:39:58 PM Inj : 1
Inj Volume : 1 µl
Acq. Method : C:\Chem32\1\DATA\AHMED\AHMED 2011-06-15 09-15-55\NAJEEB EQUITY.M
Last changed : 5/19/2011 2:30:44 PM by Noorhidayu Hairuman
Analysis Method : C:\CHEM32\1\METHODS\AHMED STD.M
Last changed : 6/27/2011 11:09:05 AM by Emran Issa Said Khamaiseh
(modified after loading)

FID1 A, Front Signal (AHMED\AHMED 2011-06-15 09-15-55\AHMED000055.D)

External Standard Report

Sorted By : Signal
Calib. Data Modified : Monday, June 27, 2011 10:47:31 AM
Multiplier : 1.0000
Dilution : 1.0000
Use Multiplier & Dilution Factor with ISTDs

Signal 1: FID1 A, Front Signal

RetTime [min]	Type	Area [pA*s]	Amt/Area	Amount [g/L]	Grp	Name
2.737	BB	256.52307	3.73097e-3	9.57079e-1		Ethanol
2.993	BB	20.14525	3.71155e-3	7.47700e-2		Acetone
3.181		-	-	-		Diethylether

Totals : 1.03185

1 Warnings or Errors :

Warning : Calibrated compound(s) not found

Instrument 1 6/27/2011 11:09:28 AM Emran Issa Said Khamaiseh Page 1 of 2

The conversion will be 99.7

The mean values of these nearest two values calculated as follow:

$$mean = \frac{99.7 + 99.42}{2} = 99.56$$

B. Hydrogen Yield

Table F. 1 GC data for the product gases and their calculations

Component	Yi from Gc	Total flow rate FT. (ml/min) (Eq. F-1)	Component flow rate=Yi*FT (Eq. F-2)	Density
H_2	0.5	115.38	57.69	0.00009
CO	0.04		4.615385	0.001165
CO_2	0.13		15	0.00184
CH_4	0.07		8.076923	0.000668
N_2	0.26		30	

Continue, Table F.1

Molecular weight	Moles of product out (Eq. F-3)	H_2 yield as in Eq. (F- 4)	Product yield (Eq. F- 5)
2	0.002596	4.3269	
28	0.000192		0.320055
44	0.000627		1.045455
16	0.000337		0.562019

1- Calculation of flow rate of ethanol IN

The total flow rate of reactants is 0.1ml/min, and the molar ration of water and ethanol is 6:1

6 mol H_2O = 108 ml H_2O, and 1mol ethanol = 58 ml ethanol, the composition of each reactant calculated as follow:

$$= \frac{58}{58 + 108} = 0.35 \; for \; ethanol$$

$$= \frac{108}{58 + 108} = 0.65 \; for \; H_2O$$

The flow rate of ethanol enter the reactor is equal to total flow rate * ethanol composition

$= 0.1 \frac{ml}{min} * 0.35 = 0.035 \frac{ml}{min} = 0.0006 \frac{mol}{min}$

Ethanol IN = 0.0006 molmin^{-1}

2- Calculation of flow rate of H_2 out

The total flow rate of gas stream out obtained. Since the nitrogen is the inert gas, the flow rate of nitrogen input equal to flow rate of nitrogen output.

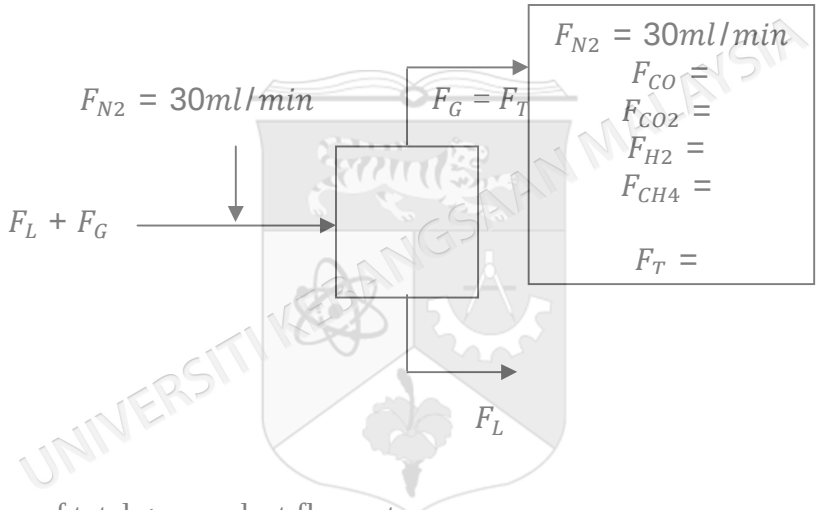

Calculation of total gas product flow rate

$$F_T = \frac{F_{N2}}{Y_{N2}} \quad \text{(F.1)}$$

where,

F_T Total flow rate (mlmin^{-1}),

F_{N2} Nitrogen flow rate, and

Y_{N2} Nitrogen composition in gas stream out (from the GC reading).

$$F_T = \frac{30}{0.26} = 115.38 \frac{ml}{min}$$

Each component flow rate can be obtained from Equation (F.2) as follow.

$$F_i = F_T * Y_i \quad \text{(F.2)}$$

where,

Y_i Composition of component i (CO. CO_2, CH_4, and H_2), and

F_i Flow rate of component i (ml/min).

For example,

$$F_{H2} = 115.38 * 0.5 = 57.69 \frac{ml}{min}$$

Now, convert $\frac{ml}{min}$ to $\frac{mol}{min}$ by means of Equation (F.3)

$$\text{Moles out of } i = \text{flow rate out } \left(\frac{\text{ml}}{\text{min}}\right) \text{of component } i * \frac{\text{Density of component } i}{\text{Molecular weight of component } i} \quad \text{(F.3)}$$

Example, flow rate of H_2 out =

$$\text{Moles of } H_2 \text{ out} = 57.69 \left(\frac{\text{ml}}{\text{min}}\right) * \frac{0.00009 \frac{\text{g}}{\text{ml}}}{2 \frac{\text{g}}{\text{mol}}} = 0.0026 \frac{mol}{min}$$

3- Calculation of hydrogen yield

Hydrogen yield is calculated as Equation (F.4)

$$H_2\ yield = \frac{Flow\ rate\ of\ H2\ out\ \ (F_{H_{2,out}})}{Flow\ rate\ of\ ethanol\ IN\ \ (F_{ETOH_{in}})} \quad \text{(F.4)}$$

$H_2\ yield = 0.0026/0.0006 = 4.33$ moles

Note that for other product, the yield calculated according to Equation (F.5).

$$Product\ yield = \frac{Flow\ rate\ of\ component\ i\ out\ \ (F_{i_{,out}})}{Flow\ rate\ of\ ethanol\ IN\ \ (F_{ETOH_{in}})} \quad \text{(F.5)}$$

APPENDIX G
STATISTICAL ANALYSIS DATA

——— 30/12/12 08:18:19 م ———————————

Response Surface Regression: H2 Y. (mol/m versus Temperature ; ...

The analysis was done using uncoded units.

Estimated Regression Coefficients for H2 Y. (mol/mol)

Term	Coef	SE Coef	T	P
Constant	-2.49304	0.606699	-4.109	0.000
Temperature (C)	0.01122	0.003733	3.007	0.005
Water to ETOH malar ratio	0.15968	0.033818	4.722	0.000
LHSV (h -1)	-1.25243	0.811626	-1.543	0.133
Temperature (C)*Temperature (C)	-0.00000	0.000005	-0.889	0.381
Water to ETOH malar ratio* Water to ETOH malar ratio	-0.00597	0.001055	-5.663	0.000
LHSV (h -1)*LHSV (h -1)	1.13158	0.607444	1.863	0.072
Temperature (C)* Water to ETOH malar ratio	0.00021	0.000043	4.850	0.000
Temperature (C)*LHSV (h -1)	0.00056	0.001039	0.541	0.593
Water to ETOH malar ratio* LHSV (h -1)	-0.01347	0.014839	-0.908	0.371

S = 0.2727 R-Sq = 96.9% R-Sq(adj) = 96.0%

Analysis of Variance for H2 Y. (mol/mol)

Source	DF	Seq SS	Adj SS	Adj MS	F	P
Regression	9	70.723	70.723	7.85810	105.69	0.000
Linear	3	65.143	3.032	1.01072	13.59	0.000
Square	3	3.748	3.748	1.24936	16.80	0.000
Interaction	3	1.832	1.832	0.61067	8.21	0.000
Residual Error	30	2.231	2.231	0.07435		
Lack-of-Fit	5	1.089	1.089	0.21782	4.77	0.003
Pure Error	25	1.141	1.141	0.04566		
Total	39	72.953				

Obs	StdOrder	H2 Y. (mol/mol)	Fit	SE Fit	Residual	St Resid	
1	9	0.540	0.816	0.135	-0.276	-1.17	
2	7	0.890	0.636	0.172	0.254	1.20	
3	26	2.100	2.830	0.172	-0.730	-3.45	R
4	4	4.800	4.737	0.172	0.063	0.30	
5	34	2.700	2.825	0.135	-0.125	-0.53	
6	16	2.800	2.593	0.066	0.207	0.78	
7	31	1.500	1.259	0.135	0.241	1.02	
8	1	0.000	-0.011	0.172	0.011	0.05	
9	39	2.600	2.593	0.066	0.007	0.03	
10	35	2.700	2.593	0.066	0.107	0.40	
11	24	4.900	4.737	0.172	0.163	0.77	
12	28	4.800	4.718	0.172	0.082	0.39	
13	22	2.400	2.601	0.172	-0.201	-0.95	
14	20	2.700	2.593	0.066	0.107	0.40	
15	33	2.900	2.794	0.135	0.106	0.45	
16	17	2.600	2.593	0.066	0.007	0.03	
17	27	0.870	0.636	0.172	0.234	1.10	
18	18	2.500	2.593	0.066	-0.093	-0.35	

19	11	1.600	1.259	0.135	0.341	1.44
20	5	0.000	0.070	0.172	-0.070	-0.33
21	3	0.890	0.803	0.172	0.087	0.41
22	29	0.580	0.816	0.135	-0.236	-1.00
23	23	0.860	0.803	0.172	0.057	0.27
24	2	2.400	2.601	0.172	-0.201	-0.95
25	13	2.700	2.794	0.135	-0.094	-0.40
26	14	2.600	2.825	0.135	-0.225	-0.95
27	19	2.700	2.593	0.066	0.107	0.40
28	25	0.000	0.070	0.172	-0.070	-0.33
29	36	2.500	2.593	0.066	-0.093	-0.35
30	8	4.700	4.718	0.172	-0.018	-0.09
31	12	2.200	2.610	0.135	-0.410	-1.73
32	32	2.100	2.610	0.135	-0.510	-2.16 R
33	21	0.000	-0.011	0.172	0.011	0.05
34	10	4.300	4.163	0.135	0.137	0.58
35	15	2.800	2.593	0.066	0.207	0.78
36	40	2.700	2.593	0.066	0.107	0.40
37	38	2.600	2.593	0.066	0.007	0.03
38	6	3.500	2.830	0.172	0.670	3.16 R
39	37	2.600	2.593	0.066	0.007	0.03
40	30	4.200	4.163	0.135	0.037	0.15

R denotes an observation with a large standardized residual.

Response Surface Regression: H2 Y. (mol/m versus Temperature ; ...

The analysis was done using uncoded units.

Estimated Regression Coefficients for H2 Y. (mol/mol)

Term	Coef	SE Coef	T	P
Constant	-2.16152	0.296126	-7.299	0.000
Temperature (C)	0.00832	0.000718	11.586	0.000
Water to ETOH malar ratio	0.13547	0.026875	5.041	0.000
LHSV (h -1)	0.03543	0.140647	0.252	0.803
Water to ETOH malar ratio*	-0.00536	0.000789	-6.786	0.000
Water to ETOH malar ratio				
Temperature (C)*	0.00021	0.000044	4.806	0.000
Water to ETOH malar ratio				

S = 0.2752 R-Sq = 96.5% R-Sq(adj) = 96.0%

Analysis of Variance for H2 Y. (mol/mol)

Source	DF	Seq SS	Adj SS	Adj MS	F	P
Regression	5	70.379	70.379	14.07575	185.88	0.000
Linear	3	65.143	10.183	3.39449	44.83	0.000
Square	1	3.487	3.487	3.48690	46.05	0.000
Interaction	1	1.749	1.749	1.74901	23.10	0.000
Residual Error	34	2.575	2.575	0.07573		
Lack-of-Fit	9	1.433	1.433	0.15925	3.49	0.006
Pure Error	25	1.141	1.141	0.04566		
Total	39	72.953				

Obs	StdOrder	H2 Y. (mol/mol)	Fit	SE Fit	Residual	St Resid
1	9	0.540	0.943	0.087	-0.403	-1.54
2	7	0.890	0.712	0.141	0.178	0.75
3	26	2.100	2.708	0.141	-0.608	-2.57 R
4	4	4.800	4.690	0.141	0.110	0.47
5	34	2.700	2.632	0.087	0.068	0.26
6	16	2.800	2.616	0.062	0.184	0.69

7	31	1.500	1.350	0.087	0.150	0.57
8	1	0.000	-0.008	0.141	0.008	0.04
9	39	2.600	2.616	0.062	-0.016	-0.06
10	35	2.700	2.616	0.062	0.084	0.31
11	24	4.900	4.690	0.141	0.210	0.89
12	28	4.800	4.721	0.141	0.079	0.34
13	22	2.400	2.677	0.141	-0.277	-1.17
14	20	2.700	2.616	0.062	0.084	0.31
15	33	2.900	2.601	0.087	0.299	1.15
16	17	2.600	2.616	0.062	-0.016	-0.06
17	27	0.870	0.712	0.141	0.158	0.67
18	18	2.500	2.616	0.062	-0.116	-0.43
19	11	1.600	1.350	0.087	0.250	0.96
20	5	0.000	0.023	0.141	-0.023	-0.10
21	3	0.890	0.681	0.141	0.209	0.88
22	29	0.580	0.943	0.087	-0.363	-1.39
23	23	0.860	0.681	0.141	0.179	0.76
24	2	2.400	2.677	0.141	-0.277	-1.17
25	13	2.700	2.601	0.087	0.099	0.38
26	14	2.600	2.632	0.087	-0.032	-0.12
27	19	2.700	2.616	0.062	0.084	0.31
28	25	0.000	0.023	0.141	-0.023	-0.10
29	36	2.500	2.616	0.062	-0.116	-0.43
30	8	4.700	4.721	0.141	-0.021	-0.09
31	12	2.200	2.701	0.087	-0.501	-1.92
32	32	2.100	2.701	0.087	-0.601	-2.30 R
33	21	0.000	-0.008	0.141	0.008	0.04
34	10	4.300	4.290	0.087	0.010	0.04
35	15	2.800	2.616	0.062	0.184	0.69
36	40	2.700	2.616	0.062	0.084	0.31
37	38	2.600	2.616	0.062	-0.016	-0.06
38	6	3.500	2.708	0.141	0.792	3.35 R
39	37	2.600	2.616	0.062	-0.016	-0.06
40	30	4.200	4.290	0.087	-0.090	-0.34

R denotes an observation with a large standardized residual.

Response Surface Regression: ETOH con. in versus Temperature ; ...

The analysis was done using uncoded units.

Estimated Regression Coefficients for ETOH con. into gases (%)

Term	Coef	SE Coef	T	P
Constant	-69.8913	13.0151	-5.370	0.000
Temperature (C)	0.3285	0.0801	4.102	0.000
Water to ETOH malar ratio	4.4995	0.7255	6.202	0.000
LHSV (h -1)	-13.2982	17.4113	-0.764	0.451
Temperature (C)*Temperature (C)	-0.0001	0.0001	-1.294	0.206
Water to ETOH malar ratio* Water to ETOH malar ratio	-0.0973	0.0226	-4.301	0.000
LHSV (h -1)*LHSV (h -1)	13.1800	13.0311	1.011	0.320
Temperature (C)* Water to ETOH malar ratio	-0.0025	0.0009	-2.693	0.011
Temperature (C)*LHSV (h -1)	0.0219	0.0223	0.983	0.333
Water to ETOH malar ratio* LHSV (h -1)	-0.5034	0.3183	-1.581	0.124

S = 5.850   R-Sq = 95.6%   R-Sq(adj) = 94.2%

Analysis of Variance for ETOH con. into gases (%)

Source	DF	Seq SS	Adj SS	Adj MS	F	P
Regression	9	22045.3	22045.3	2449.47	71.59	0.000
Linear	3	20367.0	2625.2	875.06	25.57	0.000
Square	3	1311.5	1311.5	437.18	12.78	0.000
Interaction	3	366.7	366.7	122.23	3.57	0.025
Residual Error	30	1026.5	1026.5	34.22		
Lack-of-Fit	5	358.3	358.3	71.67	2.68	0.045
Pure Error	25	668.2	668.2	26.73		
Total	39	23071.8				

Obs	StdOrder	ETOH con. into gases (%)	Fit	SE Fit	Residual	St Resid	
1	9	26.000	21.664	2.898	4.336	0.85	
2	7	25.000	22.197	3.684	2.803	0.62	
3	26	80.000	76.697	3.684	3.303	0.73	
4	4	81.000	78.847	3.684	2.153	0.47	
5	34	61.000	59.464	2.898	1.536	0.30	
6	16	58.000	55.891	1.422	2.109	0.37	
7	31	45.000	37.664	2.898	7.336	1.44	
8	1	0.000	0.097	3.684	-0.097	-0.02	
9	39	59.000	55.891	1.422	3.109	0.55	
10	35	61.000	55.891	1.422	5.109	0.90	
11	24	82.000	78.847	3.684	3.153	0.69	
12	28	79.000	79.197	3.684	-0.197	-0.04	
13	22	65.000	67.097	3.684	-2.097	-0.46	
14	20	45.000	55.891	1.422	-10.891	-1.92	
15	33	65.000	57.364	2.898	7.636	1.50	
16	17	54.000	55.891	1.422	-1.891	-0.33	
17	27	26.000	22.197	3.684	3.803	0.84	
18	18	58.000	55.891	1.422	2.109	0.37	
19	11	44.000	37.664	2.898	6.336	1.25	
20	5	0.000	3.947	3.684	-3.947	-0.87	
21	3	24.000	27.597	3.684	-3.597	-0.79	
22	29	25.000	21.664	2.898	3.336	0.66	
23	23	25.000	27.597	3.684	-2.597	-0.57	
24	2	60.000	67.097	3.684	-7.097	-1.56	
25	13	60.000	57.364	2.898	2.636	0.52	
26	14	58.000	59.464	2.898	-1.464	-0.29	
27	19	58.000	55.891	1.422	2.109	0.37	
28	25	0.000	3.947	3.684	-3.947	-0.87	
29	36	34.000	55.891	1.422	-21.891	-3.86	R
30	8	77.000	79.197	3.684	-2.197	-0.48	
31	12	52.000	52.664	2.898	-0.664	-0.13	
32	32	50.000	52.664	2.898	-2.664	-0.52	
33	21	0.000	0.097	3.684	-0.097	-0.02	
34	10	85.000	83.664	2.898	1.336	0.26	
35	15	58.000	55.891	1.422	2.109	0.37	
36	40	53.000	55.891	1.422	-2.891	-0.51	
37	38	56.000	55.891	1.422	0.109	0.02	
38	6	77.000	76.697	3.684	0.303	0.07	
39	37	56.000	55.891	1.422	0.109	0.02	
40	30	85.000	83.664	2.898	1.336	0.26	

R denotes an observation with a large standardized residual.

Response Surface Regression: ETOH con. in versus Temperature ; ...

The analysis was done using uncoded units.

Estimated Regression Coefficients for ETOH con. into gases (%)

Term	Coef	SE Coef	T	P
Constant	-57.8203	6.42866	-8.994	0.000
Temperature (C)	0.2404	0.01559	15.417	0.000
Water to ETOH malar ratio	4.3199	0.58343	7.404	0.000
LHSV (h -1)	2.4000	3.05335	0.786	0.437
Water to ETOH malar ratio* Water to ETOH malar ratio	-0.1011	0.01714	-5.902	0.000
Temperature (C)* Water to ETOH malar ratio	-0.0025	0.00095	-2.636	0.013

S = 5.974 R-Sq = 94.7% R-Sq(adj) = 94.0%

Analysis of Variance for ETOH con. into gases (%)

Source	DF	Seq SS	Adj SS	Adj MS	F	P
Regression	5	21858.3	21858.3	4371.67	122.49	0.000
Linear	3	20367.0	8506.5	2835.49	79.45	0.000
Square	1	1243.2	1243.2	1243.22	34.83	0.000
Interaction	1	248.1	248.1	248.06	6.95	0.013
Residual Error	34	1213.4	1213.4	35.69		
Lack-of-Fit	9	545.3	545.3	60.59	2.27	0.051
Pure Error	25	668.2	668.2	26.73		
Total	39	23071.8				

Obs	StdOrder	ETOH con. into gases (%)	Fit	SE Fit	Residual	St Resid	
1	9	26.000	24.750	1.889	1.250	0.22	
2	7	25.000	26.088	3.061	-1.088	-0.21	
3	26	80.000	73.087	3.061	6.913	1.35	
4	4	81.000	78.113	3.061	2.887	0.56	
5	34	61.000	56.800	1.889	4.200	0.74	
6	16	58.000	55.750	1.336	2.250	0.39	
7	31	45.000	37.100	1.889	7.900	1.39	
8	1	0.000	1.112	3.061	-1.112	-0.22	
9	39	59.000	55.750	1.336	3.250	0.56	
10	35	61.000	55.750	1.336	5.250	0.90	
11	24	82.000	78.113	3.061	3.887	0.76	
12	28	79.000	80.213	3.061	-1.213	-0.24	
13	22	65.000	70.988	3.061	-5.987	-1.17	
14	20	45.000	55.750	1.336	-10.750	-1.85	
15	33	65.000	54.700	1.889	10.300	1.82	
16	17	54.000	55.750	1.336	-1.750	-0.30	
17	27	26.000	26.088	3.061	-0.088	-0.02	
18	18	58.000	55.750	1.336	2.250	0.39	
19	11	44.000	37.100	1.889	6.900	1.22	
20	5	0.000	3.212	3.061	-3.212	-0.63	
21	3	24.000	23.988	3.061	0.012	0.00	
22	29	25.000	24.750	1.889	0.250	0.04	
23	23	25.000	23.988	3.061	1.012	0.20	
24	2	60.000	70.988	3.061	-10.987	-2.14	R
25	13	60.000	54.700	1.889	5.300	0.94	
26	14	58.000	56.800	1.889	1.200	0.21	
27	19	58.000	55.750	1.336	2.250	0.39	
28	25	0.000	3.212	3.061	-3.212	-0.63	
29	36	34.000	55.750	1.336	-21.750	-3.74	R
30	8	77.000	80.213	3.061	-3.213	-0.63	
31	12	52.000	52.100	1.889	-0.100	-0.02	
32	32	50.000	52.100	1.889	-2.100	-0.37	
33	21	0.000	1.112	3.061	-1.112	-0.22	
34	10	85.000	86.750	1.889	-1.750	-0.31	
35	15	58.000	55.750	1.336	2.250	0.39	
36	40	53.000	55.750	1.336	-2.750	-0.47	

37	38	56.000	55.750	1.336	0.250	0.04
38	6	77.000	73.087	3.061	3.913	0.76
39	37	56.000	55.750	1.336	0.250	0.04
40	30	85.000	86.750	1.889	-1.750	-0.31

R denotes an observation with a large standardized residual.

———— 01/01/13 11:49:24 ص ————————————————————————

Welcome to Minitab, press F1 for help.
Retrieving project from file: 'C:\Program Files\MINITAB 14\Data\DOE 1.MPJ'

Response Surface Regression: CO Y. (mol/m versus Temperature ; ...

The analysis was done using uncoded units.

Estimated Regression Coefficients for CO Y. (mol/mol)

Term	Coef	SE Coef	T	P
Constant	-0.064056	0.141172	-0.454	0.653
Temperature (C)	-0.000393	0.000869	-0.452	0.654
Water to ETOH malar ratio	0.033507	0.007869	4.258	0.000
LHSV (h -1)	0.083676	0.188856	0.443	0.661
Temperature (C)*Temperature (C)	0.000002	0.000001	2.025	0.052
Water to ETOH malar ratio* Water to ETOH malar ratio	-0.000728	0.000245	-2.965	0.006
LHSV (h -1)*LHSV (h -1)	-0.092616	0.141346	-0.655	0.517
Temperature (C)* Water to ETOH malar ratio	-0.000045	0.000010	-4.452	0.000
Temperature (C)*LHSV (h -1)	0.000067	0.000242	0.276	0.785
Water to ETOH malar ratio* LHSV (h -1)	-0.001224	0.003453	-0.355	0.725

S = 0.06345 R-Sq = 76.5% R-Sq(adj) = 69.5%

Analysis of Variance for CO Y. (mol/mol)

Source	DF	Seq SS	Adj SS	Adj MS	F	P
Regression	9	0.39422	0.39422	0.043802	10.88	0.000
Linear	3	0.26341	0.08442	0.028140	6.99	0.001
Square	3	0.05019	0.05019	0.016730	4.16	0.014
Interaction	3	0.08062	0.08062	0.026873	6.68	0.001
Residual Error	30	0.12077	0.12077	0.004026		
Lack-of-Fit	5	0.08480	0.08480	0.016961	11.79	0.000
Pure Error	25	0.03597	0.03597	0.001439		
Total	39	0.51499				

Obs	StdOrder	CO Y. (mol/mol)	Fit	SE Fit	Residual	St Resid
1	9	0.180	0.169	0.031	0.011	0.19
2	7	0.150	0.100	0.040	0.050	1.02
3	26	0.420	0.396	0.040	0.024	0.50
4	4	0.210	0.205	0.040	0.005	0.11
5	34	0.170	0.202	0.031	-0.032	-0.59
6	16	0.230	0.226	0.015	0.004	0.06
7	31	0.280	0.172	0.031	0.108	1.95
8	1	0.000	0.032	0.040	-0.032	-0.65

9	39	0.220	0.226	0.015	-0.006	-0.10	
10	35	0.230	0.226	0.015	0.004	0.06	
11	24	0.210	0.205	0.040	0.005	0.11	
12	28	0.210	0.190	0.040	0.020	0.41	
13	22	0.380	0.388	0.040	-0.008	-0.15	
14	20	0.260	0.226	0.015	0.034	0.55	
15	33	0.330	0.214	0.031	0.116	2.10	R
16	17	0.220	0.226	0.015	-0.006	-0.10	
17	27	0.140	0.100	0.040	0.040	0.82	
18	18	0.220	0.226	0.015	-0.006	-0.10	
19	11	0.290	0.172	0.031	0.118	2.13	R
20	5	0.000	0.023	0.040	-0.023	-0.46	
21	3	0.100	0.132	0.040	-0.032	-0.64	
22	29	0.220	0.169	0.031	0.051	0.92	
23	23	0.120	0.132	0.040	-0.012	-0.23	
24	2	0.270	0.388	0.040	-0.118	-2.38	R
25	13	0.320	0.214	0.031	0.106	1.92	
26	14	0.150	0.202	0.031	-0.052	-0.95	
27	19	0.230	0.226	0.015	0.004	0.06	
28	25	0.000	0.023	0.040	-0.023	-0.46	
29	36	0.220	0.226	0.015	-0.006	-0.10	
30	8	0.200	0.190	0.040	0.010	0.20	
31	12	0.060	0.119	0.031	-0.059	-1.08	
32	32	0.090	0.119	0.031	-0.029	-0.53	
33	21	0.000	0.032	0.040	-0.032	-0.65	
34	10	0.450	0.392	0.031	0.058	1.05	
35	15	0.230	0.226	0.015	0.004	0.06	
36	40	0.160	0.226	0.015	-0.066	-1.07	
37	38	0.110	0.226	0.015	-0.116	-1.89	
38	6	0.380	0.396	0.040	-0.016	-0.32	
39	37	0.110	0.226	0.015	-0.116	-1.89	
40	30	0.410	0.392	0.031	0.018	0.32	

R denotes an observation with a large standardized residual.

Response Surface Regression: CO Y. (mol/m versus Temperature ; ...

The analysis was done using uncoded units.

Estimated Regression Coefficients for CO Y. (mol/mol)

Term	Coef	SE Coef	T	P
Constant	-0.225756	0.070927	-3.183	0.003
Temperature (C)	0.001349	0.000183	7.375	0.000
Water to ETOH malar ratio	0.013171	0.004168	3.160	0.003
LHSV (h -1)	-0.013714	0.035806	-0.383	0.704
Temperature (C)* Water to ETOH malar ratio	-0.000045	0.000011	-4.032	0.000

S = 0.07006 R-Sq = 66.6% R-Sq(adj) = 62.8%

Analysis of Variance for CO Y. (mol/mol)

Source	DF	Seq SS	Adj SS	Adj MS	F	P
Regression	4	0.34322	0.34322	0.085804	17.48	0.000
Linear	3	0.26341	0.34163	0.113877	23.20	0.000
Interaction	1	0.07981	0.07981	0.079806	16.26	0.000
Residual Error	35	0.17177	0.17177	0.004908		
Lack-of-Fit	10	0.13581	0.13581	0.013581	9.44	0.000
Pure Error	25	0.03597	0.03597	0.001439		
Total	39	0.51499				

CO Y.

Obs	StdOrder	(mol/mol)	Fit	SE Fit	Residual	St Resid
1	9	0.180	0.093	0.019	0.087	1.29
2	7	0.150	0.131	0.034	0.019	0.31
3	26	0.420	0.407	0.034	0.013	0.21
4	4	0.210	0.225	0.034	-0.015	-0.24
5	34	0.170	0.199	0.019	-0.029	-0.42
6	16	0.230	0.205	0.011	0.025	0.37
7	31	0.280	0.231	0.019	0.049	0.73
8	1	0.000	0.055	0.034	-0.055	-0.90
9	39	0.220	0.205	0.011	0.015	0.22
10	35	0.230	0.205	0.011	0.025	0.37
11	24	0.210	0.225	0.034	-0.015	-0.24
12	28	0.210	0.213	0.034	-0.003	-0.05
13	22	0.380	0.419	0.034	-0.039	-0.64
14	20	0.260	0.205	0.011	0.055	0.80
15	33	0.330	0.211	0.019	0.119	1.77
16	17	0.220	0.205	0.011	0.015	0.22
17	27	0.140	0.131	0.034	0.009	0.15
18	18	0.220	0.205	0.011	0.015	0.22
19	11	0.290	0.231	0.019	0.059	0.88
20	5	0.000	0.043	0.034	-0.043	-0.70
21	3	0.100	0.143	0.034	-0.043	-0.70
22	29	0.220	0.093	0.019	0.127	1.88
23	23	0.120	0.143	0.034	-0.023	-0.38
24	2	0.270	0.419	0.034	-0.149	-2.44 R
25	13	0.320	0.211	0.019	0.109	1.63
26	14	0.150	0.199	0.019	-0.049	-0.72
27	19	0.230	0.205	0.011	0.025	0.37
28	25	0.000	0.043	0.034	-0.043	-0.70
29	36	0.220	0.205	0.011	0.015	0.22
30	8	0.200	0.213	0.034	-0.013	-0.21
31	12	0.060	0.178	0.019	-0.118	-1.75
32	32	0.090	0.178	0.019	-0.088	-1.31
33	21	0.000	0.055	0.034	-0.055	-0.90
34	10	0.450	0.316	0.019	0.134	1.99
35	15	0.230	0.205	0.011	0.025	0.37
36	40	0.160	0.205	0.011	-0.045	-0.64
37	38	0.110	0.205	0.011	-0.095	-1.37
38	6	0.380	0.407	0.034	-0.027	-0.44
39	37	0.110	0.205	0.011	-0.095	-1.37
40	30	0.410	0.316	0.019	0.094	1.40

APPENDIX H
SYSTEM PROTOTYPE DESIGN AND MATLAB CODE FOR HYDROGEN PREDICTION

H.1 System Prototype Design

As shown in Figure H.1, the system prototype design was constructed in order to facilitate the user prediction of the H_2 yield, CO yield, and ethanol conversion and via ethanol steam reforming. The system was called Hydrogen Production ANN System. The graphical user interface (GUI) is containing three main regions as defined in Table H.1. First region is the artificial neural network design short form (ANN-Design), its contain training and testing stages. Second region is the neural network model evaluation (Run-button), where the third region is the neural network versus the numerical model (ANN-NM). The following section contains detailed explanations of their tasks.

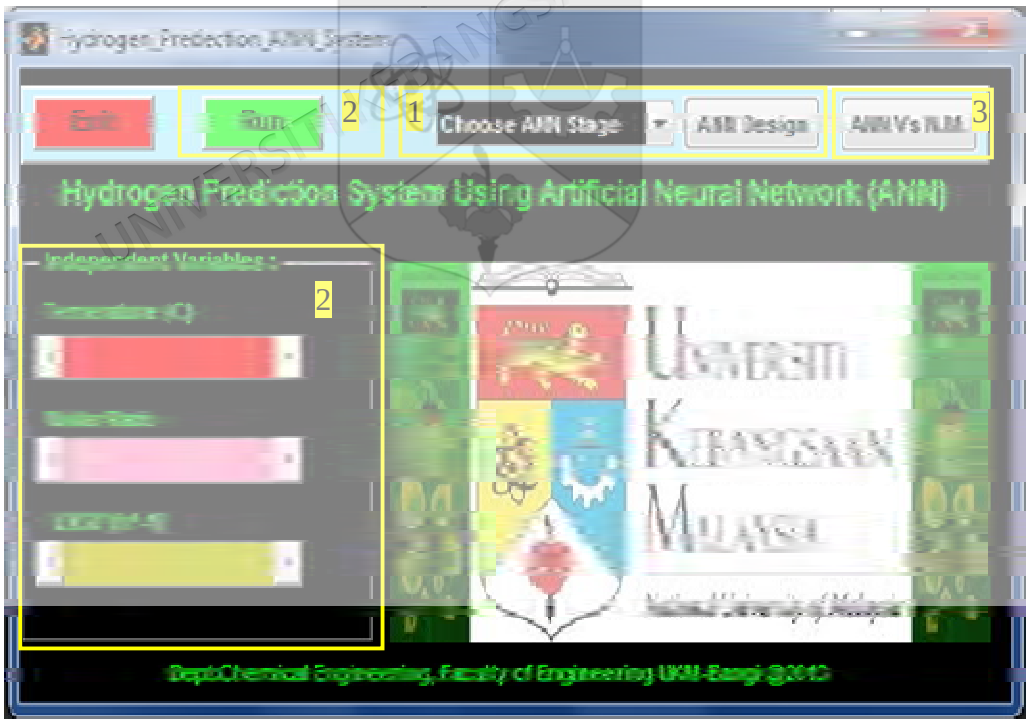

Figure H.1 Screening prototype system

Table H.1 Regions in the screening prototype system and their definitions

Menu	Description
Region 1	Artificial Neural network design (ANN-Design)
Region 2	Neural network model Evolution of (Run)
Region 3	Neural network versus Numerical model (ANN-NM)

Figure H.2 shows the block diagram of hydrogen production ANN system component that includes ANN design include training and testing stages to select the best topology model, neural network model evaluation to predict the three outputs, and nneural network versus numerical model (ANN-NM) for comparison and validation.

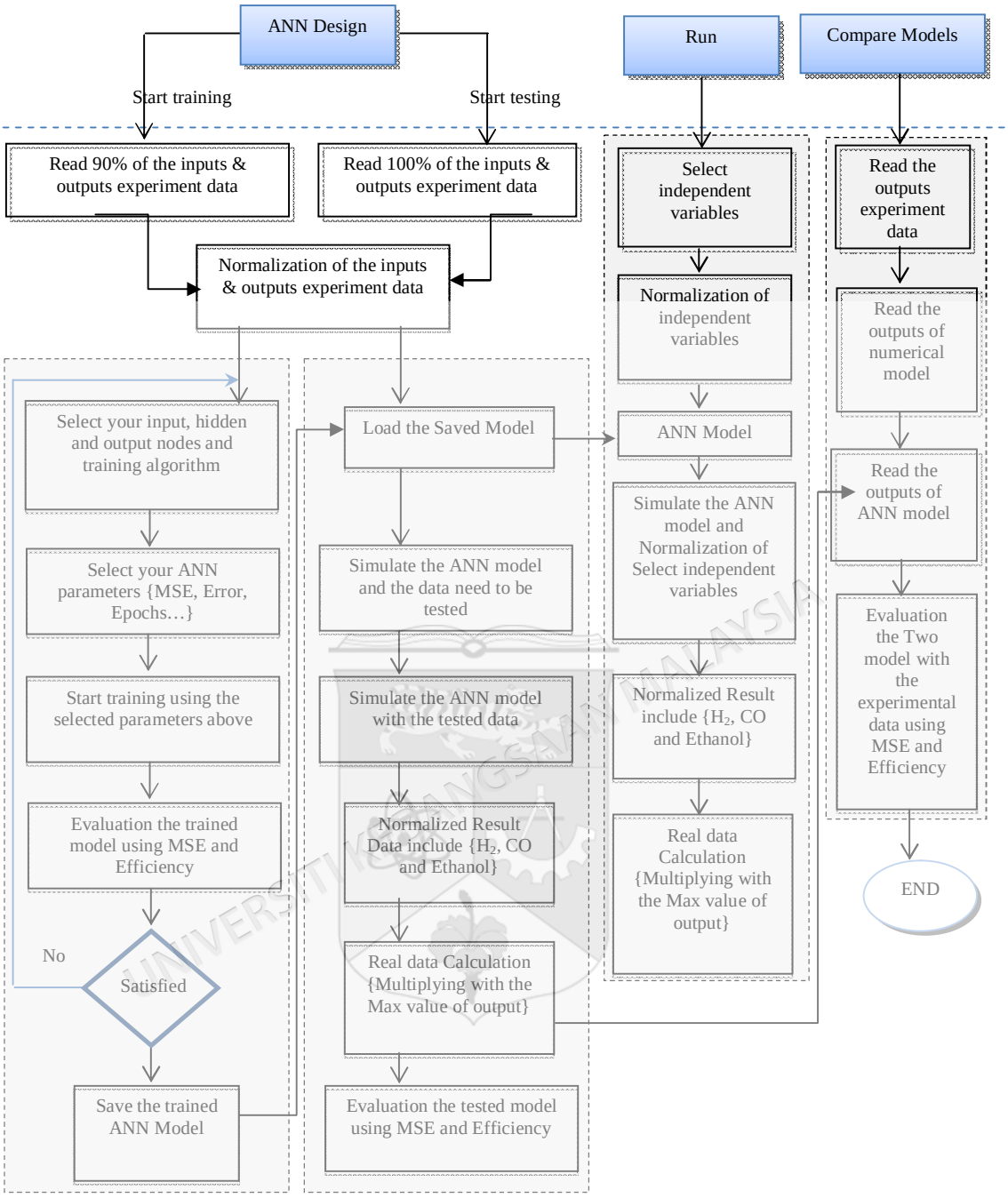

Figure H.2 Block diagram of hydrogen production ANN system components

1. Artificial neural net work design (ANN-Design)

The drop-down "Choose ANN stage" menu contained the stage of training and testing for best ANN design. This is the first step, where a user selects ANN design. If the user uses the system for training, the user should select from the drop-down “train stage " and click the ANN design bush button to execute. The same procedure carried

out for testing stage. ANN design has been used to obtain the best model topology. Figure H-3 shows the artificial neural net work design process via ANN-Design menu and the associated main tasks can be listed as:

1. Select the ANN stage (train stage or test stage)
2. Run the ANN design based on the selected item from step 1

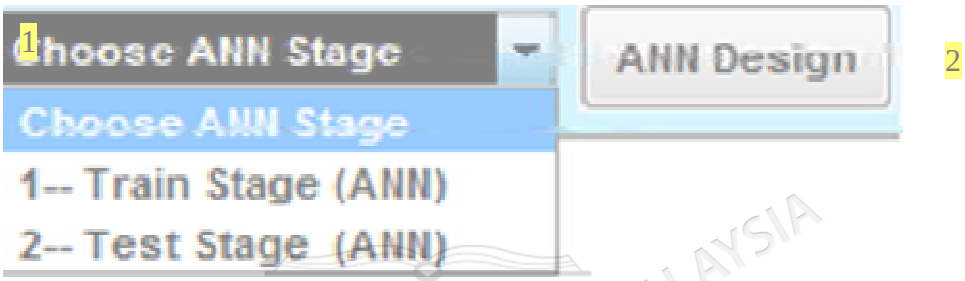

Figure H.3 Presentation of ANN design-menu include both training and testing stages

a) Training stage (ANN)

After selected the ANN stage from the drop-down “Choose ANN stage” menu, a user can use the "Train Model" button for training the data of the experimental runs or any new data from different experimental. As mentioned previously, the "trainlm, trainscg, traingdx" back-propagation algorithms with different inputs and hidden layers were use used for training the data of this study. The training iterations were repeated until the performance error decreased to an acceptable level. For a single iteration, the error is calculated and the summed errors from overall neurons are divided by the size of data used in the training process to estimate average MSE. Thereafter, the model is saved. The following flowchart shows the training stage process (Figure H-4).

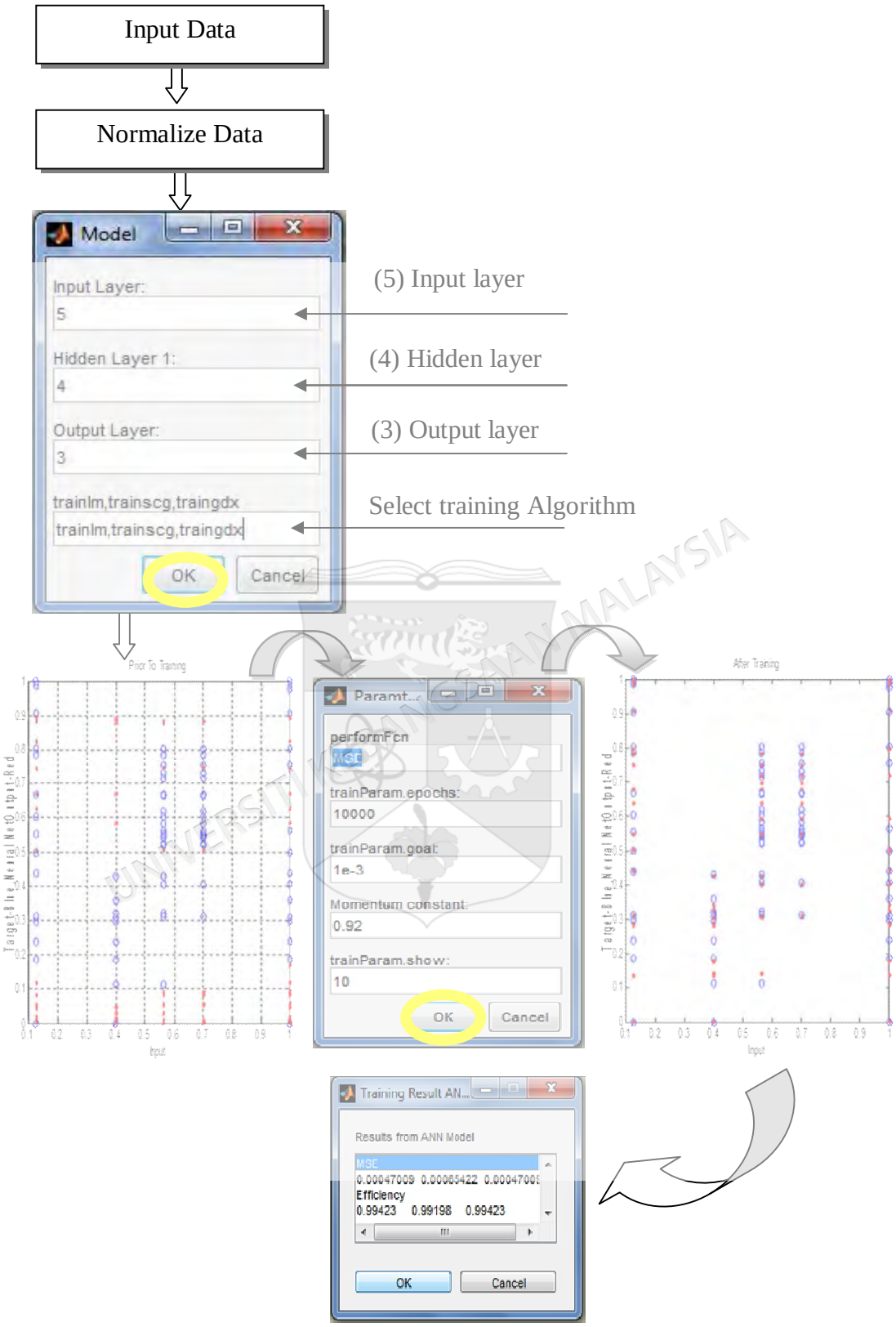

Figure H.4 Presentation of block diagram of the training stage process

b) During training ANN

During this stage, two main schemes are examined via (performance) for best training performance, which is examined by the MSE and neural network training regression. The schemes implemented are briefly shown in Figure H-5.

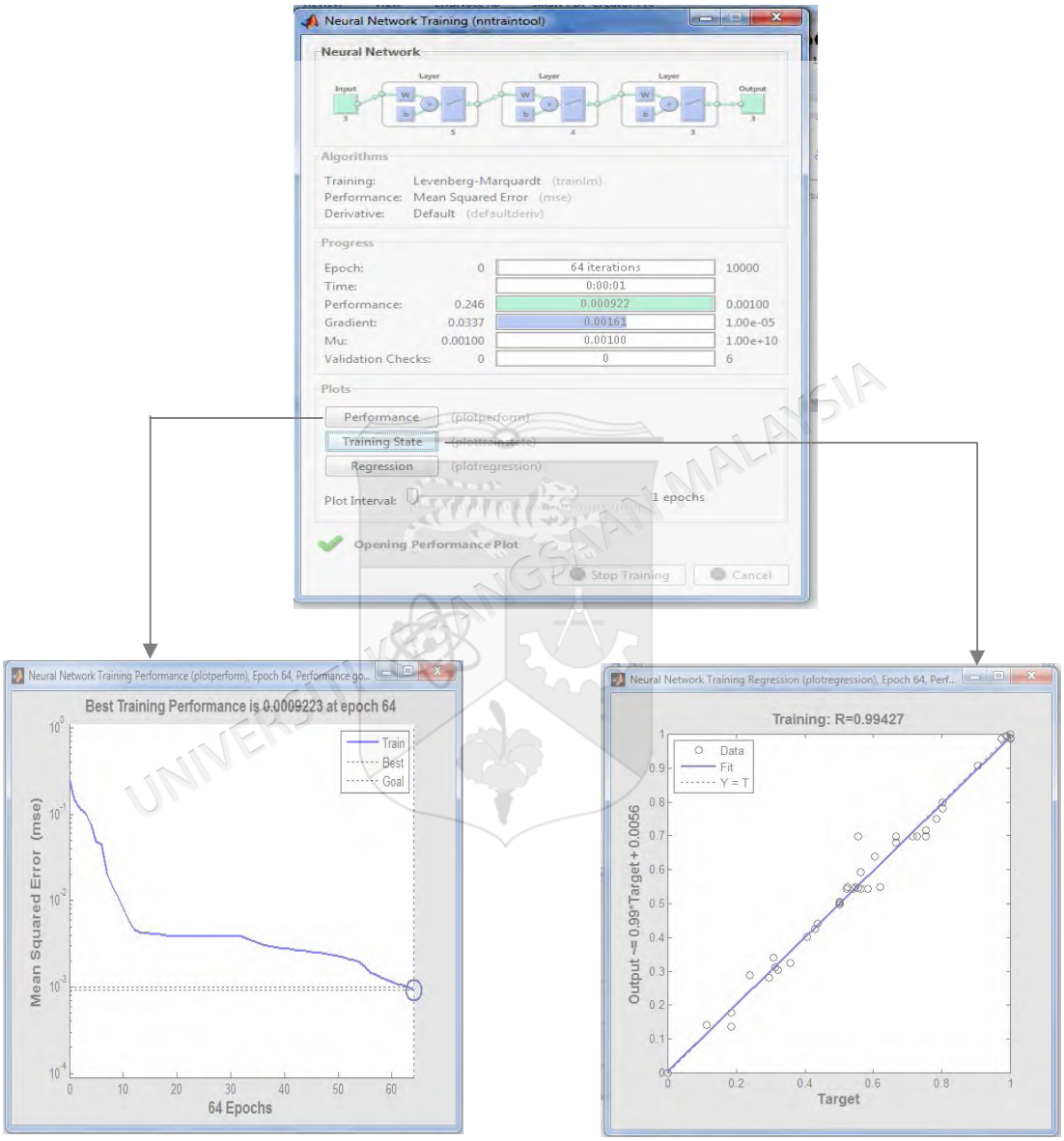

Figure H.5 Presentation of ANN-design during training ANN

c) Testing stage (ANN)

In the testing stage, the model predicts values of output based on input data values entered, where the model gained the prediction capability from the training stage. The different between the predicted outputs provided by the model and measured targets is

defined as the error. The total error is estimated in form of MSE and efficiency which used for the model evaluation. The following Figure H-6 shows a presentation of ANN-design in the testing stage process.

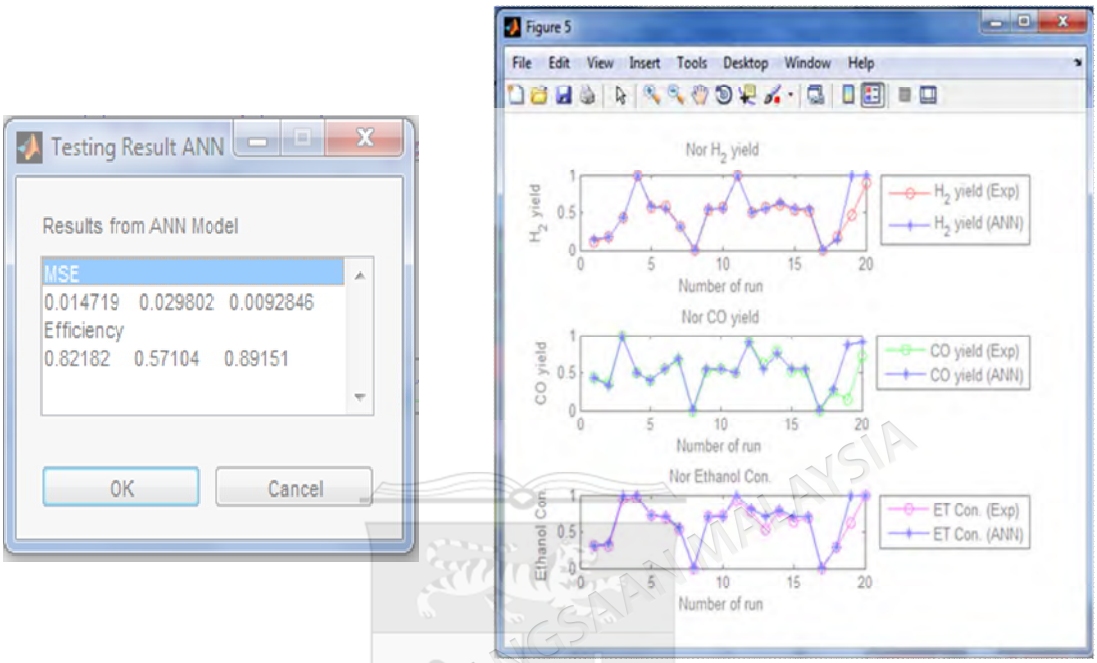

Figure H.6 Presentation of ANN-design in the ANN testing

2. Neural network model evolution (Run)

For run a new data, a user has to select the "RUN" button. At the first step, the user has to select three input parameters (temperature, molar ratio, and LHSV) from the sliders menu. If the user uses the system for a new input values, the user should select a value ruling the slider of each input. Thereafter, the appropriate ANN model based on the best selection of the study will be loaded, and H_2 yield, CO yield, and ethanol conversion values will be estimated. The Hydrogen production ANN System will subsequently display a testing result window of the predicted values of the H_2 yield, CO yield, and ethanol conversion, respectively. Figure H-7 shows presentation of the neural network model evolution menu process.

Figure H.7 Presentation of the neural network model evolution menu

3. Experimental versus ANN and numerical models

Additional bush button used to execute the comparison between experimental values versus both neural network and numerical model. Figure H.8 show the experimental value versus predicted value from numerical model and neural network model developed. This measurement result is summarized and displayed in test result window includes the efficiency of both experimental versus ANN and experimental versus Numerical model, respectively.

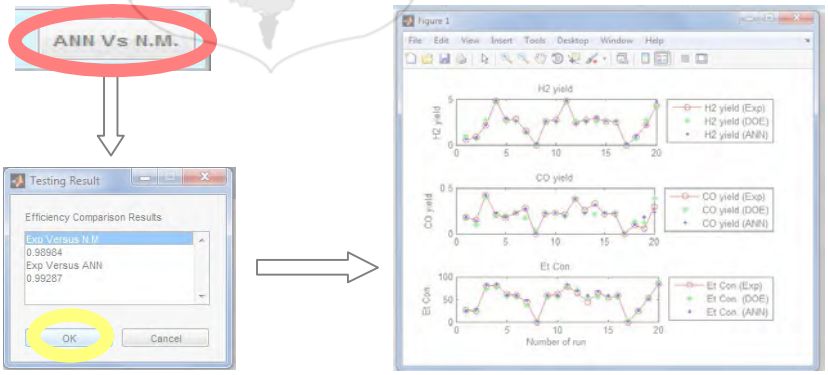

Figure H.8 Presentation of the Experimental versus ANN and numerical models

H.2 Matlab Code for Hydrogen Prediction

```
function varargout = Hydrogen_Prediction_ANN_System(varargin)
gui_Singleton = 1;
gui_State = struct('gui_Name',       mfilename, ...
```

```
                   'gui_Singleton',  gui_Singleton, ...
                   'gui_OpeningFcn',
@Hydrogen_Prediction_ANN_System_OpeningFcn, ...
                   'gui_OutputFcn',
@Hydrogen_Prediction_ANN_System_OutputFcn, ...
                   'gui_LayoutFcn',  [] , ...
                   'gui_Callback',   []);
if nargin && ischar(varargin{1})
    gui_State.gui_Callback = str2func(varargin{1});
end

if nargout
    [varargout{1:nargout}] = gui_mainfcn(gui_State, varargin{:});
else
    gui_mainfcn(gui_State, varargin{:});
end
% End initialization code - DO NOT EDIT


% --- Executes just before Hydrogen_Prediction_ANN_System is made
visible.
function           Hydrogen_Prediction_ANN_System_OpeningFcn(hObject,
eventdata, handles, varargin)
handles.output = hObject;

% Update handles structure
guidata(hObject, handles);

set(handles.slider2, 'enable', 'off');
set(handles.slider3, 'enable', 'off');
set(handles.slider4, 'enable', 'off');
D=imread('C:\MATLAB7\work\Ahmed_PhD\logo1.jpg');
axes(handles.axes1),imagesc(D),axis off

% --- Outputs from this function are returned to the command line.
function                                varargout                                =
Hydrogen_Prediction_ANN_System_OutputFcn(hObject, eventdata, handles)

varargout{1} = handles.output;


% --- Executes on slider movement.
function slider2_Callback(hObject, eventdata, handles)
sliderValue = get(hObject,'Value');
set(handles.text5, 'String', sliderValue);

% --- Executes during object creation, after setting all properties.
function slider2_CreateFcn(hObject, eventdata, handles)
% Hint: slider controls usually have a light gray background.
if                              isequal(get(hObject,'BackgroundColor'),
get(0,'defaultUicontrolBackgroundColor'))
    set(hObject,'BackgroundColor',[.9 .9 .9]);
end


% --- Executes on slider movement.
function slider3_Callback(hObject, eventdata, handles)
sliderValue = get(hObject,'Value');
```

```
set(handles.text6, 'String', sliderValue);


% --- Executes during object creation, after setting all properties.
function slider3_CreateFcn(hObject, eventdata, handles)

% Hint: slider controls usually have a light gray background.
if                              isequal(get(hObject,'BackgroundColor'),
get(0,'defaultUicontrolBackgroundColor'))
    set(hObject,'BackgroundColor',[.9 .9 .9]);
end


% --- Executes on slider movement.
function slider4_Callback(hObject, eventdata, handles)
sliderValue = get(hObject,'Value');
set(handles.text7, 'String', sliderValue);


% --- Executes during object creation, after setting all properties.
function slider4_CreateFcn(hObject, eventdata, handles)
if                              isequal(get(hObject,'BackgroundColor'),
get(0,'defaultUicontrolBackgroundColor'))
    set(hObject,'BackgroundColor',[.9 .9 .9]);
end

%%%=================================================================
======
            %% ANN_Design Function
%%%=================================================================
======
function ANN_Design_Callback(hObject, eventdata, handles)
handles = guihandles;
ANN_value=get(handles.Select_ANN,'Value');
switch ANN_value
    case 1
        warndlg('Please  Select  Train/Test  Stage...!','Warning..ANN
Model');
        return

    case 2
    %%%=================
     %%% ANN Classical
    %%%=================
        clc
        filename='C:\MATLAB7\work\Ahmed_PhD\Data.xls';

        %%%%-- Input Data
        [T]= xlsread(filename,'Sheet1','C2:C19');
        [MR]= xlsread(filename,'Sheet1','D2:D19');
        [LHSV]= xlsread(filename,'Sheet1','E2:E19');

        %%%%-- Output Data
        [H2_yield]= xlsread(filename,'Sheet1','G2:G19');
        [CO_yield]= xlsread(filename,'Sheet1','H2:H19');
        [Ethanol]= xlsread(filename,'Sheet1','I2:I19');

        %%%%-- Plot of the Input Data before Normalization
```

```
        figure(1)
        set(gca,'color',[ 0 0 0])
        set(gcf,'color',[ 1 1 1])
        subplot(221),plot(T,'r-*'),  title('Input  1'),xlabel('Number
of run'),ylabel('Temperature(C)'),%axis([0 35 300 700])
        subplot(222),plot(MR,'g-*'),  title('Input  2'),xlabel('Number
of run'),ylabel('MR'),%axis([0 35 0.04 0.105])
        subplot(223),plot(LHSV,'b-*'),title('Input  3'),xlabel('Number
of run'),ylabel('LHSV (h^-1)'),%axis([0 35 0.1 0.6])


        %%%%-- Plot of the Out Data before Normalization
        figure(2)
        set(gca,'color',[ 0 0 0])
        set(gcf,'color',[ 1 1 1])
        subplot(221),plot(H2_yield,'r-*'),              title('Output
1'),xlabel('Number of run'),ylabel('H_2 yield (Mol/Mol)'),%axis([0 35
0 70])
        subplot(222),plot(CO_yield,'g-*'),              title('Output
2'),xlabel('Number of run'),ylabel('CO yield (Mol/Mol)'),%axis([0 35
0 100])
        subplot(223),plot(Ethanol,'b-*'),title('Output
3'),xlabel('Number of run'),ylabel('Ethanol Conv.(%)'),%axis([0 35 10
100])

        %%%%-- Normalization input
        Nor_T=T./max(T);
        Nor_MR=MR./max(MR);
        Nor_LHSV=LHSV./max(LHSV);

        %%%%-- Normalization output
        Nor_H2_yield=H2_yield./max(H2_yield);
        Nor_CO_yield=CO_yield./max(CO_yield);
        Nor_Ethanol=Ethanol./max(Ethanol);

        %%%%-- Plot of the Input Data after Normalization
        figure(3)
        set(gca,'color',[ 0 0 0])
        set(gcf,'color',[ 1 1 1])
        subplot(221),plot(Nor_T,'r-*'),        title('Nor        Input
1'),xlabel('Number of run'),ylabel('Temperature(C)'),axis([0 20 0 1])
        subplot(222),plot(Nor_MR,'g-*'),       title('Nor       Input
2'),xlabel('Number of run'),ylabel('(h^-1)'),axis([0 20 0 1])
        subplot(223),plot(Nor_LHSV,'b-*'),title('Nor             Input
3'),xlabel('Number of run'),ylabel('H_2 yield (Mol/Mol)'),axis([0 20
0 1])


        %%%%-- Plot of the Output Data after Normalization
        figure(4)
        set(gca,'color',[ 0 0 0])
        set(gcf,'color',[ 1 1 1])
        subplot(221),plot(Nor_H2_yield,'r-*'),    title('Nor    Output
1'),xlabel('Number of run'),ylabel('H_2 yield (Mol/Mol)'),axis([0 20
0 1])
        subplot(222),plot(Nor_CO_yield,'g-*'),title('Nor       Output
2'),xlabel('Number of run'),ylabel('CO yield (Mol/Mol)'),axis([0 20 0
1])
```

```
        subplot(223),plot(Nor_Ethanol,'b-*'),title('Nor        Output
3'),xlabel('Number  of  run'),ylabel('Ethanol  Conv.(%)'),axis([0  20  0
1])


        Data_input=[Nor_T,Nor_MR,Nor_LHSV]';
        Target_input=[Nor_H2_yield,Nor_CO_yield,Nor_Ethanol]';


        %%%% Design ANN Model  (feed-forward backpropagation network)
        prompt={'Input     Layer:','Hidden     Layer     1:','Output
Layer:','trainlm,trainscg,traingdx'};

name='Model';numlines=1;defaultanswer={'5','4','3','trainlm,trainscg,
traingdx'};

        options.Resize='on';
        options.WindowStyle='normal';
        options.Interpreter='tex';

        answer=inputdlg(prompt,name,numlines,defaultanswer,options);
        if isempty(answer)
            msgbox('Cancelled Inputing Initialization','Model');
            return;
        end;

        InputLayer=str2num(answer{1});
        HiddenLayer1= str2num(answer{2});
        OutputLayer=str2num(answer{3});
        Algorithm=char(answer{4}) ; % Algorihm

        a=minmax(Data_input);
        net=newff([a],[InputLayer                    HiddenLayer1
OutputLayer],{'logsig','logsig','logsig'},Algorithm);%%      traingdx
trainscg, traingdm, traingda,
        net = init(net);

        Y= sim(net,Data_input) ;

        %%%After  Training
        figure(5)
        set(gcf,'color',[1 1 1]);
        set(gca,'color',[1 1 1]);
        hold on, box on

plot(Data_input,Target_input(1,:),'bo',Data_input,Y(1,:),'r.');xlabel
('Input'),ylabel('Target-Blue,Neural  NetOutput-Red'),title('Prior  To
Training')

plot(Data_input,Target_input(2,:),'bo',Data_input,Y(2,:),'r.');

plot(Data_input,Target_input(3,:),'bo',Data_input,Y(3,:),'r.');
        hold off


        pause(0.9)
        %%%-------------------------------------------------------------
--------------
```

```
prompt={'performFcn','trainParam.epochs:','trainParam.goal:','Momentu
m constant:','trainParam.show:'};
        name='Paramters';numlines=1;defaultanswer={'MSE','10000','1e-
3','0.92','10'};

        options.Resize='on';
        options.WindowStyle='normal';
        options.Interpreter='tex';

        answer=inputdlg(prompt,name,numlines,defaultanswer,options);
        if isempty(answer)
            msgbox('Cancelled Inputing Initialization','Model');
            return;
        end;

        net.performFcn =        char(answer{1}) ;       % Sum-Squared
Error performance function
        net.trainParam.epochs  =  str2num(answer{2});        % Maximum
number of epochs to train
        net.trainParam.goal =   str2num(answer{3});     % Performance
goal
        net.trainParam.mc  =      str2num(answer{4});       % Momentum
constant.
        net.trainParam.show  =    str2num(answer{5});        % Epochs
between displays (NaN for no displays)

        % 3-TRAIN  Train  Net_Orientation_Histogram  .and  seved  in  the
work space
        tic
        ANN_Model= train(net,Data_input, Target_input);grid
        save  C:\MATLAB7\work\Ahmed_PhD\ANN_Model

        YY= sim(ANN_Model,Data_input);

        %%% Before Training
        figure(6)
        set(gcf,'color',[1 1 1]);
        set(gca,'color',[1 1 1]);
        hold on, box on

plot(Data_input,Target_input(1,:),'bo',Data_input,YY(1,:),'r.');xlabe
l('Input'),ylabel('Target-Blue,Neural    NetOutput-Red'),title('After
Training')

plot(Data_input,Target_input(2,:),'bo',Data_input,YY(2,:),'r.');

plot(Data_input,Target_input(3,:),'bo',Data_input,YY(3,:),'r.');
        hold off


        %%%% MSE in EFF The Training
        [M N] = size(Target_input(1,:));
        error1 = (Target_input(1,:)-YY(1,:));
        MSE_Training1=sum(sum(error1 .* error1))/ (M * N);
        variance1=std(Target_input(1,:)).^2;
        Eff1=1-(MSE_Training1./variance1);
```

```
        %%%% MSE in EFF The Training
        [M N] = size(Target_input(2,:));
        error2 = (Target_input(2,:)-YY(2,:));
        MSE_Training2=sum(sum(error2 .* error2))/ (M * N);
        variance2=std(Target_input(1,:)).^2;
        Eff2=1-(MSE_Training2./variance2);

        %%%% MSE in EFF The Training
        [M N] = size(Target_input(1,:));
        error3 = (Target_input(1,:)-YY(1,:));
        MSE_Training3=sum(sum(error3 .* error3))/ (M * N);
        variance3=std(Target_input(1,:)).^2;
        Eff3=1-(MSE_Training3./variance3);

        MSE_Total=[MSE_Training1 MSE_Training2 MSE_Training3];
        Eff_Total=[Eff1 Eff2 Eff3];

        listdlg('PromptString','Results from ANN
Model','SelectionMode','single','ListString',{'MSE',num2str(MSE_Total
),'Efficiency',num2str(Eff_Total)},...
            'Name','Training Result ANN','ListSize',[200 80]);

   %%%====================
    %%% ANN TEST
   %%%====================
    case 3
        clear all
        filename='C:\MATLAB7\work\Ahmed_PhD\Data.xls';
        %%%%-- Input Data

        %%%%-- Input Data
        [T]= xlsread(filename,'Sheet1','C2:C21');
        [MR]= xlsread(filename,'Sheet1','D2:D21');
        [LHSV]= xlsread(filename,'Sheet1','E2:E21');

        %%%%-- Output Data
        [H2_yield]= xlsread(filename,'Sheet1','G2:G21');
        [CO_yield]= xlsread(filename,'Sheet1','H2:H21');
        [Ethanol]= xlsread(filename,'Sheet1','I2:I21');



        %%%%-- Normalization
        Nor_T=T./max(T);
        Nor_MR=MR./max(MR);
        Nor_LHSV=LHSV./max(LHSV);

        Nor_H2_yield=H2_yield./max(H2_yield);
        Nor_CO_yield=CO_yield./max(CO_yield);
        Nor_Ethanol=Ethanol./max(Ethanol);

        Data_Test=[Nor_T,Nor_MR,Nor_LHSV]';
        Target_test=[Nor_H2_yield,Nor_CO_yield,Nor_Ethanol]';


        load 'C:\MATLAB7\work\Ahmed_PhD\ANN_Model'
        Testing_ANN= sim(ANN_Model,Data_Test);
```

```
H2_yield=Testing_ANN(1,:)*4.8;
CO_yield=Testing_ANN(2,:)*0.42;
Ethanol=Testing_ANN(3,:)*85;


a=xlswrite('Data.xls',H2_yield','O2:O21');
b=xlswrite('Data.xls',CO_yield','P2:P21');
c=xlswrite('Data.xls',Ethanol','Q2:Q21');

t=1:20;
figure(5)
set(gca,'color',[ 0 0 0])
set(gcf,'color',[ 1 1 1])
subplot(311),plot(t,Target_test(1,:),'r-
o',t,Testing_ANN(1,:),'b-*'),title('Nor H_2 yield'),xlabel('Number of
run'),ylabel('H_2 yield'),%axis([0 35 0 1])
legend('H_2 yield (Exp)','H_2 yield (ANN)',-1)
subplot(312),plot(t,Target_test(2,:),'g-
o',t,Testing_ANN(2,:),'b-*'),title('Nor CO yield'),xlabel('Number of
run'),ylabel('CO yield'),%axis([0 35 0 1])
legend('CO yield (Exp)','CO yield (ANN)',-1)
subplot(313),plot(t,Target_test(3,:),'m-
o',t,Testing_ANN(3,:),'b-*'),title('Nor Ethanol Con.'),xlabel('Number
of run'),ylabel('Ethanol Con.'),%axis([0 35 0 1])
legend('ET Con. (Exp)','ET Con. (ANN)',-1)



%         %%%%-- Output Data DEO
%         [H2_yield]= xlsread(filename,'Sheet1','G2:G21');
%         [CO_yield]= xlsread(filename,'Sheet1','H2:H21');
%         [Ethanol]= xlsread(filename,'Sheet1','I2:I21');


%%%% MSE in EFF The Testing
[M N] = size(Target_test(1,:));
error1 = (Target_test(1,:)-Testing_ANN(1,:));
MSE_Testing1=sum(sum(error1 .* error1))/ (M * N);
varianceT1=std(Target_test(1,:)).^2;
Eff_T1=1-(MSE_Testing1./varianceT1);

%%%% MSE in EFF The Testing
[M N] = size(Target_test(2,:));
error2 = (Target_test(2,:)-Testing_ANN(2,:));
MSE_Testing2=sum(sum(error2 .* error2))/ (M * N);
varianceT2=std(Target_test(2,:)).^2;
Eff_T2=1-(MSE_Testing2./varianceT2);

%%%% MSE in EFF The Testing
[M N] = size(Target_test(3,:));
error3 = (Target_test(3,:)-Testing_ANN(3,:));
MSE_Testing3=sum(sum(error3 .* error3))/ (M * N);
varianceT3=std(Target_test(3,:)).^2;
Eff_T3=1-(MSE_Testing3./varianceT3);

MSE_Test_Total=[MSE_Testing1 MSE_Testing2 MSE_Testing3];
Eff_Test_Total=[Eff_T1 Eff_T2 Eff_T3];
```

```
        listdlg('PromptString','Results from ANN
Model','SelectionMode','single','ListString',{'MSE',num2str(MSE_Test_
Total),'Efficiency',num2str(Eff_Test_Total)},...
             'Name','Testing Result ANN','ListSize',[200 80]);

end


% --- Executes on button press in Close.
function Close_Callback(hObject, eventdata, handles)

selection=questdlg(['Do You Want to Close '
get(handles.figure1,'Name') '?'],...
                   [' ' get(handles.figure1,'Name') '...'],...
                   'Yes','No','No');
                   if strcmp(selection,'No')
                       return
                   end
                   close('Hydrogen Predection System (HPS-ANN)')
%%%%================================================================
======
function Run_Callback(hObject, eventdata, handles)
sliderStatus = get(handles.slider2, 'enable');
%%% Demand fulfilment

if  isequal(sliderStatus,'off')
    set(handles.slider2, 'enable', 'on');
    set(handles.slider2, 'Value', 200);
    set(handles.slider2, 'Max', 500);
    set(handles.slider2, 'Min', 200);
    set(handles.slider2, 'SliderStep', [0.1 0.1]);

    set(handles.slider3, 'enable', 'on');
    set(handles.slider3, 'Value', 3);
    set(handles.slider3, 'Max', 24);
    set(handles.slider3, 'Min', 3);
    set(handles.slider3, 'SliderStep', [0.1 0.1]);

    set(handles.slider4, 'enable', 'on');
    set(handles.slider4, 'Value', 0.125);
    set(handles.slider4, 'Max',  1);
    set(handles.slider4, 'Min',0.125);
    set(handles.slider4, 'SliderStep', [0.1 0.1]);

else
    Temperature = get(handles.slider2, 'Value');
    set(handles.slider2, 'Value',Temperature);

    MR = get(handles.slider3, 'Value');
    set(handles.slider3, 'Value', MR);

    LHSV= get(handles.slider4, 'Value');
    set(handles.slider4, 'Value', LHSV);


%     Factors=[Temperature,MR,LHSV]'
```

```
    Nor_Temperature=Temperature./500;
    Nor_MR=MR./24;
    Nor_LHSV=LHSV./1;


    Data_Test=[Nor_Temperature,Nor_MR, Nor_LHSV]';

    load 'C:\MATLAB7\work\Ahmed_PhD\ANN_Model'
    ANN_Test= sim(ANN_Model,Data_Test);

    H2_yield=ANN_Test(1)*4.8;
    CO_yield=ANN_Test(2)*0.42;
    Ethanol=ANN_Test(3)*85;

    listdlg('PromptString','Results from ANN Model',...
            'SelectionMode','single',                'ListString',{'H2
yield',num2str(H2_yield),...
            'CO yield',num2str( CO_yield),...
            'Ethanol Con.',num2str(Ethanol)},...
            'Name','Testing Result','ListSize',[200 80]);


end

%%%=================================================================
======
                %%% Compare_Callback
%%%=================================================================
======
function Compare_Callback(hObject, eventdata, handles)
        clear all
        filename='C:\MATLAB7\work\Ahmed_PhD\Data.xls';
        %%%%-- Output Data exp
        [H2_yield_exp]= xlsread(filename,'Sheet1','G2:G21');
        [CO_yield_exp]= xlsread(filename,'Sheet1','H2:H21');
        [Ethanol_exp]= xlsread(filename,'Sheet1','I2:I21');


        %%%%-- Output Data DOE
        [H2_yield_DOE]= xlsread(filename,'Sheet1','K2:K21');
        [CO_yield_DOE]= xlsread(filename,'Sheet1','L2:L21');
        [Ethanol_DOE]= xlsread(filename,'Sheet1','M2:M21');


        %%%%-- Output Data ANN
        [H2_yield_ANN]= xlsread(filename,'Sheet1','O2:O21');
        [CO_yield_ANN]= xlsread(filename,'Sheet1','P2:P21');
        [Ethanol_ANN]= xlsread(filename,'Sheet1','Q2:Q21');


        %% statistic Mesurement

        Static_exp=[H2_yield_exp; CO_yield_exp; Ethanol_exp];
        Static_DOE=[H2_yield_DOE; CO_yield_DOE; Ethanol_DOE];
        Static_ANN=[H2_yield_ANN; CO_yield_ANN; Ethanol_ANN];
```

```
        %%%% MSE in EFF The Testing
        [M1 N1] = size(Static_exp);
        error1 = (Static_DOE-Static_exp);
        MSE1=sum(sum(error1 .* error1))/ (M1 * N1);
        variance1=std(Static_exp).^2;
        Eff_exp_DOE=1-(MSE1./variance1)

        %%%% MSE in EFF The Testing
        [M2 N2] = size(Static_exp);
        error2 = (Static_ANN-Static_exp);
        MSE2=sum(sum(error2 .* error2))/ (M2 * N2);
        variance2=std(Static_exp).^2;
        Eff_exp_ANN=1-(MSE2./variance2);


        listdlg('PromptString','Efficiency Comparison Results',...
            'SelectionMode','single',    'ListString',{'Exp    Versus
N.M',num2str(Eff_exp_DOE),...
            'Exp Versus ANN',num2str(Eff_exp_ANN)},...
            'Name','Testing Result','ListSize',[200 80]);




        figure(1)
        set(gca,'color',[ 0 0 0])
        set(gcf,'color',[ 1 1 1])

        t=1:20;
        subplot(311),plot(t,H2_yield_exp,'r-o'), hold on
        subplot(311),plot(t,H2_yield_DOE,'g*')
        subplot(311),plot(t,H2_yield_ANN,'b.'), hold off
        legend('H2 yield (Exp)','H2 yield (DOE)','H2 yield (ANN)', -
1),
        title('H2 yield'),ylabel('H2 yield'),%axis([0 20 0 6])


        subplot(312),plot(t,CO_yield_exp,'r-o'), hold on
        subplot(312),plot(t,CO_yield_DOE,'g*')
        subplot(312),plot(t,CO_yield_ANN,'b.'), hold off
        legend('CO yield (Exp)','CO yield (DOE)','CO yield (ANN)', -
1),
        title('CO yield'),ylabel('CO yield'),%axis([0 20 0 6])


        subplot(313),plot(t,Ethanol_exp,'r-o'), hold on
        subplot(313),plot(t,Ethanol_DOE,'g*')
        subplot(313),plot(t,Ethanol_ANN,'b.'), hold off
        legend('Et Con.(Exp)','Et Con. (DOE)','Et Con. (ANN)', -1),
        title('Et    Con.'),xlabel('Number    of    run'),ylabel('Et
Con.'),%axis([0 20 0 6])

%%%==================================================================
======
                %%% Exit_Callback
```

```
%%%================================================================
======
function Exit_Callback(hObject, eventdata, handles)
selection=questdlg(['Do      You      Want      to      Close      '
get(handles.figure1,'Name') '?'],...
                   [' ' get(handles.figure1,'Name') '...'],...
                   'Yes','No','No');
                   if strcmp(selection,'No')
                       return
                   end
                   close('Hydrogen_Predection_ANN_System')

% --- Executes on selection change in Select_ANN.
function Select_ANN_Callback(hObject, eventdata, handles)



% --- Executes during object creation, after setting all properties.
function Select_ANN_CreateFcn(hObject, eventdata, handles)
if        ispc        &&        isequal(get(hObject,'BackgroundColor'),
get(0,'defaultUicontrolBackgroundColor'))
    set(hObject,'BackgroundColor','white');
end
```

APPENDIX I
LIST OF PUBLICATIONS

PAPARS

Bshish, A., Yaakob, Z., Narayanan, B., Ramakrishnan, R., & Ebshish, A. 2011. Steam-reforming of ethanol for hydrogen production. *Chemical Papers*, 65(3): 251-266.

Ebshish, A., Yaakob, Z., Taufiq-Yap, Y. H., Bshish, A., & Tasirin, S. M. 2012. Review of hydrogen production via glycerol reforming. *Proceedings of the Institution of Mechanical Engineers, Part A: Journal of Power and Energy*, 226(8): 1060-1075.

Ebshish, A., Yaakob, Z., Taufiq-Yup, Y., Bshish, A., & Shiabani, A. 2013. Catalytic Steam Reforming of Glycerol Over Cerium and Palladium-Based Catalysts for Hydrogen Production. *Journal of fuel cell science and technology*, 10(2):

Bshish, A., Yaakob, Z., Ebshish, A. & Alhasan, F. 2013. Hydrogen Production Via Ethanol Steam Reforming Over Ni/Al_2O_3 Catalysts: Effect of Ni Loading. *J. Energy Resour. Technol.*, 136(1): 012601.

Yaakob, Z., Bshish, A., Ebshish, A., Tasirin, S. M., & Alhasan, F. H. 2013. Hydrogen Production by Steam Reforming of Ethanol over Nickel Catalysts Supported on Sol Gel Made Alumina: Influence of Calcination Temperature on Supports. *Materials*, 6(6): 2229-2239.

Bshish, A., Yaakob, Z., Ebshish, A. & Abushammala, M.F.M. 2013. Statistical Design Optimization of Hydrogen Production through Ethanol Steam Reforming using a Ni/Al_2O_3 Catalyst. *Materials.* (Submitted).

CONFRENCES

Bshish, A., Yaakob, Z., Narayanan, B., Ramakrishnan, R. & Ebshish, A. 2010, Cyclohexane Oxidation over Ni/Cu Bimetal Doped Alumina. ^{6}th International Conference on Environmental Catalysis, September 12-15, 2010, Beijing China.

Bshish, A., Yaakob, Z., Narayanan, B. & Ebshish, A. 2011. Effect of Ni Loading on Hydrogen Production by Steam Reforming of Ethanol over Ni/Al_2O_3 Catalysts. *The 3rd International Conference on Fuel Cell & Hydrogen Technology (ICFCHT). 22-23 November, Kuala Lumpur, Malaysia.*

Yaakob, Z., Narayanan, B., Silija P. & Bshish, A. 2010. $Na_2Si_2O_5$ Solid Catalyst for the Transesterification of Ethylacetate. Sixth Tokyo Conference on Advanced Science and Technology, July 18-23, Sapporo, Japan**.**

Bshish, A., Yaakob, Z., Narayanan, B. & Ebshish, A. 2011. 4rd Engineering Postgraduate Conference (EPC). 4 – 5 October. Puri Pujangga – Universiti Kebangsaan Malaysia.

CITATION OF OUR PUBLICATION

Ahmed Bshish Edit
PhD Candidate Edit
Catalyst - Chemical Engineering - Hydrogen Production. Edit
No verified email Edit
My profile is private Edit Add homepage
Change photo
Photo updated.

Google scholar
Search Authors
My Citations - Help
Add co-authors
Wan Ramli Wan D... Add -
View all co-authors
Co-authors
No co-authors
Name
Email
Inviting co-author
Send invitation

Citation indices

	All	Since 2009
Citations	45	44
h-index	2	2
i10-index	1	1

Citations to my articles

Select: All, None Actions 1-7

Title / Author	Cited by	Year
Steam-reforming of ethanol for hydrogen production A Bshish, Z Yaakob, B Narayanan, R Ramakrishnan, A Ebshish Chemical Papers 65 (3), 251-266	36	2011
Steam reforming of glycerol over ni supported alumina xerogel for hydrogen production A Ebshish, Z Yaakob, B Narayanan, A Bshish, WRW Daud Energy Procedia 18, 552-559	4	2012
Review of hydrogen production via glycerol reforming A Ebshish, Z Yaakob, YH Taufiq-Yap, A Bshish, SM Tasirin Proceedings of the Institution of Mechanical Engineers, Part A: Journal of ...	2	2012
The Activity of Ni-Based Catalysts on Steam Reforming of Glycerol for Hydrogen Production ALIS EBSHISH, Z Yaakob, B Narayanan, AM Bshish, WR Wan Daud International Journal of Integrated Engineering 3 (1)	2	2011
Catalytic Steam Reforming of Glycerol Over Cerium and Palladium-Based Catalysts for Hydrogen Production A Ebshish, Z Yaakob, YH Taufiq-Yap, A Bshish, A Shaibani Journal of Fuel Cell Science and Technology 10 (2), 021003	1	2013
Hydrogen Production Via Ethanol Steam Reforming Over Ni/Al2O3 Catalysts: Effect of Ni Loading A Bshish, Z Yaakob, A Ebshish, FH Alhasan Journal of Energy Resources Technology 136 (1), 012601		2014
Hydrogen Production by Steam Reforming of Ethanol over Nickel Catalysts Supported on Sol Gel Made Alumina: Influence of Calcination Temperature on Supports Z Yaakob, A Bshish, A Ebshish, SM Tasirin, FH Alhasan Materials 6 (6), 2229-2239		2013

Select: All, None Actions 1-7

Dates and citation counts are estimated and are determined automatically by a computer program.